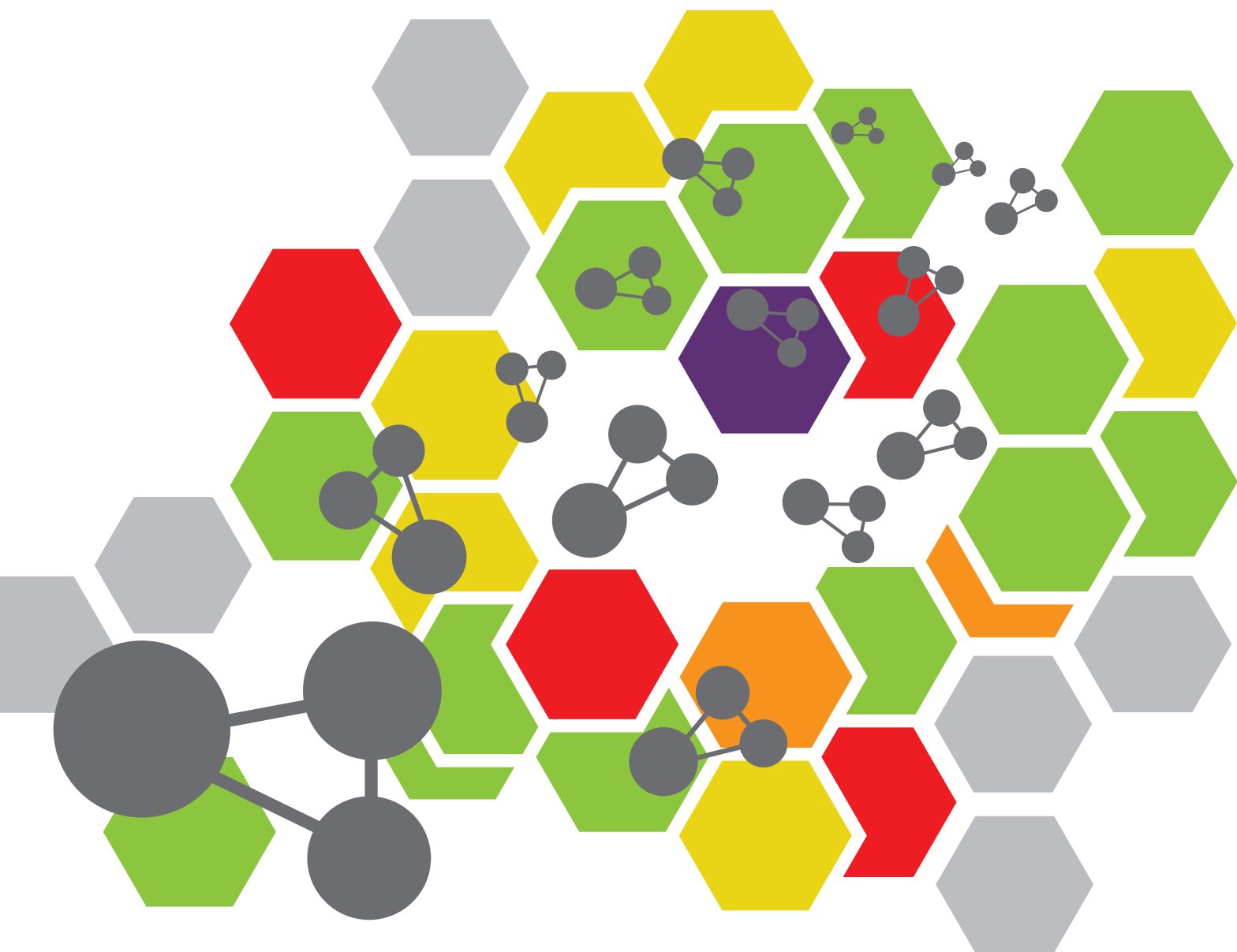


DESIGN, SYNTHESIS, AND APPLICATION OF NOVEL Π -CONJUGATED MATERIALS

EDITED BY: Haichang Zhang, Taotao Ai and Qixin Zhou
PUBLISHED IN: Frontiers in Chemistry





frontiers

Frontiers eBook Copyright Statement

The copyright in the text of individual articles in this eBook is the property of their respective authors or their respective institutions or funders. The copyright in graphics and images within each article may be subject to copyright of other parties. In both cases this is subject to a license granted to Frontiers.

The compilation of articles constituting this eBook is the property of Frontiers.

Each article within this eBook, and the eBook itself, are published under the most recent version of the Creative Commons CC-BY licence.

The version current at the date of publication of this eBook is CC-BY 4.0. If the CC-BY licence is updated, the licence granted by Frontiers is automatically updated to the new version.

When exercising any right under the CC-BY licence, Frontiers must be attributed as the original publisher of the article or eBook, as applicable.

Authors have the responsibility of ensuring that any graphics or other materials which are the property of others may be included in the CC-BY licence, but this should be checked before relying on the CC-BY licence to reproduce those materials. Any copyright notices relating to those materials must be complied with.

Copyright and source acknowledgement notices may not be removed and must be displayed in any copy, derivative work or partial copy which includes the elements in question.

All copyright, and all rights therein, are protected by national and international copyright laws. The above represents a summary only. For further information please read Frontiers' Conditions for Website Use and Copyright Statement, and the applicable CC-BY licence.

ISSN 1664-8714

ISBN 978-2-88966-481-8

DOI 10.3389/978-2-88966-481-8

About Frontiers

Frontiers is more than just an open-access publisher of scholarly articles: it is a pioneering approach to the world of academia, radically improving the way scholarly research is managed. The grand vision of Frontiers is a world where all people have an equal opportunity to seek, share and generate knowledge. Frontiers provides immediate and permanent online open access to all its publications, but this alone is not enough to realize our grand goals.

Frontiers Journal Series

The Frontiers Journal Series is a multi-tier and interdisciplinary set of open-access, online journals, promising a paradigm shift from the current review, selection and dissemination processes in academic publishing. All Frontiers journals are driven by researchers for researchers; therefore, they constitute a service to the scholarly community. At the same time, the Frontiers Journal Series operates on a revolutionary invention, the tiered publishing system, initially addressing specific communities of scholars, and gradually climbing up to broader public understanding, thus serving the interests of the lay society, too.

Dedication to Quality

Each Frontiers article is a landmark of the highest quality, thanks to genuinely collaborative interactions between authors and review editors, who include some of the world's best academicians. Research must be certified by peers before entering a stream of knowledge that may eventually reach the public - and shape society; therefore, Frontiers only applies the most rigorous and unbiased reviews.

Frontiers revolutionizes research publishing by freely delivering the most outstanding research, evaluated with no bias from both the academic and social point of view. By applying the most advanced information technologies, Frontiers is catapulting scholarly publishing into a new generation.

What are Frontiers Research Topics?

Frontiers Research Topics are very popular trademarks of the Frontiers Journals Series: they are collections of at least ten articles, all centered on a particular subject. With their unique mix of varied contributions from Original Research to Review Articles, Frontiers Research Topics unify the most influential researchers, the latest key findings and historical advances in a hot research area! Find out more on how to host your own Frontiers Research Topic or contribute to one as an author by contacting the Frontiers Editorial Office: frontiersin.org/about/contact

DESIGN, SYNTHESIS, AND APPLICATION OF NOVEL Π -CONJUGATED MATERIALS

Topic Editors:

Haichang Zhang, Qingdao University of Science and Technology, China

Taotao Ai, Shaanxi University of Technology, China

Qixin Zhou, University of Akron, United States

Citation: Zhang, H., Ai, T., Zhou, Q., eds. (2021). Design, Synthesis, and Application of Novel π -Conjugated Materials. Lausanne: Frontiers Media SA.
doi: 10.3389/978-2-88966-481-8

Table of Contents

- 05 Editorial: Design, Synthesis, and Application of Novel π -Conjugated Materials**
Zhicheng Dai, Taotao Ai, Qixin Zhou and Haichang Zhang
- 07 Efficient Colorimetric Fluoride Anion Chemosensors With Varied Colors Based on Simple Aminobenzodifuranone Organic Π -Conjugated Dyes**
Zhi Feng Deng, Rui Li, Jie Ting Geng, Meng Zheng, Lei Quan Li, Xin Shi, Wen Qi Ren, Zi Yue Meng, Zhuo Ting Ji and Jing Hua
- 13 Synthesis of 2,1,3-Benzoxadiazole Derivatives as New Fluorophores—Combined Experimental, Optical, Electro, and Theoretical Study**
Tiago E. A. Frizon, André A. Vieira, Fabricia N. da Silva, Sumbal Saba, Giliandro Farias, Bernardo de Souza, Eduardo Zapp, Michell N. Lôpo, Hugo de C. Braga, Felipe Grillo, Sergio F. Curcio, Thiago Cazati and Jamal Rafique
- 27 Development of Light-Responsive Poly(γ -Benzyl-L-Glutamate) as Photo Switches by a One-Step NCA Method**
Pin Chen, Jingyang Kong, Xin Wang, Weiye Ma, Xia Yang, Yuqing Qin and Xiaohong Hu
- 39 Electrochemical Synthesis and Electro-Optical Properties of Dibenzothiophene/Thiophene Conjugated Polymers With Stepwise Enhanced Conjugation Lengths**
Kaiwen Lin, Caiting Li, Wang Tao, Jilong Huang, Qinghua Wu, Zijin Liu, Yangfan Zhang, Da Wang and Xi Liu
- 48 Diketopyrrolopyrrole (DPP)-Based Materials and Its Applications: A Review**
Wei Wei Bao, Rui Li, Zhi Cheng Dai, Jian Tang, Xin Shi, Jie Ting Geng, Zhi Feng Deng and Jing Hua
- 54 Rational Design of π -Conjugated Tricoordinated Organoboron Derivatives With Thermally Activated Delayed Fluorescent Properties for Application in Organic Light-Emitting Diodes**
Ruifa Jin and Jingfan Xin
- 63 Metal-Ligand Coordination Induced Ionochromism for π -Conjugated Materials**
Jinhui Liu, Long Han, Jieting Geng, Jing Hua and Zhaobo Wang
- 72 Terpyridine-Containing π -Conjugated Polymers for Light-Emitting and Photovoltaic Materials**
Pan Liu, Ganhui Shi and Xuegang Chen
- 78 The Application of Organic Semiconductor Materials in Spintronics**
Yixiao Zhang, Lidan Guo, Xiangwei Zhu and Xiangnan Sun
- 86 IDTI Dyes for Fluoride Anion Chemosensors**
Xinqiang Yuan, Xin Shi, Cheng Wang, Yuqian Du, Peng Jiang, Xizhou Jiang, Yongqiang Sui, Xiaoli Hao and Lin Li

91 *The Crystallinity Control of Polymer Donor Materials for High-Performance Organic Solar Cells*

Dingding Qiu, Muhammad Abdullah Adil, Kun Lu and Zhixiang Wei

112 *A Quantum-Mechanical Looking Behind the Scene of the Classic G-C Nucleobase Pairs Tautomerization*

Ol'ha O. Brovarets', Alona Muradova and Dmytro M. Hovorun



Editorial: Design, Synthesis, and Application of Novel π -Conjugated Materials

Zhicheng Dai¹, Taotao Ai², Qixin Zhou³ and Haichang Zhang^{1*}

¹ Key Laboratory of Rubber-Plastics of Ministry of Education/Shandong Province (QUST), School of Polymer Science & Engineering, Qingdao University of Science & Technology, Qingdao, China, ² National and Local Joint Engineering Laboratory for Slag Comprehensive Utilization and Environmental Technology, School of Material Science and Engineering, Shaanxi University of Technology (SNUT), Hanzhong, China, ³ National Center for Education and Research on Corrosion and Materials Performance, Department of Chemical and Biomolecular Engineering, The University of Akron, Akron, OH, United States

Keywords: π -conjugated materials, electronics, OPV, OLED, sensor

Editorial on the Research Topic

Design, Synthesis, and Application of Novel π -Conjugated Materials

In recent years, extensive research efforts have been dedicated to the development of novel π -conjugated materials, including small molecules, oligomers, and polymers. These materials have been adapted to various applications, such as in organic-field effect transistors (OFET), organic photovoltaic (OPV) sensors, and organic light emitting diodes (OLED), etc. Among these, π -Conjugated materials with various applications have been designed with specific molecular concepts in mind. This Research Topic includes 12 articles outlining original research and reviewing and describing a series of novel π -conjugated materials with various applications. The articles provide an overview of different types of π -conjugated materials and how they are designed and characterized, providing an overview of progress and development in this field.

Among the articles selected for this Research Topic, seven are original research articles. The development of high-sensitivity naked-eye detection sensors for fluoride anions is crucial and challenging because fluoride anions play a key role in human health and chemical engineering. Yuan et al. reported a new type of colorimetric chemosensor dye based on indaceno(1,2-b:5,6-b')dithiophene]-2,7-diylbis(methanylylidene) bis(indolin-2-one) (IDTI). IDTI can interact with fluoride anions to exhibit color changes that are visible to the naked eye, with changes occurring from red to orange or yellow and from purple to green or blue under ambient light and 365-nm UV light, respectively. The spectroscopic studies indicated that IDTI could be used to quantitatively analyze the fluoride concentration with a detection limit as low as 1×10^{-7} M, which is one of the highest sensitivity fluoride sensors reported (Yuan et al.). Another research paper describes how Deng's group developed a simple compound based on aminobenzodifuranone (ABDF) to detect fluoride anions. ABDF responds to only the fluoride anion among various anions and exhibits a color change from dark blue to various colors (colorless, yellow, orange, and red) in different common organic solvents. This work provides new insights into the development of highly sensitive and selective fluoride chemosensors, and the functionality required to detect the polarity of the solvents (Deng et al.).

The structure-performance relationship of conjugated polymers has drawn significant attention. Frizon et al. prepared and characterized a series of novel π -conjugated fluorescent materials based on derivatives of 2,1,3-benzoxadiazole (BTD). The photophysical behavior of the compounds was investigated using spectroscopic techniques (Frizon et al.). In another study included in this Research Topic, Lin et al. synthesized six conjugated polymers using a similar polymer backbone with different numbers of thiophene units, using electrochemical polymerization, showing that increasing the π -conjugated length could significantly improve the electrochemical stability of polymers.

OPEN ACCESS

Edited and reviewed by:

Iwao Ojima,
Stony Brook University, United States

*Correspondence:

Haichang Zhang
haichangzhang@hotmail.com

Specialty section:

This article was submitted to
Organic Chemistry,
a section of the journal
Frontiers in Chemistry

Received: 28 November 2020

Accepted: 14 December 2020

Published: 11 January 2021

Citation:

Dai Z, Ai T, Zhou Q and Zhang H
(2021) Editorial: Design, Synthesis,
and Application of Novel
 π -Conjugated Materials.
Front. Chem. 8:634698.
doi: 10.3389/fchem.2020.634698

Thermally activated delayed fluorescent (TADF) materials have been considered as one of the most promising candidates in OLED because of their capability in harvesting all the triplet excitons. However, designing high performance TADF materials is challenging. Jin and Xin designed and investigated a series of π -conjugated materials with a donor-acceptor system. The authors discovered that efficient separation could be observed between donor and acceptor fragments: a rational design for efficient TADF materials and charge transport materials in OLED applications (Jin and Xin).

Synthesized polypeptide is a chemical component and secondary structure to a natural protein that plays a key role in bio-related fields. However, polypeptide exhibits no switching properties and shows no benefits as a potential control component. Hu's group synthesized and characterized light-responsive poly(γ -benzyl-L-glutamate)s using a simple one-step NCA method, which could facilitate the trans \rightarrow cis transition and shorten the recovery time of the cis \rightarrow trans process under different conditions (Chen et al.).

Tautomerism has been an active area of research over the past few decades. Upon investigation of a series of G-C nucleobase pairs for the first time, Brovarets's group established that the G-C base pair is incorporated into the DNA/RNA double helix with parallel strands in the form of the $G^* \cdot C \cdot O_2 C^*_{O_2}$ (rWC), $G \cdot C^*$ (rw_{WC}), and $G^* \cdot C$ (rw_{WC}) tautomers, which are in rapid tautomeric equilibrium with each other (Brovarets' et al.).

This Research Topic also includes five review articles. Diketopyrrolopyrrole (DPP) and its derivatives as an electron-deficient unit have been developed in various applications and attracted significant attention in recent years due to its distinctive properties. The Research Topic also includes a study by Deng et al. on the use of DPP-based materials in OFETs, OPVs, sensors, two-photon absorption, and coatings, etc. In addition, a prospective study provides insights into ways of further functionalizing DPP and its derivatives, such as enlargement of π -conjugation, modification of alkyl chain, design of high-performance polymers for the promotion in π -conjugated materials applications (Bao et al.).

Supramolecular polymeric materials are widely used in many fields and have been rapidly progressing in the past decade. From the perspective of the terpyridine-based polymers, Liu et al. not only summarized the development of some novel molecules in the field of energy conversion but also highlighted the Zn(II)- and Ru(II)-containing supramolecular polymers in light-emitting materials and photovoltaic materials. This review also showed that terpyridine-based materials with easy modification, organic/inorganic hybrid, definite structure, etc., open a new pathway to construct novel structures with interesting properties in photoelectric materials (Liu et al.).

Ionochromism is realized through the coordination between metal and ligand, resulting in sensitivity to metal ions, which could be used as metal sensors. Liu et al. reviewed not only an overview of the developments of ionochromic effect according to the type of ligands, but also highlighted the mechanism of ionochromism, metal recognition sensitivity, and their application in sensors. Additionally, the authors pointed out that the preparation of chemical sensors with

high sensitivity, long-term stability, and selectivity is still a critical challenge. This review provides a rational structure design and evaluation of chemosensors. Apart from that, π -conjugated materials with semiconductor behavior are regarded as promising spin-transport materials due to the weak spin-orbit coupling interaction and hence long spin relaxation time (Liu et al.). Zhang et al. reviewed organic semiconductors from the perspectives of spin transport, spin functional devices, all-organic spin devices, spin manipulation, and then summarized their challenges. Furthermore, the authors observe that various organic semiconductors need to be tested and that the strategic step design of semiconductors should be explored to overcome the present challenges (Zhang et al.).

OPV is one of the most promising energy generation technologies. To build high performance OPV, the crystalline control of the materials is crucial. However, this topic has yet to attract enough attention in the scientific and industrial community. In their contribution, Qiu et al. review the structure and crystallinity of the representative polymer donor materials and corresponding device properties. Several typical methods for controlling the crystallinity of materials were also addressed. The author claimed that only the effort of all the scientists in terms of materials design, theoretical research, device optimization, and OSCs could then be widely used in everyday life, with exceptional market prospects in the next few years (Qiu et al.).

The 12 research articles included here indicate that the optical and electrochemical properties, solubility, charge transferability, and other intrinsic physical and chemical properties of materials could be easily controlled by adjusting molecular structures. Thus, the molecular design concept plays a critical role in high performance π -conjugated materials and their potential applications.

AUTHOR CONTRIBUTIONS

ZD prepared the manuscript. TA, QZ, and HZ revised the manuscript and are topic editors of this Research Topic. All authors contributed to the article and approved the submitted version.

ACKNOWLEDGMENTS

The authors acknowledged the support from Natural Science Foundation of China, under Grant 21805151, Natural Science Foundation of Shandong Province, China, under Grant ZR2018MB024, Young Taishan Scholars under Grant 201909120, and Shaanxi University of Technology (SLGPT2019KF01-01, SLG1901).

Conflict of Interest: The authors declare that the research was conducted in the absence of any commercial or financial relationships that could be construed as a potential conflict of interest.

Copyright © 2021 Dai, Ai, Zhou and Zhang. This is an open-access article distributed under the terms of the Creative Commons Attribution License (CC BY). The use, distribution or reproduction in other forums is permitted, provided the original author(s) and the copyright owner(s) are credited and that the original publication in this journal is cited, in accordance with accepted academic practice. No use, distribution or reproduction is permitted which does not comply with these terms.



Efficient Colorimetric Fluoride Anion Chemosensors With Varied Colors Based on Simple Aminobenzodifuranone Organic Π -Conjugated Dyes

Zhi Feng Deng^{1*†}, Rui Li^{2†}, Jie Ting Geng², Meng Zheng², Lei Quan Li¹, Xin Shi¹, Wen Qi Ren¹, Zi Yue Meng¹, Zhuo Ting Ji¹ and Jing Hua^{2*}

¹ National and Local Joint Engineering Laboratory for Slag Comprehensive Utilization and Environmental Technology, School of Materials Science and Engineering, Shaanxi University of Technology (SUT), Hanzhong, China, ² Key Laboratory of Rubber-Plastics of Ministry of Education, Shandong Province, School of Polymer Science & Engineering, Qingdao University of Science & Technology, Qingdao, China

OPEN ACCESS

Edited by:

Qixin Zhou,
University of Akron, United States

Reviewed by:

Haoran Wang,
University of Akron, United States
Yang Zhou,
Teknor Apex, United States

*Correspondence:

Zhi Feng Deng
dengzf@sut.edu.cn
Jing Hua
huajing72@qust.edu.cn

[†]These authors have contributed
equally to this work

Specialty section:

This article was submitted to
Organic Chemistry,
a section of the journal
Frontiers in Chemistry

Received: 09 January 2020

Accepted: 10 March 2020

Published: 15 April 2020

Citation:

Deng ZF, Li R, Geng JT, Zheng M,
Li LQ, Shi X, Ren WQ, Meng ZY, Ji ZT
and Hua J (2020) Efficient Colorimetric
Fluoride Anion Chemosensors With
Varied Colors Based on Simple
Aminobenzodifuranone Organic
 Π -Conjugated Dyes.
Front. Chem. 8:231.
doi: 10.3389/fchem.2020.00231

High selectivity and sensitivity detection of fluoride anions (F^-) in an organic solution by the naked eye has always been a challenge. In this investigation, a simple compound based on aminobenzodifuranone (ABDF) was designed and synthesized. Deprotonation of the amino moiety caused by F^- is responsible for a color change from dark blue to various colors (colorless, yellow, orange, and red) in different common organic solvents due to a blue shift over 200 nm in the UV/Vis spectrum. The color change is quite visible to the naked eye under ambient light. The detection limit for F^- can reach a concentration of as low as 5.0×10^{-7} M with high selectivity, even in a solution containing multiple anions.

Keywords: sensors, dyes, aminobenzodifuranone, fluoride anion, hydrogen bonding, detection

HIGHLIGHTS

- A simple aminobenzodifuranone (ABDF) dye was synthesized and used as fluoride anion sensor.
- ABDF is highly selectivity and sensitivity for fluoride anion with detection limitation as low as 5×10^{-7} M.
- ABDF detect fluoride anion in different solvent in response varied colors which is sensitive for the naked eye detection.
- The deprotonation of amino moiety caused by F^- is responsible for the color change which is sensitive for the naked eye.

INTRODUCTION

As one of the smallest anions and the most electronegative atom, fluoride with high charge density has special functions in chemical industry, organic synthesis, military fields, and medical and biological processes (Wade et al., 2010; Zhou et al., 2014). Environmental pollution by fluoride anions (F^-) is one of the main problems to be addressed in the treatment of drinking water (Li et al., 2017). With the rapid development of the chemical industry, F^- has come to exist not only in the aqueous environment but also in organic media such as fluoride anion-containing

pesticides and waste organic liquor (Clark, 1980). Recognition and detection of fluoride in organic solvent with a simple sensor and minimal instrumental assistance are imperative for practical applications (Yang et al., 2013; Kaur and Choi, 2015; Curnow et al., 2018; Tang et al., 2018; Murfin et al., 2020). Among various F^- sensors, fluorescence sensors have been widely investigated due to their multiple advantages (Li et al., 2017). However, those allowing naked-eye detection with high selectivity and sensitivity are more interesting, promising, and challenging due to offering simple and straightforward F^- detection without using auxiliary equipment.

Fluoride anions exist in various organic solutions during chemical synthesis. Many studies have been reported on that focused on materials that detect F^- in a single organic solution, such as tetrahydrofuran (Sun et al., 2017), acetonitrile (Han et al., 2007), or chloroform (Lee et al., 2001). To the best of our knowledge, F^- sensors with naked-eye detection in different solutions, signaling via color changes, have not yet been developed. Such sensors might be possible in materials with

solvatochromic behavior since they exhibit different colors in different solvents. Amino-substituted benzodifuranone (ABDF, **Figure 1A**) is a deep blue-colored dye that has attracted our attention due to its good photo-stability and interesting solvatochromic behavior (Zhang et al., 2014; Deng et al., 2018). The NH unit in the ABDF dye can undergo hydrogen bonding with the carbonyl group in the ABDF core (Deng et al., 2018). Zhang and others reported that the hydrogen bond formed could be associated with the molecular packing in the solid state (Yao et al., 2015; Oh et al., 2016). Further, Du and Hu's research group reported that thin film with good packing or crystallinity is beneficial for charge carrier mobility (Hu et al., 2000; Zhang et al., 2017, 2018; Du et al., 2018; Muhammad et al., 2020). Hence, the small ABDF molecule has been used in organic field-effect transistors with high performance, as reported by our group (Deng et al., 2018). Very recently, Zhang and co-authors also developed pigments with an amino unit in the color-changing coating and a UV-resistant coating (Zeng et al., 2018, 2019; Zhang et al., 2020). In this work, the amino units might

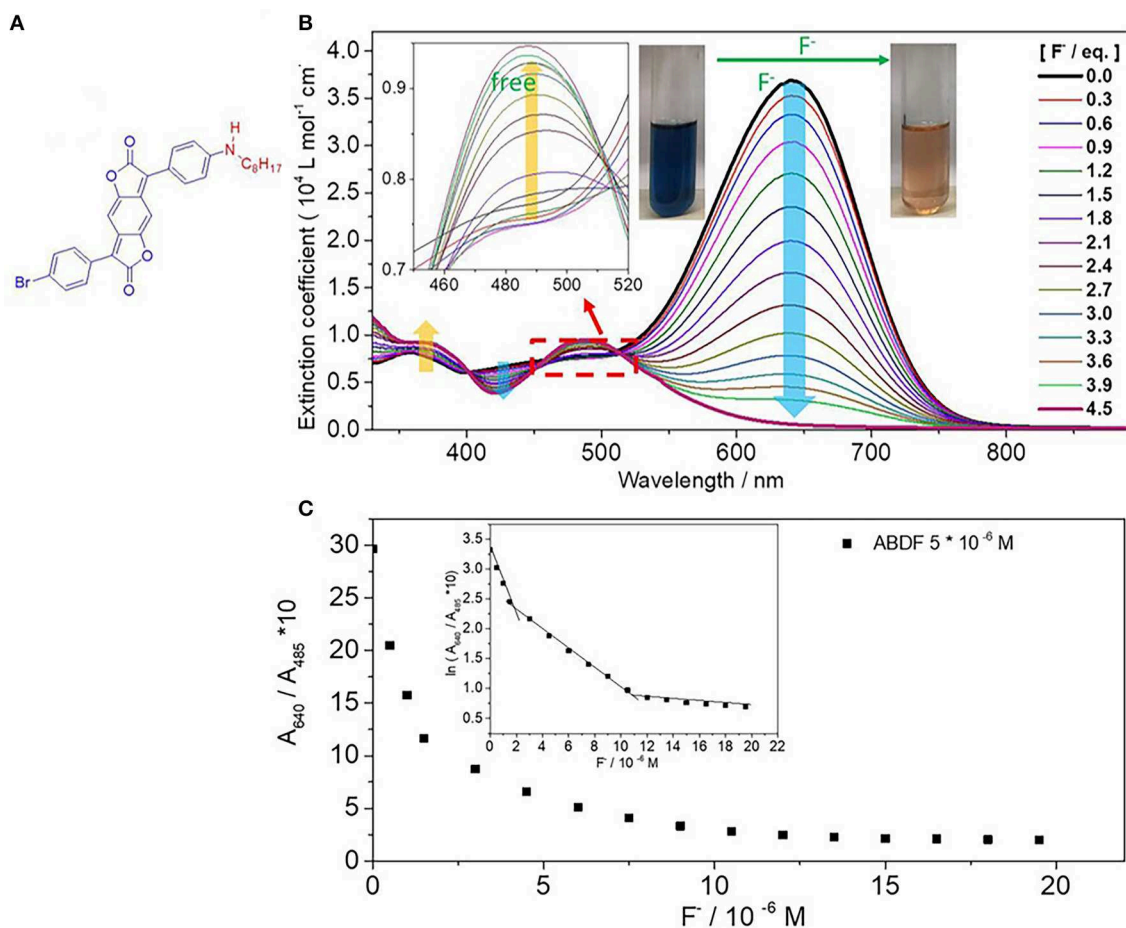


FIGURE 1 | (A) Chemical structure of ABDF. **(B)** UV/Vis absorption spectra of ABDF (1.0×10^{-5} M) in the presence of F^- (0–4.5 eq.) in THF. The insets are the enlargement of UV/Vis spectra from 450 to 520 nm and color change of ABDF upon adding F^- . **(C)** Ten times the absorption intensity ratio of ABDF (5×10^{-6} M after mixing with F^- in THF) between 640 and 485 nm (A_{640}/A_{485} nm) vs. fluoride anion concentration. The inset is the natural logarithm of 10 times the absorption intensity ratio A_{640}/A_{485} nm vs. fluoride anion concentration.

be deprotonation in F^- solution, leading to a color variance detectable by the naked eye. ABDF exhibits diverse colors in different solutions, which may cause this chromophore to exhibit varied colors in different solvents. In addition, ABDF is soluble in most common organic solutions, with a high extinction coefficient of up to $6.5 \times 10^4 \text{ L mol}^{-1} \text{ cm}^{-1}$ (in dichloromethane, DCM) (Zhang et al., 2018). This could lead ABDF to be highly sensitive to F^- . In this work, ABDF as a chemosensor for F^- was firstly investigated.

RESULTS AND DISCUSSION

The synthesis of ABDF was described in our previous work with B. Tieke' groups (Zhang et al., 2018; Muhammad et al., 2020), and the details are described in the **Supporting Information**. The interaction between ABDF chromophore and F^- was firstly investigated in THF solution through spectrophotometric titration experiments. A standard solution of tetrabutylammonium fluoride (TBAF, $1.0 \times 10^{-3} \text{ M}$) was gradually added into a $1.0 \times 10^{-5} \text{ M}$ solution of ABDF in THF. As can be seen from **Figure 1B**, ABDF exhibits a high extinction coefficient of up to $3.7 \times 10^4 \text{ L mol}^{-1} \text{ cm}^{-1}$. With progressive addition of fluoride anion, the absorption intensity of the spectral peak at 640 nm is gradually decreased and finally disappears, while a new absorption peak at 485 nm emerges and increases. In addition, the absorption intensity at a broad band between 398 and 445 nm exhibits a steady decrease; meanwhile, the absorption intensity band between 330 and 400 nm is increased. The inset of **Figure 1B** shows that the color of the ABDF solution is changed from dark blue to orange upon adding F^- . Both colors can be sensed by the naked eye under ambient light. ABDF is thus a F^- sensor allowing the naked-eye detection.

To examine the sensitivity of the sensors toward F^- in THF solution, the ratiometric curve was investigated. **Figure 1C** shows the ratiometric curves of the absorption intensity ratio of ABDF in THF between 640 and 485 nm vs. F^- concentration, which seems to be a quadratic function. The natural logarithm of **Figure 1C** results in the inset figure. As can be seen from the inset of **Figure 1C**, there are three slopes in the correlation, and the cross points of fitting lines are at $1.7 \times 10^{-6} \text{ M}$ and $1.1 \times 10^{-5} \text{ M}$, respectively. The linear fit relationships between absorption intensity and F^- concentration are: $\ln(A_{640}/A_{485} \text{ nm}) = -0.57 [F^-] + 3.31$ ($5.0 \times 10^{-7} \text{ M} \leq [F^-] < 1.7 \times 10^{-6} \text{ M}$), $\ln(A_{640}/A_{485} \text{ nm}) = -0.16 [F^-] + 2.60$ ($1.7 \times 10^{-6} \text{ M} \leq [F^-] < 1.1 \times 10^{-5} \text{ M}$), and $\ln(A_{640}/A_{485} \text{ nm}) = -0.16 [F^-] + 2.60$ ($1.1 \times 10^{-5} \text{ M} \leq [F^-] \leq 2.0 \times 10^{-5} \text{ M}$). The signal output discrimination is still distinct at a F^- concentration of $5.0 \times 10^{-7} \text{ M}$, which indicates that the sensor is highly sensitive for F^- concentration and can offer quantitative information.

For the purposes of examining the sensing selectivity of ABDF to F^- , a THF solution containing other anions, namely Cl^- , Br^- , I^- , NO_3^- , SO_4^{2-} , SCN^- , ClO_4^- , ACO^- , and $H_2PO_4^-$ (as tetrabutylammonium salts), was used. **Figure 2A** shows that ABDF solution does not change color when any additional anions except for F^- are added. Mixing the solution with multiple anions afforded no noticeable color change. Once F^- is added into the

mixture, the color changes immediately from blue to orange (**Figure 2A**). This indicates that ABDF is a highly selective sensor for F^- and that the presence of other anions does not alter its effectiveness.

Figures 2B,C show photographs and normalized UV/vis spectra of ABDF in various common organic solutions with different polarities. ABDF exhibits positive solvatochromic behavior and various colors in different solvents (**Figure 2B**). The UV/Vis spectra of ABDF exhibit a red-shift from non-polar solvent to polar solvent (**Figure 2C**), which could be ascribed to several specific and non-specific solute-solvent interactions. As can be seen from **Figure S1**, the proton signals of ABDF in DCM- d_2 are shifted to the low field compared with in DMSO- d_6 . It should be noticed that the signals from amino (NH) units with a chemical shift of 4.34 ppm moved to 7.06 ppm. This could be ascribed to change in the chemical structure; a suggested mechanism is shown in **Figure S2**. Interestingly, the ABDF solution exhibited various colors (colorless, blue, orange, red) in different F^- solvents (**Figure 2B**). This could provide ABDF with detection performance not only for F^- but also for the polarity (polar or non-polar) of the solvent of F^- . To the best of our knowledge, this is the first time that sensor detection of fluoride anions in different organic solvents, showing varied colors, has been reported.

In order to further investigate the detection performance of ABDF for F^- in polar solvent, we measured and analyzed a series of UV/Vis spectra of ABDF with a concentration of $1.0 \times 10^{-5} \text{ M}$ in DMSO in the presence of F^- from 0.0 to 4.5 eq. and the absorption intensity ratio of ABDF ($5 \times 10^{-6} \text{ M}$ in DMSO) between 673 and 494 nm vs. F^- concentration (**Figures S3, S4**). Similar to **Figure 1**, with progressive addition of fluoride anions, the absorption intensity of the spectral peak at 673 nm gradually decreases and finally disappears, while the absorption intensity at 494 nm steadily increases. The inset of **Figure S3** shows that the color of the ABDF solution is changed from dark blue to red upon adding F^- . The color change is significantly different to that of ABDF in THF solution with F^- . We assumed that the different colors originated from different chemical structures (**Figure S2**). **Figure S4** shows that the detection limit of ABDF for F^- in DMSO (polar solvent) is as low as $1.0 \times 10^{-6} \text{ M}$. ABDF is a sensitive fluoride anion sensor allowing naked-eye detection in various organic solvents. After F^- sensing, the UV/Vis absorption spectra exhibited a blue-shift (**Figure 2C**). To the best of our knowledge, most F^- sensors exhibit a red-shift with F^- detection (Lee et al., 2001; Han et al., 2007; Yang et al., 2013; Sun et al., 2017). **Figure 2C** shows that the UV/Vis absorption of ABDF exhibits a blue-shift over 200 nm once it has interacted with F^- . This could be ascribed to the donor ability of the amino units being weaker after sensing F^- , which decreases the push-pull electron effect within the ABDF molecular structure.

The color change of ABDF in the presence of F^- may be due to the deprotonation of the amino moiety (NH) by F^- (inter-molecular proton transfer, IPT; **Figure 2D**, **Figure S2**). To confirm our assumption and further understand the interaction between F^- and the donor, ^1H NMR experiments were carried out in $CDCl_3$. As shown in **Figure 2D**, the specific signal for

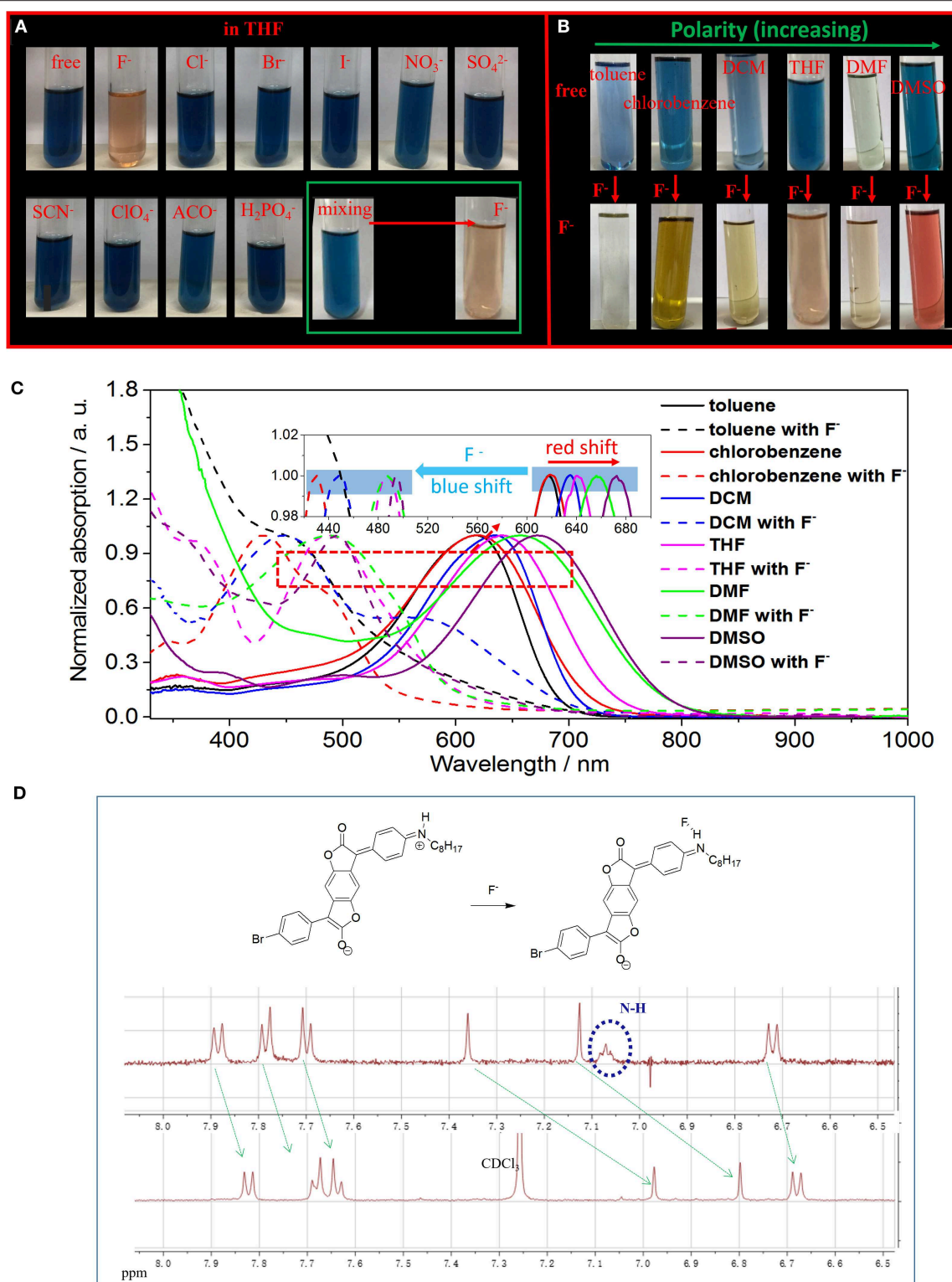


FIGURE 2 | (A) Photographs of ABDF in THF solution before and after the addition of 4.5 eq. of different anions or together with F^- (lower, right corner). **(B)** Photographs of ABDF in various solutions before and after the addition of 4.5 eq. of F^- . **(C)** Normalized UV/Vis spectra of ABDF in various organic solutions before and after addition of 4.5 eq. of F^- . **(D)** Proposed mechanism for single fluoride anion detection of ABDF, and the partial 1H NMR titration spectra of ABDF in $CDCl_3$ in the presence of 5 eq. of TBAF.

amino protons at 7.06 ppm disappeared, and other proton signals from the core of ABDF shifted to lower ppm. This indicates the occurrence of an IPT event and the formation of hydrogen bonding between F^- and the proton on the amino N-H. ABDF is electronically neutral in the absence of F^- , while a negatively charged species with one negative charge is formed in the presence of F^- (Figure 2D).

CONCLUSION

In this article, a new kind of colorimetric chemosensor based on aminobenzodifuranone that has high selectivity and sensitivity for F^- was developed. ABDF responds to only F^- among various anions and has a detection limit as low as 5.0×10^{-7} M. A large absorption blue-shift of 200 nm occurred upon adding F^- , which is manifested as a color change from dark blue to various colors (colorless, yellow, orange, and red) in different common organic solvents. All the colors are detectable by the naked eye under ambient light, which means the ABDF is not only a highly sensitive and selective F^- sensor allowing naked-eye detection, but it can also detect the polarity (polar or non-polar) of F^- solvents. The analyses of 1H NMR titration spectra have confirmed that F^- causes deprotonation of the amino moiety. ABDF is a promising colorimetric chemosensor for fluoride anion.

REFERENCES

- Clark, J. H. (1980). Fluoride ion as a base in organic synthesis. *Chem. Rev.* 80, 429–452. doi: 10.1021/cr60327a004
- Curnow, O. J., MacFarlane, D. R., and Walst, W. J. (2018). Fluoride ionic liquids in salts of ethylmethylimidazolium and substituted cyclopropenium cation families. *Front. Chem.* 6:603. doi: 10.3389/fchem.2018.00603
- Deng, Z. F., Yang, K., Li, L. Q., Bao, W. W., Hao, X. L., Ai, T. T., et al. (2018). Solution processed air-stable p-channel organic crystal field-effect transistors of Aminobenzodifuranone. *Dye Pigm.* 151, 173–178. doi: 10.1016/j.dyepig.2017.12.052
- Du, H. L., Ma, C. Y., Ma, W. X., and Wang, H. T. (2018). Microstructure evolution and dielectric properties of Ce-doped $SrBi_4Ti_4O_{15}$ ceramics synthesized via glycine-nitrate process. *Appl. Ceram.* 12, 303–312. doi: 10.2298/PAC1804303D
- Han, F., Bao, Y. H., Yang, Z. G., Fyles, T. M., Zhao, J. Z., Peng, X. J., et al. (2007). Simple bithiocarbonohydrazones as sensitive, selective, colorimetric, and switch-on fluorescent chemosensors for fluoride anions. *Chem. Eur. J.* 13, 2880–2892. doi: 10.1002/chem.200600904
- Hu, Y. H., Motzer, H. R., Etcheberria, A. M., Fernandez-Berridi, M. J., Iruin, J. J., Painter, P. C., et al. (2000). Concerning the self-association of N-vinyl pyrrolidone and its effect on the determination of equilibrium constants and the thermodynamics of mixing. *Macromol. Chem. Phys.* 201, 705–714. doi: 10.1002/(SICI)1521-3935(20000301)201:6<705::AID-MACP705>3.0.CO;2-9
- Kaur, M., and Choi, D. H. (2015). Diketopyrrolopyrrole: brilliant red pigment dye-based fluorescent probes and their applications. *Chem. Soc. Rev.* 44, 58–77. doi: 10.1039/C4CS00248B
- Lee, K. H., Lee, H.-Y., Lee, D. H., and Hong, J.-I. (2001). Fluoride-selective chromogenic sensors based on azophenol. *Tetrahedron Lett.* 42, 5477–5449. doi: 10.1016/S0040-4039(01)01011-5
- Li, M., Liu, Z. J., Wang, H. C., Sedgwick, A. C., Gardiner, J. E., Bull, S. D., et al. (2017). Dual-function cellulose composites for fluorescence detection and removal of fluoride. *Dye Pigm.* 149, 669–675. doi: 10.1016/j.dyepig.2017.11.033
- Muhammad, A., Du, H. L., Javed, M. S., Asghari, M., Iqra, A., Shahid, H., et al. (2020). Fabrication, structure, and frequency-dependent electrical and dielectric properties of Sr-doped $BaTiO_3$ ceramics. *Ceram. Int.* 46, 2238–2246. doi: 10.1016/j.ceramint.2019.09.208
- Murfin, L. C., Chiang, K. X. L., Williams, G. T., Jenkins, T., James, T. D., and Lewis, S. E. (2020) A colorimetric chemosensor based on a Nozoe azulene that detects fluoride in aqueous/alcoholic media. *Front. Chem.* 8:10. doi: 10.3389/fchem.2020.00010
- Oh, J. Y., Rondeau-Gagné, S., Chiu, Y.-C., Chortos, A., Lissel, F., Wang, G.-J. N., et al. (2016). Intrinsically stretchable and healable semiconducting polymer for organic transistors. *Nature* 539, 411–415. doi: 10.1038/nature.20102
- Sun, Q. K., Chen, M. S., Liu, Z. W., Zhang, H. C., and Yang, W. J. (2017). Efficient colorimetric fluoride anion chemosensors based-on simple naphthodipyrrolidone dyes. *Tetrahedron Lett.* 58, 2711–2714. doi: 10.1016/j.tetlet.2017.05.079
- Tang, Q. Z., Duan, T. D., Li, P., Zhang, P., and Wu, D. S. (2018). Enhanced defluoridation capacity from aqueous media via hydroxyapatite decorated with carbon nanotube. *Front. Chem.* 6:104. doi: 10.3389/fchem.2018.00104
- Wade, C. R., Broomsgrove, A. E. J., Aldridge, S., and Gabbai, F. P. (2010). Fluoride ion complexation and sensing using organoboron compounds. *Chem. Rev.* 110, 3958–3984. doi: 10.1021/cr900401a
- Yang, C., Zheng, M., Li, Y. P., Zhang, B. L., Li, J. F., Bu, L. Y., et al. (2013). N-Monoalkylated 1,4-diketo-3,6-diphenylpyrrolo[3,4-c]pyrroles as effective one- and two-photon fluorescence chemosensors for fluoride anions. *J. Mater. Chem.* 1, 5172–5178. doi: 10.1039/C3TA00160A
- Yao, J., Yu, C., Liu, Z., Luo, H., Yang, Y., Zhang, G., et al. (2015). Significant improvement of semiconducting performance of the diketopyrrolopyrrole-quaterthiophene conjugated polymer through side-chain engineering via hydrogen-bonding. *J. Am. Chem. Soc.* 138, 173–185. doi: 10.1021/jacs.5b09737
- Zeng, W. X., Deng, Z. F., Wang, H. R., Zhang, H. C., and Zhou, Q. X. (2019). Benzodifuranone based color-changing epoxy-polyamine coating. *Dyes Pigm.* 164, 198–205. doi: 10.1016/j.dyepig.2019.01.016

DATA AVAILABILITY STATEMENT

All datasets generated for this study are included in the article/**Supplementary Material**.

AUTHOR CONTRIBUTIONS

ZD and RL prepared materials and carried out in experiments. JG, MZ, and LL helped to analyze experimental data. XS, WR, ZM, and ZJ helped to characterize materials. JH supervised the work. All authors contributed to revise the manuscript, approved the final version and agreed to be accountable for all aspects of this work.

FUNDING

This study was financially supported by the Research Projects of Shaanxi University of Technology (SLGPT2019KF01-01, SLG1901).

SUPPLEMENTARY MATERIAL

The Supplementary Material for this article can be found online at: <https://www.frontiersin.org/articles/10.3389/fchem.2020.00231/full#supplementary-material>

- Zeng, W. X., Zhou, Q. X., Zhang, H. C., and Qi, X. N. (2018) One-coat epoxy coating development for the improvement of UV stability by DPP pigments. *Dyes Pigm.* 151, 157–164. doi: 10.1016/j.dyepig.2017.12.058
- Zhang, H. C., Deng, R. N., Wang, J., Li, X., Chen, Y. M., and Liu, K. W., et al. (2017). Crystalline organic pigment-based field-effect transistors. *ACS Appl. Mater. Interfaces* 9, 21891–21899. doi: 10.1021/acsami.7b03170
- Zhang, H. C., Ghasimi, S., Tieke, B., Spange, A., and Schade, S. (2014). Aminobenzodione-based polymers with low bandgaps and solvatochromic behavior. *Polym. Chem.* 5, 3817–3823. doi: 10.1039/C3PY01702H
- Zhang, H. C., Liu, K. W., Wu, K. Y., Chen, Y. M., Deng, R., Xiang, L., et al. (2018). Hydrogen-bonding-mediated solid-state self-assembled isoepindolidiones (isoEpi) crystal for organic field-effect transistor. *Phys. Chem. C* 122, 5888–5895. doi: 10.1021/acs.jpcc.7b11992
- Zhang, H. C., Zeng, W. X., Du, H. L., Ma, Y. T., Ji, Z. T., Deng, Z. F., et al. (2020) Comparison for color change between benzodifuranone and benzodipyrrolidone based epoxy coating. *Dyes Pigm.* 175:108171. doi: 10.1016/j.dyepig.2019.108171
- Zhou, Y., Zhang, J. F., and Yoon, J. (2014). Fluorescence and colorimetric chemosensors for fluoride-ion detection. *Chem. Rev.* 114, 5511–5571. doi: 10.1021/cr400352m

Conflict of Interest: MZ was employed by company Qingdao Haiwan Science and Technology Industry Research Institute Co., Ltd.

The remaining authors declare that the research was conducted in the absence of any commercial or financial relationships that could be construed as a potential conflict of interest.

Copyright © 2020 Deng, Li, Geng, Zheng, Li, Shi, Ren, Meng, Ji and Hua. This is an open-access article distributed under the terms of the Creative Commons Attribution License (CC BY). The use, distribution or reproduction in other forums is permitted, provided the original author(s) and the copyright owner(s) are credited and that the original publication in this journal is cited, in accordance with accepted academic practice. No use, distribution or reproduction is permitted which does not comply with these terms.



Synthesis of 2,1,3-Benzoxadiazole Derivatives as New Fluorophores—Combined Experimental, Optical, Electro, and Theoretical Study

Tiago E. A. Frizon^{1*}, André A. Vieira^{2*}, Fabricia N. da Silva², Sumbal Saba^{3*}, Giliandro Farias⁴, Bernardo de Souza⁴, Eduardo Zapp⁵, Michell N. Lôpo⁶, Hugo de C. Braga⁷, Felipe Grillo⁸, Sergio F. Curcio⁹, Thiago Cazati⁹ and Jamal Rafique^{6*}

OPEN ACCESS

Edited by:

Haichang Zhang,
Qingdao University of Science and
Technology, China

Reviewed by:

Xiang Li,
University of Akron, United States
Shian Ying,
Shandong University of Science and
Technology, China

*Correspondence:

Tiago E. A. Frizon
tiago.frizon@ufsc.br
André A. Vieira
vieira.andre@ufba.br
Sumbal Saba
sumbal6s@gmail.com;
sumbal.saba@ufabc.edu.br
Jamal Rafique
jamal.chm@gmail.com;
jamal.rafique@ufms.br

Specialty section:

This article was submitted to
Organic Chemistry,
a section of the journal
Frontiers in Chemistry

Received: 01 March 2020

Accepted: 07 April 2020

Published: 12 May 2020

Citation:

Frizon TEA, Vieira AA, da Silva FN,
Saba S, Farias G, de Souza B,
Zapp E, Lôpo MN, Braga HdC,
Grillo F, Curcio SF, Cazati T and
Rafique J (2020) Synthesis of
2,1,3-Benzoxadiazole Derivatives as
New Fluorophores—Combined
Experimental, Optical, Electro, and
Theoretical Study.
Front. Chem. 8:360.
doi: 10.3389/fchem.2020.00360

¹ Department of Energy and Sustainability, Federal University of Santa Catarina, Araranguá, Brazil, ² Institute of Chemistry, Federal University of Bahia, Salvador, Brazil, ³ Center for Natural and Human Sciences-CCNH, Federal University of ABC, Santo André, Brazil, ⁴ Chemistry Department, Federal University of Santa Catarina, Florianópolis, Brazil, ⁵ Department of Exact Sciences and Education, Federal University of Santa Catarina, Blumenau, Brazil, ⁶ Institute of Chemistry, Federal University of Mato Grosso do Sul, Campo Grande, Brazil, ⁷ Institute of Science and Technology, Federal University of São Paulo, São José dos Campos, Brazil, ⁸ Department of Materials and Metallurgy, Federal Institute of Espírito Santo, Vitória, Brazil, ⁹ Physics Department, Federal University of Ouro Preto, Ouro Preto, Brazil

Herein, we report the synthesis and characterization of fluorophores containing a 2,1,3-benzoxadiazole unit associated with a π -conjugated system (D- π -A- π -D). These new fluorophores in solution exhibited an absorption maximum at around ~ 419 nm (visible region), as expected for electronic transitions of the π - π^* type ($\epsilon \sim 2.7 \times 10^7$ L mol⁻¹ cm⁻¹), and strong solvent-dependent fluorescence emission ($\Phi_{FL} \sim 0.5$) located in the bluish-green region. The Stokes' shift of these compounds is ca. 3,779 cm⁻¹, which was attributed to an intramolecular charge transfer (ICT) state. In CHCl₃ solution, the compounds exhibited longer and shorter lifetimes, which was attributed to the emission of monomeric and aggregated molecules, respectively. Density functional theory was used to model the electronic structure of the compounds **9a–d** in their excited and ground electronic states. The simulated emission spectra are consistent with the experimental results, with different solvents leading to a shift in the emission peak and the attribution of a π - π^* state with the characteristics of a charge transfer excitation. The thermal properties were analyzed by thermogravimetric analysis, and a high maximum degradation rate occurred at around 300°C. Electrochemical studies were also performed in order to determine the band gaps of the molecules. The electrochemical band gaps (2.48–2.70 eV) showed strong correlations with the optical band gaps (2.64–2.67 eV).

Keywords: 2,1,3-benzoxadiazole, heterocycles, luminescence, fluorophore, tetrazole

INTRODUCTION

Conjugated organic compounds, such as benzochalcogenodiazoles, have attracted attention because of their versatility and advantages, including low cost, improved electronic device performance, flexibility, and tuning through structural design (Liu et al., 2015). This class of compounds has been applied in field-effect transistors, sensors, memory devices, and

solar cells (Regis et al., 2018). In general, the incorporation of heterocyclic units with electron-donating groups (donors) and electron-accepting groups (acceptors) in the molecular structure increases the conjugation and alters the performance of organic electronic devices (Niu et al., 2007; Fu et al., 2009; Liu et al., 2015).

The derivatives of the 2,1,3-benzothiadiazole (BTD) heterocycle have been extensively investigated due to their recognized photophysical properties, such as intense fluorescence, large Stokes shift, and high extinction coefficient (Gallardo et al., 2012; Wang et al., 2014; Fang et al., 2017; Aguiar et al., 2018). However, there is very limited literature available on the behavior of molecular materials obtained from the 2,1,3-benzoxadiazole (BOX) heterocycle (Pati, 2016). Interestingly, the 7-nitro-1,2,3-benzoxadiazole is generally used as a fluorophore in the design of many analyte-responsive fluorescent probes (Pati, 2016; Wu et al., 2017).

The BOX heterocycle, also known as benzofuran, has a flat molecular and bicyclic conjugated structure, and its derivative compounds with extended conjugates are extremely fluorescent. Because of the presence of an oxygen atom in the heterocycle, BOX is more electronegative when compared to BTD (Bouffard and Swager, 2008; Lin et al., 2011; Zeng et al., 2012; Göker et al., 2014; Regis et al., 2018), and due to this electronegativity, BOX forms coplanar and quinoid structures, giving better stability to the devices manufactured (Liu et al., 2015).

The main applications of BOX are to obtain fluorescent derivatization reagents and use in the detection of heavy metals (Toyo'oka, 2004; Song et al., 2011; Sumiya et al., 2011), in solar cells, and in liquid crystals (Liu et al., 2015; Regis et al., 2018).

As part of our continued involvement in the chemistry of *N*-heterocycles (Saba et al., 2015, 2016, 2017, 2018, 2020; Rafique et al., 2016, 2018a,b; Silva et al., 2017; Bettanin et al., 2018; Peterle et al., 2018; Rodrigues et al., 2018; Tornquist et al., 2018; Meirinho et al., 2019; Neto et al., 2020; Scheide et al., 2020) and material sciences (Frizon et al., 2014, 2015, 2016, 2018; Bo et al., 2016, 2018; Westrup et al., 2016; Matzkeit et al., 2018; Regis et al., 2018), herein, we report the synthesis and characterization of BOX derivatives containing electron-donor groups (alkylated tetrazole rings) connected to the 2,1,3-BOX group as an electron-acceptor unit. In addition, thermal, electrochemical, and theoretical predictions were made and photophysical analysis was performed to study the stability, likely geometry, and luminescence properties of these compounds in their ground and excited electronic states.

MATERIALS AND METHODS

Materials and Methods

All reagents were used without further purification and were obtained from commercial sources. The solvents acquired were of commercial grade, with the exception of tetrahydrofuran (HPLC grade), and were purified by methods based on the literature (Armarego and Chai, 2003). The compounds were purified by column chromatography (silica gel) and crystallization from analytical-grade solvents. The reactions were monitored by TLC using Silica Gel 60 (Merck Kieselgel 60F254).

Infrared analysis was performed on an Agilent Cary 600 Series Fourier-transform infrared (FTIR) spectrometer in KBr discs or films. The ^1H and ^{13}C NMR spectra were recorded in chloroform-*d* at 400 and 100 MHz, respectively. The chemical shifts are reported in ppm relative to TMS (0.00 ppm), and the coupling constants are reported in Hz. The chromatograms and mass spectra were acquired on a Shimadzu GCMS-QP5050A spectrometer with a DB5-MS [(5%-phenyl)-dimethylpolysiloxane] capillary column (25 m \times 250 μm \times 0.25 μm) using an electron ionization voltage of 70 eV. The oven parameters used in the method were 80°C for 6 min, increasing at 15°C min $^{-1}$ to 280°C and remaining at this temperature for 4 min, giving a run time of 23.33 min with an initial delay of 4 min. The gas flow was He at 0.6 mL min $^{-1}$, with pressure S3 of 2.3301 psi. A Varian Cary 50 UV-Vis spectrophotometer was employed to record the absorption spectra. Fluorescence emission and excitation spectra were acquired on a Shimadzu RF5301pc spectrofluorophotometer. The quantum yield (fluorescent fragment length—FFL) was acquired using the dilute optical method. A solution of H₂SO₄ (0.5 mol L $^{-1}$) and quinine sulfate (QS) (Φ_{FL} = 0.55) was used as the Φ_{FL} standard (Crosby and Demas, 1971). The uncertainties related to the quantum yield of fluorescence ($\Delta\Phi_{\text{FL}}$) measurements using QS are of the order of 6% (Würth et al., 2011, 2013).

A DropSens BiPotentiostat/Galvanostat (model Stat 400) was used for all electrochemical measurements. The cyclic voltammetry measurements of **9a–d** were obtained in a standard electrochemical cell containing a system of three electrodes: a glassy carbon working electrode, a Pt wire counter electrode, and an Ag/Ag $^+$ (AgNO₃ 0.01 mol L $^{-1}$ in acetonitrile) reference electrode. All measurements were performed in an electrolyte solution [0.1 mol L $^{-1}$ tetra-*n*-butyl ammonium hexafluorophosphate (TBAPF₆) in CH₂Cl₂] purged with purified nitrogen gas. The ferrocene/ferricenium redox pair (Fc/Fc $^+$) was used as an internal reference. The spectra for **9a–d** used to estimate the optical band gaps were obtained on a Shimadzu UV-1800 spectrofluorophotometer. Thermogravimetric analysis (TGA) was carried out using a Shimadzu analyzer with the TGA-50 module. A PerkinElmer 2400 Series II Elemental Analyzer System was used to carry out the elemental analysis of the final compounds. The fluorescence decay was obtained through the time-correlated single-photon counting technique, using a @FluoTime200 (PicoQuant) spectrometer. The excitation was performed by a 401-nm pulsed diode laser, applying a repetition rate of 20 MHz. Fluorescence was collected perpendicular to excitation and passed through a polarizer set at the magic angle. The detection system consisted of a monochromator and a microchannel plate photomultiplier (Hamamatsu R3809U-50). Lifetimes were obtained by fitting the fluorescence decays to a convolution of the instrument response function and the sum of exponentials using FluoFit[®] software. The plots of weighted residuals and reduced chi-squared (χ^2) were used to accurately determine the quality of the fittings during the analysis procedure. The geometry optimization of **9** was carried out *in vacuo*, using the Orca 4.1 (Neese, 2012) software package and density functional theory (DFT) with the PBE0 functional

(Perdew et al., 1996, 1997) and the DEF2-TZVP(-F) basis set for all atoms (Schäfer et al., 1992, 1994; Weigend and Ahlrichs, 2005). Grimme D3 correction was used to include dispersion effects with Becke-Johnson (BJ) damping (Becke and Johnson, 2005; Johnson and Becke, 2005, 2006; Grimme et al., 2010, 2011). In order to accelerate the evaluation of the functionals, the RIJCOSX algorithm was employed, using the resolution of identity approximation for the Coulomb part (RIJ) and the chain of spheres approach for the Fock exchange (COSX) (Izsák and Neese, 2011; Izsák et al., 2013). The vibrational frequencies computed on the optimized geometry of **9** included no imaginary frequencies. In order to simulate the absorption spectra, time-dependent density functional theory (TD-DFT) with the Tamn-Dancoff approximation (TDA) (Petrenko et al., 2011) was employed to obtain the first 10 singlet excited states, using the same protocol. To simulate the emission spectra, the path integral approach implemented by our group in the ORCA_ESD module (Souza et al., 2018, 2019) was employed, using PBE0 to obtain the geometries and Hessians for both the ground and excited states. The line width was set to 450 or 500 cm^{-1} , and the default Lorentzian line shape was used to obtain a better fit to the experimental data. The frequencies below 300 cm^{-1} were removed. For the other parameters, the default options were used. Solvent effects were included in the excited-state energies by using the linear response conductor-like polarizable continuum model (LR-CPCM), while the regular CPCM was employed for the ground state (Marenich et al., 2009). Images of the complex geometries were obtained using the Chemcraft program (Chemcraft, 2019).

Synthesis

2,1,3-Benzoxadiazole-1-oxide (**6**)

A 500-mL flask was used to obtain a mixture of 2-nitroaniline (9.0 g, 6.5 mmol), tetrabutylammonium bromide (0.3 g, 1.1 mmol), diethyl ether (60 mL), and KOH solution (7 mL, 50% wt). To this mixture, a sodium hypochlorite solution (130 mL, activated chlorine > 10%) was added dropwise. After stirring at room temperature for 7 h, the organic layer was separated, the aqueous layer was extracted with CH_2Cl_2 ($3 \times 1,000$ mL), and the combined organic layers were evaporated under reduced pressure. The yellow solid was obtained without further purification. Yield: 89%. m.p. 68°C. IR (KBr) $\nu_{\text{max}}/\text{cm}^{-1}$: 3,472, 3,100, 3,080, 2,962, 2,935, 2,875, 1,649, 1,614, 1,584, 1,536, 1,484, 1,440, 1,421, 1,382, 1,351, 1,282, 1,200, 1,145, 1,124, 1,012, 963, 928, 890, 833, 743, 734, 671, 633.

2,1,3-Benzoxadiazole (**7**)

Compound **6** (1.7 g, 13 mmol), triphenylphosphine (4.0 g, 15 mmol), and toluene (150 mL) were placed in a 250 mL flask. The mix was refluxed for 3 h then cooled and filtered. The solvents were evaporated to afford the crude product. The material was chromatographed on silica gel with CH_2Cl_2 to afford the 2,1,3-benzoxadiazole **7** as a yellow solid. Yield: 80%. m.p. 69°C. IR (KBr) $\nu_{\text{max}}/\text{cm}^{-1}$: 3,100, 3,080, 3,010, 2,955, 2,924, 2,853, 2,360, 2,332, 1,969, 1,920, 1,721, 1,650, 1,614, 1,583, 1,535, 1,483, 1,440, 1,422, 1,351, 1,282, 1,263, 1,200, 1,146, 1,125, 1,046, 1,012, 973, 961, 891, 834, 742, 732, 671, 633, 617. ^1H NMR (400 MHz,

CDCl_3) δ ppm: 7.85 (dd, 2H, $J = 6.0, 4.0$ Hz), 7.41 (dd, 2H, $J = 6.0, 4.0$ Hz). Anal. Calcd. For $\text{C}_6\text{H}_4\text{N}_2\text{O}$ $[\text{M}]^+$ 120.0 found 120.0.

4,7-Dibromo-2,1,3-benzoxadiazole (**8**)

Compound **7** (1.23 g, 10 mmol) and Fe powder (0.12 g, 2.0 mmol) were placed in a round-bottom flask and heated to 100°C. Br_2 (1.5 mL, 30 mmol) was added dropwise over 2 h, and then the reaction was refluxed for 3 h. After cooling, the resulting solution was dissolved in CH_2Cl_2 (40 mL) and washed with brine (40 mL). The organic fraction was washed with saturated sodium bicarbonate solution (4×30 mL), brine (4×30 mL), and water (4×30 mL). The organic layer was dried and concentrated under vacuum. The brown crude product was chromatographed on silica gel (hexane/ethyl acetate 98:2) to produce **8** as a cream powder. Yield: 40%. m.p. 98–100°C. IR (KBr) $\nu_{\text{max}}/\text{cm}^{-1}$: 2,923, 2,852, 2,360, 2,342, 1,873, 1,717, 1,695, 1,606, 1,517, 1,493, 1,465, 1,426, 1,378, 1,377, 1,322, 1,300, 1,292, 1,261, 1,204, 1,150, 1,113, 1,085, 107, 1,028, 958, 907, 878, 867, 845, 745, 728, 638, 607. ^1H NMR (400 MHz, CDCl_3) δ ppm: 7.51 (s, 2H). GC-MS: RT: 13.92 min.; Calcd. For $\text{C}_6\text{H}_2\text{Br}_2\text{N}_2\text{O}$ $[\text{M}]^+$ 277.8 found 277.9.

5-(4-Bromophenyl)-2H-tetrazole (**2**)

First, 4-Bromobenzonitrile (1.0 g, 5.5 mmol), 20 mL of DMF, ammonium chloride (1.8 g, 33.9 mmol) and NaN_3 (2.3 g, 35 mmol) were placed in a 100 mL round-bottom flask. The mixture was refluxed for 24 h. At room temperature, the mixture was poured onto ice-water to obtain a precipitate. Then, the mixture was acidified with HCl solution to pH 1. The yellow precipitate was filtered and recrystallized in water/ethanol (1:1). Yield: 90%. IR (KBr) $\nu_{\text{max}}/\text{cm}^{-1}$: 3,448, 3,090, 3,058, 3,000, 1,905, 1,608. ESI: Anal. Calcd. for $\text{C}_7\text{H}_5\text{BrN}_4$: m/z 226.9; found m/z 246.9 $[\text{M}+\text{Na}]^+$.

General Procedure for the Synthesis of Compounds **3a–d**

Tetrazole (**2**) (2 mmol), acetone (60 mL), K_2CO_3 (2.2 mmol), and 2.2 mmol of the respective alkyl bromide (2-ethylhexyl bromide, octyl bromide, or decyl bromide) were placed in a 250 mL two-neck round-bottom flask. After 45 h of refluxing, the mixture was filtered and concentrated under reduced pressure. The white solid was obtained by recrystallization from ethanol.

5-(4-Bromophenyl)-2-(2-ethylhexyl)-2H-tetrazole (**3a**)

Yield: 72%. ^1H NMR (400 MHz, CDCl_3) δ ppm: 8.04 (d, 2H, $J = 8.8$ Hz), 7.63 (d, 2H, $J = 8.8$ Hz), 4.57 (d, 2H, $J = 6.5$ Hz), 2.10 (m, 2H), 1.33 (m, 9H), 0.95 (t, 3H, $J = 7.04$ Hz), 0.89 (t, 3H, $J = 7.04$ Hz). ^{13}C NMR (100 MHz, CDCl_3) δ ppm: 164.1, 132.1, 128.3, 126.6, 124.5, 56.3, 39.8, 30.4, 28.4, 23.8, 22.8, 14.0, 10.5.

5-(4-Bromophenyl)-2-octyl-2H-tetrazole (**3b**)

Yield: 76%. ^1H NMR (400 MHz, CDCl_3) δ ppm: 8.04 (d, 2H, $J = 8.31$ Hz), 7.64 (t, 2H, $J = 8.31$ Hz), 4.64 (t, 2H, $J = 7.34$ Hz), 2.06 (m, 2H), 1.37–1.26 (m, 12H), 0.88 (t, 3H, $J = 7.34$ Hz). ^{13}C NMR (100 MHz, CDCl_3) δ ppm: 164.2, 132.1, 128.3, 126.5, 124.6, 53.3, 31.7, 29.4, 28.9, 28.8, 26.4, 22.6, 14.1.

5-(4-Bromophenyl)-2-decyl-2H-tetrazole (3c)

Yield: 88%. ^1H NMR (400 MHz, CDCl_3) δ ppm: 8.03 (d, 2H, $J = 8.80$ Hz), 7.63 (d, 2H, $J = 8.80$ Hz), 4.64 (t, 2H, $J = 7.34$ Hz), 1.26 (m, 16H), 0.87 (t, 3H, $J = 6.85$ Hz). ^{13}C NMR (100 MHz, CDCl_3) δ ppm: 156.9, 124.8, 121.0, 119.2, 117.2, 46.0, 24.6, 22.3, 22.0, 21.6, 19.0, 15.4, 6.8.

5-(4-Bromophenyl)-2-dodecyl-2H-tetrazole (3d)

Yield: 79%. IR (KBr) $\nu_{\text{max}}/\text{cm}^{-1}$: 2,956, 2,920, 2,849, 1,610. ^1H NMR (400 MHz, CDCl_3) δ ppm: 8.03 (d, 2H, $J = 8.80$ Hz), 7.63 (d, 2H, $J = 8.31$ Hz), 4.64 (t, 2H, $J = 6.85$ Hz), 2.06 (m, 2H), 1.37 (m, 2H), 1.26 (m, 16H), 0.89 (t, 3H, $J = 6.85$ Hz). ^{13}C NMR (100 MHz, CDCl_3) δ ppm: 156.8, 124.8, 121.0, 119.2, 117.2, 46.0, 24.6, 22.3, 22.0, 21.6, 19.0, 15.4, 6.8.

General Procedure for the Synthesis of Compounds 4a–d**4-(4-(2-(2-ethylhexyl)-2H-tetrazol-5-yl)phenyl)-2-methylbut-3-yn-2-ol (4a)**

In a 125-mL two-neck round-bottom flask containing a desiccant tube of CaCl_2 , a solution was prepared of tetrazole (3a) (2.000 g, 5.95 mmol), 60 mL of dry $\text{Et}_3\text{N}/\text{THF}$ (1:1), bis(triphenylphosphine)palladium dichloride (0.183 g, 0.26 mmol), and triphenylphosphine (0.069 g, 0.26 mmol). After 48 h of reflux, the mixture was vacuum filtered and a white product was obtained by recrystallization from ethanol. Under argon, the mixture was heated to 55°C ; then, copper iodide (0.025 g; 0.13 mmol) and 2-methyl-3-butyn-2-ol (0.851 g, 10.11 mmol) in 10 mL $\text{Et}_3\text{N}/\text{THF}$ (1:1) were added dropwise over 40 min. After 6 h under reflux, the mixture was filtered at room temperature through Celite® and concentrated under reduced pressure. The resulting product was chromatographed on silica gel. For the preparation of compounds 4b, 4c, and 4d, the same methodology was followed, using 5-(4-bromophenyl)-2-octanotetrazole, 5-(4-bromophenyl)-2-decanotetrazol, and 5-(4-bromophenyl)-2-dodecanotetrazol, respectively.

4-(4-(2-(2-Ethylhexyl)-2H-tetrazol-5-yl)phenyl)-2-methylbut-3-yn-2-ol (4a)

Yield: 71%. ^1H NMR (400 MHz, CDCl_3) δ ppm: 8.1 (d, 2H, $J = 8.31$ Hz), 7.52 (t, 2H, $J = 8.31$ Hz), 4.64 (t, 2H, $J = 6.85$ Hz), 2.51 (s, 1H), 2.11 (m, 1H), 1.65 (s, 6H), 1.33 (m, 8H), 0.95 (t, 3H, $J = 7.34$ Hz), 0.90 (t, 3H, $J = 6.85$ Hz). ^{13}C NMR (100 MHz, CDCl_3) δ ppm: 164.2, 132.1, 128.3, 126.5, 124.6, 53.3, 31.7, 29.4, 28.9, 28.8, 26.4, 22.6, 14.1.

2-Methyl-4-(4-(2-octyl-2H-tetrazol-5-yl)phenyl)but-3-yn-2-ol (4b)

Yield: 77%. ^1H NMR (400 MHz, CDCl_3) δ ppm: 8.1 (d, 2H, $J = 8.80$ Hz), 7.52 (t, 2H, $J = 8.31$ Hz), 4.64 (t, 2H, $J = 7.34$ Hz), 2.47 (s, 1H), 2.05 (m, 2H), 1.64 (s, 6H), 1.27 (m, 10H), 0.87 (t, 3H, $J = 6.85$ Hz). ^{13}C NMR (100 MHz, CDCl_3) δ ppm: 164.4, 132.1, 127.2, 126.6, 124.7, 95.6, 81.7, 65.6, 53.3, 31.7, 31.5, 29.0, 28.8, 26.4, 22.6, 15.1.

4-(4-(2-Decyl-2H-tetrazol-5-yl)phenyl)-2-methylbut-3-yn-2-ol (4c)

Yield: 88%. ^1H NMR (400 MHz, CDCl_3) δ ppm: 8.10 (d, 2H, $J = 8.80$ Hz), 7.53 (d, 2H, $J = 8.80$ Hz), 4.65 (t, 2H, $J = 7.34$ Hz), 2.28 (s, 1H), 2.03 (m, 2H), 1.64 (s, 6H), 1.25 (m, 16H), 0.89 (t, 3H, $J = 6.36$ Hz). ^{13}C NMR (100 MHz, CDCl_3) δ ppm: 164.5, 132.2, 127.2, 126.6, 124.7, 95.5, 81.7, 65.6, 53.3, 31.4, 31.5, 29.4, 28.9, 26.4, 22.7, 14.1.

4-(4-(2-Dodecyl-2H-tetrazol-5-yl)phenyl)-2-methylbut-3-yn-2-ol (4d)

Yield: 96%. m.p.: 65°C . FTIR (KBr) $\nu_{\text{max}}/\text{cm}^{-1}$: 3,315, 3,051, 2,956, 2,918, 2,848. ^1H NMR (400 MHz, CDCl_3) δ ppm: 8.04 (d, 2H, $J = 8.80$ Hz), 7.64 (d, 2H, $J = 8.31$ Hz), 4.64 (t, 2H, $J = 6.85$ and 7.34 Hz), 2.06 (m, 2H), 1.26 (m, 16H), 0.89 (t, 3H, $J = 6.85$ Hz). ^{13}C NMR (100 MHz, CDCl_3) δ ppm: 164.2, 132.1, 130.2, 127.2, 126.5, 124.6, 53.3, 29.6, 29.4, 26.4, 22.7, 14.1.

General Procedure for the Synthesis of Compounds 5a–d

Compound (4a) (1.61 g, 4.73 mmol), 50 mL of toluene, and NaOH (0.246 g, 6.15 mmol) were combined in a 100 mL round-bottom flask. The solution was distilled while slowly heating, and a mixture of 8 mL toluene/acetone was also distilled. The reaction was monitored by TLC using hexane/ethyl ether (6:4) as eluent. At room temperature, the solution was filtered through Celite® and vacuum-concentrated. The crude solid was purified by column chromatography elution with a solution of hexane/ethyl acetate (95:5), resulting in the desired product at a yield of 90% [40].

2-(2-Ethylhexyl)-5-(4-ethynylphenyl)-2H-tetrazole (5a)

Yield: 90%. m.p. 67°C . IR (KBr) $\nu_{\text{max}}/\text{cm}^{-1}$: 3,291, 2,958, 2,920, 2,842. ^1H NMR (CDCl_3 , 400 MHz) δ ppm: 8.10 (d, 2H, $J = 8.31$ Hz), 7.52 (d, 2H, $J = 8.31$ Hz), 4.57 (d, 2H, $J = 6.85$ Hz), 2.10 (m, 1H), 1.39–1.26 (m, 8H), 0.94 (t, 3H, $J = 7.34$ Hz), 0.89 (t, 3H, $J = 6.85$ Hz). ^{13}C NMR (CDCl_3 , 100 MHz) δ ppm: 164.3, 132.1, 127.1, 126.6, 124.6, 95.6, 81.7, 56.2, 39.8, 31.4, 30.3, 28.4, 23.8, 22.8, 13.9, 10.4.

5-(4-Ethynylphenyl)-2-octyl-2H-tetrazole (5b)

Yield: 88%. m.p. 65°C . IR (KBr) $\nu_{\text{max}}/\text{cm}^{-1}$: 3,286, 2,954, 2,916, 2,846. ^1H NMR (CDCl_3 , 400 MHz) δ ppm: 8.02 (d, 2H, $J = 8$ Hz), 7.62 (d, 2H, $J = 8$ Hz), 4.64 (t, 2H, $J = 8$ Hz), 2.05 (q, 2H, $J = 6.8$ Hz), 1.41–1.32 (m, 2H), 1.32–1.17 (m, 8H), 0.86 (t, 3H, $J = 6.46$ Hz). ^{13}C NMR (CDCl_3 , 100 MHz) δ ppm: 164.0, 131.9, 128.1, 126.4, 124.4, 53.2, 31.5, 29.2, 28.7, 26.2, 22.5, 13.9.

2-Decyl-5-(4-ethynylphenyl)-2H-tetrazole (5c)

Yield: 87%. m.p. 60°C . IR (KBr) $\nu_{\text{max}}/\text{cm}^{-1}$: 3,286, 2,954, 2,916, 2,846. ^1H NMR (CDCl_3 , 400 MHz) δ ppm: 8.02 (d, 2H, $J = 8$ Hz), 7.62 (d, 2H, $J = 8$ Hz), 4.63 (t, 2H, $J = 6$ Hz), 2.05 (q, 2H, $J = 8$ Hz), 1.4–1.32 (m, 2H), 1.40–1.32 (m, 12H), 0.87 (t, 3H, $J = 6$ Hz). ^{13}C NMR (CDCl_3 , 100 MHz) δ ppm: 164.1, 132.0, 128.2, 125.4, 124.5, 53.2, 31.8, 29.4, 29.2, 28.8, 26.3, 22.6, 14.0. Anal. Calcd. for C, 73.51%; H, 8.44%; N, 18.05% found C, 72.8%; H, 8.56%; N, 18.27%.

2-Dodecyl-5-(4-ethynylphenyl)-2H-tetrazole (5d)

Yield: 88%. m.p. 56°C. IR (KBr) $\nu_{\text{max}}/\text{cm}^{-1}$: 3,290, 2,950, 2,920, 2,844. ^1H NMR (400 MHz, CDCl_3) δ ppm: 8.10 (d, 2H, $J = 8.22$ Hz), 7.53 (d, 2H, $J = 8.22$ Hz), 4.64 (t, 2H, $J = 7.04$ Hz), 2.52 (s, 1H), 2.04 (m, 2H), 1.65 (s, 6H), 1.26 (m, 16H), 0.88 (t, 3H, $J = 6.46$ Hz). ^{13}C NMR (100 MHz, CDCl_3) δ ppm: 164.4, 132.1, 126.6, 124.7, 95.6, 81.7, 65.6, 53.3, 31.9, 31.5, 29.6, 29.3, 29.5, 28.9, 26.3, 22.7, 14.1.

General Procedure for the Synthesis of Compounds 9a–d

In a 100 mL three-neck round-bottom flask, were mixed compound **8** (0.190 g, 0.68 mmol), 45 mL of dry Et_3N , bis(triphenylphosphine)palladium (II) dichloride (0.022 g, 0.03 mmol), and triphenylphosphine (0.080 g, 0.30 mmol). After heating to 55°C, copper iodide (0.030 g, 16 mmol) was added. A 15-ml solution of respective aryl acetylene **5a** (0.50 g, 1.47 mmol) in dry Et_3N was then slowly added dropwise. The reaction remained under reflux for 2 h, being monitored by TLC using a mixture of hexane/ethyl ether (8:2) as the eluent. The mixture was filtered, and the retained solid was dissolved in chloroform and filtered. After concentrating the solvent, a yellow solid was obtained at 71% yield.

4,7-Bis((4-(2-(2-ethylhexyl)-2H-tetrazol-5-yl)phenyl)ethynyl)benzo[c][1,2,5]oxadiazole (9a)

Yield: 71 %. m.p. 175°C. IR (KBr) $\nu_{\text{max}}/\text{cm}^{-1}$: 2,970, 2,951, 2,810, 2,211. ^1H NMR (400 MHz, CDCl_3) δ ppm: 8.20 (dd, 4H, $J = 6.8$ Hz, 2.0 Hz), 7.77 (dd, 4H, $J = 6.8$ Hz, 1.6 Hz), 7.61 (s, 2H), 4.66 (t, 4H, $J = 7.2$ Hz), 2.07 (q, 4H, $J = 7.2$ Hz), 1.42–1.23 (m, 20H), 0.88 (t, 6H, $J = 6.8$ Hz). ^{13}C NMR (100 MHz, CDCl_3) δ ppm: 164.3, 149.4, 134.4, 132.6, 128.4, 126.9, 123.7, 112.6, 98.8, 85.3, 53.4, 31.7, 29.4, 29.0, 28.9, 26.4, 22.6, 14.1. ESI HRMS: calcd for $[\text{C}_{40}\text{H}_{44}\text{N}_{10}\text{O}+\text{H}]^+$ 681.3772, found 681.3768.

4,7-Bis((4-(2-(2-octyl)-2H-tetrazol-5-yl)phenyl)ethynyl)benzo[c][1,2,5]oxadiazole (9b)

Yield: 77 %. m.p. 206°C. IR (KBr) $\nu_{\text{max}}/\text{cm}^{-1}$: 2955, 2914, 2842, 2207. ^1H NMR (400 MHz, CDCl_3) δ ppm: 8.21 (dd, 4H, $J = 6.8$, 1.6 Hz), 7.77 (dd, 4H, $J = 6.8$ Hz, 1.6 Hz), 7.64 (s, 2H), 4.67 (t, 4H, $J = 7.2$ Hz), 2.07 (q, 4H, $J = 7.2$ Hz), 1.40–1.19 (m, 28H), 0.88 (t, 6H, $J = 6.8$ Hz) ppm. ^{13}C NMR (100 MHz, CDCl_3) δ ppm: 164.3, 149.4, 134.4, 132.5, 128.4, 126.8, 123.7, 112.6, 98.7, 85.3, 53.4, 31.9, 29.44, 29.38, 29.34, 29.2, 28.9, 26.4, 22.7, 14.1. ESI HRMS: calcd for $[\text{C}_{44}\text{H}_{52}\text{N}_{10}\text{O}+\text{H}]^+$ 737.4398, found 737.4400.

4,7-Bis((4-(2-decyl)-2H-tetrazol-5-yl)phenyl)ethynyl)benzo[c][1,2,5]oxadiazole (9c)

Yield: 82 %. m.p. 202°C. IR (KBr) $\nu_{\text{max}}/\text{cm}^{-1}$: 3,035, 2,968, 2,922, 2,850, 2,202. ^1H NMR (400 MHz, CDCl_3) δ ppm: 8.21 (d, 4H, $J = 8.4$ Hz), 7.78 (d, 4H, $J = 8.4$ Hz), 7.28 (s, 2H), 4.67 (t, 4H, $J = 7.2$ Hz), 2.08 (q, 4H, $J = 7.2$ Hz), 1.41–1.17 (m, 36H), 0.88 (t, 6H, $J = 7.2$ Hz). ^{13}C NMR (100 MHz, CDCl_3) δ ppm: 164.3, 149.4, 134.4, 132.6, 128.4, 126.8, 123.7, 112.6, 98.7, 85.3, 53.4, 31.9, 29.6, 29.5, 29.4, 29.3, 28.9, 26.4, 22.7, 14.1. ESI HRMS: calcd for $[\text{C}_{48}\text{H}_{60}\text{N}_{10}\text{O}+\text{H}]^+$ 793.5024, found 793.5027.

4,7-Bis((4-(2-dodecyl)-2H-tetrazol-5-yl)phenyl)ethynyl)benzo[c][1,2,5]oxadiazole (9d)

Yield: 79 %. m.p. 199°C. IR (KBr) $\nu_{\text{max}}/\text{cm}^{-1}$: 3,031, 2,950, 2,918, 2,850, 2,209. ^1H NMR (400 MHz, CDCl_3) δ ppm: 8.21 (d, 4H, $J = 8.4$ Hz), 7.78 (d, 4H, $J = 8.4$ Hz), 7.64 (s, 2H), 4.59 (d, 4H, $J = 6.8$ Hz), 2.13 (q, 2H, $J = 6.4$ Hz), 1.40–1.27 (m, 16H), 0.97 (t, 6H, $J = 7.2$ Hz), 0.90 (t, 6H, $J = 6.8$ Hz). ^{13}C NMR (100 MHz, CDCl_3) δ ppm: 164.3, 149.4, 134.4, 132.5, 128.4, 126.8, 123.7, 112.6, 98.7, 85.3, 53.4, 31.9, 29.44, 29.38, 29.34, 29.2, 28.9, 26.4, 22.7, 14.1. ESI HRMS: calcd for $[\text{C}_{40}\text{H}_{44}\text{N}_{10}\text{O}+\text{H}]^+$ 681.3772, found 681.3777.

RESULTS AND DISCUSSION

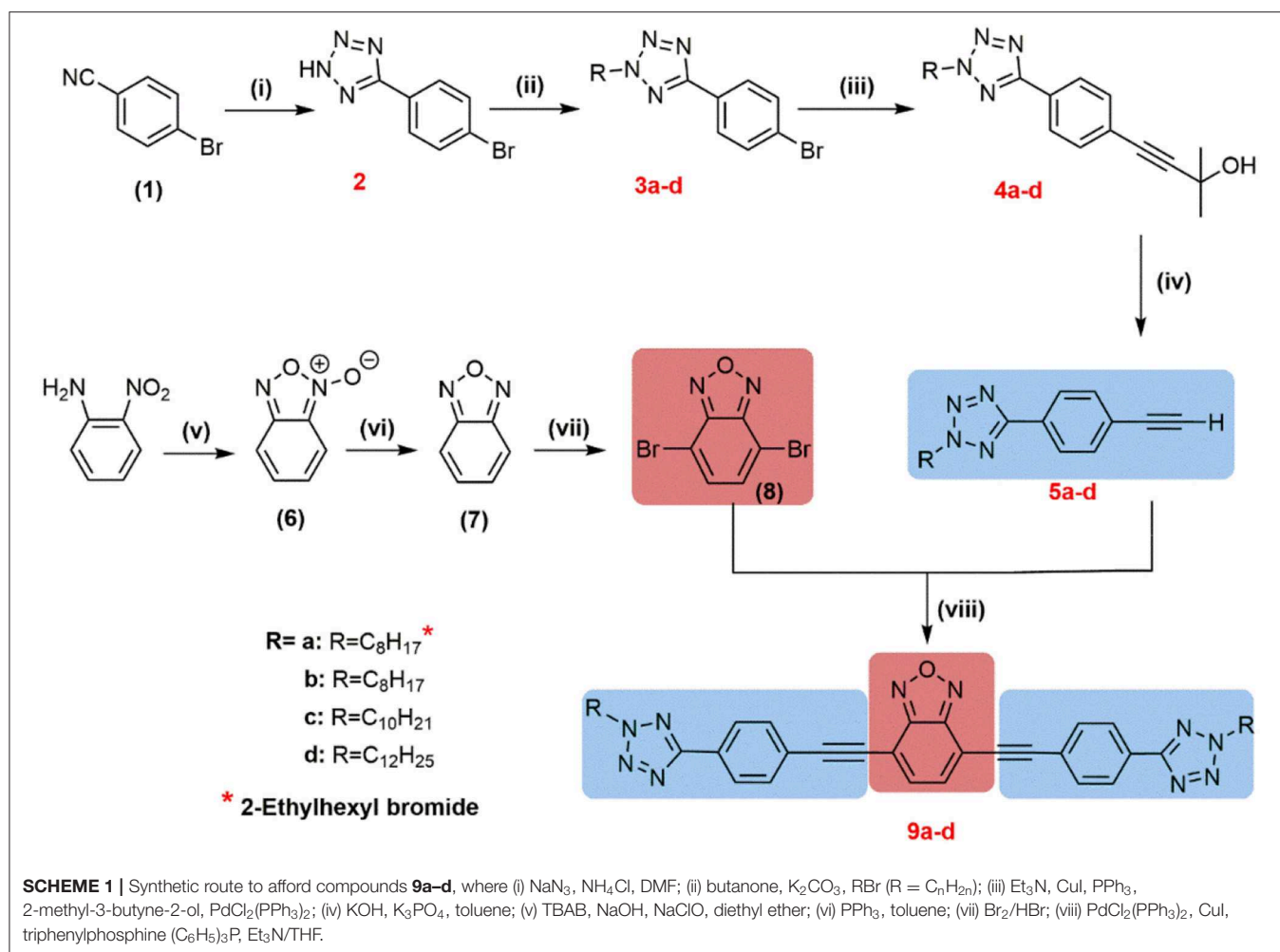
Synthesis and Spectroscopic Characterization

The synthetic route for the preparation of the final desired compounds, based on 1,2,5-benzoxadiazole **9a–d**, is shown in **Scheme 1**. The synthesis procedure adopted has been described in a previous publication (Frizon et al., 2018). The synthesis starts from the cyclization of 2-nitroaniline with sodium hypochlorite with the catalyst TBAB (tetrabutylammonium bromide) in a basic medium to obtain the *N*-oxide **6**. In sequence, the reduction of the *N*-oxide group using PPh_3 in xylene gives the heterocycle 2,1,3-benzoxadiazole **7** at 75% yield. In the next stage, the selective bromination reaction of 2,1,3-benzoxadiazole **7** at positions 4 and 7 was performed to obtain the 4,7-dibromo-2,1,3-benzoxadiazole (**8**). The Sonogashira coupling reaction between the aryl dibromide **8** and two equivalents of terminal aryl acetylenes **5a–d**, synthesized previously, allowed the desired compounds **9a–d** to be obtained. After purification in a chromatographic column, the final desired compounds were obtained at good yields (71–82%). All of the final compounds **9a–d** synthesized were characterized by proton and carbon-13 NMR, IR spectroscopy, and mass spectrometry.

Photophysical Characterization UV-Vis and Fluorescence

The photophysical properties of compounds **9a–d** were determined in chloroform solution at room temperature and are presented in **Table 1**.

The absorption and emission spectra obtained for **9a–d** in chloroform solution are shown in **Figure 1**. All compounds displayed similar absorption spectra with maxima at 419 nm, which are attributed to a π - π^* transition and showed high molar absorption coefficients ($\sim 3.4 \times 10^{-4} \text{ L mol}^{-1} \text{ cm}^{-1}$), which is characteristic of the benzoxadiazole heterocycle. Also, after excitation at the lower energy band, all compounds showed a strong bluish-green fluorescence emission in solution ($\lambda_{\text{FL}} = 450$ – 650 nm), with emission maxima ranging from 494 to 498 nm. The values for the Stokes shifts for compounds **9a–d** are in the range of $3,738$ – $3,786 \text{ cm}^{-1}$, indicating a possible intramolecular charge transfer (ICT) in the excited state (Neto et al., 2007). The fluorescence quantum yields (Φ_{FL}) of **9a–d** were determined in chloroform using quinine sulfate as the standard ($\Phi_r = 0.55$ in $0.5 \text{ mol L}^{-1} \text{ H}_2\text{SO}_4$). The Φ_{FL}



values could be calculated using the equation (Fery-Forgues and Lavabre, 1999): $\Phi_{FL} = \Phi_r (F_s/F_r)(A_r/A_s)(\eta_s/\eta_r)$, where s and r denote the sample and reference, respectively, η is the solvent refractive index, F is the integrated fluorescence intensity, and A is the value of absorbance at the excitation wavelength used to record the fluorescence spectrum. The values obtained are summarized in **Table 1**, where it can be noted that all compounds presented quantum yields (Φ_{FL}) of 0.51 to 0.54. The values obtained for compounds **9a–d** are considerably higher than those reported in our previous articles for compounds containing the heterocycles 2,1,3-benzoselenadiazole (Regis et al., 2018) and 2,1,3-benzotiadiazole (Frizon et al., 2016).

The singlet excited-state lifetimes of compounds **9a–d** in CHCl_3 solvent were investigated by time-resolved fluorescence spectroscopy, using a wavelength of 401 nm for the excitation. Compounds **9a–d** were evaluated in chloroform solution because of the higher affinity of this solvent (due to the alkyl chains) with the aromatic center. The singlet excited-state average lifetimes for compounds **9a–d** are shown in **Table 1**, and their values are similar. All fluorescence decays at emission maxima of compounds **9a–d** (see **Figure S1**) were best fitted by a bi-exponential function. The excited-state lifetimes and

TABLE 1 | Photophysical properties of **9a–d** in CHCl_3 solution.

Compound	$\lambda_{\text{Abs}}^{\text{max}}/\text{nm}^a$ ($\epsilon/10^4 \text{ mol L}^{-1} \text{ cm}^{-1}$) ^b	$\lambda_{\text{FL}}^{\text{max}}/\text{nm}^{a,c}$	Stokes Shift/ cm^{-1a}	Φ_{FL}^d	τ_f^e/ns
9a	417 (3.0)	494	3,738	0.54	2.73
9b	419 (2.7)	498	3,786	0.52	2.68
9c	417 (3.6)	495	3,779	0.52	2.68
9d	419 (4.2)	498	3,786	0.51	2.68

^a $\text{L mol}^{-1} \text{ cm}^{-1}$. ^bIn chloroform solution ($1.0 \times 10^{-5} \text{ mol L}^{-1}$). ^cExcited at absorption maxima. ^dQuantum yields were determined with the quinine sulfate solution as reference ($\Phi_F = 0.55$ in $0.5 \text{ mol L}^{-1} \text{ H}_2\text{SO}_4$). ^eAverage lifetimes were calculated using $\tau_f = \Sigma \tau_i^2 A_i / \Sigma \tau_i A_i$ due to multi-exponential profile. Fluorescence decays were measured at maxima of the emission intensities of the compounds after excitation at 401 nm.

their relative amplitudes for **9a–d** in chloroform solution are shown in **Table S1** (see **ESI**). The longer lifetimes (τ_1) were attributed here to the emission of monomeric **9a–d**, while the shorter lifetimes (τ_2) were attributed to the emission of **9a–d** aggregated in chloroform solution, even at $10^{-5} \text{ mol L}^{-1}$, since the molecular aggregation could reduce the excited-state lifetimes due to the enhanced radiationless path of the

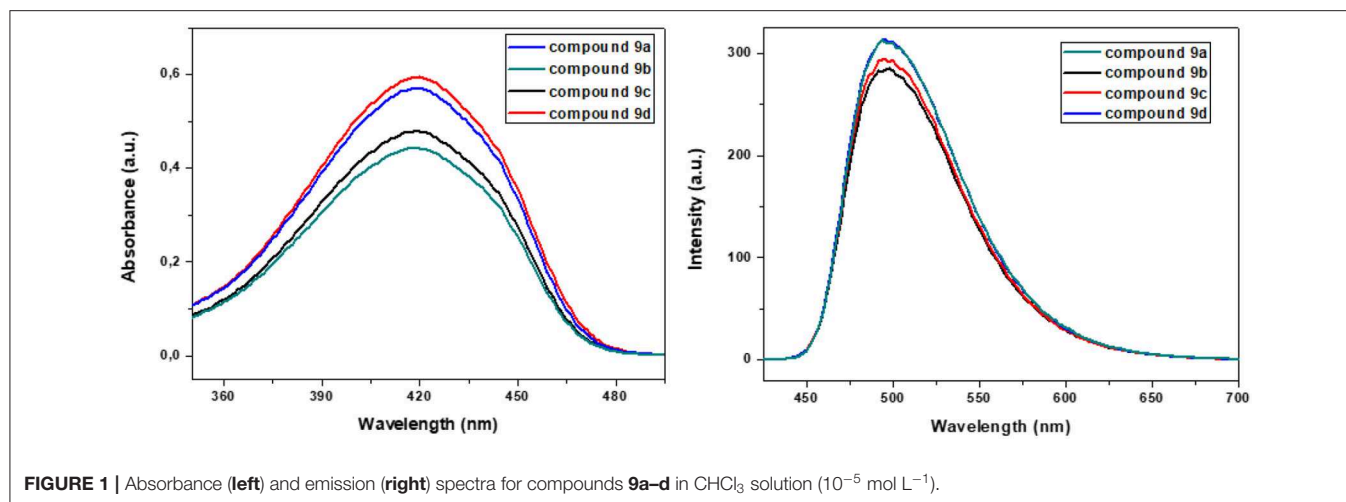


FIGURE 1 | Absorbance (left) and emission (right) spectra for compounds **9a–d** in CHCl_3 solution (10^{-5} mol L^{-1}).

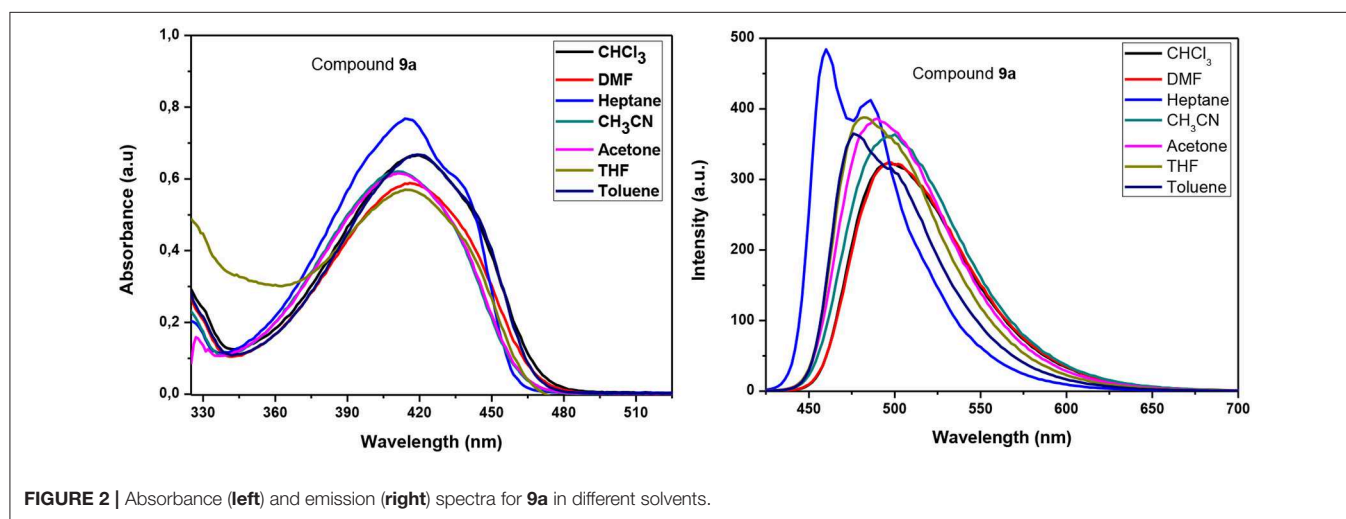


FIGURE 2 | Absorbance (left) and emission (right) spectra for **9a** in different solvents.

excited-state deactivation. With the exception of **9a**, the relative amplitudes of aggregate emissions (A_2) were higher than 70% in dilute chloroform solution (see **Figure S1**). The relative amplitude A_2 of **9a** was close to 50%, showing the possible influence of the branched chain in forming fewer aggregates than the linear chain. A hypothesis of the aggregation of **9a–d** in chloroform solution is proposed based on the fluorescence excitation measurements. The fluorescence excitation spectra for **9a–d** in chloroform solution are shown in **Figure S2** and compared with the absorption spectra. The excitation spectra for the compounds show a different vibrational progression and are red-shifted when compared to the absorption spectra, suggesting aggregation, since the excitation spectrum should be identical in shape to the absorption spectrum, provided that there is a single species in the ground state. In contrast, the excitation and absorption spectra are no longer superimposable when species exist in different forms, such as aggregates, in the ground state (Valeur, 2012). When compared with similar benzothiadiazole derivatives previously reported by our group (Westrup et al., 2016), the benzoxadiazole-based compounds **9a–d** showed a

greater tendency toward aggregate formation. This could be associated with the benzoxadiazole moiety and the higher dipole moment of this heterocycle (Tobiason et al., 1973).

It was observed that the size of the alkyl chain did not significantly influence the deactivation of the excited states, suggesting that only the conjugated aromatic part contributes to the frontier orbitals (HOMO and LUMO), which are responsible for the radiative processes.

Solvatochromism

A solvatochromic study of compounds **9a–d** was performed to ascertain the role of solvent polarity in the absorption and fluorescence emission. The UV-vis absorption and fluorescence emission properties were measured in heptane (Hep), toluene (Tol), chloroform (CHCl_3), tetrahydrofuran (THF), acetone (Acet), *N,N*-dimethylformamide (DMF), and acetonitrile (CH_3CN) solutions. The UV-Vis absorption and emission spectra for **9a** in various solvents are shown in **Figure 2**, and the specifics of the absorption and fluorescence emission of these compounds are listed in **Table 2**.

With increasing solvent polarity, the absorption bands of compound **9a** showed a slight red-shift, indicating a small solvatochromic effect on the ground state. The fluorescence spectra showed a notable hypsochromic shift of the maximum emission in heptane, toluene, and THF (less polar solvents) and higher vibrational resolution when compared to CHCl_3 . The largest hypsochromic shifts were observed for THF and toluene (15 and 22 nm, respectively). This type of optical behavior in apolar organic solvents is similar to that exhibited by benzothiadiazole (Westrup et al., 2016). With the use of a more polar solvent like *N,N*-dimethylformamide or acetonitrile, a small hypsochromic shift in the emission maxima compared to CHCl_3 was also registered. This solvatochromism behavior is observed in molecules exhibiting larger dipole moments and charge transfer characteristics in the excited state, that is, an ICT state (Liang et al., 2015).

The excited-state lifetimes and relative amplitudes of **9a** at $10^{-5} \text{ mol L}^{-1}$ in heptane, toluene, tetrahydrofuran, and acetone are shown in Table S2. In all solvents, **9a** exhibited two excited-state lifetimes. Except in heptane, the longer excited-state lifetimes (τ_1) were over 3 ns and the shorter lifetimes (τ_2) ranged from 2.2 to 1.8 ns. In addition, the shortest lifetime dominates the fluorescence (A_2) of compound **9a**. The longer excited-state lifetimes (τ_1) were attributed here to monomeric emission of **9a**, while the shorter excited-state lifetimes (τ_2) could be associated with the emission provided by aggregates of molecules **9a** in toluene, tetrahydrofuran (THF), and acetone solutions. In heptane solution, the longest lifetime (τ_1) of molecule **9a** was found to be 2.1 ns and the shortest lifetime (τ_2) around 1.4 ns, which could be related to the poor stabilization of the excited state by the non-polar solvent. In addition, the contributions of the longest lifetime (A_1) and the shortest lifetime (A_2) to the emission of **9a** in heptane were similar, suggesting that the emission of **9a** in heptane solution is provided equally by the monomer and the aggregate of **9a**.

The quantum yields of **9a** in different solvents are shown in Table S2. The quantum yields increase with increasing affinity of the solvent for compound **9a**. The quantum yields for **9a** were 0.27 in heptane solution and 0.71 in acetone solution. In toluene, THF, and acetone solutions, the emission lifetime results suggest that the aggregate dominates the emission of compound

9a; however, monomeric emission of **9a** also contributes to the fluorescence, mainly in acetone solution. As the ICT state is known to be able to non-radiatively deactivate excited species, the quantum yield results are in agreement with the proposed molecular aggregation, which suppresses the ICT in the excited state of the monomer and increases the quantum yield in polar solvents (Liang et al., 2015).

Theoretical Modeling of the Electronic Structure and Fluorescence

To gain a better understanding of the absorption and luminescence properties of **9a–d**, we carried out calculations using DFT for a representative molecule without the aliphatic carbon chains (**9**). The calculated frontier orbitals are shown in Figure 3. It can be observed that the HOMO has major contributions from the benzene ring of the benzoxadiazole moiety and from the triple bonds, whereas the LUMO is mostly a π^* orbital delocalized over the benzoxadiazole. The HOMO (−2) and HOMO (−1) are more evenly spread through the molecule, while the LUMO (+1) is more centered in the benzoxadiazole ring and LUMO (+2) in the benzene rings close to the tetrazole.

TD-DFT calculations were performed to acquire information related to the excited states. The absorption spectra were calculated and convoluted with Gaussians, reproducing the experimental spectra, as shown for each molecule in Figure 4. Table 3 shows some of the first two calculated transitions, which were observed in the experimental spectra. To simulate the solvent dependence, the linear response CPCM was used to account for the effect of the solvent on the energy. The two transitions predicted for **9** correspond to those observed in the measured spectra, and, in all solvents, the lowest energy transition originates from a HOMO \rightarrow LUMO (95) excitation. The calculated spectra showed the same solvent-dependence observed in the UV-Vis spectra. With increasing solvent polarity, the first excited state is predicted to be stabilized and the transition matrix element of the dipole moment operator decreases. These results, together with an analysis of the molecular orbitals involved in the first electronic transition, lead to the assignment of a π - π^* transition with the characteristics of a charge transfer excitation, thus explaining the large transition dipole moment and Stokes shift observed.

The fluorescence spectra were also calculated for **9** using the path integral approach developed by our group (Souza et al., 2018, 2019). The PBE0 functional was chosen to obtain the adiabatic electronic energy differences. The emission spectra, shown in Figure 5, are also consistent with the experimental results. The emission peak was shifted for the different solvents; for example, hexane and toluene showed emission at higher energy compared with the other solvents. The main vibrational progression observed in the experimental spectra of non-polar solvents is due to the C=C and C=N stretching modes, with the energy separation of these peaks beginning at around 0.15 eV ($1,200 \text{ cm}^{-1}$).

Thermal Properties

The thermal properties of compounds **9a–d** were obtained by thermogravimetric analysis (TGA) (Figure 6). The DTG

TABLE 2 | The absorption and emission wavelengths, molar absorption coefficient, and Stokes shifts of compound **9a** in various solvents.

Compound	Absorption ^b $\lambda_{\text{max}}(\text{nm}) (\epsilon)^a$	Emission ^c $\lambda_{\text{max}} (\text{nm})$	Stokes shift (cm^{-1})
9a (Hept)	416 (2.7×10^7)	487	3,505
9a (Tol)	420 (2.8×10^7)	477	2,845
9a (CHCl_3)	420 (2.8×10^7)	499	3,769
9a (THF)	416 (2.7×10^7)	484	3,377
9a (Acet)	413 (2.7×10^7)	491	3,846
9a (DMF)	417 (2.8×10^7)	499	3,941
9a (CH_3CN)	413 (2.7×10^7)	499	4,173

^a $\text{L mol}^{-1} \text{ cm}^{-1}$. ^b $[c] = 1.5 \times 10^{-5} \text{ mol L}^{-1}$. ^cExcited at absorption maxima.

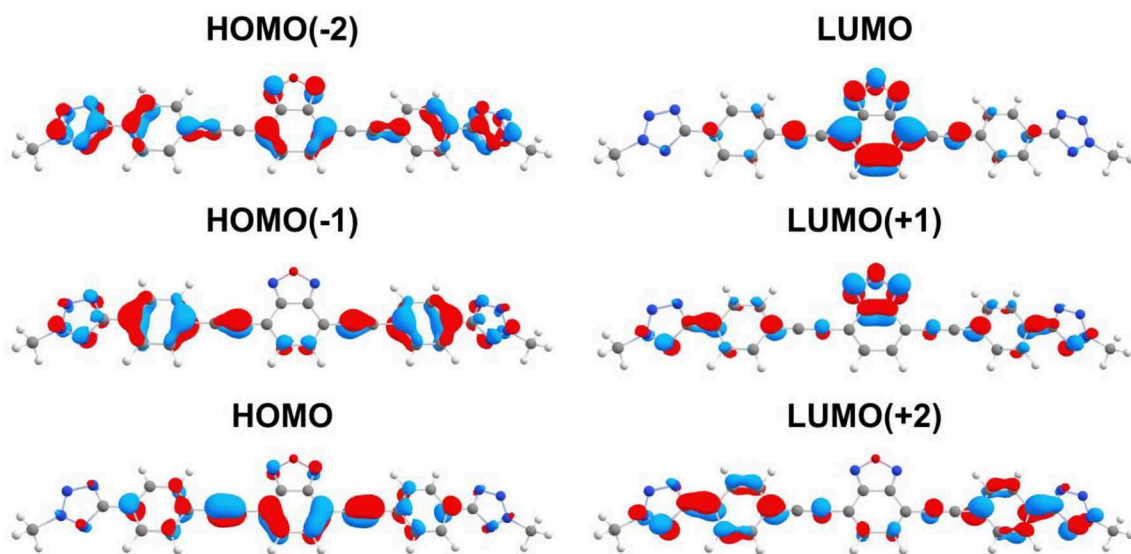


FIGURE 3 | Frontier molecular orbitals of **9** calculated using PBE0/def2-TZVP(-f).

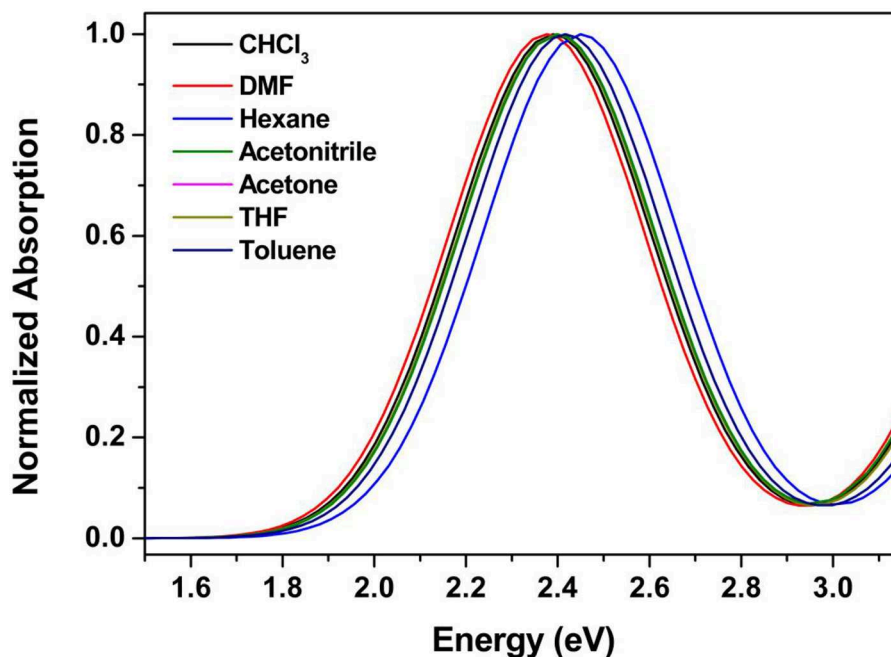


FIGURE 4 | Theoretical absorption spectra calculated in different solvents using PBE0/def2-TZVP(-f) and convoluted with Gaussians of 0.25 eV width.

curves for the final compounds were processed from the TGA curves. The complete degradation process indicates a mass loss of around 100%. Three thermal events were observed for these compounds, corresponding to a mass loss of almost 55% at an initial decomposition temperature of 220°C, with a maximum degradation rate observed at around 300°C. The second thermal event was detected at approximately 305°C, and this event is related to a loss of 51%. A small thermal

event was detected at ~650°C, and this event is related to a loss of 4%.

Electrochemical Characterization

Compounds **9a–d** show very distinct reduction processes in the negative scan (**Figure 7**). The first may be associated with a quasi-reversible reduction of the benzoxadiazole, indicating that the benzochalcogen ring is reduced in preference to the triple

bond. Benzochalcogen is a well-known heteroatomic compound with a high electron-accepting part, because it has two electron-withdrawing imine groups (C=N) (Omer et al., 2009).

TABLE 3 | Data for the TD-DFT excitations using PBE0/def2-TZVP(-f).

State	Energy		<i>f</i>	<I μ F> ²	Attribution ^a
	eV	Solvent shift			
Hexane					
S ₁	2.45	0.14	1.7804	29.67	H → L (95)
S ₂	3.04	0.19	0.0002	0.004	H-1 → L (88)
Toluene					
S ₁	2.42	0.18	1.7323	29.25	H → L (95)
S ₂	3.00	0.23	0.0003	0.004	H-1 → L (88)
CHCl ₃					
S ₁	2.40	0.18	1.6547	28.19	H → L (95)
S ₂	2.98	0.23	0.0003	0.004	H-1 → L (88)
THF					
S ₁	2.40	0.17	1.6347	27.83	H → L (95)
S ₂	2.99	0.22	0.0003	0.004	H-1 → L (88)
Acetone					
S ₁	2.40	0.16	1.6038	27.29	H → L (95)
S ₂	2.99	0.21	0.0003	0.004	H-1 → L (89)
DMF					
S ₁	2.38	0.18	1.5804	27.15	H → L (95)
S ₂	2.95	0.90	0.0037	0.0521	H-3 → L (94)
Acetonitrile					
S ₁	2.40	0.16	1.5962	27.16	H → L (95)
S ₂	3.00	0.21	0.0003	0.004	H-1 → L (89)

^a Transitions with high percentage contributions are shown in parentheses.

Thus, in the case of **9a–d**, this peak can be attributed to the benzoxadiazole group and the reduction peak can probably be assigned to the anion radical species. The second process that occurs at much more cathodic values may be associated with an irreversible electrochemical process with triple bond reduction (Neto et al., 2005, 2013). In the positive scan, various oxidation processes were observed, which probably include oxidation of the tetrazole portion of the molecule, and this process could involve the formation of an intermediate radical cation species.

The energies of HOMO and LUMO boundary orbitals of π -conjugated systems (D- π -A- π -D), such as benzochalcogenic derivatives, can be defined by the electron affinity (EA) and ionization potential (IP). These can be accessed by the evaluation of electron affinity (EA) and the ionization potential (IP), based on the values of reduction and oxidation potentials obtained by electrochemical assays (Neto et al., 2013; Frizon et al., 2014). The EA and IP were determined using the following empirical formula (Neto et al., 2005): $EA = E_{\text{onset}}^{\text{red}} + 4.44 \text{ eV}$ and $IP = E_{\text{onset}}^{\text{oxi}} + 4.44 \text{ eV}$, where $E_{\text{onset}}^{\text{red}}$ and $E_{\text{onset}}^{\text{oxi}}$ are the onset potentials of reduction and oxidation, respectively. These onset potentials were corrected from Ag/Ag⁺ to NHE using the Fc/Fc⁺ pair. Analyses of the HOMO-LUMO energy level calculations of **9a–d** were performed from benzoxadiazole potentials. The band gap values obtained by cyclic voltammetry and UV-vis spectroscopy showed good agreement between the results obtained with the two different techniques. The results of the electrochemical assays conducted with **9a–d** showed that changes in the length of the alkyl group attached to the tetrazole ring did not significantly influence the redox potentials of the molecules. The $E_{\text{gap}}^{\text{ele}}$ values obtained for molecules **9a–d** were higher than those for benzoselenadiazole (Regis et al., 2018).

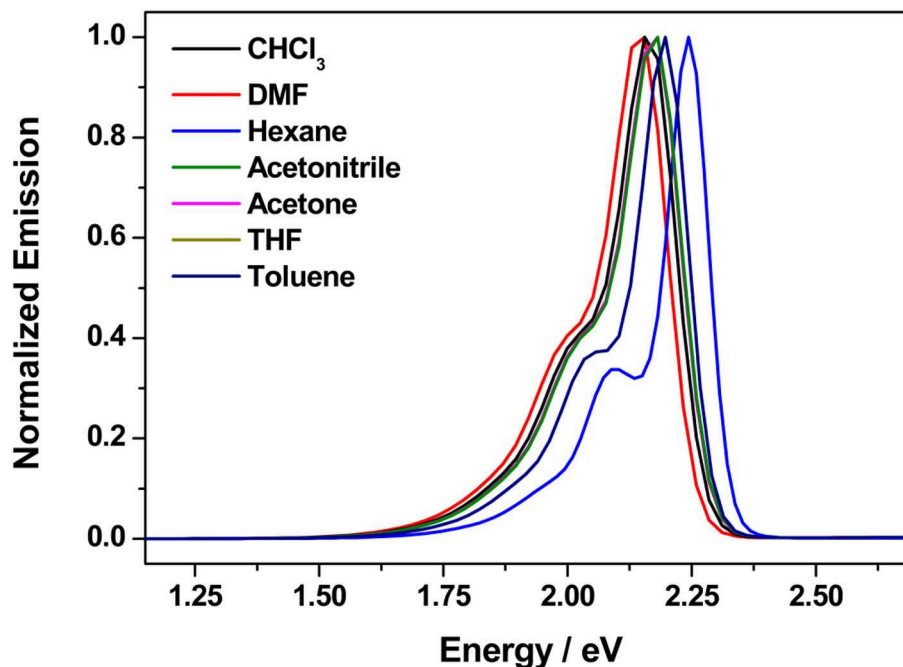


FIGURE 5 | Predicted emission spectra calculated in different solvents using PBE0/def2-TZVP(-f).

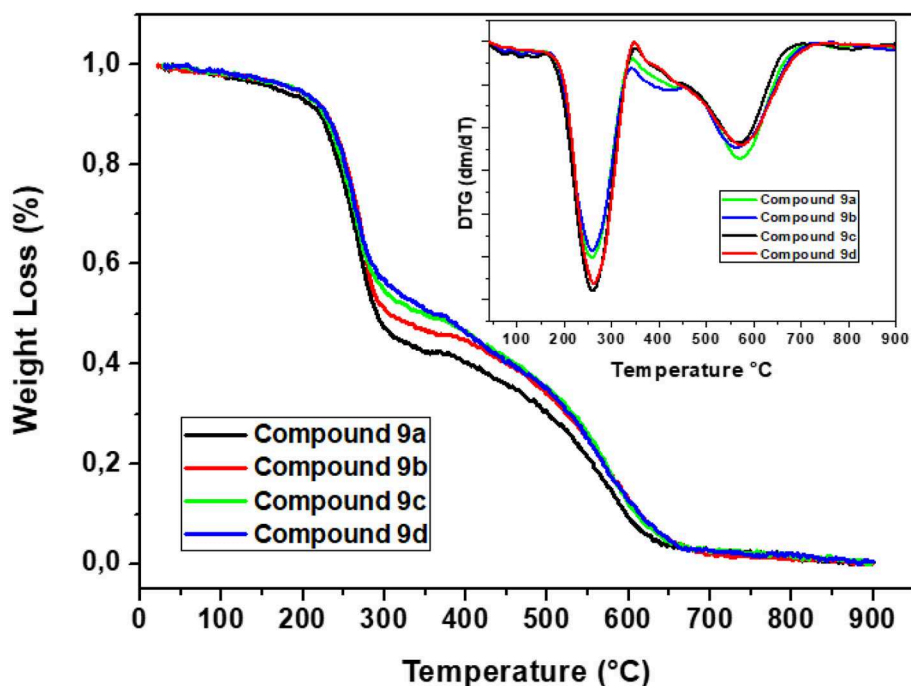


FIGURE 6 | Thermograms (TGA) and DTG curves of compounds **9a–d**.

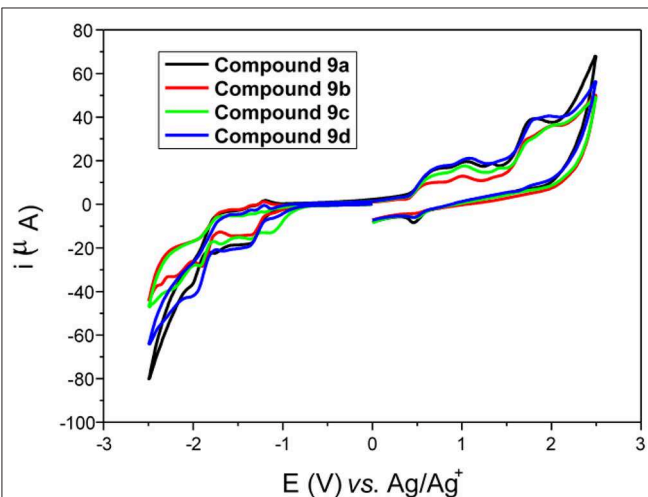


FIGURE 7 | Cyclic voltammogram of compounds **9a–d** on a glassy carbon electrode in 0.1 TBAPF₆/CH₂Cl₂ at 100 mV s⁻¹.

TABLE 4 | Optical and electrochemical properties of compounds **9a–d**, where E_{oxi}^{onset} is the onset potential of oxidation, E_{red}^{onset} is the onset potential of reduction, I_p (HOMO) is the ionization potential, E_a (LUMO) is the electron affinity, E_g is the band gap, and λ_{onset} is the absorption onset wavelength.

Parameter	Compound			
	9a	9b	9c	9d
E_{oxi}^{onset} (V) ^a	1.964	1.934	2.001	1.953
E_{red}^{onset} (V) ^a	-0.726	-0.756	-0.476	-0.746
IP (HOMO) (eV) ^b	-6.404	-6.374	-6.441	-6.393
EA (LUMO) (eV) ^c	-3.714	-3.684	-3.994	-3.964
E_{ele}^{gap} (eV)	2.69	2.69	2.48	2.70
λ_{onset} (nm)	467.1	468.9	468.8	468.1
E_{gap}^{opt} (eV) ^d	2.65	2.64	2.64	2.65

^a vs. NHE; ^b $IP = -(E_{ox} + 4.44)$ eV; ^c $EA = -(E_{red} + 4.44)$ eV; ^d Optical bandgap calculated on the low energy band edge of the absorption spectrum ($E_{gap}^{opt} = 1240/\lambda_{onset}$).

CONCLUSIONS

In this study, a new series of fluorophores, with D- π -A- π -D molecular architectures, based on 2,1,3-benzoxadiazole derivatives, was synthesized and characterized. The photophysical behavior of the compounds was evaluated by combining the following spectroscopic techniques: UV-vis absorption spectroscopy, stationary fluorescence spectroscopy, and time-resolved spectroscopy. The series of molecules in solution exhibited, in the visible region, a maximum absorption (~ 419 nm) that can be attributed to electronic transitions of the

type π - π^* ($\epsilon \sim 3.4 \times 10^{-4} \text{ L mol}^{-1}\text{cm}^{-1}$). Compounds **9a-d** exhibited intense fluorescence ($\Phi_{\text{FL}} \sim 0.5$) located in the bluish-green region (494–498 nm) with a solvent polarity dependence resulting in a large Stokes shift (ca. $3,779 \text{ cm}^{-1}$), which was associated with an ICT in the excited state. The data obtained from DFT and TD-DFT indicate that the ground and first excited states are a π -type orbital. Therefore, a π - π^* transition with the characteristics of a charge transfer excitation can be assumed, confirming the ICT state. Compounds **9a-d** showed a strong tendency to form aggregates even in dilute solution, exhibiting in CHCl_3 solution longer and shorter lifetimes, on the nanosecond timescale, which were here attributed to the emission of monomeric and aggregated molecules, respectively. The thermal characterization allowed the thermal stability of compounds **9a-d** to be evaluated, and a high maximum degradation rate was observed at around 300°C . Small electrochemical band gap (2.48 to 2.70 eV) and optical band gap (2.64 to 2.67 eV) values were obtained for compounds **9a-d**, these being in agreement with results for similar compounds previously reported in the literature. The redox potentials of **9a-d** did not change significantly with variations in the length of the alkyl group attached to the tetrazole ring. The recognition of the structure–property relationship of benzoxadiazole could guide further studies in the search for luminescent materials with better performance than benzothiadiazole.

DATA AVAILABILITY STATEMENT

All datasets generated for this study are included in the article/**Supplementary Material**.

REFERENCES

- Aguiar, L., Regis, E., Tuzimoto, P., Giroto, E., Bechtold, I. H., Gallardo, H., et al. (2018). Investigation of thermal and luminescent properties in 4,7-diphenylethynyl-2,1,3-benzothiadiazole systems. *Liq. Cryst.* 45, 49–58. doi: 10.1080/02678292.2017.1293854
- Armarego, W. L. F., and Chai, C. L. L. (2003). *Purification of Laboratory Chemicals*, 5th ed. Amsterdam; Boston, MA: Butterworth-Heinemann.
- Becke, A. D., and Johnson, E. R. (2005). A density-functional model of the dispersion interaction. *J. Chem. Phys.* 123:154101. doi: 10.1063/1.2065267
- Bettanin, L., Saba, S., Doerner, C. V., Franco, M. S., Godoi, M., Rafique, J., et al. (2018). NH_4I -catalyzed chalcogen(S/Se)-functionalization of 5-membered N-heteroaryls under metal-free conditions. *Tetrahedron* 74, 3971–3980. doi: 10.1016/j.tet.2018.05.084
- Bo, A. G. D., Durate, R. C., Cercena, R., Peterson, M., Rafique, J., Saba, S., et al. (2018). New long-chain donor-acceptor-donor pyromellitic diimide (PMDI) derivatives. A combined theoretical and experimental study. *Dyes Pigments* 157, 143–150. doi: 10.1016/j.dyepig.2018.04.053
- Bo, A. G. D., Micheletto, Y. M. S., Giancomelli, F. C., Lopez, G., Sartor, M. J. R. S., Rafique, J., et al. (2016). Synthesis of new monodendrons, gallic acid derivatives, self-assembled in a columnar phase. *Liq. Cryst.* 43, 292–304. doi: 10.1080/02678292.2015.1106013
- Bouffard, J., and Swager, T. M. (2008). Fluorescent conjugated polymers that incorporate substituted 2,1,3-benzoxadiazole and 2,1,3-benzothiadiazole units. *Macromolecules* 41, 5559–5562. doi: 10.1021/ma8010679
- Chemcraft (2019). *Graphical Program for Visualization of Quantum Chemistry Computations*. Available online at: <http://www.chemcraftprog.com/> (accessed June 7, 2019).

AUTHOR CONTRIBUTIONS

TF, AV, and JR conceived the project and wrote the manuscript. TF, JR, AV, SS, and ML performed the synthesis and characterization. AV, FS, TE, and TC studied the photophysical properties (absorption and fluorescence spectra). HB, FG, and TF studied the thermal properties. EZ performed the electrochemical studies. GF and BS made the theoretical predictions. SC and TC studied the singlet excited-state lifetimes. All authors discussed the results and commented on the manuscript.

ACKNOWLEDGMENTS

The authors gratefully acknowledge CAPES (001), CNPq (433896/2018-3), UFMS, CNPq (MCTI/CNPq N° 422750/2018-Universa; PIBIC; PIBIT; PQ-2), FAPEMIG, PROPP/UFOP (# 23109.003517/2018-85), and FAPESC (2019TR1055) for financial support. The authors acknowledge CEBIME-UFSC for the HRMS analysis.

SUPPLEMENTARY MATERIAL

The Supplementary Material for this article can be found online at: <https://www.frontiersin.org/articles/10.3389/fchem.2020.00360/full#supplementary-material>

For compounds **9a-d**, the absorption (Abs) and fluorescence excitation (Ex) spectra, NMR spectra, FTIR spectra, and HRMS are available in **Figures S3–S23**.

- Crosby, G. A., and Demas, J. N. (1971). Measurement of photoluminescence quantum yields. *Rev. J. Phys. Chem.* 75, 991–1024. doi: 10.1021/j100678a001
- Fang, H., Gao, H., Wang, T., Zhang, B., Xing, W., and Cheng, X. (2017). Benzothiadiazole-based D- π -A- π -D fluorophores: synthesis, self-assembly, thermal and photophysical characterization. *Dyes Pigments* 147, 190–198. doi: 10.1016/j.dyepig.2017.07.045
- Fery-Forgues, S., and Lavabre, D. (1999). Are fluorescence quantum yields so tricky to measure? A demonstration using familiar stationery products. *J. Chem. Educ.* 76:1260. doi: 10.1021/ed076p1260
- Frizon, T. E., Dal-Bó, A. G., Lopez, G., Silva Paula, M. M., and Silva, L. (2014). Synthesis of luminescent liquid crystals derived from gallic acid containing heterocyclic 1,3,4-oxadiazole. *Liq. Cryst.* 41, 1162–1172. doi: 10.1080/02678292.2014.909954
- Frizon, T. E. A., Duarte, R. C., Westrup, J. L., Perez, J. M., Menosso, G., Duarte, L. G. T. A., et al. (2018). Synthesis, electrochemical, thermal and photophysical characterization of quinoxaline-based π -extended electroluminescent heterocycles. *Dyes Pigments* 157, 218–229. doi: 10.1016/j.dyepig.2018.04.059
- Frizon, T. E. A., Martínez, J. C. V., Westrup, J. L., Duarte, R., Zapp, E., Domiciano, K. G., et al. (2016). 2,1,3-Benzothiadiazole-based fluorophores. Synthesis, electrochemical, thermal and photophysical characterization. *Dyes Pigments* 135, 26–35. doi: 10.1016/j.dyepig.2016.07.011
- Frizon, T. E. A., Rafique, J., Saba, S., Bechtold, I. H., Gallardo, H., and Braga, A. L. (2015). Synthesis of functionalized organoselenium materials: selenides and diselenides containing cholesterol. *Eur. J. Org. Chem.* 2015, 3470–3476. doi: 10.1002/ejoc.201500124
- Fu, H., Gao, X., Zhong, G., Zhong, Z., Xiao, F., and Shao, B. (2009). Synthesis and electroluminescence properties of benzothiazole derivatives. *J. Lumin.* 129, 1207–1214. doi: 10.1016/j.jlumin.2009.06.004

- Gallardo, H., Conte, G., Tuzimoto, P. A., Behramand, B., Molin, F., Eccher, J., et al. (2012). New luminescent liquid crystals based on 2,1,3-benzothiadiazole and bent five-membered *N*-heterocyclic cores. *Liq. Cryst.* 39, 1099–1111. doi: 10.1080/02678292.2012.698313
- Ghosh, S., Kumar, K. R., and Zade, S. S. (2018). Effects of chalcogen atom variation in chalcogenadiazole fused indolo[2,3-*a*]carbazoles. *N. J. Chem.* 42, 6889–6895. doi: 10.1039/C7NJ04661H
- Göker, S., Hizalan, G., Udum, Y. A., and Toppare, L. (2014). Electrochemical and optical properties of 5,6-bis(octyloxy)-2,1,3 benzoxadiazole containing low band gap polymers. *Synth. Met.* 191, 19–27. doi: 10.1016/j.synthmet.2014.02.010
- Grimme, S., Antony, J., Ehrlich, S., and Krieg, H. (2010). A consistent and accurate *ab initio* parametrization of density functional dispersion correction (DFT-D) for the 94 elements H-Pu. *J. Chem. Phys.* 132:154104. doi: 10.1063/1.3382344
- Grimme, S., Ehrlich, S., and Goerigk, L. (2011). Effect of the damping function in dispersion corrected density functional theory. *J. Comput. Chem.* 32, 1456–1465. doi: 10.1002/jcc.21759
- Izsák, R., and Neese, F. (2011). An overlap fitted chain of spheres exchange method. *J. Chem. Phys.* 135:44105. doi: 10.1063/1.3646921
- Izsák, R., Neese, F., and Klopper, W. (2013). Robust fitting techniques in the chain of spheres approximation to the Fock exchange: the role of the complementary space. *J. Chem. Phys.* 139:094111. doi: 10.1063/1.4819264
- Johnson, E. R., and Becke, A. D. (2005). A post-Hartree-Fock model of intermolecular interactions. *J. Chem. Phys.* 123:024101. doi: 10.1063/1.1949201
- Johnson, E. R., and Becke, A. D. (2006). A post-Hartree-Fock model of intermolecular interactions: inclusion of higher-order corrections. *J. Chem. Phys.* 124:174104. doi: 10.1063/1.2190220
- Kawashima, K., Osaka, I., and Takimiya, K. (2015). Effect of chalcogen atom on the properties of naphthobis(chalcogenadiazole)based π -conjugated polymers. *Chem. Mater.* 27, 6558–6570. doi: 10.1021/acs.chemmater.5b03124
- Liang, Z., Wang, X., Dai, G., Ye, C., Zhou, Y., and Tao, X. (2015). The solvatochromism and aggregation-induced enhanced emission based on triphenylamine-propenone. *N. J. Chem.* 39, 8874–8880. doi: 10.1039/C5NJ01072A
- Lin, Z., Bjorgaard, J., Yavuz, A. G., and Köse, M. E. (2011). Low band gap star-shaped molecules based on benzothia(oxa)diazole for organic photovoltaics. *J. Phys. Chem. C* 115, 15097–15108. doi: 10.1021/jp204593x
- Liu, Z., He, J., Zhuang, H., Li, H., Li, N., Chen, D., et al. (2015). Effect of single atom substitution in benzochalcogenadiazole acceptors on the performance of ternary memory devices. *J. Mater. Chem. C* 3, 9145–9153. doi: 10.1039/C5TC02274F
- Marenich, A. V., Cramer, C. J., and Truhlar, D. G. (2009). Universal solvation model based on solute electron density and on a continuum model of the solvent defined by the bulk dielectric constant and atomic surface tensions. *J. Phys. Chem. B* 113, 6378–6396. doi: 10.1021/jp810292n
- Matzkeit, H. Y., Tornquist, B. L., Manarin, F., Botteselle, G. B., Rafique, J., Saba, S., et al. (2018). Borophosphate glasses: synthesis, characterization and application as catalyst for bis(indolyl)methanes synthesis under greener conditions. *J. Non Cryst. Solids* 498, 153–159. doi: 10.1016/j.jnoncrysol.2018.06.020
- Meirinho, A. G., Pereira, F. V., Martins, G. M., Saba, S., Rafique, J., Braga, A. L., et al. (2019). Electrochemical oxidative C(sp²)-H bond selenylation of activated arenes. *Eur. J. Org. Chem.* 2019, 6465–6469. doi: 10.1002/ejoc.201900992
- Neese, F. (2012). The ORCA program system. *WIREs Comput Mol Sci.* 2, 73–78. doi: 10.1002/wcms.81
- Neto, B. A. D., Lapis, A. A. M., Mancilha, F. S., Vasconcelos, I. B., Thum, C., Basso, L. A., et al. (2007). New sensitive fluorophores for selective DNA detection. *Org. Lett.* 9, 4001–4004. doi: 10.1021/ol701708y
- Neto, B. A. D., Lapis, A. A. M., Silva Júnior, E. N., and da Dupont, J. (2013). 2,1,3-Benzothiadiazole and derivatives: synthesis, properties, reactions, and applications in light technology of small molecules: 2,1,3-benzothiadiazole and derivatives. *Eur. J. Org. Chem.* 2013, 228–255. doi: 10.1002/ejoc.2012.01161
- Neto, B. A. D., Lopes, A. S., Ebeling, G., Gonçalves, R. S., Costa, V. E. U., Quina, F. H., et al. (2005). Photophysical and electrochemical properties of π -extended molecular 2,1,3-benzothiadiazoles. *Tetrahedron* 61, 0975–10982. doi: 10.1016/j.tet.2005.08.093
- Neto, J. S. S., Balaguer, R. A., Franco, M. S., Macahado, V. C. S., Saba, S., Rafique, J., et al. (2020). Trihaloisocyanuric acids in ethanol: an eco-friendly system for the regioselective halogenation of imidazo-heteroarene. *Green Chem.* doi: 10.1039/D0GC00137F. [Epub ahead of print].
- Niu, Q., Xu, Y., Jiang, J., Peng, J., and Cao, Y. (2007). Efficient polymer white-light-emitting diodes with a single-emission layer of fluorescent polymer blend. *J. Luminesc.* 126, 531–535. doi: 10.1016/j.jlumin.2006.10.004
- Omer, K. M., Ku, S., Wong, K., and Bard, A. J. (2009). Green electrogenerated chemiluminescence of highly fluorescent benzothiadiazole and fluorene derivatives. *J. Am. Chem. Soc.* 131:10733. doi: 10.1021/ja904135y
- Pati, P. B. (2016). Benzazole (B, N, O, S, Se and Te) based D-A-D type oligomers: switch from electropolymerization to structural aspect. *Org. Electron.* 38, 97–106. doi: 10.1016/j.orgel.2016.07.035
- Perdew, J. P., Burke, K., and Ernzerhof, M. (1996). Generalized gradient approximation made simple. *Phys. Rev. Lett.* 77, 3865–3868. doi: 10.1103/PhysRevLett.77.3865
- Perdew, J. P., Burke, K., and Ernzerhof, M. (1997). Generalized gradient approximation made simple. *Phys. Rev. Lett.* 78, 1396–1396. doi: 10.1103/PhysRevLett.78.1396
- Peterle, M. M., Scheide, M. R., Silva, L. T., Saba, S., Rafique, J., and Braga, A. L. (2018). Copper-catalyzed three-component reaction of oxadiazoles, elemental se/s and aryl iodides: synthesis of chalcogenyl (Se/S)-oxadiazoles. *ChemistrySelect* 3, 13191–13196. doi: 10.1002/slct.201801213
- Petrenko, T., Kossmann, S., and Neese, F. (2011). Efficient time-dependent density functional theory approximations for hybrid density functionals: analytical gradients and parallelization. *J. Chem. Phys.* 134:054116. doi: 10.1063/1.3533441
- Rafique, J., Saba, S., Franco, M. S., Bettanin, L., Schneider, A. R., Silva, L. T., et al. (2018b). Direct, metal-free C(sp²)-H chalcogenation of indoles and imidazopyridines with dichalcogenides catalysed by KIO₃. *Chem. Eur. J.* 24, 4173–4180. doi: 10.1002/chem.201705404
- Rafique, J., Saba, S., Frizon, T. E. A., and Braga, A. L. (2018a). Regioselective, solvent- and metal-free chalcogenation of imidazo[1,2-*a*]pyridines by employing I₂/DMSO as the catalytic oxidation system. *ChemistrySelect* 3, 328–334. doi: 10.1002/slct.201702623
- Rafique, J., Saba, S., Rosario, A. R., and Braga, A. L. (2016). Fe₃O₄ nanoparticles: a robust and magnetically recoverable catalyst for direct C-H bond selenylation and sulfonylation of benzothiazoles. *Chem. Eur. J.* 22, 11854–11862. doi: 10.1002/chem.201600800
- Regis, E., Aguiar, L., de O. Aguiar, L., Girotto, E., Frizon, T. E., Dal, Bó A. G., et al. (2018). Effect of heteroatom exchange (S/Se) in the mesomorphism and physical properties of benzochalcogenodiazole-based liquid crystals. *Dyes Pigments* 157, 109–116. doi: 10.1016/j.dyepig.2018.04.049
- Rodrigues, J., Saba, S., Joussef, A. C., Rafique, J., and Braga, A. L. (2018). KIO₃-catalyzed C(sp²)-H bond selenylation/sulfonylation of (hetero)arenes: synthesis of chalcogenated (hetero)arenes and their evaluation for anti-Alzheimer activity. *Asian J. Org. Chem.* 7, 1819–1824. doi: 10.1002/ajoc.201800346
- Saba, S., Botteselle, G. V., Godoi, M., Frizon, T. E. A., Galetto, F. B., Rafique, J., et al. (2017). Copper-catalyzed synthesis of unsymmetrical diorganyl chalcogenides (Te/Se/S) from boronic acids under solvent-free conditions. *Molecules* 22:1367. doi: 10.3390/molecules22081367
- Saba, S., Rafique, J., and Braga, A. L. (2015). Synthesis of unsymmetrical diorganyl chalcogenides under greener conditions: use of an Iodine/DMSO system, solvent- and metal-free approach. *Adv. Synth. Catal.* 357, 1446–1452. doi: 10.1002/adsc.201500024
- Saba, S., Rafique, J., and Braga, A. L. (2016). DMSO/iodine-catalyzed oxidative C-Se/C-S bond formation: a regioselective synthesis of unsymmetrical chalcogenides with nitrogen- or oxygen-containing arenes. *Catal. Sci. Technol.* 6, 3087–3098. doi: 10.1039/C5CY01503K
- Saba, S., Rafique, S., Franco, M. S., Schneider, A., Espindola, L., Silva, D. O., et al. (2018). Rose Bengal catalysed photo-induced selenylation of indoles, imidazoles and arenes: a metal free approach. *Org. Biomol. Chem.* 16, 880–885. doi: 10.1039/C7OB03177G
- Saba, S., Santo, C. R., Zavaris, B. R., Naujorks, A. A. S., Franco, M. S., Schneider, A. R., et al. (2020). Photoinduced, direct C(sp²)-H bond azo coupling of imidazoheteroarenes and imidazoanilines with aryl diazonium salts catalyzed by Eosin Y. *Chem. Eur. J.* 26, 4461–4466. doi: 10.1002/chem.202082063
- Schäfer, A., Horn, H., and Ahlrichs, R. (1992). Fully optimized contracted Gaussian basis sets for atoms Li to Kr. *J. Chem. Phys.* 97, 2571–2577. doi: 10.1063/1.463096

- Schäfer, A., Huber, C., and Ahlrichs, R. (1994). Fully optimized contracted Gaussian basis sets of triple zeta valence quality for atoms Li to Kr. *J. Chem. Phys.* 100, 5829–5835. doi: 10.1063/1.467146
- Scheide, M. R., Schneider, A. R., Jardim, G., Martins, G. M., Durigon, D. C., Saba, S., et al. (2020). Electrochemical synthesis of selenyl-dihydrofurans via anodic selenofunctionalization of allyl-naphthol/phenol derivatives and their anti-Alzheimer activity. *Org. Biomol. Chem.* doi: 10.1039/D0OB00629G. [Epub ahead of print].
- Silva, L. T., Azeredo, J. B., Saba, S., Rafique, J., Bortoluzzi, A. J., and Braga, A. L. (2017). Solvent- and metal-free chalcogenation of bicyclic arenes using I₂/DMSO as non-metallic catalytic system. *Eur. J. Org. Chem.* 2017, 4740–4748. doi: 10.1002/ejoc.201700744
- Song, Y., Funatsu, T., and Tsunoda, M. (2011). Amino acids analysis using a monolithic silica column after derivatization with 4-fluoro-7-nitro-2,1,3-benzoxadiazole (NBD-F). *J. Chromatogr. B* 879, 335–340. doi: 10.1016/j.jchromb.2010.12.018
- Souza, B., Farias, G., Neese, F., and Izsák, R. (2019). Predicting Phosphorescence rates of light organic molecules using time-dependent density functional theory and the path integral approach to dynamics. *J. Chem. Theory Comput.* 15:1896. doi: 10.1021/acs.jctc.8b00841
- Souza, B., Neese, F., and Izsák, R. (2018). On the theoretical prediction of fluorescence rates from first principles using the path integral approach. *J. Chem. Phys.* 148:034104. doi: 10.1063/1.5010895
- Sumiya, S., Sugii, T., Shiraishi, Y., and Hirai, T. (2011). A benzoxadiazole-thiourea conjugate as a fluorescent chemodosimeter for Hg(II) in aqueous media. *J. Photochem. Photobiol. Chem.* 219, 154–158. doi: 10.1016/j.jphotochem.2011.02.005
- Tobiason, F. L., Heuestis, L., Chandler, C., Pedersen, S. E., and Peters, P. (1973). The polar nature of 2,1,3-benzoxadiazole, -benzothiadiazole, -benzoselenadiazole and derivatives as determined by their electric dipole moments. *J. Heterocycl. Chem.* 10, 773–778. doi: 10.1002/jhet.5570100516
- Tornquist, B. L., Bueno, G. P., Willig, J. C. M., Oliveira, I. M., Stefani, H. A., Rafique, J. et al. (2018). Ytterbium (III) triflate/sodium dodecyl sulfate: A versatile recyclable and water-tolerant catalyst for the synthesis of bis(indolyl)methanes (BIMs). *ChemistrySelect* 3, 6358–6363. doi: 10.1002/slct.201800673
- Toyo'oka, T. (2004). "Indirect enantioseparation by HPLC using chiral benzofurazan-bearing reagents," in *Methods in Molecular Biology. Chiral Separations: Methods and Protocols*, Vol. 43, eds. G. Gübitz and M. G. Schmidh (Totowa: Humana Press Inc.), 231–246.
- Valeur, B. (2012). *Molecular Fluorescence: Principles and Applications*, 2nd Edn. Paris: WILEY-VCH.
- Wang, B., Pan, H., Jia, J., Ge, Y.-Q., Cai, W.-Q., Wang, J.-W., et al. (2014). Highly emissive dimesitylboryl-substituted 2,1,3-benzothiadiazole derivatives: photophysical properties and efficient fluorescent sensor for fluoride anions. *Tetrahedron* 70, 5488–5493. doi: 10.1016/j.tet.2014.06.110
- Weigend, F., and Ahlrichs, R. (2005). Balanced basis sets of split valence, triple zeta valence and quadruple zeta valence quality for H to Rn: design and assessment of accuracy. *Phys. Chem. Chem. Phys.* 7:3297. doi: 10.1039/b508541a
- Westrup, J. L., Oenning, L. W., Silva Paula, M. M., Costa Duarte, R., Rodembusch, F. S., Frizon, T. E. A., et al. (2016). New photoactive D- π -A- π -D benzothiadiazole derivative: synthesis, thermal and photophysical properties. *Dyes Pigments* 126, 209–217. doi: 10.1016/j.dyepig.2015.12.003
- Wu, G., Zhang, Y., Kaneko, R., Kojima, Y., Shen, Q., Islam, A., et al. (2017). A 2,1,3-benzoxadiazole moiety in a D-A-D-type hole-transporting material for boosting the photovoltage in perovskite solar cells. *J. Phys. Chem. C* 121, 17617–17624. doi: 10.1021/acs.jpcc.7b04614
- Würth, C., Grabolle, M., Pauli, J., Spieles, M., and Resch-Genger, U. (2011). Comparison of methods and achievable uncertainties for the relative and absolute measurement of photoluminescence quantum yields. *Anal. Chem.* 83, 3431–3439. doi: 10.1021/ac2000303
- Würth, C., Grabolle, M., Pauli, J., Spieles, M., and Resch-Genger, U. (2013). Relative and absolute determination of fluorescence quantum yields of transparent samples. *Nat. Protocol.* 8, 1535–1550. doi: 10.1038/nprot.2013.087
- Zeng, S., Yin, L., Jiang, X., Li, Y., and Li, K. (2012). D-A-D low band gap molecule containing triphenylamine and benzoxadiazole/benzothiadiazole units: synthesis and photophysical properties. *Dyes Pigments* 95, 229–235. doi: 10.1016/j.dyepig.2012.04.001

Conflict of Interest: The authors declare that the research was conducted in the absence of any commercial or financial relationships that could be construed as a potential conflict of interest.

Copyright © 2020 Frizon, Vieira, da Silva, Saba, Farias, de Souza, Zapp, Lôpo, Braga, Grillo, Curcio, Cazati and Rafique. This is an open-access article distributed under the terms of the Creative Commons Attribution License (CC BY). The use, distribution or reproduction in other forums is permitted, provided the original author(s) and the copyright owner(s) are credited and that the original publication in this journal is cited, in accordance with accepted academic practice. No use, distribution or reproduction is permitted which does not comply with these terms.



Development of Light-Responsive Poly(γ -Benzyl-L-Glutamate) as Photo Switches by a One-Step NCA Method

Pin Chen, Jingyang Kong, Xin Wang, Weiye Ma, Xia Yang, Yuqing Qin and Xiaohong Hu*

School of Material Engineering, Jinling Institute of Technology, Nanjing, China

OPEN ACCESS

Edited by:

Qixin Zhou,
University of Akron, United States

Reviewed by:

Yang Zhou,
Teknor Apex Company, United States
Zhifeng Deng,
Shaanxi University of
Technology, China

*Correspondence:

Xiaohong Hu
huxiaohong07@163.com

Specialty section:

This article was submitted to
Organic Chemistry,
a section of the journal
Frontiers in Chemistry

Received: 04 May 2020

Accepted: 08 June 2020

Published: 04 August 2020

Citation:

Chen P, Kong J, Wang X, Ma W,
Yang X, Qin Y and Hu X (2020)
Development of Light-Responsive
Poly(γ -Benzyl-L-Glutamate) as Photo
Switches by a One-Step NCA
Method. *Front. Chem.* 8:591.
doi: 10.3389/fchem.2020.00591

Synthesized polypeptide is attracting an increased interests due to its excellent biological characteristic and adjustable chemical properties in bio-related fields. But polypeptide itself has no switching properties, which is harmful to the development of its application as a control component. Herein, light-responsive poly(γ -benzyl-L-glutamate)s (PBLGs) is synthesized by a one-step NCA method using p-aminoazobenzene (m-AZO) and p-diaminoazobenzene (m-DAZO) as initiators. PBLGs exhibit amorphous characteristics with obvious T_g transition, which are 14°C for PBLG1 and 21°C for PBLG2. In order to forecast the structure-property information of PBLGs, theoretical UV-vis spectra as well as the energy gap between HOMO and LUMO is calculated by DFT calculation. Experimental results of UV-vis spectra exhibit similar characteristics to those of theoretical UV-vis spectra except for the 40–50 nm red-shifting of absorbance peak. Furthermore, the absorbance intensities of PBLGs have a good linear relationship with their concentration, but their linearity range depending on concentration is completely different. Then, trans–cis transition under a different excitation source and cis–trans recovery in a dark environment are tracked in real-time by UV-vis spectra to evaluate the light response performances. It is found that UV light is the only effective excitation source for PBLG1, and blue light is another effective excitation source for PBLG2 besides UV light. Furthermore, the addition of alcohol and water as cosolvents has little effect on trans→cis transition in UV-light-excited systems, but it shortens recovery time of the cis→trans process in a dark environment. By contrast, the detectable isomerization process becomes unclear with the addition of alcohol in blue-light-excited system. Furthermore, either alcohol or water in solvents accelerate both the trans→cis and cis→trans process in a blue-light-excited system.

Keywords: PBLG, NCA method, photo switch, light response, azobenzene

INTRODUCTION

Polypeptide has a similar chemical component and secondary structure to a natural protein, which plays an essential role in biological activities (Li et al., 2017; Skoulas et al., 2017; Zhou et al., 2017; Editors, 2019; Duan and Li, 2020; Duong et al., 2020). This characteristic endows polypeptide with properties of low toxicity, good biodegradability, and good biocompatibility (Li et al., 2017; Skoulas et al., 2017; Zhou et al., 2017; Editors, 2019; Duan and Li, 2020; Duong et al., 2020). On account of these advantages, this kind of material brings an increasing amount of attention to bio-related fields like drug delivery, biosensors, biological diagnosis, and tissue engineering. Among

polypeptides, synthesized polypeptides are the main focus due to their flexible and controllable molecular structure and are usually realized by biological synthesis, solid phase peptide synthesis (SPPS), and ring-open polymerization (ROP) based on the α -amino acid *N*-carboxyanhydrides (NCA method) (Wibowo et al., 2014; Shen et al., 2015; Zhou and Li, 2018). From the aspect of commercial process, the NCA method is more suitable for polypeptide materials due to the raw materials available, low cost, high yields, and short production cycle. More recently, $\text{Zn}(\text{OAc})_2$ -catalyzing ROP of NCA was used to obtain well-defined polypeptides with controlled molecular weight (M_w) and narrow molecular weight distribution (MWD) by Nie et al. (2018). Although the method has existed for more than 100 years, it is still a research hotspot for polypeptide synthesis (Wibowo et al., 2014).

Besides fundamental biological properties, synthesized polypeptide can be endowed with other properties like stimuli-responsive properties through post-synthesis functionalization in order to suit the needs of different applications (Dong and Chen, 2011; Shen et al., 2015; Qu et al., 2018; Xiao et al., 2019). Since efficiency and effectiveness were objects of chemical synthesis, tedious steps should be avoided for functional polypeptide preparation. Thus, a facile method to fabricate functional polypeptide with fewer steps is also needed to extend the application of polypeptides. With the development of the NCA method, the initiator of primary amine is considered to be a kind of idea initiator (Wibowo et al., 2014). Once an initiator is polymerized in the ROP process, it becomes a terminal group or medial unit of synthesized polypeptides depending on the number of the initiator's amino groups. Therefore, measures that combine functional groups with initiators are presumed to be a facile way to fabricate functional polypeptide based on the NCA method.

In recent decades, as a kind of stimuli-response material, photo switches have become new favorites in fields that require switching effects, including information science and chemical sensing due to structural changes in light. As a member of the photo switches, azobenzene (AZO) possesses two different reversible isomers (trans and cis) (Beharry and Woolley, 2011; Bian et al., 2016; Michael Kathan, 2017; Chen et al., 2018; Lerch et al., 2018; Pang et al., 2018, 2019). The reversible isomerization could be realized upon light excitation and thermal transition. But the thermal transition is influenced by either the external environment or internal structure of the AZO family, which bring problems of photobleaching, instability, and uncontrollability (Pang et al., 2018, 2019). In order to overcome problems, measures of substitute modifying, grafting, copolymerization, and immobilization have been used to improve the stability and controllability including our previous studies (Deka et al., 2015; Liu et al., 2015; Lin et al., 2016, 2017). Based on previous research, the long chains of polymers would help to increase the stability and controllability of thermal transition (Pang et al., 2018, 2019). Therefore, designing an AZO-functionalized polypeptide would provide a kind of practical photo switch for its application in bio-related fields.

In consideration of requests for an NCA synthesis method and photo switches, amino-substituted AZOs have been chosen as

initiators for the ROP of NCA. Generally, γ -benzyl-L-glutamate (BLG) is a kind of readily available and low-cost amino acid with good performance (Cauchois et al., 2013; de Miguel et al., 2014; Sun et al., 2015). Also, it can be polymerized into poly(γ -benzyl-L-glutamate) (PBLG) by the NCA method through two steps, namely, synthesis of γ -benzyl-L-glutamate-*N*-carboxyanhydride (BLG-NCA) and ROP of NCA. In view of these facts, BLG was used for the design and synthesis of polypeptide photo switches in this study. Simultaneously, considering the steric hindrance in polymerization, para amino substituted AZOs were used in the work. In order to evaluate the performance of synthesized PBLG as photo switches, properties of reversible light responses and thermal recovery were investigated and analyzed in the research.

Although azobenzene-based photo switches have been designed and confirmed, the research provides an efficient and effective approach with which to synthesize an adjustable polypeptide photo switch. Moreover, the research provides basic data for clarification of isomerization mechanism and amendment of theoretical model for AZO-based photo switches.

EXPERIMENT

Material

γ -benzyl-L-glutamate (BLG), triphosgene, p-aminoazobenzene (m-AZO), and p-diaminoazobenzene (m-DAZO) were purchased from Aladdin. Tetrahydrofuran (THF), n-hexane, diethyl ether, ethyl acetate (EA), dimethylformamide (DMF), dioxane, and alcohol were obtained from Sinopharm Chemical Reagent Co., Ltd, China. All other reagents and solvents were of analytical grade and used as received.

Synthesis and Characterization of BLG-NCA

γ -benzyl-L-glutamate-*N*-carboxyanhydride (BLG-NCA) was synthesized by a reaction between BLG and triphosgene. Briefly, 14 g BLG was dissolved in 200 mL anhydrous THF in reaction vessel with condensing reflux unit at stirring state. Then the solution was heated to 50°C, and 20 g triphosgene was added. The reaction continued until the solution turned from cloudy to clear. The reaction was cooled to room temperature, and N_2 was concurrently inlet into the reaction system until the liquid volume did not decrease any more. The solution was precipitated by n-hexane. After being purified by EA/n-hexane and dried in a vacuum oven, BLG-NCA was obtained and characterized by ^1H nuclear magnetic resonance (^1H NMR, Bruker, AV300) using CDCl_3 as a solvent.

Synthesis and Characterization of PBLGs

PBLG was synthesized by ROP. Briefly, 1 g dried BLG-NCA was dissolved in 20 mL dioxane in an anaerobic environment, and 76 μmol initiator (m-AZO or m-DAZO) in DMF solution was added batches of eight by way of injection. After the reaction had lasted for 72 h, the reaction solution was precipitated by diethyl ether. After being purified by THF/diethyl ether and dried in a vacuum oven, PBLG was obtained. When the initiator was m-AZO, final PBLG was denoted as PBLG1. When the initiator was m-DAZO, final PBLG was denoted as PBLG2.

Synthesized PBLGs were characterized by ^1H NMR (Bruker, AV300) using D₆-DMSO as a solvent and differential scanning calorimetry detection (PerkinElmer, DSC 4000). Furthermore, the degree of polymerization (DP), namely the number of repeated units, was calculated according to relative normalized H content between structural unit and initiator residue, which was obtained from integration area of ^1H NMR. Moreover, UV-vis spectra of PBLGs solution were tracked as a function of polymer concentration in order to characterize their characteristic peak and concentration dependence.

Investigation of Effective Excitation Sources for PBLGs

PBLG (PBLG1 or PBLG2) was dissolved in DMF to obtain dilute solution. Four different excitation sources, which were a UV lamp (240–365 nm, 3.6 W), blue light lamp (450–457 nm, 3.6 W), yellow light lamp (580–595 nm, 3.6 W), and a red light lamp (620–625 nm, 3.6 W), were used to excite isomerization for two polymers with a light density of 1000 Lux and at room temperature, respectively. After light irradiation, the recovery process was realized in a dark environment at room temperature. Real-time UV-vis spectra were recorded during irradiation process and recovery process, respectively. In the next step, repeated irradiation and recovery methods were applied to demonstrate fatigue resistance of PBLGs.

DFT Calculations for Azobenzene-Based Molecules

The calculating model was constructed using an azobenzene-based structural unit (initiator unit) including nearby BLG for PBLG. All calculations were carried out with Gaussian 09 programs at a CAM-B3LYP/6-31G (d, p) level (Ransil, 1961; Boys and Bernardi, 1970; Frisch et al., 2009). The UV-vis spectra and the vertical excitation potential for the first singlet excited state (S₁) were calculated by time-dependent DFT (TDDFT) calculations at the optimized S₀ geometry at the same level. Solvent effects were taken into account within the polarizing continuum model (PCM) framework in all the geometry optimization and excited state calculations.

Response-Recovery Performance of PBLGs

Besides excitation sources, the effects of solvents on the response-recovery performance of synthesized PBLGs were investigated. Besides DMF, water and alcohol were used to adjust the property of solvents. Similarly, the real-time UV-vis spectrum in the irradiation process as well as that in recovery time under a dark environment was recorded. Light density was set at 1000 Lux, and temperature was set at room temperature.

RESULTS AND DISCUSSIONS

Synthesis of PBLGs

Before synthesis of PBLGs, a BLG monomer was synthesized by elimination reaction with participation of triphosgene. The ^1H NMR spectrum of BLG is shown in **Figure 1A**, which was analyzed as follows: chemical shifts from 7.2 to 7.4 ppm were

attributed to protons on benzene ring at positions 6–8 with an integration of 4.7; the chemical shift at 6.5 ppm was attributed to proton of secondary amine at position 1 with an integration of 1.0; the chemical shift at 5.2 ppm was attributed to protons of methylene at position 5 with an integration of 2.0; the chemical shift at 4.4 ppm was attributed to the proton of methyne at position 2 with an integration of 1.0; the chemical shift at 2.7 ppm was attributed to protons of methylene at position 4 with an integration of 2.0; the chemical shifts from 2.1 to 2.4 ppm were attributed to protons of methylene at position 3 with an integration of 2.0. Since areas of resonance peaks are proportional to the number of protons, the ratio of different peak area is equal to ratio of proton number at different positions. Therefore, both the existence of the -NH- group at position 1 and the H atom ratio of position 1 to other positions confirmed the successful synthesis of BLG-NCA. Furthermore, no other chemicals were found in the ^1H NMR spectrum, which indicated high purity of synthesized BLG-NCA. Moreover, it was found from the experiment that the yield of this reaction for BLG-NCA was 70–75% w/w.

PBLG was obtained by the ROP method. When the initiator was m-AZO, AZO existed as a terminal group of PBLG1 (**Figure 1B**). The ^1H NMR spectrum of PBLG1 is also shown in **Figure 1B**, which was analyzed as follows: the chemical shifts from 7.9 to 8.6 ppm were attributed to protons at positions 7–9, chemical shifts from 7.0 to 7.8 ppm were attributed to protons at positions 1–3; and a chemical shift at 5.1 ppm was attributed to protons of methylene at position 4. These results not only confirmed the successful synthesis of PBLG1, but it also provided quantitative information of DP, which was calculated to be 14 according to the average normalized peak area (integration, **Figure 1B**) ratio of BLG units (positions 1–4) to AZO residue (positions 7–9). When the initiator was m-DAZO, AZO existed as a medium group of PBLG2 (**Figure 1C**). Chemical shifts of the ^1H NMR spectrum for PBLG2 in **Figure 1C** were attributed as follows: chemical shifts from 8.1 to 8.7 ppm belonging to protons at positions 7–8; chemical shifts from 6.6 to 7.6 ppm belonging to protons at positions 1–3; chemical shift at 5.1 ppm belonging to protons at position four; and chemical shifts from 1.6 to 3.0 ppm belonging to protons at positions –6. Also, the integration of these peaks was listed in **Figure 1C**. Similarly, the DP of synthesis PBLG2 was calculated to be 22.

Characterization and Calculation of PBLGs

DSC curves of PBLGs were detected to clarify structural characteristic, which are shown in **Figure 2**. No obvious phase transformation was found in the DSC curves of either PBLG1 (**Figure 2A**) or PBLG2 (**Figure 2B**), which indicated that the two polymers were both amorphous polymers. For PBLG1, an obvious T_g transition was found at 14°C (**Figure 2A**). For PBLG2, a T_g transition was found at 21°C (**Figure 2B**). Using common sense, we can see that the T_g transition was directly dependent on the length, free volume, and polarity of the domain. On account of the structural similarity of the two polymers, their polarities were also similar. Therefore, higher T_g might be the result of one of two things. One was that the domain length for PBLG2 was greater than that for PBLG1 if the DP of the polymers was not greater than one domain. The other was that the free

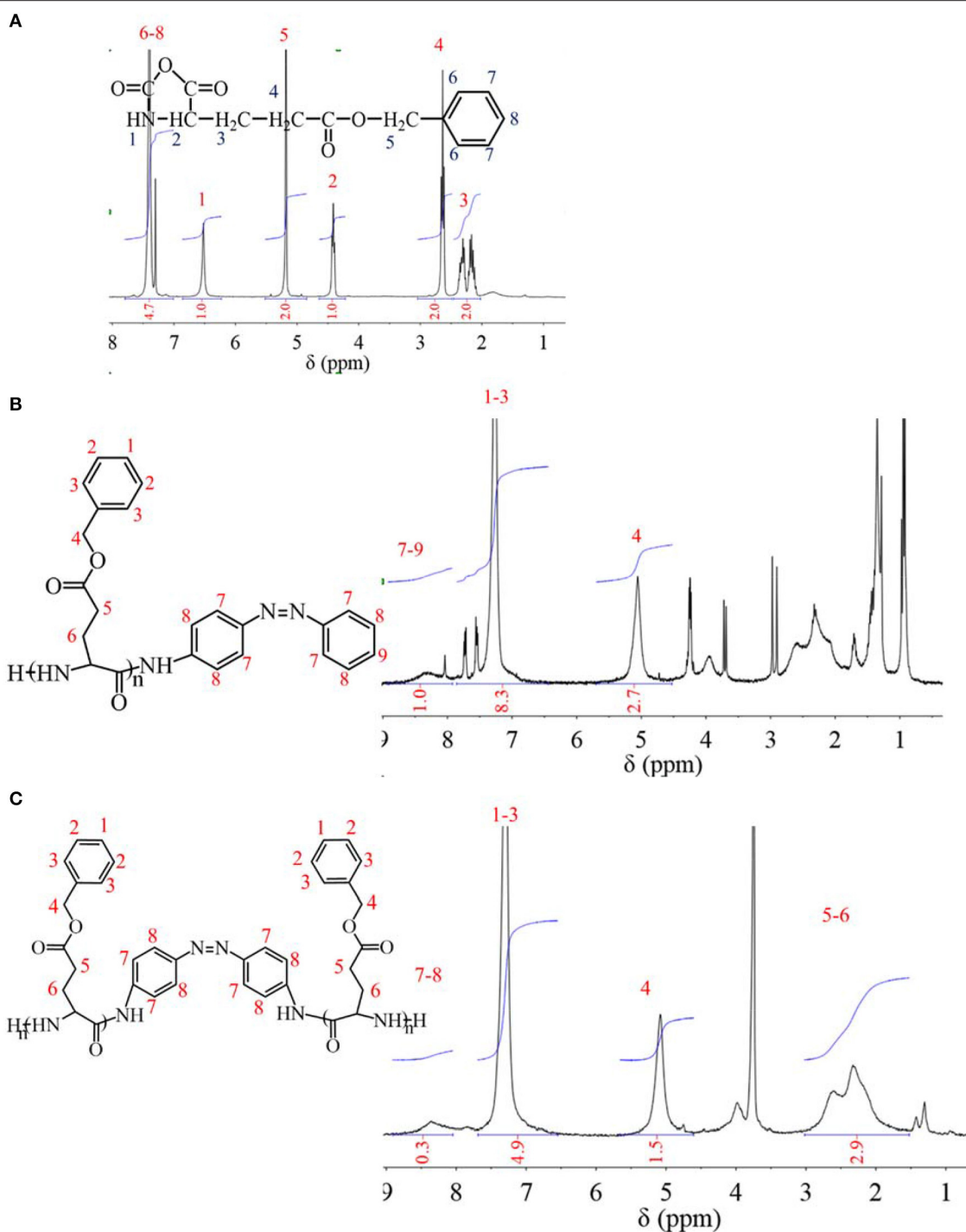
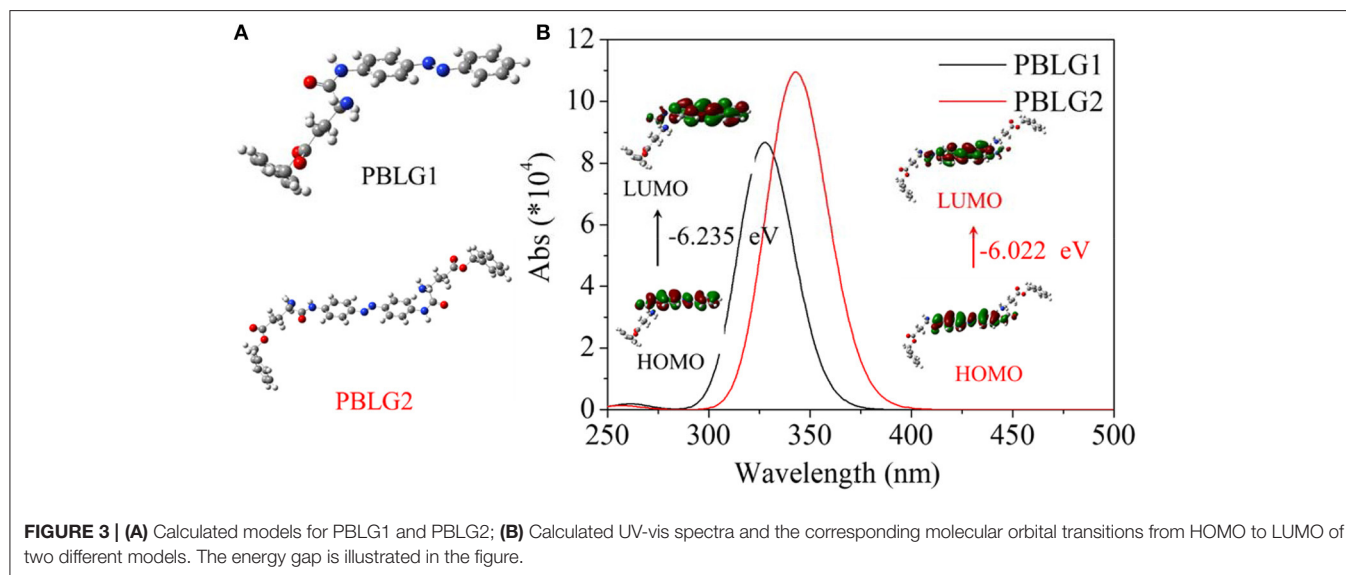
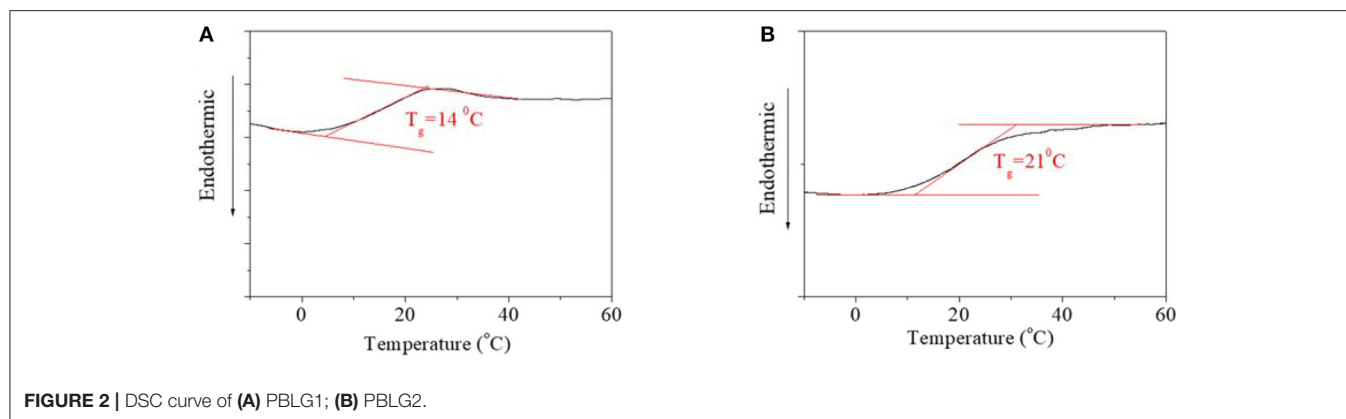


FIGURE 1 | ^1H NMR spectra of (A) BLG-NCA monomer; (B) PBLG1; (C) PBLG2.

volume of PBLG2 was smaller than that of PBLG1 in the same environment, which meant PBLG2 possessed a more compacted structure than PBLG1 due to the position of the AZO unit.

In order to forecast isomerization characteristics for PBLGs, DFT was used to calculate UV-vis spectra and the corresponding

molecular orbital transitions from HOMO to LUMO using simplified molecular models constructed by a central AZO unit and one or two nearby structural unit(s) (Figure 3A). Calculated results are shown in Figure 3B. It was found that PBLG1 had a maximum absorbance peak at 327 nm in theoretical



UV-vis spectra, and PBLG2 had a maximum absorbance peak at 343 nm red-shifting 16 nm away from that of PBLG1. Besides the different of wavelength between two PBLGs, the absorbance intensity of PBLG2 was higher than that of PBLG1 of the same status. Furthermore, the energy gap between HOMO and LUMO for PBLG2 was also lower than that for PBLG1 (**Figure 3B**). According to existing theories, the maximum peak belonged to π - π^* transition for the trans-isomer of an AZO unit, and trans \rightarrow cis transition included two process, from S0 up to S1 and from S1 down to S2 (base state for the cis isomer). Therefore, the excited energy of PBLG2 from S0 (base state for trans isomer) to S1 (excited state) was lower than that of PBLG1, which resulted in the absorbance peak red-shifting and absorbance intensity increasing since UV-vis absorbance is generally associated with electron transition. Simultaneously, the effective excitation wavelength for trans \rightarrow cis transition was inferred to be related to maximum UV-vis absorbance wavelength.

In an experimental system, UV spectra of PBLGs in DMF solution and their concentration dependence were characterized and shown in **Figure 4**. On the UV spectrum, PBLG1 exhibited a maximum absorbance peak at 390 nm, and the absorbance

increased with PBLG1 concentration (**Figure 4A**). Similarly, the maximum absorbance peak for PBLG2 occurred at 400 nm and also increased with its concentration (**Figure 4C**). The experimental position of the maximum absorbance peak was 55–70 nm, red-shifted from a theoretical position, which was reasonable, as that theoretical calculation could not involve all effects of a practical experiment. But the tendency to red-shift would not change. Furthermore, the absorbance intensity exhibited a good linear relationship with the polymer concentration (**Figures 4B,D**). The absorbance intensity of PBLG2 was, however, several times that of PBLG1 in the same concentration. Additionally, the linearity would help to quantify the polymer in terms of its application as a standard method.

Effective Excitation Sources for PBLGs

Since reversible response and recovery performance were indispensable properties for photo switches, they were investigated in detail. Four excitation sources were firstly used to excite isomerization transformation for PBLGs. UV light as a kind of excitation source could induce isomerization transformation of PBLG1, which is shown in **Figure 5**. Excited

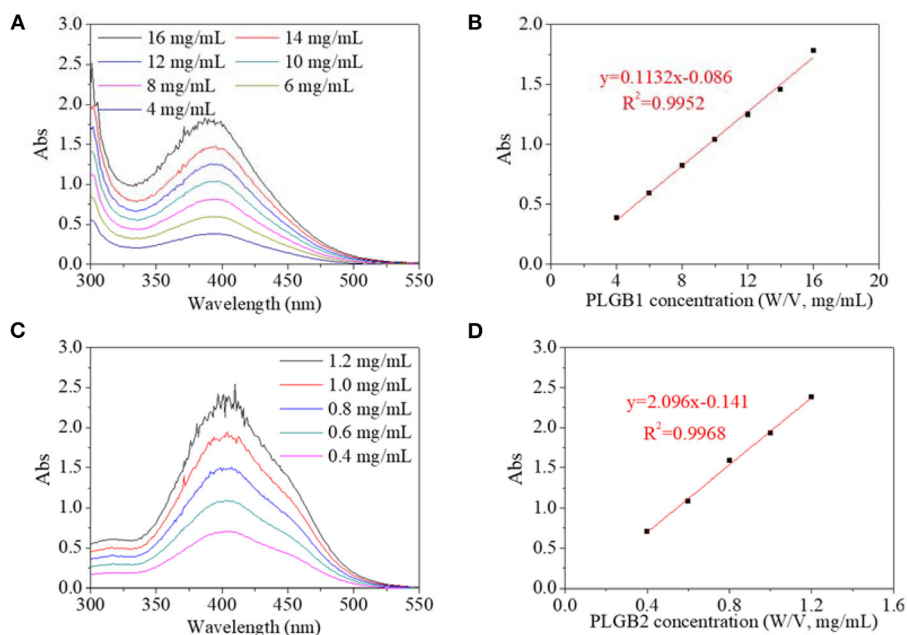


FIGURE 4 | UV spectra of (A) PBLG1 and (B) PBLG2 with different polymer concentration; (C) absorbance of PBLG1 at 390 nm as a function of PBLG1 concentration; (D) absorbance of PBLG2 at 400 nm as a function of PBLG2 concentration.

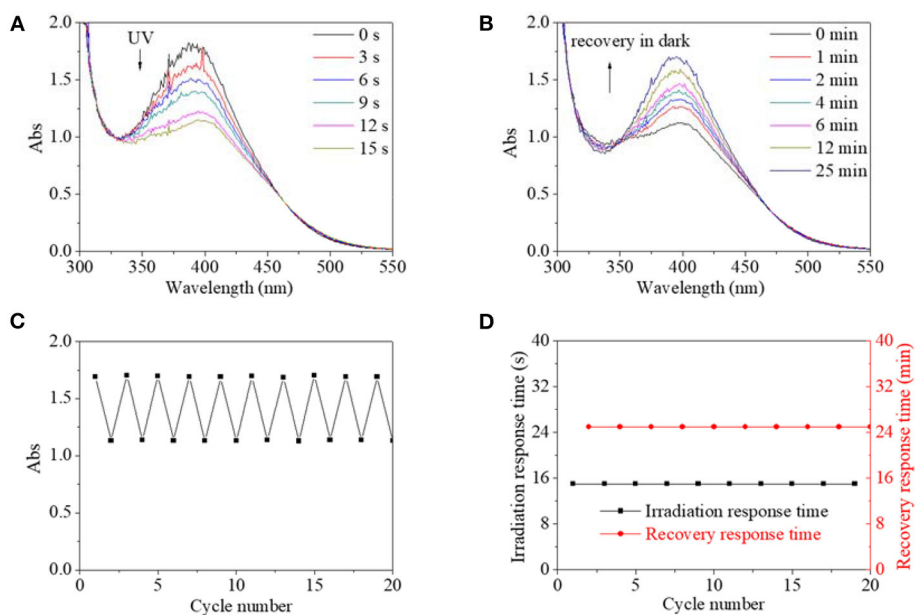


FIGURE 5 | UV spectra of PBLG1 DMF solution as a function of irradiation time (A) and recovery time (B). (C) Absorbance at 390/400 nm of PBLG1 DMF solution as a function of cycle number. (D) Irradiation response time and recovery response time as a function of cycle number. Irradiation was performed under UV light, and the recovery process was performed under darkness and room temperature. Polymer concentration was 17 mg/mL.

by UV light, absorbance intensity at 390 nm decreased rapidly along with irradiation time until the value stabilized at 61% of its original value with an equilibrium time of 15 s and a simultaneous red-shift of the absorbance peak to 400 nm (Figure 5A). The phenomenon indicated the successful

trans-to-cis transformation of PBLG1 according to the above analysis and existing theory for an AZO structure. After irradiation, the decreased absorbances could gradually recover to their original value in the dark within 25 min, which was indicative of the cis-to-trans recovery process (Figure 5B).

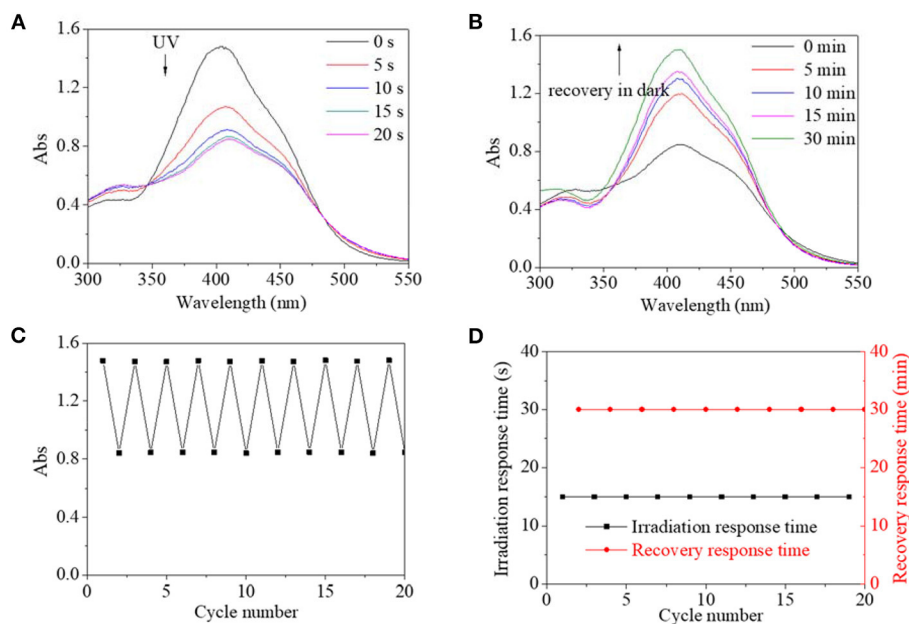


FIGURE 6 | UV spectra of PBLG2 DMF solution as a function of irradiation time (A) and recovery time (B). (C) Absorbance at 400/410 nm of PBLG2 DMF solution as a function of cycle number. (D) Irradiation response time and recovery response time as a function of cycle number. Irradiation was performed under UV light, and recovery process was performed under darkness and room temperature. Polymer concentration was 0.8 mg/mL.

Moreover, maximum and minimum absorbance at 390/400 nm of PBLG1 solution as well as response time and recovery time were recorded to evaluate the fatigue by repeated on/off irradiation to the same PBLG1 solution. The maximum absorbance at 390 nm was stabilized around 1.7, and the minimum absorbance at 400 nm was stabilized around 1.7 regardless of cycle number (Figure 5C). Furthermore, the response time was stabilized at 15 s and the recovery time at 25 min regardless of cycle number (Figure 5D). These results confirmed not only good fatigue durability but also controllable stability for PBLG1 as a photo switch. Except for UV light, any other excitation source (blue, yellow, and red light) could not induce isomerization transformation. In conclusion, UV light was the only effective excitation source for PBLG1.

Similarly, excited by UV light, the absorbance intensity at 400 nm of PBLG2 solution decreased rapidly from 1.5 to 0.8, about 53% of its original value within an equilibrium time of 15 s; simultaneously, the absorbance peak red-shifted to 410 nm (Figure 6A). After irradiation, the decreased absorbances could gradually recover to their original value in dark within 30 min (Figure 6B). Moreover, by repeated on/off irradiation, the maximum absorbance/the minimum absorbance at 400/410 nm was recorded to stabilize around 1.5/0.8 regardless of cycle number (Figure 6C), and the response time/the recovery time was stabilized at 15 s/30 min regardless of cycle number (Figure 6D). Besides the UV light, blue light could excite trans-to-cis transition for PBLG2, which is shown in Figure 7. Excited by blue light, absorbance intensity at 400 nm of PBLG2 solution decreased gradually from 1.5 to 0.9, about 60% of its original value, within an equilibrium time of 10 min (Figure 7A). After irradiation, the decreased absorbance could gradually recover

to their original value in dark within 12 min (Figure 7B). Moreover, the maximum absorbance/ minimum absorbance at 400 nm was stabilized around 1.5/0.9 regardless and the response time/the recovery time was stabilized at 10/15 min regardless of the cycle number (Figures 7C,D). These results confirmed that reversible isomerization transformation for PBLG2 could be effectively excited by both UV and blue light with stable and controllable transition processes and good fatigue durability, which indicated that both UV and blue light were effective excitation sources for PBLG2. Except for UV and blue light, any other excitation source (yellow and red light) could not induce isomerization transformation.

Generally, the effective excitation wavelength of a light source should surround the maximum absorbance wavelength of a UV-vis spectrum for an AZO structure since the UV-vis absorbance peak is directly related to electron transition from the base state to excited state. Simultaneously, combined with the results in the calculation part, PBLG2 exhibited lower excitation energy and higher maximum UV-vis absorbance wavelength. Therefore, PBLG2 could be excited by a light source of a higher wavelength (blue light). Since blue light was a low-energy light source belonging to visible light, PBLG2 exhibited some characteristics of a visible-light-driven photo switch. This characteristic would be beneficial to its potential biomedical application. Thus, PBLG2 as a better photo switch was researched, particularly as it related to considering the solvent and pH effects.

Solvent Effects on Isomerization for PBLG2

In view of different polarity, alcohol and water were introduced to the solvent system. Alcohol's effect on the trans→cis excitation process was investigated, as seen in Figures 8, 9.

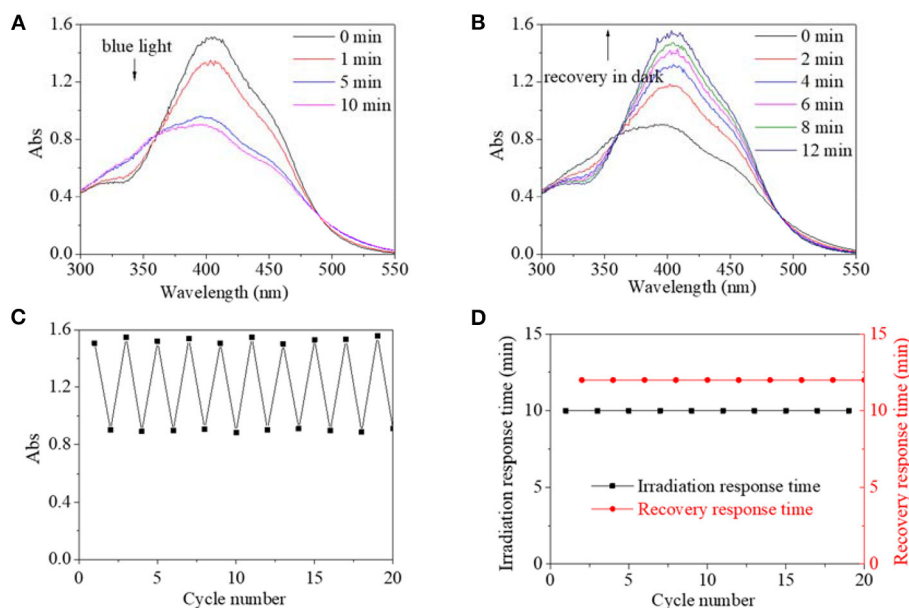


FIGURE 7 | UV spectra of PBLG2 DMF solution as a function of irradiation time (A) and recovery time (B). (C) Absorbance at 400 nm of PBLG2 DMF solution as a function of cycle number. (D) Irradiation response time and recovery response time as a function of cycle number. Irradiation was performed under blue light, and the recovery process was performed under darkness and room temperature. Polymer concentration was 0.8 mg/mL.

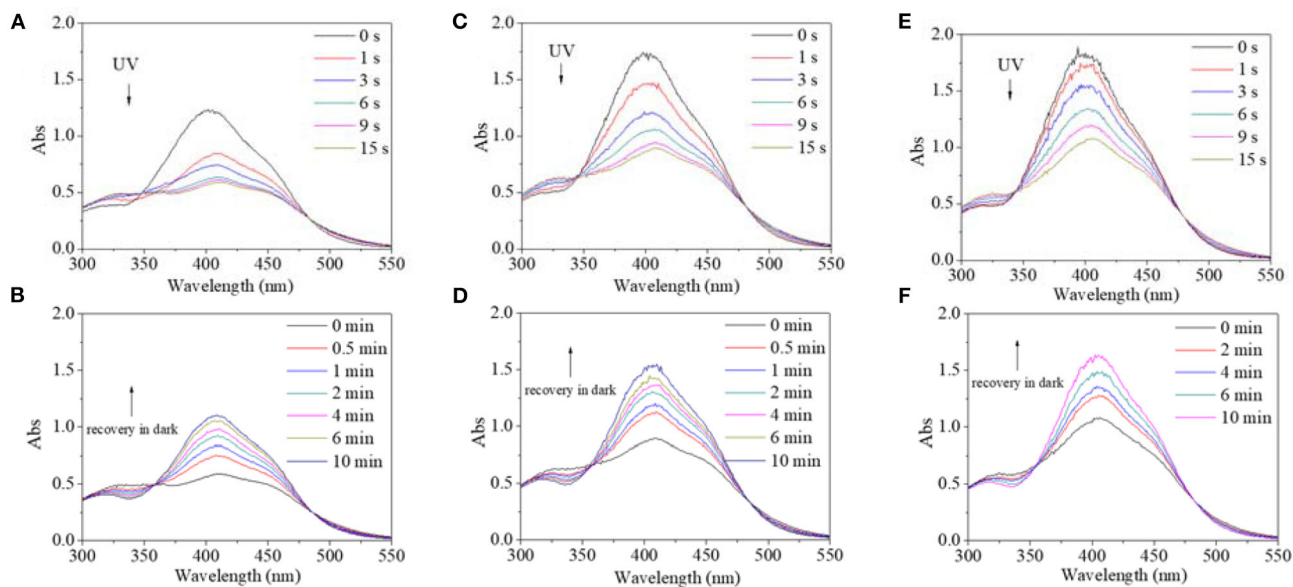
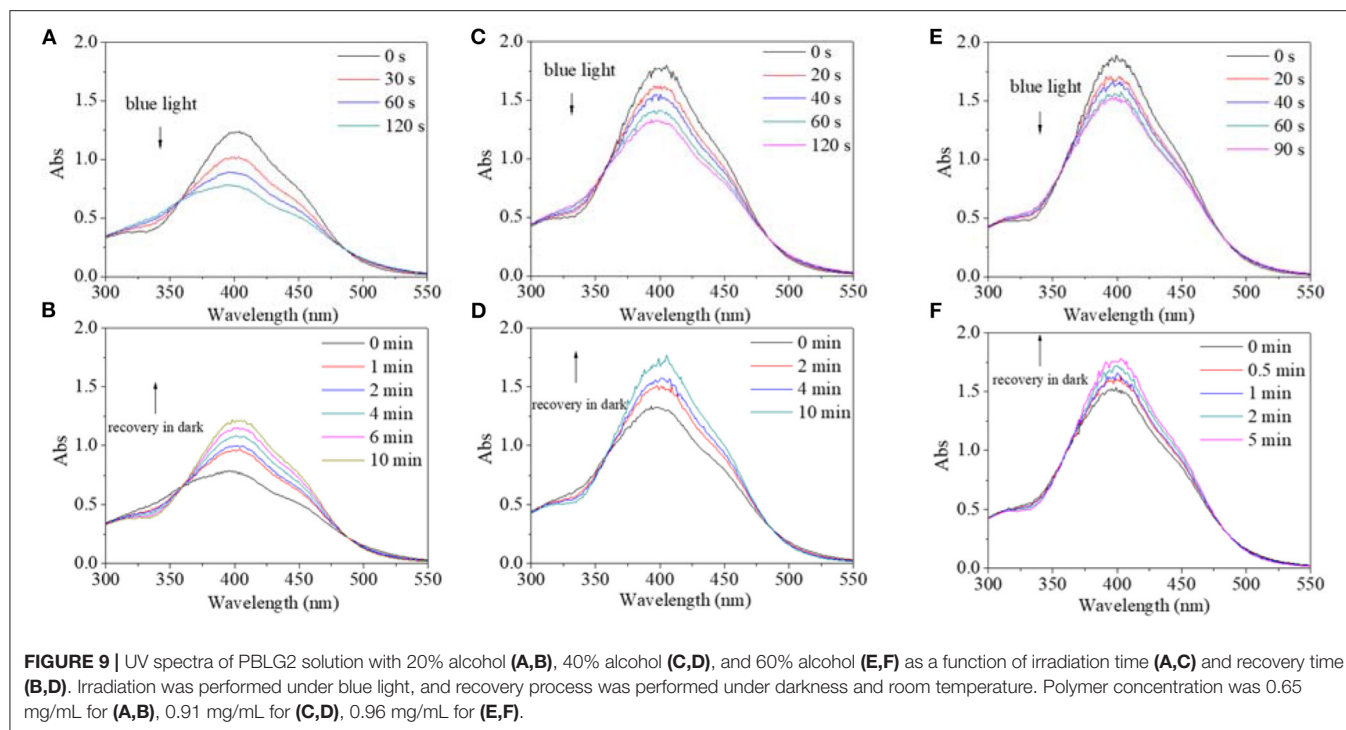


FIGURE 8 | UV spectra of PBLG2 solution with 20% alcohol (A,B), 40% alcohol (C,D) and 60% alcohol (E,F) as a function of irradiation time (a, c) and recovery time (B,D). Irradiation was performed under UV light, and recovery process was performed under darkness and room temperature. Polymer concentration was 0.65 mg/mL for (A,B), 0.88 mg/mL for (C,D), 0.94 mg/mL for (E,F).

Excited by UV light, absorbance intensity decreased rapidly to a constant value (50–55% of the original value) in 15 s in terms of a used solvent containing alcohol, indicating an obvious trans→cis process (Figures 8A,C,E). Likewise, in the dark, decreased values could gradually recover to their original

values within 10 min, indicating that there is a cis→trans process (Figures 8B,D,F). Alcohol seemed to have little effect on isomerization transformation initiated by UV light. But the situation was different when blue light was used as excitation source (Figure 9). Upon using blue light, the detectable



isomerization process become unclear with the addition of alcohol (Figures 9A,C,E). In more detail, absorbance decreased to 62% of original value within 120 s for the solution with 20/80% alcohol/DMF (Figure 9A), 74% of original value within 120 s for the solution with 40/60% alcohol/DMF (Figure 9C), and 82% of original value within 90 s for the solution with 60/40% alcohol/DMF (Figure 9E). In the dark, the decreased value could gradually recover to its original value, but recovery time shortened with its minimum absorbance after irradiation (Figures 9B,D,F). In more detail, the recovery time was 10 min for the solution with 20/80% alcohol/DMF (Figure 9B), 10 min for the solution with 40/60% alcohol/DMF (Figure 9D), and 5 min for the solution with 60/40% alcohol/DMF (Figure 9E).

Besides alcohol, the effect of water on the trans→cis excitation process had similar tendencies (Figures 10, 11). Water content was set to not be higher than 10% because PBLG2 will precipitate if water content is higher than 10%. Excited by UV light, absorbance intensity decreased rapidly to a constant value (50–55% of original value) in 15–18 s regardless of water content (Figures 10A,C). Likewise, in the dark, the decreased value could gradually recover to its original value within 10 min regardless of water content (Figures 10B,D). On account of this similarity, it was inferred that <10% water has little effect on isomerization transformation initiated by UV light. Upon use of blue light, the absorbance at 400 nm decreased to 64% of its original value with the addition of water making it <10% (Figures 11A,B). Also, the deceased absorbance could recover to its original value in the dark (Figures 11C,D). But both response and recovery time in water containing a solvent were shorter than in pure DMF (Figure 11).

In summary, the addition of alcohol and water as cosolvents had little effect on isomerization transformation initiated by UV light except for a shortened recovery time. Furthermore, either alcohol or water in a solvent would accelerate both the trans→cis and cis→trans processes in a blue-light-excited system.

CONCLUSION

BLG-NCA was successfully synthesized with a yield of 70–75%. PBLGs were successfully synthesized by use of the NCA method (using m-AZO and m-DAZO as initiators, respectively). DP was calculated to be 14 for PBLG1 initiated by m-AZO and 22 for PBLG2 initiated by m-DAZO. PBLGs exhibited amorphous characteristics with an obvious T_g transition, which were 14°C for PBLG1 and 21°C for PBLG2. In calculated UV-vis spectra, PBLG2 had a higher wavelength and larger intensity absorbance peak than PBLG1. Also, the energy gap between HOMO and LUMO for PBLG2 was lower than that for PBLG1, as calculated by DFT. In the experimental system, PBLG1 had a maximum absorbance peak at 390 nm, and PBLG2 had a maximum absorbance peak at 400 nm, red-shifting 40–50 nm from theoretical value. Furthermore, the absorbance intensity of PBLGs had a good linear relationship to their concentration, but the absorbance intensity of PBLG2 was several times that of PBLG1 in the same concentration. Trans→cis transition of PBLG1 could be excited rapidly by UV light. In a dark environment, the cis form could recover to its original trans isomer. Also, good fatigue durability for PBLG1 as a photo switch was confirmed by our results. Other light sources,

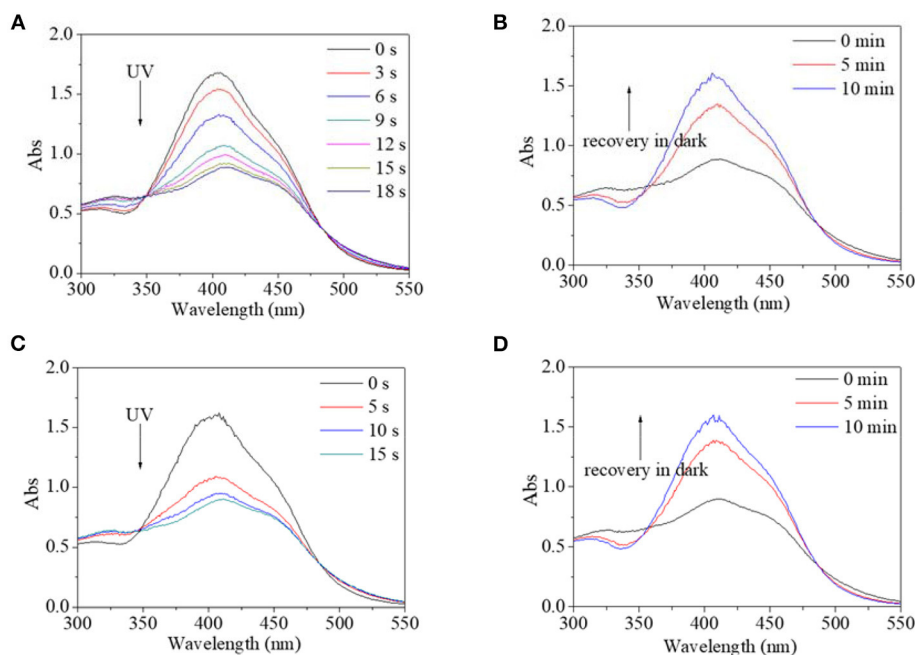


FIGURE 10 | UV spectra of PBLG2 solution with 5% water (A,B) and 10% water (C,D) as a function of irradiation time (A,C) and recovery time (B,D). Irradiation was performed under UV light, and recovery process was performed under darkness and room temperature. Polymer concentration was 0.87 mg/mL for (A,B), 0.83 mg/mL for (C,D).

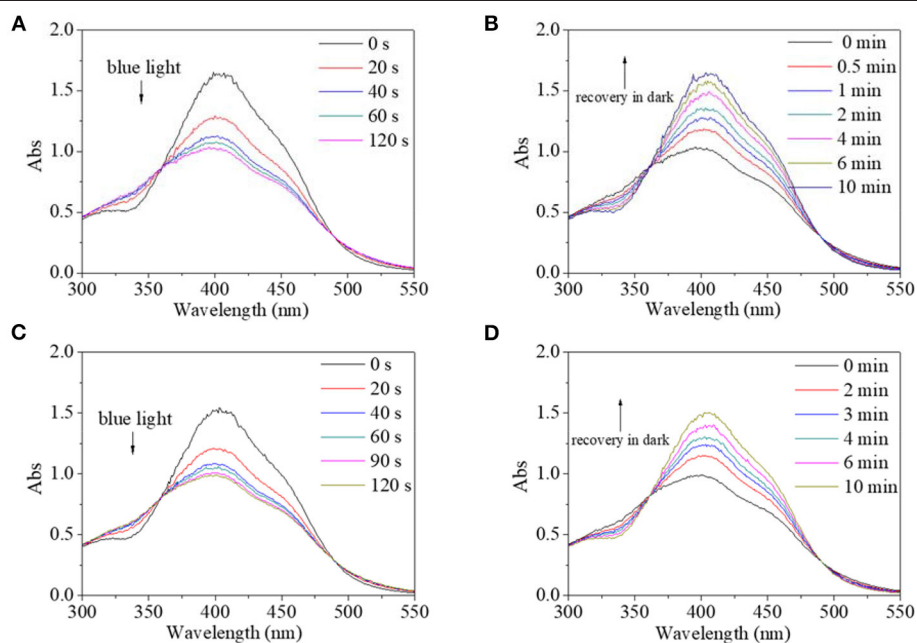


FIGURE 11 | UV spectra of PBLG2 solution with 5% water (A,B) and 10% water (C,D) as a function of irradiation time (A,C) and recovery time (B,D). Irradiation was performed under blue light, and recovery process was performed under darkness and room temperature. Polymer concentration was 0.85 mg/mL.

except for UV light, could not induce detectable isomerization for PBLG1. Upon use of UV light, PBLG2 exhibited similar isomerization characteristic to PBLG1. Blue light, however,

was also verified to be another effective excitation source for PBLG2. When it came to solvent effects, the addition of alcohol and water as cosolvents had little effect on the trans→cis

transition in UV-light-excited systems, but it shortened the recovery time of cis→trans processes in dark environments. In contrast, the detectable isomerization process becomes unclear with the addition of alcohol in the blue-light-excited system. Furthermore, either alcohol or water in solvents would accelerate both the trans→cis and cis→trans processes in a blue-light-excited system.

DATA AVAILABILITY STATEMENT

The original contributions presented in the study are included in the article/supplementary material, further inquiries can be directed to the corresponding author/s.

REFERENCES

- Beharry, A. A., and Woolley, G. A. (2011). Azobenzene photoswitches for biomolecules. *Chem. Soc. Rev.* 40, 4422–4437. doi: 10.1039/c1cs15023e
- Bian, Q., Wang, W., Han, G., Chen, Y., Wang, S., and Wang, G. (2016). Photoswitched cell adhesion on azobenzene-containing self-assembled films. *Chemphyschem* 17, 2503–2508. doi: 10.1002/cphc.201600362
- Boys, S. F., and Bernardi, F. (1970). Calculation of small molecular interactions by differences of separate total energies some procedures with reduced errors. *Mol. Phys.* 19:553. doi: 10.1080/00268977000101561
- Cauchois, O., Segura-Sanchez, F., and Ponchel, G. (2013). Molecular weight controls the elongation of oblate-shaped degradable poly(gamma-benzyl-L-glutamate)nanoparticles. *Int. J. Pharm.* 452, 292–299. doi: 10.1016/j.ijpharm.2013.04.074
- Chen, C., Zhao, J., Gao, M., Meng, X., Fan, A., Wang, Z., et al. (2018). Photo-triggered micelles: simultaneous activation and release of microtubule inhibitors for on-demand chemotherapy. *Biomater. Sci.* 6, 511–518. doi: 10.1039/C7BM01053B
- de Miguel, L., Noiray, M., Surpateanu, G., Iorga, B. I., and Ponchel, G. (2014). Poly(gamma-benzyl-L-glutamate)-PEG-alendronate multivalent nanoparticles for bone targeting. *Int. J. Pharm.* 460, 73–82. doi: 10.1016/j.ijpharm.2013.10.048
- Deka, S. R., Yadav, S., Mahato, M., and Sharma, A. K. (2015). Azobenzene-aminoglycoside: self-assembled smart amphiphilic nanostructures for drug delivery. *Colloids Surf. B Biointerfaces* 135, 150–157. doi: 10.1016/j.colsurfb.2015.07.026
- Dong, C. M., and Chen, Y. (2011). Stimuli-responsive polypeptide-based reverse micellar hydrogel. *J. Control Release* 152(Suppl. 1), e13–e14. doi: 10.1016/j.jconrel.2011.08.092
- Duan, T., and Li, H. (2020). *In situ* phase transition of elastin-like polypeptide chains regulates thermoresponsive properties of elastomeric protein-based hydrogels. *Biomacromolecules* 21, 2258–2267. doi: 10.1021/acs.biomac.0c00206
- Duong, H. T. T., Yin, Y., Thambi, T., Kim, B. S., Jeong, J. H., and Lee, D. S. (2020). Highly potent intradermal vaccination by an array of dissolving microneedle polypeptide cocktails for cancer immunotherapy. *J. Mater. Chem. B* 8, 1171–1181. doi: 10.1039/C9TB02175B
- Editors, P. O. (2019). Expression of concern: synthesized multiple antigenic polypeptide vaccine based on B-cell epitopes of human heparanase could elicit a potent antimetastatic effect on human hepatocellular carcinoma *in vivo*. *PLoS ONE* 14:e0226124. doi: 10.1371/journal.pone.0226124
- Frisch, M. J., Trucks, G. W., Schlegel, H. B., Scuseria, G. E., Robb, M. A., Cheeseman, J. R., et al. (2009). *Gaussian 09, Revision A.02*. Wallingford, CT: Gaussian Inc.
- Lerch, M. M., Szymanski, W., and Feringa, B. L. (2018). The (photo)chemistry of Stenhouse photoswitches: guiding principles and system design. *Chem. Soc. Rev.* 47, 1910–1937. doi: 10.1039/C7CS00772H
- Li, L. L., Qiao, S. L., Liu, W. J., Ma, Y., Wan, D., Pan, J., et al. (2017). Intracellular construction of topology-controlled polypeptide nanostructures with diverse biological functions. *Nat. Commun.* 8:1276. doi: 10.1038/s41467-017-01296-8
- Lin, L. R., Tang, H. H., Wang, Y. G., Wang, X., Fang, X. M., and Ma, L. H. (2017). Functionalized lanthanide(III) complexes constructed from azobenzene derivative and beta-diketone ligands: luminescent, magnetic, and reversible trans-to-Cis photoisomerization properties. *Inorg. Chem.* 56, 3889–3900. doi: 10.1021/acs.inorgchem.6b02819
- Lin, L. R., Wang, X., Wei, G. N., Tang, H. H., Zhang, H., and Ma, L. H. (2016). Azobenzene-derived tris-beta-diketone lanthanide complexes: reversible trans-to-cis photoisomerization in solution and solid state. *Dalton Trans.* 45, 14954–14964. doi: 10.1039/C6DT01310D
- Liu, G. F., Ji, W., Wang, W. L., and Feng, C. L. (2015). Multiresponsive hydrogel coassembled from phenylalanine and azobenzene derivatives as 3D scaffolds for photoguiding cell adhesion and release. *ACS Appl. Mater. Interfaces* 7, 301–307. doi: 10.1021/am506202s
- Michael Kathan, S. H. (2017). Photoswitchable molecules as key ingredients to drive systems away from the global thermodynamic minimum. *Chem. Soc. Rev.* 46, 5536–5550. doi: 10.1039/C7CS00112F
- Nie, Y., Zhi, X., Du, H., and Yang, J. (2018). Zn(OAc)(2)-catalyzing ring-opening polymerization of N-carboxyanhydrides for the synthesis of well-defined polypeptides. *Molecules* 23:760. doi: 10.3390/molecules23040760
- Pang, J., Gao, Z., Tan, H., Mao, X., Wang, H., and Hu, X. (2019). Design, synthesis, investigation and application of a macromolecule photoswitch. *Front. Chem.* 7:86. doi: 10.3389/fchem.2019.00086
- Pang, J., Gao, Z. Y., Zhang, L., Wang, H., and Hu, X. H. (2018). Synthesis and characterization of photoresponsive macromolecule for biomedical application. *Front. Chem.* 6:217. doi: 10.3389/fchem.2018.00217
- Qu, J., Wang, Q. Y., Chen, K. L., Luo, J. B., Zhou, Q. H., and Lin, J. (2018). Reduction/temperature/pH multi-stimuli responsive core cross-linked polypeptide hybrid micelles for triggered and intracellular drug release. *Colloids Surf. B Biointerfaces* 170, 373–381. doi: 10.1016/j.colsurfb.2018.06.015
- Ransil, B. (1961). Studies in molecular structure. IV. Potential curve for the interaction of two Helium atoms in single configuration LCAO MO SCF approximation. *J. Chem. Phys.* 34:2109. doi: 10.1063/1.1731829
- Shen, Y., Fu, X., Fu, W., and Li, Z. (2015). Biodegradable stimuli-responsive polypeptide materials prepared by ring opening polymerization. *Chem. Soc. Rev.* 44, 612–622. doi: 10.1039/C4CS00271G
- Skoulas, D., Christakopoulos, P., Stavroulaki, D., Santorinaios, K., Athanasiou, V., and Iatrou, H. (2017). Micelles formed by polypeptide containing polymers synthesized via N-carboxy anhydrides and their application for cancer treatment. *Polymers* 9:208. doi: 10.3390/polym9060208
- Sun, W., Fang, J., Yong, Q., Li, S., Xie, Q., Yin, J., et al. (2015). Subcutaneous construction of engineered adipose tissue with fat lobule-like structure using injectable poly-benzyl-L-glutamate microspheres loaded with adipose-derived stem cells. *PLoS ONE* 10:e0135611. doi: 10.1371/journal.pone.0135611
- Wibowo, S. H., Sulistio, A., Wong, E. H., Blencowe, A., and Qiao, G. G. (2014). Polypeptide films via N-carboxyanhydride ring-opening polymerization. (NCA-ROP): past, present and future. *Chem Commun.* 50, 4971–4988. doi: 10.1039/c4cc00293h

AUTHOR CONTRIBUTIONS

PC wrote the manuscript. JK synthesized polymer. XW investigated PBLGs. WM characterized PBLG2. XY characterized PBLG1. YQ researched the photo responsive properties. XH gave the idea and instructed the whole research. All authors contributed to the article and approved the submitted version.

FUNDING

This study was financially supported by the Natural Science Foundation of Jiangsu Province (BK20171113) and the Six Talent Peaks project in Jiangsu Province (JY-071).

- Xiao, Y., Tang, C., Chen, Y., and Lang, M. (2019). Dual stimuli-responsive polypeptide prepared by thiol-ene click reaction of poly(l-cysteine) and N, N-dimethylaminoethyl acrylate. *Biopolymers* 110:e23318. doi: 10.1002/bip.23318
- Zhou, W., Liu, L., Xue, Y., Zheng, J., Liu, X., Ma, J., et al. (2017). Combination of endothelial-monocyte-activating polypeptide-ii with temozolomide suppress malignant biological behaviors of human glioblastoma stem cells via miR-590-3p/MACC1 Inhibiting PI3K/AKT/mTOR signal pathway. *Front. Mol. Neurosci.* 10:68. doi: 10.3389/fnmol.2017.00068
- Zhou, X., and Li, Z. (2018). Advances and biomedical applications of polypeptide hydrogels derived from alpha-amino acid N-carboxyanhydride. *Polymer. Adv. Healthc. Mater.* 7:e1800020. doi: 10.1002/adhm.201800020

Conflict of Interest: The authors declare that the research was conducted in the absence of any commercial or financial relationships that could be construed as a potential conflict of interest.

Copyright © 2020 Chen, Kong, Wang, Ma, Yang, Qin and Hu. This is an open-access article distributed under the terms of the Creative Commons Attribution License (CC BY). The use, distribution or reproduction in other forums is permitted, provided the original author(s) and the copyright owner(s) are credited and that the original publication in this journal is cited, in accordance with accepted academic practice. No use, distribution or reproduction is permitted which does not comply with these terms.



Electrochemical Synthesis and Electro-Optical Properties of Dibenzothiophene/Thiophene Conjugated Polymers With Stepwise Enhanced Conjugation Lengths

Kaiwen Lin^{1*}, Caiting Li², Wang Tao³, Jilong Huang¹, Qinghua Wu², Zijin Liu², Yangfan Zhang², Da Wang³ and Xi Liu^{2*}

¹ Department of Materials and Food, Zhongshan Institute, University of Electronic Science and Technology of China, Zhongshan, China, ² School of Textile Materials and Engineering, Wuyi University, Jiangmen, China, ³ School of Applied Physics and Materials, Wuyi University, Jiangmen, China

OPEN ACCESS

Edited by:

Haichang Zhang,
Qingdao University of Science and
Technology, China

Reviewed by:

Kun Yang,
Southern University of Science and
Technology, China
Maning Liu,
Tampere University, Finland

*Correspondence:

Kaiwen Lin
kevinlin1990@163.com
Xi Liu
liuxi_wyu@163.com

Specialty section:

This article was submitted to
Organic Chemistry,
a section of the journal
Frontiers in Chemistry

Received: 07 July 2020

Accepted: 04 August 2020

Published: 08 September 2020

Citation:

Lin K, Li C, Tao W, Huang J, Wu Q,
Liu Z, Zhang Y, Wang D and Liu X
(2020) Electrochemical Synthesis and
Electro-Optical Properties of
Dibenzothiophene/Thiophene
Conjugated Polymers With Stepwise
Enhanced Conjugation Lengths.
Front. Chem. 8:819.
doi: 10.3389/fchem.2020.00819

A total of six conjugated polymers, namely PDBT-Th, PDBT-Th:Th, PDBT-2Th, PDBT-Th:2Th, PDBT-2Th:Th, and PDBT-2Th:2Th, consisting of dibenzothiophene, thiophene, and bithiophene were electrochemically synthesized. Their electrochemical and electrochromic properties were investigated in relation to the conjugation chain lengths of the thiophene units in the conjugated backbones. Density functional theory (DFT) calculations showed that longer conjugation lengths resulted in decreased HOMO-LUMO gaps in the polymers. The optical band gaps ($E_{g,opt}$) and electrochemical band gaps ($E_{g,cv}$) were decreased from PDBT-Th to PDBT-Th:Th, however, PDBT-Th:2Th, PDBT-2Th, PDBT-2Th:Th and PDBT-2Th:2Th displayed the similar band gaps. The conjugation length increments significantly improved the electrochemical stability of the conjugated polymers and exhibited reversible color changes due to the formation of polarons and bipolarons. The results suggest that the conjugated polymers prepared herein are promising candidates for fabricating flexible organic electrochromic devices.

Keywords: dibenzothiophene, electrochemical synthesis, electrochromism, conjugation lengths, color changes, electrochemical stability

INTRODUCTION

It is indispensable for the preparation of high-performance conjugated polymers and development of state-of-the-art applications to explore the structure-performance relationship of conjugated polymers. Breakthroughs in organic optoelectronics, including organic solar cells, dye-sensitized solar cells, organic field effect transistors, and electrochromism (Zhang et al., 2013; Jin et al., 2014; Zhou et al., 2015; Li et al., 2019a), has been performed by altering the main conjugation length. Strategies for altering the main conjugation length of organic optoelectronic materials include chemical and electrochemical polymerization methods (Jin et al., 2014; Zhou et al., 2015).

Electrochemical polymerization is often used in organic optoelectronics and employs a working electrode on which the polymer films simultaneously polymerize and are deposited by an applied voltage (Li et al., 2009; Jiang et al., 2018). Electrochemical polymer preparation exhibits several advantages: (1) It is high-throughput for synthesizing polymer films, formed only on the electrodes without any observed in solution; (2) It is highly efficient for synthesizing polymer films,

since the reaction can be conducted in several seconds or minutes, while conventional chemical synthesis of a similar polymer requires several hours or days; (3) The electropolymerization method uses cheap supporting electrolytes instead of specific catalysts and expensive complexants for solution-phase synthesis; (4) The reaction can be performed at room temperature, whereas conventional chemical synthesis usually requires harsh conditions with high temperatures under an inert atmosphere (Gu et al., 2015; Yuan and Lei, 2020). The extension of the main chain conjugation length *via* electrochemical polymerization is effectively concentrated in electrochromism (Ak et al., 2008; Camurlu et al., 2008; Kavak et al., 2015; Sheberla et al., 2015; Gu et al., 2018; Li et al., 2019b; Zhang et al., 2019; Lu et al., 2020). Electrochromism is often defined as the visible and reversible changes in the transmittance and color of a material caused by an applied voltage (Argun et al., 2004; Beaujuge and Reynolds, 2010; Lin et al., 2017). For example, Zhao et al., verified the stepwise enhancement of the electrochemical and electrochromic performances of polyselenophene *via* electropolymerization of mono-, bi-, and triselenophene. Polyselenophene that was electropolymerized from triselenophene exhibited the lowest optical band gap (1.72 eV), highest redox stability, as well as the best electrochromic nature of optical contrast up to 75%, coloration efficiency up to 450 cm² C⁻¹, and switching time (0.7 and 0.4 s for oxidation and reduction, respectively) compared to polyselenophene prepared from mono- and biselenophene (Lu et al., 2020). Zhang et al., prepared a cross-linked copolymer (pTPhSNS-EDOT) *via* electrochemical polymerization that exhibited a fast coloring time of 0.58 s and discoloring time of

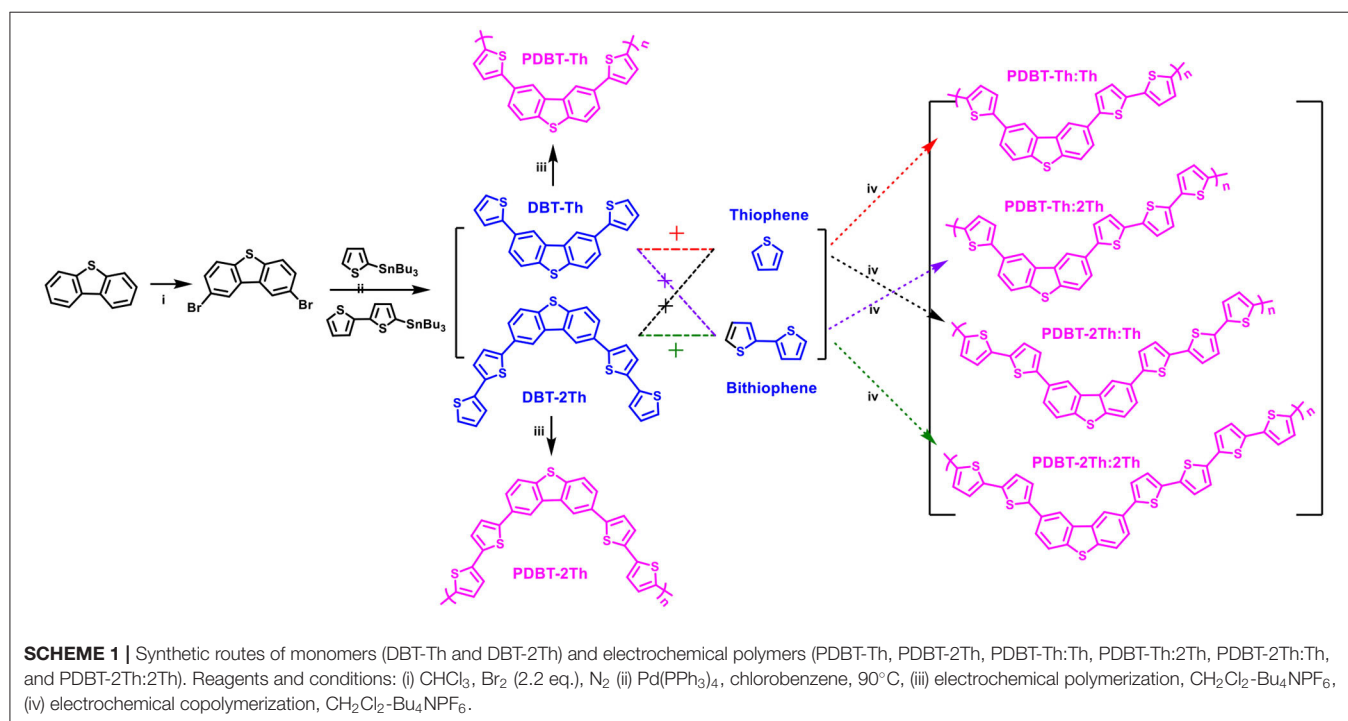
0.38 s, high optical contrast of 40%, excellent color stability, and improved color memory behavior compared to the pTPhSNS homopolymer (Dai et al., 2017). Therefore, extension of the main chain conjugation length is beneficial for obtaining excellent electrochemical and electrochromic properties.

Herein, thiophene, and thiophene derivatives were used to construct electrochromic polymers with stepwise enhancement of the main chain conjugation lengths *via* electrochemical copolymerization. The relationship between the main chain conjugation length and electrochromic properties, as well as the electrochemical redox activity and stability of the conjugated polymer, were studied in detail. Significantly, this study provides theoretical guidance for the development of related fields.

RESULT AND DISCUSSION

Synthesis and Characterization

The synthetic routes for the monomers (DBT-Th and DBT-2Th) and electrochemical polymers (PDBT-Th, PDBT-2Th, PDBT-Th:Th, PDBT-Th:2Th, PDBT-2Th:Th, and PDBT-2Th:2Th) are illustrated in **Scheme 1**. Poly[2,8-bis-(thiophen-2-yl)-dibenzothiophene] (PDBT-Th) and poly[2,8-Bis-(bithiophen-2-yl)-dibenzothiophene] (PDBT-2Th) were prepared from the 2,8-bis-(thiophen-2-yl)-dibenzothiophene (DBT-Th) and 2,8-Bis-(bithiophen-2-yl)-dibenzothiophene (DBT-2Th) monomers (0.01 mol L⁻¹) and Bu₄NPF₆ (0.1 mol L⁻¹) in DCM *via* electrochemical polymerization. PDBT-Th:Th and PDBT-Th:2Th were electrochemical polymerized from 0.005 mol L⁻¹ DBT-Th and 0.005 mol L⁻¹ thiophene (Th)/bithiophene (2Th), respectively. PDBT-2Th:Th and PDBT-2Th:2Th were



obtained from 0.005 mol L⁻¹ DBT-2Th and 0.005 mol L⁻¹ Th/2Th *via* electrochemical copolymerization. From the synthetic routes of DBT-Th and DBT-2Th, dibenzothiophene (DBT) was used to prepare the corresponding bromide (2,8-dibromodibenzothiophene) *via* bromination. The above dibromide was reacted with tributyltin substituted Th/2Th to afford the target products using a Pd(PPh₃)₄ catalyst. The ¹H NMR and ¹³C NMR spectra of target monomers are presented in Figures S1–S4.

Electrochemical Polymerization of DBT-Th, DBT-2Th and Electrochemical Copolymerization of DBT-Th, DBT-2Th, Th, and 2Th

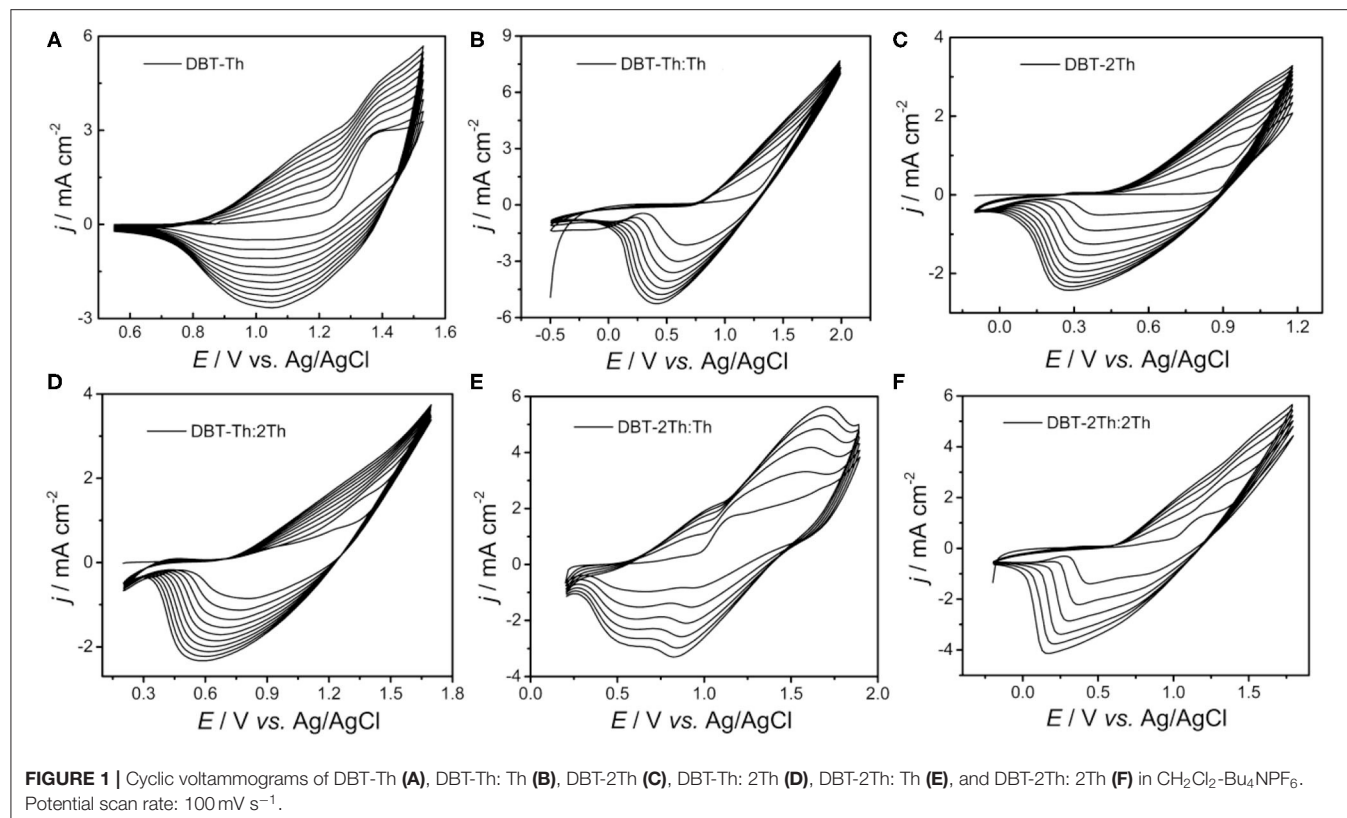
From their anodic oxidation curves (Figure S5), the onset oxidation potentials (E_{onset}) were initiated at 1.11, 1.30, 0.85, 1.27, 1.07, and 0.98 V for DBT-Th, DBT-Th:Th, DBT-2Th, DBT-Th:2Th, DBT-2Th:Th, and DBT-2Th:2Th, respectively. The polymers were prepared by the potentiostatic method (adding about 0.2 V of E_{onset}) along with similar charge of about 5 mC. In this electrochemical deposition condition, the thickness of polymer films were about 200 nm, which is in agreement with the reported research (Lin et al., 2020b).

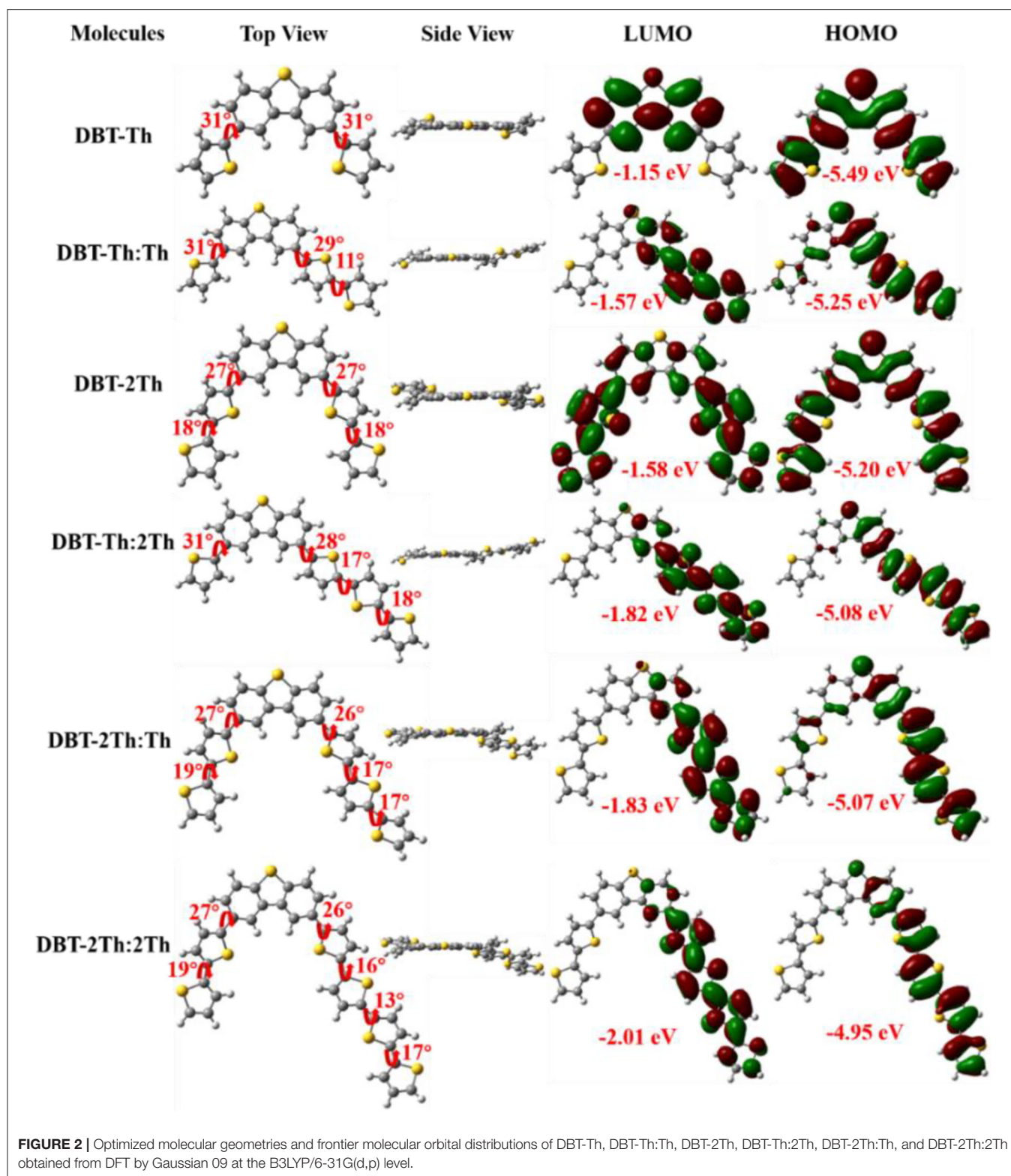
Figure 1 shows the obtained cyclic voltammograms (CVs) corresponding to the potentiodynamic electropolymerization of the polymeric precursor monomers DBT-Th and DBT-2Th as well as the potentiodynamic electrochemical copolymerization

of the polymeric precursor comonomers DBT-Th, DBT-2Th, Th, and 2Th. The current density increased gradually as a function of scanning cycles for all systems. Meanwhile, the corresponding conducting polymers on the working electrode grew prominently, indicating that the as-prepared conducting polymers exhibited good electrochemical redox activity. Meanwhile, all systems exhibited an increasingly obvious voltage drop (ΔV) from 0.6 to 1.0 V of the reduction peak with stepwise enhanced conjugation lengths, which were ascribed to the wide distribution of polymer chain lengths. Because of the additional potential required to balance the increased polymeric electrical resistance and slow mass transport, an obvious potential shift of the anodic and cathodic peaks was observed during polymer growth (Chen and Xue, 2005; Lin et al., 2020a; Lu et al., 2020).

Theoretical Calculations

The ground-state optimized molecular geometries and frontier molecular orbital distributions of DBT-Th, DBT-Th:Th, DBT-2Th, DBT-Th:2Th, DBT-2Th:Th, and DBT-2Th:2Th were determined using density functional theory (DFT) by Gaussian 09 at the B3LYP/6-31G(d,p) level (Figure 2). All optimized molecular geometries exhibited slightly twisted, n-shaped structures, with dihedral angles of < 31° owing to the steric hindrance effect. The dihedral angles of DBT and adjacent thiophene decreased with enhanced conjugation lengths, which resulted in improved regularity. For all models, the electron density distribution of the lowest unoccupied molecular orbitals





(LUMOs) and highest occupied molecular orbitals (HOMOs) were localized in the sectional conjugated skeleton. The longer the conjugation lengths resulted in lower energy LUMO and

HOMO levels (Liu et al., 2017). The HOMO-LUMO gaps of all models gradually decreased from 4.34 to 2.94 eV with stepwise enhancement of the conjugation lengths.

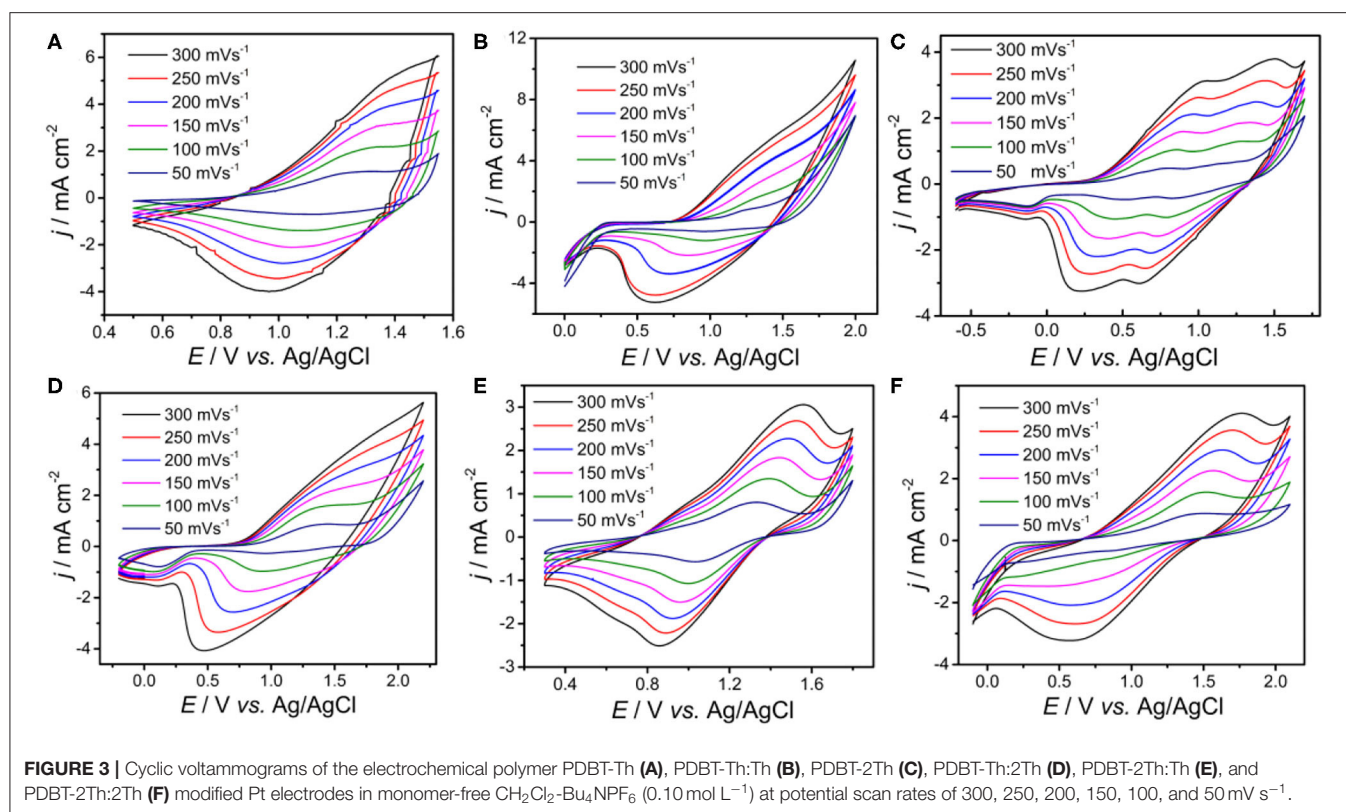


FIGURE 3 | Cyclic voltammograms of the electrochemical polymer PDBT-Th (A), PDBT-Th:Th (B), PDBT-2Th (C), PDBT-Th:2Th (D), PDBT-2Th:Th (E), and PDBT-2Th:2Th (F) modified Pt electrodes in monomer-free CH_2Cl_2 - Bu_4NPF_6 (0.10 mol L^{-1}) at potential scan rates of 300, 250, 200, 150, 100, and 50 mV s^{-1} .

TABLE 1 | Electrochemical, optical properties and theoretical calculation of polymers.

Polymers	$E_{\text{ox,onset}}$ (V)	$E_{\text{red,onset}}$ (V)	HOMO		LUMO		$E_{\text{g,cv}}$ (eV)	HOMO-LUMO gaps (eV)	$E_{\text{g,opt}}$ (eV)
			Experimental value	Theoretical value	Experimental value	Theoretical value			
PDBT-Th	0.88	-1.95	-5.68	-5.10	-2.85	-1.73	2.83	3.37	2.59
PDBT-Th:Th	0.70	-1.75	-5.50	-5.00	-3.05	-1.97	2.45	3.03	2.53
PDBT-2Th	0.55	-1.74	-5.35	-4.90	-3.06	-2.09	2.29	2.81	2.25
PDBT-Th:2Th	0.56	-1.72	-5.36	-4.92	-3.08	-2.10	2.28	2.82	2.29
PDBT-2Th:Th	0.54	-1.75	5.34	-4.84	-3.05	-2.19	2.29	2.65	2.24
PDBT-2Th:2Th	0.52	-1.77	-5.32	-4.81	-3.03	-2.25	2.29	2.56	2.23

Electrochemistry of the Polymers

To obtain deeper insight of the electrochemical activity, the electrochemical behaviors of PDBT-Th, PDBT-Th:Th, PDBT-2Th, PDBT-Th:2Th, PDBT-2Th:Th, and PDBT-2Th:2Th were investigated *via* CVs in monomer-free CH_2Cl_2 - Bu_4NPF_6 (0.1 mol L^{-1} ; **Figure 3**). All polymers were prepared using the potentiostatic method at a constant potential of 1.30 V for DBT-Th, 1.50 V for DBT-Th:Th, 1.05 V for DBT-2Th, 1.45 V for DBT-Th:2Th, 1.3 V for DBT-2Th:Th, and 1.2 V for DBT-2Th:2Th. All polymers showed obvious redox peaks with hysteresis (potential drift) between the anodic and cathodic peak potentials. The potential shifts of the redox peaks among the CVs were attributed to slow heterogeneous electron transfer, local rearrangement of the polymer chains, slow mutual transformation of various electronic species, and electronic charging of the interfacial

exchange at the metal/polymer and polymer/solution interfaces (Inzelt et al., 2000).

In addition, the cyclic voltammetry was employed to evaluate the experimental HOMO and LUMO energy levels of polymers through the empirical Equations (1) and (2) in the Supporting Information (Sun et al., 2011). Meanwhile, the theoretical calculated HOMO/LUMO energy levels of polymers (simplified by two repeating units) were illustrated comparatively. The values were presented in **Table 1**. The experimental and theoretical calculated HOMO both exhibited up lifted values when the conjugation length was increased. The HOMO-LUMO gaps by theoretical calculation decreased gradually. The optical band gaps ($E_{\text{g,opt}}$) and electrochemical band gaps ($E_{\text{g,cv}}$) were decreased from PDBT-Th to PDBT-Th:Th, however, PDBT-Th:2Th, PDBT-2Th,

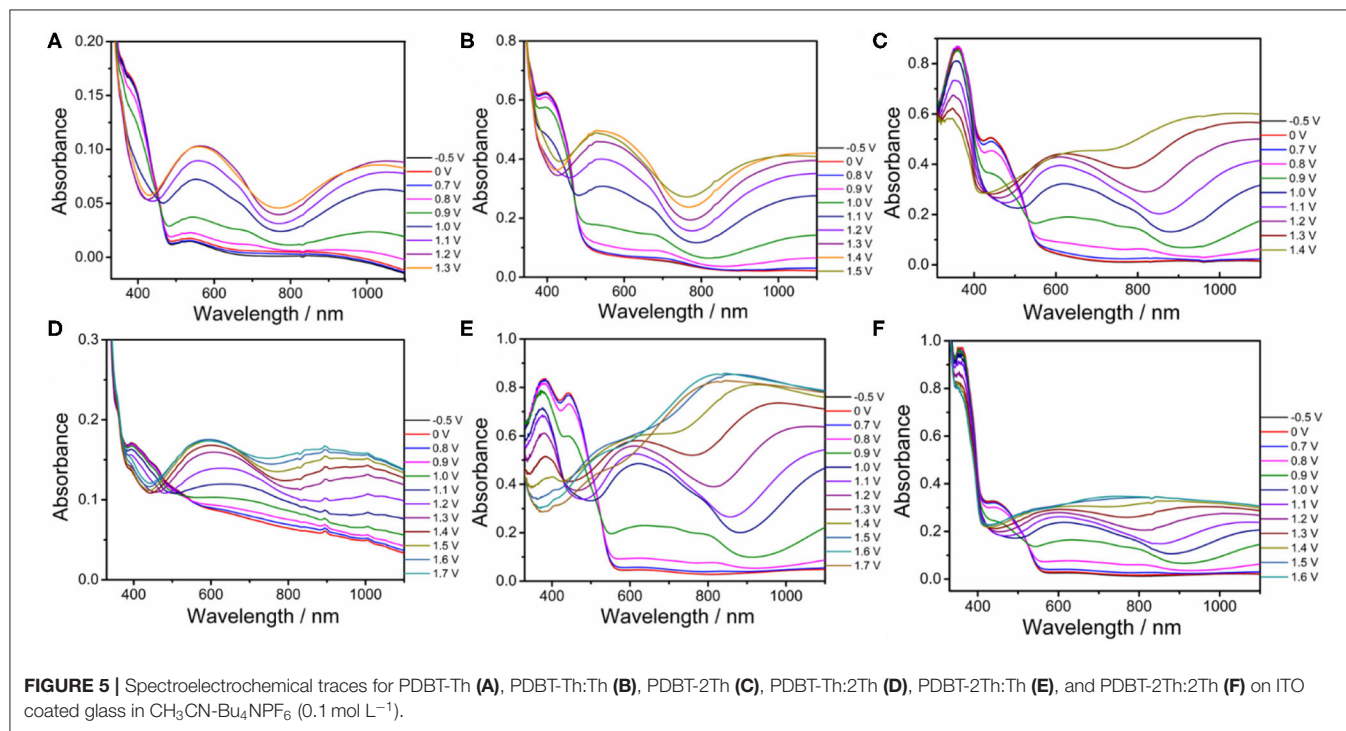
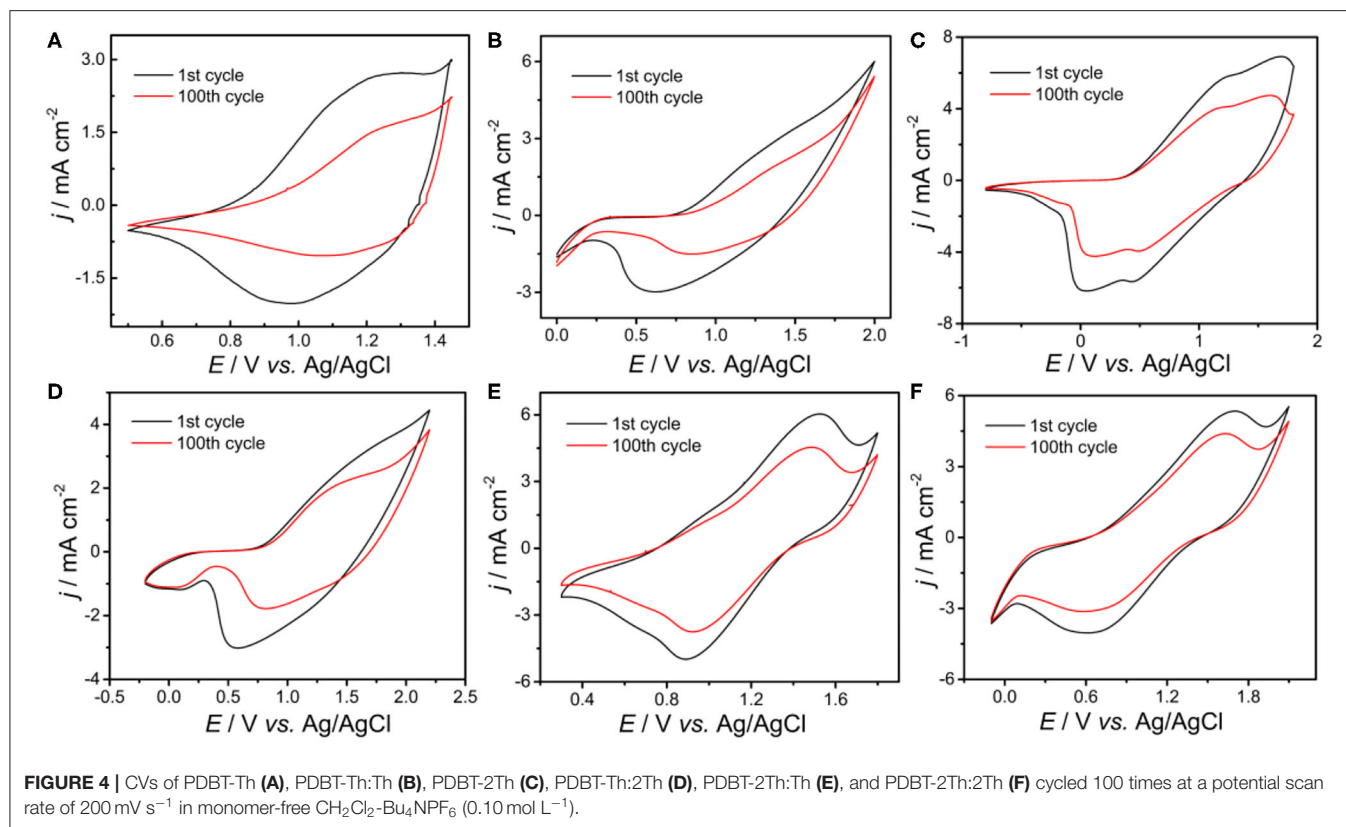














TABLE 2 | Colorimetric parameters for the prepared polymers.

Polymers	CIE color coordinates			Colors of polymers	
		Neutral	Oxidized	Neutral	Oxidized
PDBT-Th	L*	98.7235	92.2886		
	a*	-2.2272	1.6750		
	b*	6.5666	-3.7137		
PDBT-Th:Th	L*	87.0708	67.1116		
	a*	-8.4870	4.7474		
	b*	32.6390	-3.4195		
PDBT-2Th	L*	82.3156	79.7525		
	a*	-1.3602	-4.6198		
	b*	20.1580	4.5149		
PDBT-Th:2Th	L*	98.8370	94.9152		
	a*	-0.2581	-0.1172		
	b*	5.9035	-4.5872		
PDBT-2Th:Th	L*	84.1909	69.1127		
	a*	11.1086	-2.1452		
	b*	63.0452	-9.6235		
PDBT-2Th:2Th	L*	88.6797	76.6157		
	a*	6.0639	-1.6808		
	b*	33.9582	-4.6985		

PDBT-2Th:Th and PDBT-2Th:2Th displayed the similar band gaps.

The stabilities of all polymers were studied in a monomer-free CH_2Cl_2 - Bu_4NPF_6 system. A total of 100 cycles were performed to study the doping and dedoping abilities of all polymers, as shown in **Figure 4**. The redox activity of PDBT-Th was maintained at 56% after scanning 100 cycles, exhibiting generally good redox stability. However, increasing conjugation length significantly improved electrochemical stability, achieving moderate stability at 62, 79, 76, 85, and 90% remaining activity for PDBT-Th:Th, PDBT-2Th, PDBT-Th:2Th, PDBT-2Th:Th, and PDBT-2Th:2Th, respectively, after scanning 100 cycles. The improved electrochemical stability could benefit from the more stable thiophene bridge.

Electrochromic Properties

Spectroelectrochemical analyses were performed by recording the absorption changes of the polymers under different potentials (**Figure 5**). In the neutral state, all polymers showed the absorbance peaks centered at approximately 410 nm arising from the π - π^* transition. DBT-2Th based polymers PDBT-2Th (c), PDBT-2Th:Th (e), and PDBT-2Th:2Th (f) clearly showed two absorbance peaks with red shift on the absorbance edges, which was ascribed to the enhanced conjugation lengths. The optical

band gaps (**Table 1**, empirical Equation (3) in the Supporting Information) of the corresponding polymers were gradually reduced from 2.59 eV (PDBT-Th) to 2.53 eV (PDBT-Th:Th), 2.29 eV (PDBT-Th:2Th), 2.25 eV (PDBT-2Th), 2.24 eV (PDBT-2Th:Th), and 2.23 eV (PDBT-2Th:2Th). With increasing effective conjugated chain length of those polymers by introducing thiophene as bridge unit, the optical band gaps were gradually reduced, and tend to the same. Notably, with increasing voltage, new bands resulting from the polaron at approximately 600 nm and bipolaron at approximately 1,000 nm increased in intensity (Zhu et al., 2009; Lu et al., 2014; Yang et al., 2014; Lin et al., 2015; Ming et al., 2020). During this process, all polymers displayed a conspicuous color change under doped (oxidized) and dedoped (neutral) conditions (**Table 2**). To determine the color change, the CIE 1976 (L^* , a^* , b^*) color space and photographs were determined, in which L^* is the parameter of the lightness, a^* is the red-green balance and b^* is yellow-blue balance ($-a^*$ and $+a^*$ correspond to green and red and $-b^*$ and $+b^*$ correspond to blue and yellow, respectively) (Dyer et al., 2011). As presented in **Table 2**, PDBT-Th, PDBT-Th:Th, PDBT-2Th, and PDBT-Th:2Th showed $-a^*$ and $+b^*$ directions in the neutral state, therefore, the polymers exhibited yellow green color. PDBT-2Th:Th and PDBT-2Th:2Th exhibited noteworthy color of claybank (neutral state), which was attributed to the value of $+a^*$ and $+b^*$ directions. Isosbestic points at 450 nm of DBT-Th based polymers and 500 nm of DBT-2Th based polymers appeared in the spectra, indicating that these polymers were easily interconverted between neutral and oxidized states (Balan et al., 2011; Lin et al., 2020b).

CONCLUSION

Thiophene was used as a fundamental unit to progressively construct conjugated polymers of various lengths by electrochemical polymerization from polymeric precursor monomers (DBT-Th and DBT-2Th) and comonomers (thiophene and bithiophene). Theoretical DFT calculations, electrochemical, and electrochromic properties were measured and compared. All polymeric precursor systems exhibited increasingly significant voltage drops (ΔV) of their reduction peaks with enhanced conjugation length. All conjugated polymers exhibited decreased HOMO-LUMO gaps, significantly improved electrochemical stability, and noteworthy color changes when transitioning from the oxidized to neutral state with increasing conjugation length.

DATA AVAILABILITY STATEMENT

The raw data supporting the conclusions of this article will be made available by the authors, without undue reservation.

AUTHOR CONTRIBUTIONS

KL and XL designed the experiments. KL, JH, CL, WT, QW, ZL, and YZ performed the experiments. KL, DW, and XL analyzed the experimental results. KL and XL wrote the manuscript. All

authors commented on the manuscript. KL and XL supervised the project.

ACKNOWLEDGMENTS

This work was supported by the Guangdong Basic and Applied Basic Research Fund (nos. 2019A1515110944 and 2019A1515010848) and the Youth Innovation Talent Project for the Universities of Guangdong Province (Grants: 2019KQNCX161 and 2019KQNCX190). We are also grateful to

Zhongshan Science and Technology Public Projects (2019B2061) and PhD Early Development Program of University of Electronic Science and Technology of China Zhongshan Institute (419YKQN16) for their financial support of this study.

SUPPLEMENTARY MATERIAL

The Supplementary Material for this article can be found online at: <https://www.frontiersin.org/articles/10.3389/fchem.2020.00819/full#supplementary-material>

REFERENCES

- Ak, M., Tanyeli, C., Akhmedov, I. M., and Toppare, L. (2008). Optoelectrochemical Properties of the Copolymer of 2,5-Di(4-methylthiophen-2-yl)-1-(4-nitrophenyl)-1H-pyrrole Monomer with 3,4-Ethylenedioxythiophene. *Thin Solid Films* 516, 4334–4341. doi: 10.1016/j.tsf.2008.01.013
- Argun, A. A., Aubert, P. H., Thompson, B. C., Schwendeman, I., Gaupp, C. L., Hwang, J., et al. (2004). *Chem. Mater.* 16, 4401–4412. doi: 10.1021/cm049669l
- Balan, A., Baran, D., and Toppare, L. (2011). Benzotriazole containing conjugated polymers for multipurpose organic electronic applications. *Polym. Chem.* 2, 1029–1043. doi: 10.1039/c1py00007a
- Beaujuge, P. M., and Reynolds, J. R. (2010). Color control in π -conjugated organic polymers for use in electrochromic devices. *Chem. Rev.* 110, 268–320. doi: 10.1021/cr900129a
- Camurlu, P., Sahmetlioglu, E., Sahin, E., Akhmedov, I. M., Tanyeli, C., and Toppare, L. (2008). Fine tuning of color via copolymerization and its electrochromic device application. *Thin Solid Films* 516, 4139–4144. doi: 10.1016/j.tsf.2007.10.098
- Chen, W., and Xue, G. (2005). Low potential electrochemical syntheses of heteroaromatic conducting polymers in a novel solvent system based on trifluoroborate-ethyl ether. *Prog. Polym. Sci.* 30, 783–811. doi: 10.1016/j.progpolymsci.2005.03.002
- Dai, Y. Y., Li, W. J., Qu, X. X., Liu, J., Yan, S. M., Ouyang, M., et al. (2017). Electrochemistry, electrochromic and color memory properties of polymer/copolymer based on novel dithienylpyrrole structure. *Electrochim. Acta* 229, 271–280. doi: 10.1016/j.electacta.2017.01.156
- Dyer, A. L., Thompson, E. J., and Reynolds, J. R. (2011). Completing the color palette with spray-processable polymer electrochromics. *ACS Appl. Mater. Interfaces* 3, 1787–1795. doi: 10.1021/am200040p
- Gu, C., Huang, N., Chen, Y. C., Qin, L. Q., Xu, H., Zhang, S. T., et al. (2015). π -conjugated microporous polymer films: designed synthesis, conducting properties, and photoenergy conversions. *Angew. Chem. Int. Ed.* 127, 13798–13802. doi: 10.1002/anie.201506570
- Gu, H., Lin, K. W., Liu, X. M., Jian, N. N., Qu, K., and Xu, J. K. (2018). Enhanced redox stability and optical contrast of electrochromic copolymers from selenophene and 3-methylthiophene. *J. Solid State Electrochem.* 22, 599–611. doi: 10.1007/s10008-017-3803-0
- Inzelt, G., Pineri, M., Schultze, J. W., and Vorotyntsev, M. A. (2000). Electron and proton conducting polymers: recent developments and prospects. *Electrochim. Acta* 45, 2403–2421. doi: 10.1016/S0013-4686(00)00329-7
- Jiang, Y. Y., Xu, K., and Zeng, C. C. (2018). Use of electrochemistry in the synthesis of heterocyclic structures. *Chem. Rev.* 118, 4485–4540. doi: 10.1021/acs.chemrev.7b00271
- Jin, X. H., Sheberla, D., Shimon, L. J. W., and Bendikov, M. (2014). Highly coplanar very long oligo(alkylfuran)s: a conjugated system with specific head-to-head defect. *J. Am. Chem. Soc.* 136, 2592–2601. doi: 10.1021/ja411842g
- Kavak, E., Us, C. N., Yavuz, E., Kivrak, A., and Özkut, M. (2015). A camouflage material: p- and n-type dopable furan based low band gap electrochromic polymer and its EDOT based copolymer. *Electrochim. Acta* 182, 537–543. doi: 10.1016/j.electacta.2015.09.148
- Li, C., Bai, H., and Shi, G. Q. (2009). Conducting polymer nanomaterials: electrosynthesis and applications. *Chem. Soc. Rev.* 38, 2397–2409. doi: 10.1039/b816681c
- Li, C. T., Kuo, Y. L., Kumar, C. P., Huang, P. T., and Lin, J. T. (2019a). Tetraphenylethylene tethered phenothiazine based double-anchored sensitizers for high performance dye-sensitized solar cells. *J. Mater. Chem. A* 7, 23225–23233. doi: 10.1039/c9ta09025h
- Li, W. J., Luo, F. F., Zhang, L., Yan, S. M., Zhao, R. Y., Ren, N., et al. (2019b). Synthesis, electrochemistry, and electrochromic properties of branched thiophene polymers with different conjugation lengths. *J. Polym. Sci. Pol. Chem.* 57, 2340. doi: 10.1002/pola.29538
- Lin, K. W., Chen, S., Lu, B. Y., and Xu, J. K. (2017). Hybrid π -conjugated polymers from dibenzo pentacyclic centers: precursor design, electrosynthesis and electrochromics. *Sci. China Chem.* 60, 38–53. doi: 10.1007/s11426-016-0298-2
- Lin, K. W., Jian, N. N., Zhang, X. B., Zhang, Y. S., Ming, S. L., Zhen, S. J., et al. (2020b). Star-shaped trithiophene and hexathiophene functionalized truxenes: synthesis, electropolymerization, and electrochromism. *React. Funct. Polym.* 154:104674. doi: 10.1016/j.reactfunctpolym.2020.104674
- Lin, K. W., Ming, S. L., Chen, S., Zhang, X. B., Wang, K., Wang, Y. H., et al. (2020a). Yellow-to-transmissive Electrochromic Poly(dibenzothiophene/dibenzofuran-bithiophene). *J. Solid State Electrochem.* 24, 1387–1396. doi: 10.1007/s10008-020-04623-0
- Lin, K. W., Ming, S. L., Zhen, S. J., Zhao, Y., Lu, B. Y., and Xu, J. K. (2015). Molecular design of DBT/DBF hybrid thiophenes π -conjugated systems and comparative study of their electropolymerization and optoelectronic properties: from comonomers to electrochromic polymers. *Polym. Chem.* 6, 4575–4587. doi: 10.1039/c5py00410a
- Liu, M. N., Makuta, S., Tsuda, S., Russo, S., Seki, S., Terao, J., et al. (2017). Fluorene-thiophene copolymer wire on TiO₂: mechanism achieving long charge separated state lifetimes. *J. Phys. Chem. C* 121:25672. doi: 10.1021/acs.jpcc.7b07295
- Lu, B. Y., Jian, N. N., Qu, K., Hu, F. Q., Liu, X. M., Xu, J. X., et al. (2020). Stepwise enhancement on optoelectronic performances of polyselenophene via electropolymerization of mono-, Bi-, and triselenophene. *Electrochim. Acta* 340:135974. doi: 10.1016/j.electacta.2020.135974
- Lu, B. Y., Zhen, S. J., Zhang, S. M., Xu, J. K., and Zhao, G. Q. (2014). Highly stable hybrid selenophene-3,4-ethylenedioxythiophene as electrically conducting and electrochromic polymers. *Polym. Chem.* 5, 4896–4908. doi: 10.1039/c4py00529e
- Ming, S. L., Li, Z. Y., Zhen, S. J., Liu, P. P., Jiang, F. X., Nie, G. M., et al. (2020). High-performance D-A-D type electrochromic polymer with π spacer applied in supercapacitor. *Chem. Eng. J.* 390:124572. doi: 10.1016/j.cej.2020.124572
- Sheberla, D., Patra, S., Wijsboom, Y. H., Sharma, S., Sheynin, Y., Haj-Yahia, A. E., et al. (2015). Conducting polyfurans by electropolymerization of oligofurans. *Chem. Sci.* 6, 360–371. doi: 10.1039/c4sc02664k
- Sun, Y., Chien, S. C., Yip, H. L., Zhang, Y., Chen, K. S., Zeigler, D. F., et al. (2011). High-mobility low-bandgap conjugated copolymers based on indacenodithiophene and thiadiazolo[3,4-c]pyridine units for thin film transistor and photovoltaic applications. *J. Mater. Chem.* 21, 13247–13255. doi: 10.1039/c1jm11564b
- Yang, K., He, T., D., Chen, X. Y., Cheng, S. Z. D., and Zhu, Y. (2014). Patternable conjugated polymers with latent hydrogen-bonding on the main chain. *Macromolecules* 47, 8479–8486. doi: 10.1021/ma501960t

- Yuan, Y., and Lei, A. W. (2020). Is electrosynthesis always green and advantageous compared to traditional methods? *Nat. Commun.* 11:802. doi: 10.1038/s41467-020-14322-z
- Zhang, L., Colella, N. S., Liu, F., Trahan, S., Baral, J. K., Winter, H. H., et al. (2013). Synthesis, electronic structure, molecular packing/morphology evolution, and carrier mobilities of pure oligo-/poly(alkylthiophenes). *J. Am. Chem. Soc.* 135, 844–854. doi: 10.1021/ja3104796
- Zhang, L., Luo, F. F., Li, W. J., Yan, S. M., Chen, Z. X., Zhao, R. Y., et al. (2019). Conjugation-broken thiophene-based electropolymerized polymers with well-defined structures: effect of conjugation lengths on electrochromic properties. *Phys. Chem. Chem. Phys.* 21, 24092–24100. doi: 10.1039/c9cp04308j
- Zhou, N. J., Guo, X. G., Ortiz, R. P., Harschneck, T., Manley, E. F., Lou, S. J., et al. (2015). Marked consequences of systematic oligothiophene catenation in thieno[3,4-c]pyrrole-4,6-dione and bithiopheneimide photovoltaic copolymers. *J. Am. Chem. Soc.* 137, 12565–12579. doi: 10.1021/jacs.5b06462
- Zhu, Y., Zhang, K., and Tieke, B. (2009). Electrochemical polymerization of Bis(3,4-ethylenedioxythiophene)-substituted 1,4-Diketo-3,6-diphenylpyrrolo[3,4-c]pyrrole (DPP) derivative. *Macromol. Chem. Phys.* 210, 431–439. doi: 10.1002/macp.200800507

Conflict of Interest: The authors declare that the research was conducted in the absence of any commercial or financial relationships that could be construed as a potential conflict of interest.

Copyright © 2020 Lin, Li, Tao, Huang, Wu, Liu, Zhang, Wang and Liu. This is an open-access article distributed under the terms of the Creative Commons Attribution License (CC BY). The use, distribution or reproduction in other forums is permitted, provided the original author(s) and the copyright owner(s) are credited and that the original publication in this journal is cited, in accordance with accepted academic practice. No use, distribution or reproduction is permitted which does not comply with these terms.



Diketopyrrolopyrrole (DPP)-Based Materials and Its Applications: A Review

Wei Wei Bao^{1†}, Rui Li^{2†}, Zhi Cheng Dai², Jian Tang², Xin Shi¹, Jie Ting Geng², Zhi Feng Deng^{1*} and Jing Hua^{2*}

¹ National and Local Joint Engineering Laboratory for Slag Comprehensive Utilization and Environmental Technology, School of Materials Science and Engineering, Shaanxi University of Technology, Hanzhong, China, ² Key Laboratory of Rubber-Plastic of Ministry of Education (QUST), School of Polymer Science and Engineering, Qingdao University of Science and Technology, Qingdao, China

OPEN ACCESS

Edited by:

Qixin Zhou,
University of Akron, United States

Reviewed by:

Maning Liu,
Tampere University, Finland
Xiang Li,
University of Akron, United States

*Correspondence:

Zhi Feng Deng
dengzf@sntu.edu.cn
Jing Hua
huajing72@qust.edu.cn

[†]These authors have contributed
equally to this work

Specialty section:

This article was submitted to
Organic Chemistry,
a section of the journal
Frontiers in Chemistry

Received: 30 May 2020

Accepted: 30 June 2020

Published: 10 September 2020

Citation:

Bao WW, Li R, Dai ZC, Tang J, Shi X,
Geng JT, Deng ZF and Hua J (2020)
Diketopyrrolopyrrole (DPP)-Based
Materials and Its Applications: A
Review. *Front. Chem.* 8:679.
doi: 10.3389/fchem.2020.00679

Diketopyrrolopyrrole (DPP) and its derivatives have been widely studied in the past few years due to its intrinsic physical and chemical properties, such as strong electron-withdrawing, deep color, high charge carrier mobility, strong aggregation, good thermal/photo-stability. In the 1970s, DPP was developed and used only in inks, paints, and plastics. Later, DPP containing materials were found to have potential other applications, typically in electronic devices, which attracted the attention of scientists. In this feature article, the synthesis pathway of DPP-based materials and their applications in organic field-effect transistors, photovoltaic devices, sensors, two photo-absorption materials, and others are reviewed, and possible future applications are discussed. The review outlines a theoretical scaffold for the development of conjugated DPP-based materials, which have multiple potential applications.

Keywords: DPP, OFETs, OPVs, sensor, TPA

INTRODUCTION

In the past few years, extensive research has developed novel π -conjugated materials, examining different ways to use them in various applications, including organic field-effect transistors (OFET), solar cells, organic light emitting diodes (OLED), coatings, sensors, and so on (Eom et al., 2017; Huang and Li, 2018; Deng et al., 2019; Kwon et al., 2020). These materials offer many technological advantages compared to their inorganic counterparts, such as their low weight, low fabrication cost, foldability, and easy conformation onto non-flat surfaces. Recently, increasing numbers of chemists and physicists have expressed interest in diketopyrrolo-[3,4-c]pyrrole (DPP) pigments, since DPP-based materials show excellent electronic properties with good thermal and photo-stability (Tieke et al., 2010; Kaur and Choi, 2015).

DPP pigments were commercialized in the 1980s when a crucial structural unit in an important class of red pigments with deep color was first made available. In the beginning, DPP were developed as dyes and pigments and used in inks, paints, and plastics (Iqbal et al., 1988). There were only a few articles on DPP pigments, and the first thiophene-flanked DPP-based polymer semiconductor for OFETs was reported in 2008, which showed hole mobility (μ_h) of $0.1 \text{ cm}^2 \text{ V}^{-1} \text{ s}^{-1}$ and electron mobility (μ_e) up to $0.09 \text{ cm}^2 \text{ V}^{-1} \text{ s}^{-1}$, respectively. Since then, DPP-based conjugated materials have received increasing attention from scientists (Bürgi et al., 2008).

DPP pigments were often constructed by a DPP core with two flanked aromatic groups (Figure 2). The core of DPP contains two amine units and carbonyl groups with bicyclic,

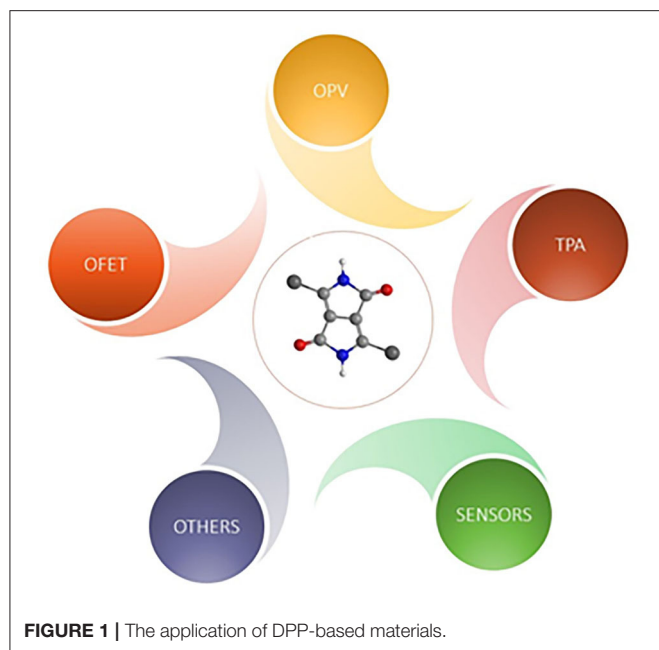
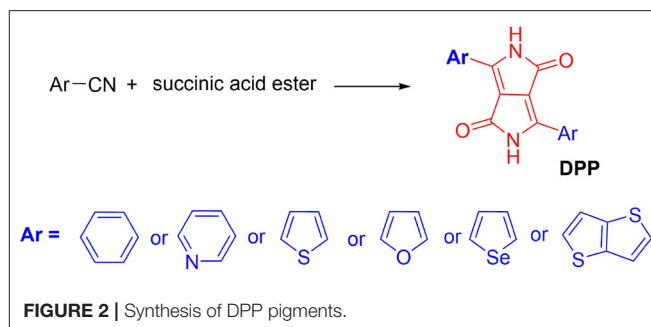


FIGURE 1 | The application of DPP-based materials.

which endow the DPP pigments with strong electron deficiency properties that can be used for the construction of donor-acceptor (D-A) conjugated materials. DPP-based materials have often exhibited extraordinarily strong π - π interaction and aggregation properties between the neighboring DPP moieties, resulting in the materials having beneficial properties for electronic devices (Qu and Tian, 2012). Till now, the DPP chromophore and its derivatives have played a key role in the molecular design and construction of high-performance materials in electronic devices, including sensors, and so on. Based on the DPP chromophores with numerous advantages, several articles have reviewed its applications in OFETs, sensors, and solar cells separately (Qu and Tian, 2012; Kaur and Choi, 2015; Zhao et al., 2019). However, a comprehensive review of the DPP chromophore and its derivative application has not yet been reported. This article discusses the synthesis pathways, before examining some applications of DPP-based materials, such as OFET, OPV, sensors, two photo absorption materials, coatings, hole transfer materials in perovskite solar cells, etc. (seen in **Figure 1**), and later, suggests future applications.

SYNTHESIS OF DPP-BASED MATERIALS

In 1974, Farnum and co-authors first designed and synthesized the DPP pigment flanked with two phenyl units in the low yield (Donald Parnum et al., 1974). The obtained 8- π electron fused ring hydrocarbon pentalene was highly insoluble in most common organic solvents and brilliant red color. Later, Iqbal et al. modified the synthesis pathway by a single reaction step between aromatic nitrile with dialkyl succinate (**Figure 2**) with a high yield (Iqbal et al., 1988). Subsequently, a large number of DPP derivatives have been designed and reported with the color from



red to blue, for example, isomer-DPP, phenyl-/pyridyl-/thienyl-/furanyl-/selenenyl-/thienothiophenyl- flanked DPP (**Figure 2**), DPP with distinct alkyl chain (branch or linear, various length, functionalization, etc.), and so on (Chen et al., 2012; Yiu et al., 2012; Zhang et al., 2013; Yi et al., 2015; Jiang X. et al., 2017; Jiang Z. et al., 2017). These flanked groups could affect the planarity of the DPP pigment, energy levels, and π - π stacking distance. DPP pigments contain two carbonyl and amine units in the core which could form strong hydrogen bonding (NH...OC) in the solid states, resulting in poor solubility in most common organic solvents (Zhang et al., 2017). However, the alkylation could break the hydrogen bonding association, acquiring a good solubility. The soluble DPP with two functional groups, such as bromine, could render it suitable for polymerization (Tieke et al., 2010). Through the Stille coupling reaction, Yu et al. reported the first DPP-based polymers containing phenyl-flanked DPP and phenylene in the backbone in 1993 (Chan et al., 1993). Later, other approaches including the Suzuki coupling, electrochemical polymerization (Liu et al., 2017), and Buchwald coupling, were developed to synthesize DPP-based polymers (Tieke et al., 2010). Compared with the small molecules or oligomers, D-A typed DPP polymers are more popular in electronic devices. The desirable properties of DPP-based polymers originated from the strong electron deficiency and good planarity of the DPP unit, large π -conjugation system, and remarkable aggregation properties. Further modification of the DPP chromophore is crucial for the application of DPP-based materials.

APPLICATIONS

Organic Field-Effect Transistors (OFETs)

Since the first DPP polymer was reported with the μ_h of $0.1 \text{ cm}^2 \text{ V}^{-1} \text{ s}^{-1}$ and μ_e up to $0.09 \text{ cm}^2 \text{ V}^{-1} \text{ s}^{-1}$, the DPP chromophore and its derivatives have obtained a tremendous amount of attention as an electron acceptor in building D-A typed semiconductor materials (Bürgi et al., 2008). DPP-based materials in OFETs can be divided into polymers and small molecule OFETs. Polymers, due to the large π -conjugation system, often show high inter-molecular charge transport mobility. Kim's group have reported a series of DPP-based polymers by varying the ratio between poly [DPP-(E)-[2,2-bithiophen]-5-yl]-3-(thiophen-2-yl) acrylonitrile (CNTVT)] unit and DPP-selenophene-vinylene-selenophene (SVS) unit (Khim et al., 2016). In this work, the author found

that the charge transport mobility could be effectively modulated from p-channel ($\mu_h = 6.63 \text{ cm}^2 \text{ V}^{-1} \text{ s}^{-1}$, $\mu_e = 0.08 \text{ cm}^2 \text{ V}^{-1} \text{ s}^{-1}$, CNTVT:SVS = 1:9) to n-channel ($\mu_e = 7.89 \text{ cm}^2 \text{ V}^{-1} \text{ s}^{-1}$, $\mu_h = 0.88 \text{ cm}^2 \text{ V}^{-1} \text{ s}^{-1}$, CNTVT:SVS = 9:1) dominated by modifying the CNTVT and SVS units. Later, Zhang's groups introduced hydrogen bonding through alkyl-chain engineering to build the OFETs with μ_h even up to $12 \text{ cm}^2 \text{ V}^{-1} \text{ s}^{-1}$ (Yao et al., 2016). Very soon, Zhang's group investigated thionation isoDPP to isoDTPP could not only improve charge mobility but also result in ambipolar transporting properties (Zhang et al., 2018b).

To the best of our knowledge, the highest charge transfer mobility based on DPP materials was reported by Luo et al. (2016). The author introduced tetramethylammonium iodide into the DPP polymer thin film, which showed the μ_h up to $26 \text{ cm}^2 \text{ V}^{-1} \text{ s}^{-1}$ and μ_e to $4.4 \text{ cm}^2 \text{ V}^{-1} \text{ s}^{-1}$. Such high charge carrier mobilities are ascribed to the more ordered lamellar packing of the alkyl side chains and inter-chain π - π interactions. For small molecular OFETs, since the molecular packing with more crystalline can be easily modified by the chemical structure, they often showed good intra-molecular charge transport ability. Recently, hydrogen bonding association in DPP-based materials enhanced the charge carrier mobility, as reported by Zhang and other groups (Oh et al., 2016; Zhang et al., 2017, 2020). Through hydrogen bonding association, the crystal-to-crystal transition was studied in crystal DPP-based semiconductors by Zhang et al. (2017). Even the hole mobility was only $0.26 \text{ cm}^2 \text{ V}^{-1} \text{ s}^{-1}$, this work provided a simple and useful approach to obtain high crystallinity OFET devices with insoluble pigment molecules through their soluble precursors.

Compared with other types of organic material semiconductors, more DPP-based materials were reported with high charge carrier mobility, typically over $1 \text{ cm}^2 \text{ V}^{-1} \text{ s}^{-1}$. DPP-based materials show high charge carrier mobilities. This is probably due to its strong electron-deficient ability, good planarity, and strong aggregation, which cause the materials to have good inter-/intra- charge transport ability within the semiconductor layer. Design of DPP chromophore, such as modification with the flanked aromatic groups, alkyl chain, and the core of the DPP, etc., is crucial for achieving good semiconductor materials.

Organic Photovoltaics (OPVs)

Among the various renewable energy sources, solar energy, renewable, and carbon-neutral energy sources are unarguably the most exploitable sources. More solar energy reaches our planet in 1 h that is consumed by mankind in an entire year (Hammarström and Hammes-Schiffer, 2009). Thus, photovoltaic cells, which directly convert solar energy to electrical energy, represent the most promising renewable energy device. Up to date, the organic solar cell (OSCs) has received a large amount of attention due to its promising performance, its simple solution-processable fabrication technique, low cost, and sustainability (Chen et al., 2020; He et al., 2020). Recently, more scientists have turned their attention to chemical structure modification, regarding organic materials. Among these, the DPP pigment has a high profile and often plays an important role

in the molecular design concept for high-performance materials in OSCs.

In 2008, Janssen's group reported a polymer containing thiophene-flanked DPP and bithiophene and used it to construct bulk-heterojunction (BHJ) solar cells with C_{60} and PC_{70}BM , which showed a power conversion efficiency (PCE) up to 4.0% with open-circuit voltage (V_{oc}) of 0.61 V (Wienk et al., 2008). In this OSC, the DPP-based polymer operated as a donor and fullerene worked as an electron acceptor. Later, the same group modified the alkyl chain and donor unit (phenyl instead of bithiophene) for polymerization. The obtained polymer exhibited slightly higher PCE (5.5%) and higher V_{oc} (0.8 V) (Bijleveld et al., 2010). The higher V_{oc} could be ascribed to: (i) in most cases, the V_{oc} in BHJ solar cells are related to the energy difference between the lowest unoccupied molecular orbital (LUMO) levels of the acceptor and the highest occupied molecular orbital (HOMO) levels of the donor (conjugated materials); (ii) the donor units in the materials mainly contribute to the HOMO levels; (iii) phenyl showed weak donor ability compared to thiophene. This also has been studied in the DPP-based oligomers (Qu et al., 2012).

Compared with the fullerene OSCs, the non-fullerene (NF) OSCs are more popular due to various advantages such as tunable absorption, structure versatility, energy levels, and crystalline (Qu and Tian, 2012; Gao et al., 2019; Zhao et al., 2019). DPP-based materials in OSCs belong to state-of-the-art materials in NFOSCs, due to its strong electron-withdrawing ability and broad optical absorption even into the near-infrared (NIR) region. Li's group reported DPP-based polymers containing Th-DPP and oligothiophene segments (Jiang X. et al., 2017). These polymers showed strong absorption between 500 and 1,000 nm, which match well with the solar spectrum. Using these polymers as electron donor and 3,9-bis(2-methylene-(3-(1,1-dicyanomethylene)-indanone))-5,5,11,11-tetrakis(4-hexylphenyl)-dithieno[2,3-d:2',3'-d']-s-indaceno[1,2-b:5,6-b']dithiophene (ITIC) as electron acceptor to build NFOSCs resulted in the PCE of 1.9–4.1%. These studies indicated that it is crucial to tune the miscibility between donor and acceptor for improving the performance of NFOSCs. Compared to polymers, small molecules and oligomers are purified and modify the chemical structure more easily. In 2019, Gao et al. reported two NIR absorbing DPP-based oligomers and used them as acceptors combined with 6TIC as a donor to construct NFSOCs (Gao et al., 2019). To the best of our knowledge, these NFSOCs showed the best performance among the DPP-based solar cells with the PCE up to 12.08%. The high device performance could be ascribed not only to the chemical and physical properties of the oligomer structure, but also the good film morphology. DPP-based conjugated materials, typically the thiophene-flanked DPP, often showed broad absorption spectra with NIR tail, high charge carrier mobility, and crystallinity, thus it is widely used in OSCs. Further functionalization of DPP materials, such as furanone-/selenenyl-flanked DPP or isoDPP, combined with optimizing device fabrication, might be critical in realizing high performance OSCs.

Sensors

A chromophore bonded with a specific analyte can cause either an increase or decrease in the emission/absorption intensity, accompanied by the phenomenon of a red or blue shift of the emission band or absorption band. These kinds of chromophores were widely used as sensors (Kaur and Choi, 2015). Recently, DPP molecules have been popular in ions sensors because of functional units such as carbonyl and amine groups. In 2018, Zhang et al. reported that a DPP-based polymer film contains lactam amide units. This work firstly indicates that the DPP-based polymer film can be used not only as a renewable fluoride anion chemosensor with detection limits as low as 10^{-6} – 10^{-8} M, but also a promising fluoride anion extractor (Zhang et al., 2018a). Jang's group reported the DPP small molecule for detection cyanide anion due to the functional carbonyl units of the DPP core (Jeong et al., 2012). The original DPP small molecule in the solution shows green color with strong emission. However, once the cyanide anion was added, the solution color changed into red with quenching fluorescence.

Through molecular design, DPP-based materials with NIR absorption and emission are popular in cell sensors. This could be attributed to the fact that the low energy from the NIR light can minimize photo-damage to biological cells and deeply penetrate tissue for cell recognition (Kaur and Choi, 2015). Wiktorowski et al. reported water-soluble DPP derivatives with NIR fluorescence and internalized it into live-cell images of CHO cells using a confocal fluorescence microscope (Wiktorowski et al., 2014). The result showed that the intra-cellular fluorescence quantum yield (ϕ_f) of the DPP derivative was 34%. Compared with the most used indocyanine green, DPP derivatives showed not only high intra-cellular ϕ_f but also improved intra-cellular photostability. Further modification DPP derivatives, typically focusing on good photostability, high ϕ_f , water solubility, along with two-photon absorption and emission, is crucial for the development cell or DNA sensors.

Two-Photon Absorption (TPA)

Conjugated molecules exhibiting large TPA cross sections (δ) can be applied in the photo-sciences, for example in two-photon fluorescence imaging, optical power limiting, two-photon up conversion lasing, three-dimensional optical data storage and so on (Xu et al., 2020). Although there are numerous conjugated materials with TPA properties, few among them exhibit large δ . In 2008, Yang's group reported that the phenyl amine-DPPs small molecule showed large δ up to 1,200 GM (Guo et al., 2009). Later, this group studied the DPP-based polymer, which also displayed high δ (859 GM) (Zhang et al., 2011). Since then, the DPP chromophore was widely studied and used in the design of TPA materials. Ftouni et al. reported a series of DPP-based small molecules with δ being 750 GM, and successfully coupled these molecules to a synthetic Tat-derived peptide as a two-photon fluorescent tag for living cell microscopy with low power excitation (Ftouni et al., 2013). Later, Hua's group reported DPP oligomer with not only large δ (1,140 GM) and high fluorescence brightness after aggregation (39.02%), but also strong aggregation-induced emission properties (Jiang et al.,

2016). These kinds of materials are promising in terms of bio-application, except for bio-imaging, and DPP materials with TPA properties used in heavy metal sensors, such as Hg^{+} , as reported by Nie and co-authors (Nie et al., 2018). Till now, the DPP-based TPA materials have a large space and research has explored multi-photon absorption, but examinations of three-photon absorption are quite rare. In 2017, Ye et al. firstly reported a series of DPP oligomers with three-photon absorption through computation (Ye et al., 2017). Unfortunately, these materials have not been synthesized, but through the development of molecular design concepts, multi-photon absorption materials based on DPP derivatives are on the way.

Other Applications

With the exception of the application described above, the intrinsic physical and chemical properties of DPP-based materials mean they are widely used in other applications. Reversible electrochromism properties regarding DPP-based polymers were reported by Tieke's group (Zhang et al., 2013). These studies reveal that DPP-based materials had potential in color-change windows. In the beginning, DPP pigment was developed as a dye in inks and paints due to its weather resistance and deep color. Based on these properties, Zhang and Zhou et al. introduced DPP into the one-coat epoxy coating, which showed improvement in UV-stability compared to the pure epoxy coating, due to the DPP pigment creating strong UV-light absorption (Zeng et al., 2018). DPP chromophore, typically the thiophene-flanked DPP with high hole transfer mobility, were used in dopant-free hole transfer materials (HTM) in perovskite solar cells, which not only improved the device stability but also reduced the cost of HTMs compared to the state-of-art HTMs (spiro-OMeTAD) (Li et al., 2019; Zhang et al., 2019; Chang and Wang, 2020). Data's group reported phenyl-, furanyl- and thienyl-flanked DPP as emitters in OLED devices, which showed the EQE up to 12.1% (Data et al., 2016).

CONCLUSION AND OUTLOOK

In summary, we have provided an overview of the synthesis and applications of DPP-based π -conjugated materials. Various aromatic-flanked DPP derivatives were described. DPPs are insoluble pigment due to the strong hydrogen bonding, which through alkylation of the amide units and bromination of the aromatic units could be converted into soluble monomers for polymerization. DPP chromophore exhibits strong electron-deficient properties, good planarity backbone, and strong aggregation in the solid-state. It has been widely used in the construction of D-A typed high performance semiconductor materials. Due to its broad optical absorption combined with high charge transfer mobility and good photo-/thermal-stability, DPP-based materials were widely used in solar cells, typically non-fullerence solar cells. The carbonyl and amine groups in the DPP core lead to DPP derivatives suitable for many ion sensors and cell sensors, particularly in the NIR region sensor and TPA biological sensor. Moreover, the application of DPP in other fields, such as coating, chemical color change window,

photo-detector, OLED, etc., would also benefit from exploration in the future.

Compared with the phenyl- and thienyl-flanked DPP, the selenenyl- and pyridyl-flanked DPP are less studied. The pyridyl-flanked DPP might display low LUMO levels with good electron transfer mobility. The selenenyl-flanked DPP might show improved planarity and good aggregation, thus high charge transfer mobility is expected. It would be worthwhile to further functionalize for DPP and its derivatives, such as enlargement of π -conjugation, modification of alkyl chain, design of high-performance polymers for the promotion in π -conjugated materials applications. DPP-based conjugated materials might play a key role in realizing high performance electronics as well as other applications, thus further design of DPP-based materials and development of its applications are required.

REFERENCES

- Bijleveld, J. C., Gevaerts, V., S., Di Nuzzo, D., Turbiez, M., Mathijssen, S., et al. (2010). Efficient solar cells based on an easily accessible diketopyrrolopyrrole polymer. *Adv. Mater.* 22, E242–246. doi: 10.1002/adma.201001449
- Bürgi, L., Turbiez, M., Pfeiffer, R., Bienewald, F., H., Kirner, J., and Winnewisser, C. (2008). High-mobility ambipolar near-infrared light-emitting polymer field-effect transistors. *Adv. Mater.* 20, 2217–2224. doi: 10.1002/adma.200702775
- Chan, W. K., Chen, Y., and Peng Z., and Yu, L. (1993). Rational designs of multifunctional polymers. *J. Am. Chem. Soc.* 115, 11735–11743. doi: 10.1021/ja00078a012
- Chang, C., and Wang, C. (2020). Enhanced stability and performance of air-processed perovskite solar cells via defect passivation with a thiazol-bridged diketopyrrolopyrrole-based-bridged diketopyrrolopyrrole-based π -conjugated polymers. *J. Mater. Chem. A* 8, 8593–8604. doi: 10.1039/D0TA00978D
- Chen, G., Cheng, D., Zou, W., Cai, Z., Xie, Y., Chen, Y., et al. (2020). Dibenzothiophene-S,S-dioxide-bispyridinium-fluorene-based polyelectrolytes for cathode buffer layers of polymer solar cells. *Polym. Chem.* 11, 3605–3614. doi: 10.1039/D0PY00416B
- Chen, H., Guo, Y., Yu, G., Zhao, Y., Zhang, J., Gao, D., et al. (2012). Highly π -extended copolymers with diketopyrrolopyrrole moieties for high-performance field-effect transistors. *Adv. Mater.* 24, 4618–4622. doi: 10.1002/adma.201201318
- Data, P., Kurowska, A., Pluczyk, S., Zassowski, P., Pander, P., Jedrysiak, R., et al. (2016). Exciplex enhancement as a tool to increase OLED device efficiency. *J. Phys. Chem. C* 120, 2070–2078. doi: 10.1021/acs.jpcc.5b11263
- Deng, Z., Ai, T., Li, R., Yuan, W., Zhang, K., Du, H., et al. (2019). Conjugated polymers containing building blocks 1,3,4,6-tetraarylpyrrolo[3,2-b]pyrrole-2,5-dione (isoDPP), benzodipyrrolidone (BDP) or naphthodipyrrolidone (NDP): a review. *Polymers* 11:1683. doi: 10.3390/polym11101683
- Donald Parnum, G., Goverdhan Mehta, George Moore, G. I., and Frederick Siegal, P. (1974). Attempted reformatkii reaction of benzonitrile, 1,4-diketo-3,6-diphenylpyrrolo[3,4-c]pyrrole. a lactam analogue of pentalene. *Tetrahedron Lett.* 29:2549. doi: 10.1016/S0040-4039(01)93202-2
- Eom, S. H., Nam, S. Y., Do, H. J., Lee, J., Jeon, S., Shin, T. J., et al. (2017). Dark current reduction strategies using edge-on aligned donor polymers for high detectivity and responsivity organic photodetectors. *Polym. Chem.* 8, 3612–3621. doi: 10.1039/C7PY00497D
- Ftouni, H., Bolze, F., de Rocquigny, H., and Nicoud, J. F. (2013). Functionalized two-photon absorbing diketopyrrolopyrrole-based fluorophores for living cells fluorescent microscopy. *Bioconjug. Chem.* 24, 942–950. doi: 10.1021/bc300623q
- Gao, K., Jo, S. B., Shi, X., Nian, L., Zhang, M., Kan, Y., et al. (2019). Over 12% efficiency nonfullerene all-small-molecule organic solar cells with sequentially evolved multilength scale morphologies. *Adv. Mater.* 31:1807842. doi: 10.1002/adma.201807842

AUTHOR CONTRIBUTIONS

WB and RL collected the articles and wrote the first manuscript. ZD and XS collected the articles and modified the format. JT organized references and revised the manuscript. JG wrote the part of Other applications. ZD revise the manuscript and approved the final version. JH conceived of the topic and supervised the whole work. All authors contributed to revise the manuscript, approved the final version and agreed to be accountable for all aspects of this work.

FUNDING

The authors acknowledge the support from Shaanxi University of Technology (SLGPT2019KF01-01, SLGPT2019KF01-03, SLG1901).

- Guo, E. Q., Ren, P. H., Zhang, Y. L., Zhang, H. C., and Yang, W. J. (2009). Diphenylamine end-capped 1,4-diketo-3,6-diphenylpyrrolo[3,4-c]pyrrole (DPP) derivatives with large two-photon absorption cross-sections and strong two-photon excitation red fluorescence. *Chem Commun.* 2009, 5859–5861. doi: 10.1039/b911808j
- Hammarström, L., and Hammes-Schiffer, S. (2009). Artificial photosynthesis and solar fuels acc. *Chem. Res.* 42:1859. doi: 10.1021/ar900267k
- He, B., Yin, Q., Xie, B., Zhang, J., Xie, R., Hu, Z., et al. (2020). Influence of the –CN substitution position on the performance of dicyanodistyrylbenzene-based polymer solar cells. *Polym. Chem.* 11, 653–1662. doi: 10.1039/C9PY01781J
- Huang, J., and Li, Y. (2018). BN embedded polycyclic π -conjugated systems: synthesis, optoelectronic properties, and photovoltaic applications. *Front Chem* 6:341. doi: 10.3389/fchem.2018.00341
- Iqbal, A., Jost, M., Kirchmayr, R., Pfenniger, J., Rochat, A., and Wallquist, O. (1988). The synthesis and properties of 1,4-diketo-pyrrolo[3,4-c]pyrrol. *Bull. SOC. Chim. Belg.* 97, 8–9. doi: 10.1002/bscb.19880970804
- Jeong, Y. H., Lee, C. H., and Jang, W. D. (2012). A diketopyrrolopyrrole-based colorimetric and fluorescent probe for cyanide detection. *Chem. Asian. J.* 7, 1562–1566. doi: 10.1002/asia.201101038
- Jiang, T., Li, D., Hang, Y., Gao, Y., Zhang, H., Zhao, X., et al. (2016). Tetraphenylethene end-capped diketopyrrolopyrrole fluorogens with AIE and large two-photon absorption cross-sections features and application in bioimaging. *Dyes Pigments* 133, 201–213. doi: 10.1016/j.dyepig.2016.05.043
- Jiang, X., Xu, Y., Wang, X., Wu, Y., Feng, G., Li, C., et al. (2017). Non-fullerene organic solar cells based on diketopyrrolopyrrole polymers as electron donors and ITIC as an electron acceptor. *Phys. Chem. Chem. Phys.* 19, 8069–8075. doi: 10.1039/C7CP00494J
- Jiang, Z., Ni, Z., Wang, H., Wang, Z., Zhang, J., Qiu, G., et al. (2017). Versatile asymmetric thiophene/benzothiophene flanked diketopyrrolopyrrole polymers with ambipolar properties for OFETs and OSCs. *Polym. Chem.* 8, 5603–5610. doi: 10.1039/C7PY00940B
- Kaur, M., and Choi, D. H. (2015). Diketopyrrolopyrrole: brilliant red pigment dye-based fluorescent probes and their applications. *Chem. Soc. Rev.* 44, 58–77. doi: 10.1039/C4CS00248B
- Khim, D., Cheon, Y., R., Xu, Y., Park, W.-T., Kwon, S.-K., et al. (2016). Facile route to control the ambipolar transport in semiconducting polymers. *Chem. Mater.* 28, 2287–2294. doi: 10.1021/acs.chemmater.6b00298
- Kwon, N. Y., Kang, H., Park, S. H., Kim, H. J., Kim, C. Y., Park, S., et al. (2020). Rational design of a novel isoindigo-based conjugated terpolymer with panchromatic absorption and its application to polymer solar cells. *Dyes Pigments* 179:108391. doi: 10.1016/j.dyepig.2020.108391
- Li, W., Wang, Y., Li, M., Garbarini, L. P., and Omenetto, F. G. (2019). Inkjet printing of patterned, multispectral, and biocompatible photonic crystals. *Adv. Mater.* 31:e1901036. doi: 10.1002/adma.201901036
- Liu, M., Makuta, S., Tsuda, S., Russo, S., Seki, S., Terao, J., et al. (2017). Fluorene-thiophene copolymer wire on TiO₂: mechanism achieving long

- charge separated state lifetimes. *J. Phys. Chem. C* 121, 25672–25681. doi: 10.1021/acs.jpcc.7b07295
- Luo, H., Yu, C., Liu, Z., Zhang, G., Geng, H., Yi, Y., et al. (2016). Remarkable enhancement of charge carrier mobility of conjugated polymer field-effect transistors upon incorporating an ionic additive. *Sci. Adv.* 2:e1600076. doi: 10.1126/sciadv.1600076
- Nie, K., Xu, S., Duan, X., Shi, H., Dong, B., Long, M., et al. (2018). Diketopyrrolopyrrole-doped hybrid FONs as two-photon absorbing and dual-emission fluorescent nanosensors for Hg²⁺. *Sensors Actuators B: Chem.* 265, 1–9. doi: 10.1016/j.snb.2018.03.026
- Oh, J. Y., Rondeau-Gagné, S., Chiu, Y. C., Chortos, A., Lissel, F., Wang, G. J. N., et al. (2016). Intrinsically stretchable and healable semiconducting polymer for organic transistors. *Nature* 539, 411–415. doi: 10.1038/nature20102
- Qu, S., and Tian, H. (2012). Diketopyrrolopyrrole (DPP)-based materials for organic photovoltaics. *Chem. Commun.* 48, 3039–3051. doi: 10.1039/c2cc17886a
- Qu, S., Wang, B., Guo, F., Li, J., Wu, W., Kong, C., et al. (2012). New diketo-pyrrolo-pyrrole (DPP) sensitizer containing a furan moiety for efficient and stable dye-sensitized solar cells. *Dyes Pigments* 92, 1384–1393. doi: 10.1016/j.dyepig.2011.09.009
- Tieke, B., Rabindranath, A., R., Zhang, K., and Zhu, Y. (2010). Conjugated polymers containing diketopyrrolopyrrole units in the main chain. *Beilstein J. Org. Chem.* 6, 830–845. doi: 10.3762/bjoc.6.92
- Wienk, M. M., Turbiez, M., Gilot, J., and Janssen, R. A., J. (2008). Narrow-bandgap diketo-pyrrolo-pyrrole polymer solar cells: the effect of processing on the performance. *Adv. Mater.* 20, 2556–2560. doi: 10.1002/adma.200800456
- Wiktorowski, S., Rosazza, C., Winterhalder, M., J., Daltrozzi, E., and Zumbusch, A. (2014). Water-soluble pyrrolopyrrole cyanine (PPCy) NIR fluorophores. *Chem. Commun.* 50, 4755–4758. doi: 10.1039/C4CC01014K
- Xu, X., Sun, D., Yang, J., Zhu, G., Fang, Y., Gros, C., et al. (2020). Truxene-BODIPY dyads and triads: Synthesis, spectroscopic characterization, one and two-photon absorption properties and electrochemistry. *Dyes Pigments* 179:108183. doi: 10.1016/j.dyepig.2020.108380
- Yao, J., Yu, C., Liu, Z., Luo, H., Yang, Y., and Zhang, G. (2016). Significant improvement of semiconducting performance of the diketopyrrolopyrrole-quaterthiophene conjugated polymer through side-chain engineering via hydrogen-bonding. *J. Am. Chem. Soc.* 138, 173–185. doi: 10.1021/jacs.5b09737
- Ye, C. X., Zhang, J. M., Lin, X. D., Zhang, T., Wang, B., and He, T. C. (2017). Multiphoton absorption of three chiral diketopyrrolopyrrole derivatives in near-infrared window I and II. *Optical Mater. Express* 7, 3529–3537. doi: 10.1364/OME.7.003529
- Yi, Z., Wang, S., and Liu, Y. (2015). Design of high-mobility diketopyrrolopyrrole-based pi-conjugated copolymers for organic thin-film transistors. *Adv. Mater.* 27, 3589–3606. doi: 10.1002/adma.201500401
- Yiu, A. T., Beaujuge, P. M., Lee, O. P., Woo, C. H., Toney, M. F., and Frechet, J. M. (2012). Side-chain tunability of furan-containing low-band-gap polymers provides control of structural order in efficient solar cells. *J. Am. Chem. Soc.* 134, 2180–2185. doi: 10.1021/ja2089662
- Zeng, W., Zhou, Q., Zhang, H., and Qi, X. (2018). One-coat epoxy coating development for the improvement of UV stability by DPP pigments. *Dyes Pigments* 151, 157–164. doi: 10.1016/j.dyepig.2017.12.058
- Zhang, B., Zhang, H., Li, X., Li, W., Sun, P., and Yang, W. (2011). Synthesis, characterization, and large two-photon absorption cross-sections of solid red-emitting 1,4-diketo-3,6-diphenylpyrrolo[3,4-c]pyrrole/3,6-carbazole/terfluorene copolymers. *J. Polym. Sci. Part A: Polym. Chem.* 49, 3048–3057. doi: 10.1002/pola.24741
- Zhang, H., Deng, R., Wang, J., Li, X., Chen, Y. M., Liu, K., et al. (2017). Crystalline organic pigment-based field-effect transistors. *ACS Appl. Mater. Interfaces* 9, 21891–21899. doi: 10.1021/acsami.7b03170
- Zhang, H., Li, R., Deng, Z., Cui, S., Wang, Y., Zheng, M., et al. (2020). π -Conjugated oligomers based on aminobenzodifuranone and diketopyrrolopyrrole. *Dyes Pigments* 181:108552. doi: 10.1016/j.dyepig.2020.108552
- Zhang, H., Liu, M., Yang, W., Judin, L., Hukka, T., Priimagi, A., et al. (2019). Thionation enhances the performance of polymeric dopant-free hole-transporting materials for perovskite solar cells. *Adv. Mater. Interfaces* 6:1901036. doi: 10.1002/admi.201901036
- Zhang, H., Welterlich, I., Neudörfl, J.-M., Tieke, B., Yang, C., Chen, X., et al. (2013). Synthesis and characterization of 1,3,4,6-tetraarylpyrrolo[3,2-b]-pyrrole-2,5-dione (isoDPP)-based donor-acceptor polymers with low band gap. *Polym. Chem.* 4, 4682–4689. doi: 10.1039/c3py00570d
- Zhang, H., Yang, K., Chen, C., Wang, Y., Zhang, Z., Tang, L., et al. (2018a). 1,4-diketo-pyrrolo[3,4-c]pyrroles (DPPs) based insoluble polymer films with lactam hydrogens as renewable fluoride anion chemosensor. *Polymer* 149, 266–272. doi: 10.1016/j.polymer.2018.07.011
- Zhang, H., Yang, K., Zhang, K., Zhang, Z., Sun, Q., and Yang, W. (2018b). Thionating iso-diketopyrrolopyrrole-based polymers: from p-type to ambipolar field effect transistors with enhanced charge mobility. *Polym. Chem.* 9, 1807–1814. doi: 10.1039/C8PY00292D
- Zhao, C., Guo, Y., Zhang, Y., Yan, N., You, S., and Li, W. (2019). Diketopyrrolopyrrole-based conjugated materials for non-fullerene organic solar cells. *J. Mater. Chem. A* 7, 10174–10199. doi: 10.1039/C9TA01976F

Conflict of Interest: The authors declare that the research was conducted in the absence of any commercial or financial relationships that could be construed as a potential conflict of interest.

Copyright © 2020 Bao, Li, Dai, Tang, Shi, Geng, Deng and Hua. This is an open-access article distributed under the terms of the Creative Commons Attribution License (CC BY). The use, distribution or reproduction in other forums is permitted, provided the original author(s) and the copyright owner(s) are credited and that the original publication in this journal is cited, in accordance with accepted academic practice. No use, distribution or reproduction is permitted which does not comply with these terms.



Rational Design of π -Conjugated Tricoordinated Organoboron Derivatives With Thermally Activated Delayed Fluorescent Properties for Application in Organic Light-Emitting Diodes

Ruifa Jin^{1,2*} and Jingfan Xin^{1,2}

¹ College of Chemistry and Life Sciences, Chifeng University, Chifeng, China, ² Inner Mongolia Key Laboratory of Photoelectric Functional Materials, Chifeng University, Chifeng, China

OPEN ACCESS

Edited by:

Qixin Zhou,
University of Akron, United States

Reviewed by:

Yang Zhou,
Teknor Apex Company, United States
Weiwei Bao,
Shaanxi University of
Technology, China

*Correspondence:

Ruifa Jin
Ruifajin@163.com

Specialty section:

This article was submitted to
Organic Chemistry,
a section of the journal
Frontiers in Chemistry

Received: 30 June 2020

Accepted: 26 August 2020

Published: 30 September 2020

Citation:

Jin R and Xin J (2020) Rational Design
of π -Conjugated Tricoordinated
Organoboron Derivatives With
Thermally Activated Delayed
Fluorescent Properties for Application
in Organic Light-Emitting Diodes.
Front. Chem. 8:577834.
doi: 10.3389/fchem.2020.577834

A series of donor–acceptor (D–A) tricoordinated organoboron derivatives (**1–10**) have been systematically investigated for thermally activated delayed fluorescent (TADF)-based organic light-emitting diode (OLED) materials. The calculated results show that the designed molecules exhibit small singlet-triplet energy gap (ΔE_{ST}) values. Density functional theory (DFT) analysis indicated that the designed molecules display an efficient separation between donor and acceptor fragments because of a small overlap between donor and acceptor fragments on HOMOs and LUMOs. Furthermore, the delayed fluorescence emission color can be tuned effectively by introduction of different polycyclic aromatic fragments in parent molecule **1**. The calculated results show that molecules **2**, **3**, and **4** possess more significant Stokes shifts and red emission with small ΔE_{ST} values. Nevertheless, other molecules exhibit green (**1**, **7**, and **8**), light green (**6** and **10**), and blue (**5** and **9**) emissions. Meanwhile, they are potential ambipolar charge transport materials except that **4** and **10** can serve as electron and hole transport materials only, respectively. Therefore, we proposed a rational way for the design of efficient TADF materials as well as charge transport materials for OLEDs simultaneously.

Keywords: tricoordinated organoboron derivatives, thermally activated delayed fluorescent (TADF), photophysical properties, reorganization energy, organic light-emitting diodes (OLEDs)

INTRODUCTION

Organic light-emitting diodes (OLEDs) have drawn considerable attention for applications in displaying and lighting fields owing to their outstanding advantages nowadays (Choy et al., 2014; Zhang et al., 2015; Im et al., 2017a; Liu et al., 2017b, 2018; Pal et al., 2018; Zhu et al., 2018). Unfortunately, their commercialization applications are still limited by the low device performance at high luminance and low external quantum efficiency (EQE) of the emitters. It is noteworthy that charge recombination results in 25% singlet and 75% triplet excitons in the traditional fluorescence process (Tang and Vanslyke, 1987; Burroughes et al., 1990). The triplet excitons cannot be directly utilized by emitters because they are spin forbidden and decay is non-emissive in producing undesired heat. As a consequence, the internal quantum efficiency (IQE)

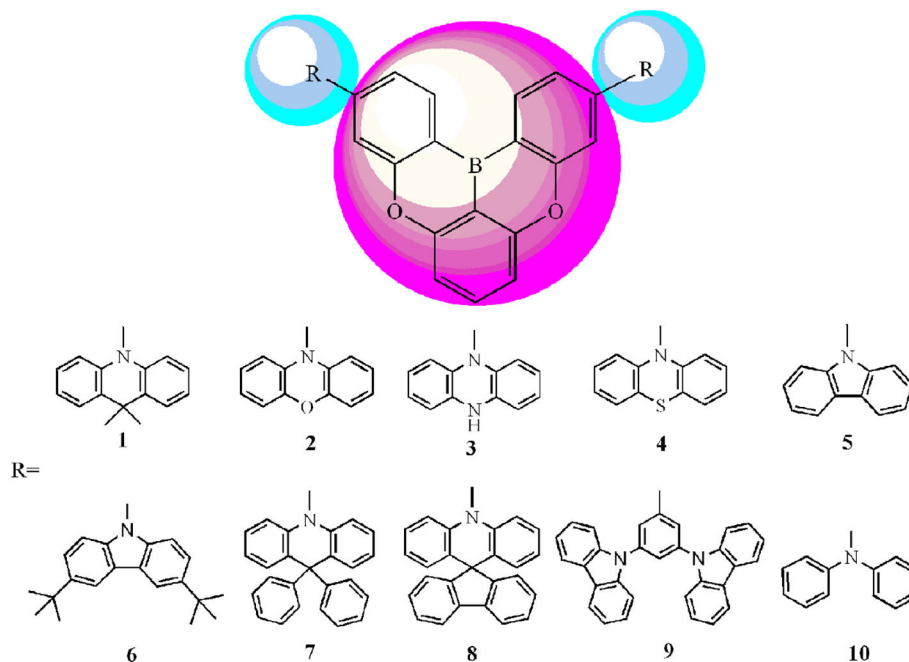
of OLEDs does not exceed 25% using singlet excitons for traditional fluorescent materials. Remarkably, it is challenging to develop highly efficient emitters utilizing triplet excitons. The phosphorescent emitters incorporating heavy metals can reach an IQE of nearly 100% by enhancing electron spin-orbit coupling (Baldo et al., 1998; Adachi et al., 2001; Xia et al., 2014). However, the applications of phosphorescent materials containing heavy metals are limited owing to their high cost and environmental contamination (Li et al., 2013; Liu et al., 2017a; Wang et al., 2018). Accordingly, it is critically important to develop novel metal-free materials, which can be functionalized as efficient emitters and exhibit environment friendliness. To address this issue, thermally activated delayed fluorescence (TADF) materials have been considered recently as promising candidates because of their potential in achieving 100% IQEs by harvesting all the triplet excitons (Uoyama et al., 2012; Wu et al., 2017; Yang et al., 2017; Chatterjee and Wong, 2019; Wang et al., 2019). As for TADF materials, a small energy gap (ΔE_{ST}) between the lowest singlet (S_1) and triplet (T_1) states promotes efficient spin conversion from the triplet to singlet manifold by thermal activation through reverse intersystem crossing (RISC), subsequently resulting in fluorescence from the converted S_1 to the ground (S_0) states (Evans et al., 2018; Li et al., 2018b; Zhu et al., 2019). It is noteworthy that a small ΔE_{ST} is favorable for the RISC process and may obtain TADF. Furthermore, it is noticeable that the interplay between theory and experiment is capable of providing a deeper insight into the understanding of the optical and electronic properties of molecules in ground as well as excited states. Many theoretical research efforts have been made in this regard. It is critically important to get the relationship between topologic structure and optical as well as electronic properties for designing novel materials with improved properties. Density functional theory (DFT) and time-dependent DFT (TD-DFT) approaches have been remarkably successful in accurately evaluating a variety of ground and excited-state properties, in particular for TADF materials (Lu et al., 2015a,b; Wang et al., 2017; Hussain et al., 2019). In this regard, the rational design of a twisted donor-acceptor (D-A)-type structure can endow the molecules with TADF characteristics. These systems can efficiently reduce ΔE_{ST} in virtue of their separating the highest occupied molecular orbitals (HOMOs) and the lowest unoccupied molecular orbitals (LUMOs) (Geng et al., 2017; Li et al., 2018a). Additionally, D-A architectures are beneficial for the intramolecular charge transfer (ICT) in the excited states (Santos et al., 2016; Deng et al., 2019; Zhang et al., 2020). In addition, TADF materials with different donor moieties such as 9,9-dimethyl-9,10-dihydroacridine, 10H-phenoxazine, 5,10-dihydrophenazine, 10H-phenothiazine, 9H-carbazole, 3,6-di-tert-butyl-9H-carbazole, 9,9-diphenyl-9,10-dihydroacridine 9H-spiro[4,5]fluorene-9,10-dihydroacridine, 9-(3-(9H-carbazol-9-yl)phenyl)-9H-carbazole, and diphenylamine possess excellent electroluminescence performance (Bezvikonnyi et al., 2019; Hosokai et al., 2019; Jin et al., 2019; Joo et al., 2019; Kim et al., 2019; Sharma et al., 2019; Zhong et al., 2019). Meanwhile, there are many TADF materials with different acceptor moieties such as benzonitrile, triazines, sulfones, benzophenone, quinoxaline, and naphthalimide reported in

literature (Li et al., 2016; Nobuyasu et al., 2016; Tsujimoto et al., 2017; Sommer et al., 2018; Wu et al., 2018; Yu et al., 2018). The HOMO/LUMO distribution and energy levels of the typical donor and acceptor moieties have been found in the relevant literature (Im et al., 2017b). Among the numerous reported TADF materials, organoboron compounds have drawn significant interest recently owing to their appealing optical properties in OLEDs. Because of the lack of electrons in the P_z orbital, the central boron atoms in the organoboron compounds exhibit strong electron-accepting ability through p- π conjugations, which is favorable for the ICT (Ji et al., 2017; Giustra and Liu, 2018; Liang et al., 2018; Meng et al., 2019).

Considering the merits and characteristics mentioned above, in this work, we design a series of novel D-A tricoordinated organoboron compounds with 5,9-dioxo-13b-boranaphtho[3,2,1-de]anthracene (DOBA) as electron acceptors and different polycyclic aromatic fragments as electron donors for TADF molecules (**Scheme 1**). Applying DFT and TD-DFT approaches, optoelectronic properties including frontier molecular orbital (FMO) energies (E_{HOMO} and E_{LUMO}), HOMO-LUMO gaps (E_g), adiabatic ionization potentials (AIP), adiabatic electron affinities (AEA), reorganization energy (λ), and ΔE_{ST} were systematically investigated. The absorption, fluorescence, and phosphorescence spectra of the designed molecules were predicted using the TD-DFT method. This provides a useful insight for designing novel TADF materials as well as charge transport materials for OLEDs.

COMPUTATIONAL DETAILS

Geometry optimizations for all the designed molecules in the S_0 states were accomplished using the DFT method in the Gaussian 09 package (Frisch et al., 2009). The corresponding frequency calculations were carried out at the same level to prove the nature of each stationary point. Using the TD-DFT approach, the structures in S_1 and T_1 states were optimized. Under the optimized structures in S_0 , S_1 , and T_1 states, their absorption, fluorescence, and phosphorescence spectra were predicted by using the TD-DFT method. Meanwhile, the ΔE_{ST} values were evaluated by adiabatic excitation energy. The 6-31G (d,p) basis set was selected for all the calculations in this work. With the aim to select reasonable exchange correlation functionals, six functionals including B3LYP (Becke, 1993), PBE0 (Adamo and Barone, 1999), ω B97XD (Chai and Head-Gordon, 2008), M062X (Zhao and Truhlar, 2008), and CAM-B3LYP (Yanai et al., 2004) were employed to optimize the geometries of molecule **1** in S_0 , S_1 , and T_1 states. On the basis of the optimized geometries in S_0 and S_1 states, the absorption and fluorescence spectra were predicted using the corresponding TD-DFT method. The ΔE_{ST} values were also calculated using the different methods. The corresponding results as well as the experimental data are shown in **Figure 1** and **Supplementary Table 1**. As visualized in **Figure 1**, obviously, the fluorescence emission wavelength (λ_{fl}) obtained using the B3LYP functional (567 nm) is quite close to the experimental value (557 nm) (Meng et al., 2019), with the deviation of 10 nm. Furthermore, both the ΔE_{ST} values



SCHEME 1 | Molecule models of **1–10** investigated in this work.

of molecule **1** obtained using B3LYP and PBE0 functionals (0.0068 and 0.0107 eV) are close to the experimental value (0.0091 eV). Additionally, comparing the optimized geometries of **1** (for the atom numbering, see **Supplementary Figure 1**) in S_0 states with its crystal structure data [CCDC 1887610], one can find that the main geometrical parameters obtained using the B3LYP/6-31G(d,p) method are in better agreement with crystal structure data than those obtained with other methods (**Supplementary Table 2**). Therefore, geometry optimizations in S_0 , S_1 , and T_1 states, band gaps E_g , ΔE_{ST} , absorption, fluorescence, and phosphorescence spectra of molecules under investigation were performed by the B3LYP/6-31G(d,p) and TD-B3LYP/6-31G(d,p) methods.

The reorganization energy λ is composed of external and internal reorganization energies (λ_{ext} and λ_{int}). We focus only on the λ_{int} because λ_{ext} is quite complicated to predict at this stage. λ_{int} can be expressed as (Köse et al., 2007; Sancho-García, 2007):

$$\lambda = \lambda_1 + \lambda_2 = (E_{\pm}^* - E_{\pm}) + (E^* - E) \quad (1)$$

Here, E_{\pm} and E stand for the energies of the charged and neutral states in the ground states, respectively; E_{\pm}^* corresponds to the energy of the charged state with the optimized neutral molecule structure. E^* represents the energy of neutral molecule with the optimized charged geometry. Furthermore, AIP and AEA were calculated by the adiabatic potential-energy surfaces of neutral/charged species. AIP can be obtained with the energy difference between cation and neutral specie. AEA was determined by the energy difference between neutral and anion specie. The AIP , AEA , and λ for the electron (λ_e) and hole

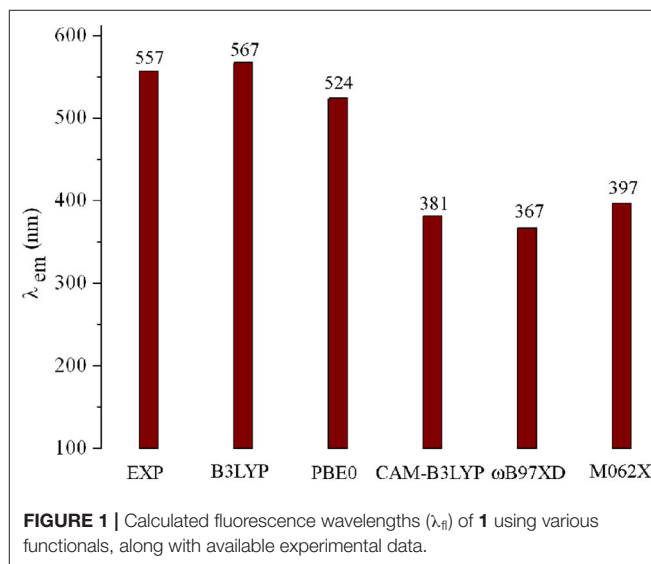


FIGURE 1 | Calculated fluorescence wavelengths (λ_{fl}) of **1** using various functionals, along with available experimental data.

(λ_h) of the designed molecules were predicted at the B3LYP/6-31G(d,p) level.

RESULTS AND DISCUSSION

Molecular Geometries in the Ground and Excited States

The main geometrical parameters of the designed molecules in S_0 , S_1 , and T_1 states are given in **Supplementary Table 3**. The

results displayed in **Supplementary Table 3** reveal that there are no significant changes in the bond lengths of acceptor DOBA fragments for the designed molecules in S_0 states. Compared with the parent molecule **1**, the bond length change mainly appears on the bonds which connect the DOBA acceptor and different donor fragments. Obviously, the lengths of C_5-N_{22} bonds for molecules **2**, **3**, **5–8**, and **10** have been decreased by 0.005, 0.003, 0.02, 0.022, 0.001, and 0.024 Å, while the corresponding values of C_5-N_{22} for **4** and C_5-C_{22} for **9** have lengthened by 0.002 and 0.05 Å with respect to that of molecules **1**, respectively. Similar phenomena are found for $C_{18}-N_{24}$ bonds for **2–8** and **10** and $C_{18}-C_{24}$ bond for **9**. Furthermore, the designed molecules display a large twist angle (β) between their acceptor and donor fragments in the S_0 states owing to their large steric hindrance. The β values of **1–4**, **7**, and **8** are about 81–100°, while the corresponding values of **5**, **6**, **9**, and **10** are about 34–51°, respectively. The large β values facilitate for disrupting the electronic communication between D and A fragments. Comparing the geometrical parameters of the designed molecules in S_1 states with those in the S_0 states, the bond lengths of B_1-C_2 , C_4-C_5 , C_6-C_7 , C_9-C_{10} , $C_{13}-C_{14}$, B_1-C_{15} , $C_{17}-C_{18}$, and $C_{19}-C_{20}$ (0.002–0.025 Å) are shortened, while other bond lengths are enlarged (0.001–0.025 Å), respectively. The more obvious bond length variations are found for the connecting bonds between acceptor and donor fragments for the designed molecules. The C_5-N_{12} and $C_{18}-N_{24}$ bonds for **1–8** and **10** are stretched (0.005–0.038 Å and 0.005–0.038 Å) in the S_1 states as compared to those in the S_0 states, respectively. However, compared with the C_5-C_{12} and $C_{18}-C_{24}$ bonds for **9** in the S_0 state, obviously, they are shortened by 0.036 and 0.003 Å in the S_1 state, respectively. Additionally, it can be seen that the twist angle β is closer to 90° in the S_1 state as compared to those in the S_0 states for the designed molecules except for **9**, whose two β values in the S_1 state are smaller than those in S_0 states, respectively. Apparently, inspection of **Supplementary Table 3** reveals that the geometrical parameters in T_1 states are similar to those in S_1 states for **1–4**, **7**, and **8**. On the contrary, the molecular geometries in T_1 states for **5**, **6**, **9**, and **10** are closer to those in S_0 states, respectively.

Frontier Molecular Orbitals

It is worth noting that the FMO energies (E_{HOMO} and E_{LUMO}) and E_g play dominant roles for the optical and electronic properties. The molecular geometry is affected by electron density redistribution that is caused by an electronic excitation (Forés et al., 1999; Helal et al., 2011). The distributions of HOMO and LUMO in S_0 states for the designed molecules are plotted in **Supplementary Figure 2**. Additionally, we investigated the contributions of A and D fragments to the FMOs and the overlap value (ρ) between D and A fragments on HOMOs and LUMOs, as displayed in **Supplementary Table 4**. An inspection in **Supplementary Figure 2** reveals clearly that the HOMOs of **1–10** are mainly localized on the D fragments, whereas the corresponding LUMOs predominantly reside at the A fragments. The contributions of D fragments for HOMOs in **1–4** and **7–9** are 93.1, 94.4, 95.6, 95.4, 93.1, 92.8, and 99.4%, while the corresponding contributions for **5**, **6**, and **10** are 83.1, 85.8, and 66.5%, respectively. For the LUMOs, the contributions of A

fragments in **1–8** are larger than 90%, while the corresponding contributions for **9** and **10** are 75.9 and 84.5%, respectively. Apparently, the HOMO to LUMO transitions lead the electronic density to flow from D to A fragments. The percentages of charge transfer are in the order of **4** (89.3%) > **3** (88.9%) > **2** (87.5%) > **7** (86.4%) > **8** (85.9%) > **1** (85.7%) > **6** (76.9%) > **9** (75.3%) > **5** (74.8%) > **10** (51%). Moreover, the overlap (ρ) between D and A fragments on HOMOs is in the range of 0.001–0.040, while the corresponding ρ values for LUMOs are 0.013–0.026, for the designed molecules except for **10**, whose ρ values on its HOMO and LUMO are 0.082 and 0.037, respectively. It indicates that the HOMO to LUMO transitions exhibit a strong charge transfer nature and slight electron exchange energy, resulting in small ΔE_{ST} values.

The qualitative HOMOs and LUMOs in S_1 states for **1–10** are shown in **Figure 2**. The calculated E_{HOMO} , E_{LUMO} , and E_g , the overlap (ρ) between D and A fragments, and the contributions of A and D fragments (in %) to the FMOs of **1–10** are summarized in **Table 1**. Comparing the HOMOs and LUMOs in S_1 states with those in S_0 states, we find that the electron density plots of both HOMOs and LUMOs in S_1 states are similar to those in S_0 states for all the investigated molecules, respectively. The HOMOs are mainly centralized on the D fragments, whereas the corresponding LUMOs predominantly distributed on the A fragments. The contributions of D fragments for HOMOs are about 91.2–99.9%. The contributions of A fragments for the LUMOs are about 90.5–93.8% except that the contribution of A fragment for **9** is 68.7%. The percentages of charge transfer from D to A fragments are in the order of **3** (89.5%) > **4** (89.1%) > **2** (88.6%) > **6** (88.1%) > **5** (87.8%) > **7** (87.3%) > **8** (86.6%) > **1** (86.3%) > **10** (81.7%) > **9** (68.6%). Clearly, the charge transfer character in S_1 states is more significant than that in S_0 states. Furthermore, the ρ values for HOMOs are in the range of 0.001–0.019, while the corresponding ρ values for LUMOs are about 0.014–0.037. It suggests that the HOMOs and LUMOs are also separated efficiently in the S_1 state. This implies the efficient separation between D and A fragments, which display the potential TADF features. The sequence of E_{HOMO} and E_{LUMO} is **3** > **4** > **2** > **1** > **8** > **10** > **7** > **6** > **5** > **9** and **10** > **3** > **6** > **1** > **7** > **8** > **5** > **2** > **4** > **9**, respectively. Thus, the E_g values are in the order of **5** > **10** > **9** > **6** > **7** > **8** > **1** > **2** > **4** > **3**. It suggests that the E_g values of **2–4** decrease, while the corresponding value of **5–10** increases compared with that of **1**. Therefore, one can conclude that **2–4** may possess a red shift, whereas **5–10** could exhibit a blue shift in their emission spectra in comparison with the parent molecule **1**. It implies that the introduction of different aromatic heterocyclic donors can tune effectively the E_{HOMO} , E_{LUMO} , and E_g values for the designed molecules. Furthermore, we investigated the qualitative HOMO and LUMO plots in T_1 states for **1–10** (**Supplementary Figure 3**). One can find that the qualitative HOMOs and LUMOs in T_1 states are similar to those in S_1 states for all the investigated molecules. It is also favorable for the RISC process from T_1 to S_1 states.

Singlet-Triplet Energy Gap

Table 2 collected the vertical excitation energy (E_{S1} and E_{T1}) in S_1 and T_1 states and ΔE_{ST} of **1–10** at the TD-B3LYP/6-31G (d,p)

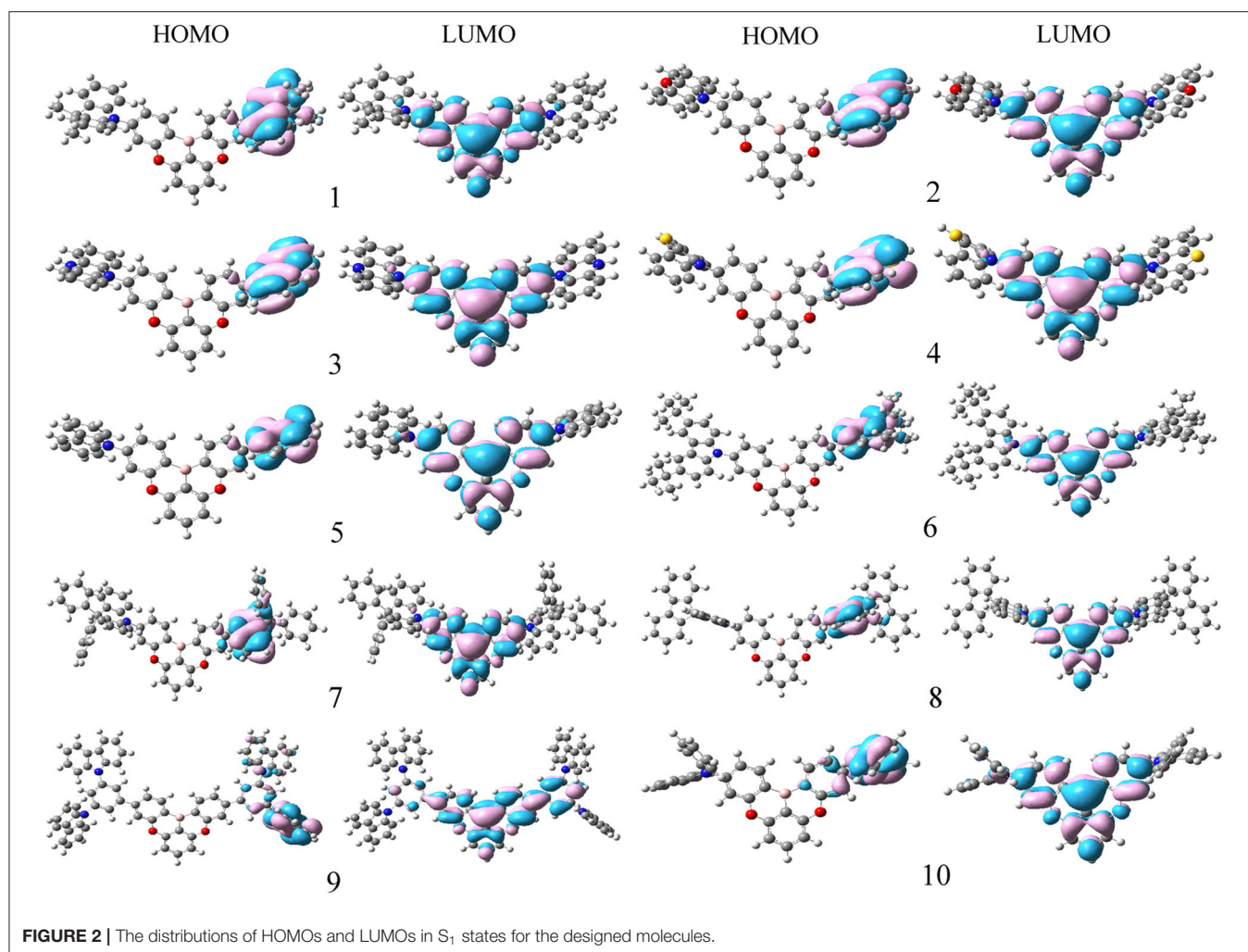


FIGURE 2 | The distributions of HOMOs and LUMOs in S_1 states for the designed molecules.

TABLE 1 | The FMO energies E_{HOMO} and E_{LUMO} , HOMO–LUMO gaps E_g (all in eV), HOMO and LUMO contributions (%), and the overlap between D and A fragments on HOMOs and LUMOs (ρ) of **1–10** in S_1 states.

Species	HOMO				LUMO				E_g
	E_{HOMO}	A	D	ρ	E_{LUMO}	A	D	ρ	
1	−4.829	6.5	93.5	0.009	−2.146	92.8	7.2	0.017	2.683
2	−4.521	4.9	95.1	0.011	−2.269	93.5	6.5	0.014	2.253
3	−3.974	3.9	96.1	0.008	−2.115	93.4	6.6	0.015	1.858
4	−4.494	4.0	96.0	0.007	−2.275	93.1	6.9	0.016	2.219
5	−5.321	6.0	94.0	0.013	−2.196	93.8	6.2	0.014	3.125
6	−5.080	5.5	94.5	0.011	−2.129	93.6	6.4	0.014	2.952
7	−4.946	5.9	94.1	0.011	−2.159	93.2	6.8	0.016	2.787
8	−4.912	6.5	93.5	0.010	−2.195	93.1	6.9	0.018	2.717
9	−5.369	0.1	99.9	0.001	−2.394	68.7	31.3	0.037	2.976
10	−4.914	8.8	91.2	0.019	−1.918	90.5	9.5	0.021	2.996

A, electron acceptors fragments; D, electron donors fragments.

TABLE 2 | The vertical excitation energy (E_{S1} and E_{T1}) and singlet triplet energy gap (ΔE_{ST}) of **1–10** at the TD-B3LYP/6-31G(d,p) level (in eV).

Species	E_{S1}	E_{T1}	ΔE_{ST}
1	2.186	2.180	0.0068
2	1.773	1.768	0.0065
3	1.707	1.702	0.0057
4	1.763	1.758	0.0062
5	2.643	2.645	0.1257
6	2.480	2.552	0.0618
7	2.290	2.285	0.0078
8	2.222	2.216	0.0069
9	2.556	2.556	0.2600
10	2.510	2.452	0.2659
Exp			0.0091

Exp, experimental results of **1** were taken from Meng et al. (2019).

level. It is noticeable that the lower the ΔE_{ST} values, the easier the RISC process from the T_1 to S_1 states. The E_{S1} and E_{T1} values

are in the orders **5** > **9** > **10** > **6** > **7** > **8** > **1** > **2** > **4** > **3** and **5** > **9** > **6** > **10** > **7** > **8** > **1** > **2** > **4** > **3**, respectively. As expected, the order of E_{S1} values is similar to those E_g values

except that a sequential interchange is found between **9** and **10**. Moreover, the sequence of E_{T1} values is similar to E_{S1} values except that a sequential interchange is found between **6** and **10**. One can find that all the designed molecules possess small ΔE_{ST} values. The prediction of ΔE_{ST} values is in the sequence **10** (0.2659) > **9** (0.2600) > **5** (0.1257) > **6** (0.0618) > **7** (0.0078) > **8** (0.0069) > **1** (0.0068) > **2** (0.0065) > **4** (0.0062) > **3** (0.0057). The results displayed in **Table 2** reveal that the ΔE_{ST} values of **2–4**, **7**, and **8** (0.0057–0.0078 eV) are similar to that for the parent molecule **1** (0.0068 eV). On the contrary, molecules **5**, **6**, **9**, and **10** have larger ΔE_{ST} values than the parent molecule **1**, especially for molecules **9** and **10**, whose ΔE_{ST} values are 0.2600 and 0.2659 eV, respectively. The reason might be that **2–4**, **7**, and **8** own the more effective separation between their donor/acceptor compositions (%) of the FMOs in the S_1 state than those larger than 90% (**Table 1** and **Figure 2**). Additionally, β is closer to 90° in the S_1 state as compared to those of **5**, **6**, **9**, and **10**. For molecules **5** and **6**, among their two β , β values are both close to 90°, while another β values are –60.6 and 59.1°, respectively. However, molecule **6** has two electron donor tert-butyl groups in donor fragments, which is more favorable for charge transfer and in turn decreases the ΔE_{ST} value. As a consequence, the ΔE_{ST} value of **6** is smaller than that of **5**. For molecules **9** and **10**, their smaller two β values may decrease the effective separation between their donor and acceptor fragments. Two β values are –12.7 and 32.4° for **9** and –51.7 and 77.2° for **10** in S_1 states. It indicates that the introduction of 10H-phenoxazine (**2**), 5,10-dihydrophenazine (**3**), 10H-phenothiazine (**4**), 9,9-diphenyl-9,10-dihydroacridine (**7**), and 9H-spiro[4.5]fluorene-9,10-dihydroacridine (**8**) donor fragments does not significantly affect the ΔE_{ST} values compared with the parent molecule with 9,9-dimethyl-9,10-dihydroacridine donor fragments (**1**). On the contrary, the introduction of 9H-carbazole (**5**), 3,6-di-tert-butyl-9H-carbazole (**6**), 9-(3-(9H-carbazol-9-yl)phenyl)-9H-carbazole (**9**), diphenylamine (**10**), and donor fragments increase the ΔE_{ST} values compared with parent molecule **1**. As a consequence, the RISC rate constant (k_{RISC}) of **1–4**, **7**, and **8** should be higher than those of molecules **5**, **6**, **9**, and **10** because a small ΔE_{ST} value is beneficial for the high k_{RISC} value.

Photophysical Properties

The calculated wavelength of delayed fluorescence emission (λ_{TADF}), phosphorescence emission (λ_{ph}), absorption (λ_{abs}), and Stokes shift of **1–10** are listed in **Table 3**. As visualized in **Figure 2** and **Supplementary Figures 2, 3**, the FMO distributions in S_0 , S_1 , and T_1 states possess π characteristics. The results presented in **Table 3** show that the λ_{abs} values of **2–10** have slight bathochromic shifts compared with that of the parent compound **1**, respectively. The λ_{TADF} values of **1–10** follow the tendency **3** > **4** > **2** > **1** > **8** > **7** > **6** > **10** > **9** > **5**, which is similar to the reverse order of E_g values. By comparing with parent molecule **1**, the λ_{TADF} values of **2–4** exhibit bathochromic shifts, 132.2, 159.5, and 136.9 nm, respectively, due to the increased electron-donating ability of the donor fragments. Conversely, it can be noted that the λ_{TADF} values of **5–10** have hypsochromic shifts, 97.9, 67.2, 25.7, 9.1, 82, and 73.1 nm compared with that of **1**, respectively. Obviously, **2–4** possess more significant Stokes shifts

TABLE 3 | The delayed fluorescence emission wavelength (λ_{TADF}) and phosphorescence emission wavelength (λ_{ph}), corresponding to the absorption wavelength (λ_{abs}), and Stokes shift of **1–10** at the TD-B3LYP/6-31G (d,p) level.

Species	λ_{abs}	λ_{TADF}	λ_{ph}	Stokes shift
1	370.4	567.1	568.6	196.7
2	372.7	699.3	701.4	326.6
3	406.6	726.6	728.7	320.0
4	372.6	703.1	705.2	330.5
5	409.2	469.2	468.7	60.0
6	424.9	499.9	485.8	75.0
7	371.6	541.4	542.7	169.8
8	374.9	558.0	559.5	183.1
9	417.0	485.1	485.2	68.1
10	401.7	494.0	505.7	92.2
Exp	386	557	533	171

Exp, experimental results of **1** were taken from Meng et al. (2019).

(326.6, 320.0, and 330.5 nm) and red emission with small ΔE_{ST} values (0.0065, 0.0057, and 0.0062 eV). Nevertheless, **1**, **7**, and **8** exhibit green emissions with Stokes shifts, 196.7, 169.8, and 183.1 nm, respectively. In addition, **6** and **10** show light green emissions, while **5** and **9** display blue emissions with small Stokes shifts. The Stokes shifts of **5**, **6**, **9**, and **10** are 60.0, 75.0, 68.1, and 92.2 nm, respectively. Accordingly, the delayed fluorescence emission color can be tuned effectively by introduction of different polycyclic aromatic fragments as electron donors in the parent molecule. This implies that the designed molecules are expected to be the promising candidates for TADF materials, particularly for **2–4**, **7**, and **8**. Furthermore, the λ_{ph} values are similar to the λ_{TADF} values. The small difference between the λ_{TADF} and λ_{ph} values should facilitate for achieving the TADF phenomenon.

Charge Transport Properties

It is quite clear that the charge injection and charge transfer play dominant roles in the device performance of OLEDs. λ can be used to estimate the charge transfer rate. The AIP and AEA are used to evaluate the energy barrier for the injection of holes and electrons. Generally, the low λ value corresponds to the big charge transfer rate (Marcus, 1964, 1993). The smaller the AIP value and the larger the AEA value, the easier the injection of holes and electrons, respectively. The calculated λ_e , λ_h , AIP, and AEA of **1–10** are listed in **Table 4**. As presented in **Table 4**, we find that **3** and **5** have the smallest and largest AIP values (5.151 and 6.387 eV), respectively. The AIP values of **1–10** are observed in the following: **5** > **9** > **6** > **7** > **10** > **8** > **1** > **4** > **2** > **3**, suggesting that the hole injection and transportations of **2–4** are expected to be easier than the others with respect to parent molecule **1**. On the other hand, the AEA values of **3**, **5**, **6**, and **10** are lower, while the corresponding values of **2**, **4**, and **7–9** are higher than that of **1** (0.878 eV). The order of the AEA of **1–10** is as follows: **9** > **4** > **2** > **8** > **7** > **1** > **5** > **3** > **6** > **10**; this implies that the abilities to accept electrons in **2**, **4**, and **7–9** are improved with respect to parent molecule **1**.

TABLE 4 | Calculated molecular λ_e , λ_h , AIP , and AEA (all in eV) of **1–10** at the B3LYP/6-31G(d,p) level.

Species	λ_h	λ_e	AIP	AEA
1	0.204	0.135	5.858	0.878
2	0.115	0.144	5.681	0.991
3	0.215	0.136	5.151	0.831
4	0.390	0.140	5.832	1.000
5	0.051	0.183	6.387	0.868
6	0.061	0.192	6.086	0.822
7	0.120	0.151	5.968	0.906
8	0.067	0.134	5.877	0.968
9	0.033	0.249	6.196	1.235
10	0.072	0.383	5.947	0.546

So, we can deduce that the introduction of 10H-phenoxazine (**2**) and 10H-phenothiazine (**4**) donor fragments will enhance both the hole and electron injection abilities, whereas the introduction of 9,9-diphenyl-9,10-dihydroacridine (**7**), 9H-spiro[4,5]fluorene-9,10-dihydroacridine (**8**), and 9-(3-(9H-carbazol-9-yl)phenyl)-9H-carbazole (**9**) donor fragments can improve the electron injection ability only compared with that of parent molecule **1**.

For charge transport materials in OLEDs, generally, TPD ($\lambda_h = 0.290$ eV) and Alq3 ($\lambda_e = 0.276$ eV) are used as typical hole and electron transport materials, respectively (Gruhn et al., 2002; Lin et al., 2005). According to **Table 4**, the calculated λ_h values of **1–3** and **5–10** are smaller than those of TPD. It suggests that the hole transfer rates of the designed molecules except for **4** may be higher than that of TPD. The λ_h values are in the order **4** > **3** > **1** > **2** > **7** > **10** > **8** > **6** > **5** > **9**. On the other hand, the λ_e values of **1–9** are smaller than that of Alq3. It implies that the electron transfer rates of **1–9** may be higher than that of Alq3, suggesting that their electron transfer rates might be lower than that of Alq3. The order of the predicted λ_e is as follows: **10** > **9** > **6** > **5** > **7** > **2** > **3** > **6** > **1** > **8**. Remarkably, the difference between λ_h and λ_e for **1–3**, **5–9** (0.029–0.216 eV) is small enough, suggesting that they are potential ambipolar charge transport materials. Nevertheless, **4** and **10** can serve as electron and hole transport materials only, respectively.

CONCLUSION

In summary, a series of novel D–A tricoordinated organoboron derivatives have been systematically investigated for TADF-based

OLED materials. The calculated results show that the designed molecules exhibit small ΔE_{ST} values, suggesting that they can be used as excellent TADF candidates. DFT analysis indicated that the designed molecules display efficient separation between donor and acceptor fragments because of the small overlap between donor and acceptor fragments (ρ) on HOMOs and LUMOs. Furthermore, the delayed fluorescence emission color can be tuned effectively by introduction of different polycyclic aromatic fragments in the parent molecule. Molecules **2**, **3**, and **4** possess more significant Stokes shifts (326.6, 320.0, and 330.5 nm) and red emission with small ΔE_{ST} values (0.0065, 0.0057, and 0.0062 eV). Nevertheless, other molecules exhibit green (**1**, **7**, and **8**), light green (**6** and **10**), and blue (**5** and **9**) emissions. Meanwhile, they are potential good ambipolar charge transport materials except that **4** and **10** can serve as electron and hole transport materials only, respectively. Therefore, we proposed a rational way for the design of efficient TADF materials as well as charge transport materials for OLEDs simultaneously.

DATA AVAILABILITY STATEMENT

The original contributions presented in the study are included in the article/**Supplementary Material**, further inquiries can be directed to the corresponding author/s.

AUTHOR CONTRIBUTIONS

RJ conceived and designed the research, and headed, wrote, and revised the manuscript. JX contributed to the performance and analysis of the frontier molecular orbitals, absorption fluorescence, and phosphorescence spectra, and the reorganization energies. Both authors contributed to the manuscript revision and read and approved the submitted version.

FUNDING

This work was supported by NSFC (No. 21563002) and Natural Science Foundation of Inner Mongolia Autonomous Region (No. 2015MS0201).

SUPPLEMENTARY MATERIAL

The Supplementary Material for this article can be found online at: <https://www.frontiersin.org/articles/10.3389/fchem.2020.577834/full#supplementary-material>

REFERENCES

- Adachi, C., Baldo, M. A., Thompson, M. E., and Forrest, S. R. (2001). Nearly 100% internal phosphorescence efficiency in an organic light-emitting device. *J. Appl. Phys.* 90, 5048–5051. doi: 10.1063/1.1409582
- Adamo, C., and Barone, V. (1999). Toward reliable density functional methods without adjustable parameters: the PBE0 model. *J. Chem. Phys.* 110, 6158–6170. doi: 10.1063/1.478522
- Baldo, M. A., O'Brien, D. F., You, Y., Shoustikov, A., Sibley, S., Thompson, M. E., et al. (1998). Highly efficient phosphorescent emission from organic electroluminescent devices. *Nature* 395, 151–154. doi: 10.1038/25954
- Becke, A. D. (1993). Density functional thermochemistry. III. The role of exact exchange. *J. Chem. Phys.* 98, 5648–5652. doi: 10.1063/1.464913
- Bezvikonnyi, O., Gudeika, D., Volyniuk, D., Mimaite, V., Sebastine, B. R., and Grazulevicius, J. V. (2019). Effect of donor substituents on thermally activated delayed fluorescence of diphenylsulfone derivatives. *J. Lumin.* 206, 250–259. doi: 10.1016/j.jlumin.2018.10.018

- Burroughes, J. H., Bradley, D. D. C., Brown, A. R., Marks, R. N., MacKay, K., Friend, R. H., et al. (1990). Light-emitting diodes based on conjugated polymers. *Nature* 347, 539–541. doi: 10.1038/348352a0
- Chai, J. D., and Head-Gordon, M. (2008). Long-range corrected hybrid density functionals with damped atom-atom dispersion corrections. *Phys. Chem. Chem. Phys.* 10, 6615–6620. doi: 10.1039/B810189B
- Chatterjee, T., and Wong, K.-T. (2019). Perspective on host materials for thermally activated delayed fluorescence organic light emitting diodes. *Adv. Opt. Mater.* 7:1800565. doi: 10.1002/adom.201800565
- Choy, W. C. H., Chan, W. K., and Yuan, Y. (2014). Recent advances in transition metal complexes and light-management engineering in organic optoelectronic devices. *Adv. Mater.* 26, 5368–5399. doi: 10.1002/adma.201306133
- Deng, Z., Ai, T., Li, R., Yuan, W., Zhang, K., Du, H., et al. (2019). Conjugated polymers containing building blocks 1,3,4,6-tetraarylpyrrolo[3,2-b]pyrrole-2,5-dione (isoDPP), benzodipyrrolidone (BDP) or naphthodipyrrolidone (NDP): a review. *Polymers* 11:1683. doi: 10.3390/polym11101683
- Evans, E. W., Olivier, Y., Puttisong, Y., Myers, W. K., Hele, T. J. H., Menke, S. M., et al. (2018). Vibrationally assisted intersystem crossing in benchmark thermally activated delayed fluorescence molecules. *J. Phys. Chem. Lett.* 9, 4053–4058. doi: 10.1021/acs.jpclett.8b01556
- Forés, M., Duran, M., Solà, M., and Adamowicz, L. (1999). Excited-state intramolecular proton transfer and rotamerism of 2-(2'-hydroxyvinyl)benzimidazole and 2-(2'-hydroxyphenyl)imidazole. *J. Phys. Chem. A* 103, 4413–4420. doi: 10.1021/jp9844765
- Frisch, M. J., Trucks, G. W., Schlegel, H. B., Scuseria, G. E., Robb, M. A., Cheeseman, J. R., et al. (2009). *Gaussian 09*. Wallingford, CT: Gaussian, Inc.
- Geng, Y., D'Aleo, A., Inada, K., Cui, L. S., Kim, J. U., Nakanotani, H., and Adachi, C. (2017). Donor- σ -acceptor motifs: thermally activated delayed fluorescence emitters with dual upconversion. *Angew. Chem. Int. Ed.* 56, 16536–16540. doi: 10.1002/anie.201708876
- Giustra, Z. X., and Liu, S. Y. (2018). The state of the art in azaborine chemistry: new synthetic methods and applications. *J. Am. Chem. Soc.* 140, 1184–1194. doi: 10.1021/jacs.7b09446
- Gruhn, N. E., da Silva Filho, D. A., Bill, T. G., Malagoli, M., Coropceanu, V., Kahn, A., et al. (2002). The vibrational reorganization energy in pentacene: molecular influences on charge transport. *J. Am. Chem. Soc.* 124, 7918–7919. doi: 10.1021/ja0175892
- Helal, A., Rashid, M. H. O., Choi, C. H., and Kim, H. S. (2011). Chromogenic and fluorogenic sensing of Cu^{2+} based on coumarin. *Tetrahedron* 67, 2794–2802. doi: 10.1016/j.tet.2011.01.093
- Hosokai, T., Nakanotani, H., Santou, S., Noda, H., Nakayama, Y., and Adachi, C. (2019). TADF activation by solvent freezing: the role of nonradiative triplet decay and spin-orbit coupling in carbazole benzonitrile derivatives. *Synthet. Met.* 252, 62–68. doi: 10.1016/j.synthmet.2019.04.005
- Hussain, A., Yuan, H., Li, W., and Zhang, J. (2019). Theoretical investigations of the realization of sky-blue to blue TADF materials via CH/N and H/CN substitution at the diphenylsulphone acceptor. *J. Mater. Chem. C* 7, 6685–6691. doi: 10.1039/C9TC01449G
- Im, Y., Byun, S. Y., Kim, J. H., Lee, D. R., Oh, C. S., Yook, K. S., et al. (2017a). Recent progress in high-efficiency blue-light-emitting materials for organic light-emitting diodes. *Adv. Funct. Mater.* 27:1603007. doi: 10.1002/adfm.201603007
- Im, Y., Kim, M., Cho, Y. J., Seo, J.-A., Yook, K. S., and Lee, J. Y. (2017b). Molecular design strategy of organic thermally activated delayed fluorescence emitters. *Chem. Mater.* 29, 1946–1963. doi: 10.1021/acs.chemmater.6b05324
- Ji, L., Griesbeck, S., and Marder, T. B. (2017). Recent developments in and perspectives on three-coordinate boron materials: a bright future. *Chem. Sci.* 8, 846–863. doi: 10.1039/C6SC04245G
- Jin, J., Ying Gao, Y., and Geng, Y. (2019). A theoretical investigation on the thermally activated delayed fluorescence characteristics of the isomers of DTCB Py. *J. Mol. Graph. Model.* 86, 125–131. doi: 10.1016/j.jmgm.2018.10.002
- Joo, C. W., Huseynova, G., Yifei, J., Yoo, J. M., and Kim, Y. H., Cho, N. S., et al. (2019). Highly efficient solution-processed blue organic light-emitting diodes based on thermally activated delayed fluorescence emitters with spiroacridine donor. *J. Ind. Eng. Chem.* 78, 265–270. doi: 10.1016/j.jiec.2019.06.003
- Kim, J. H., Lee, K. H., and Lee, J. Y. (2019). Design of thermally activated delayed fluorescent assistant dopants to suppress the nonradiative component in red fluorescent organic light-emitting diodes. *Chem. Eur. J.* 25, 9060–9070. doi: 10.1002/chem.201901135
- Köse, M. E., Mitchell, W. J., Kopidakis, N., Chang, C. H., Shaheen, S. E., Kim, K., et al. (2007). Theoretical studies on conjugated phenyl-cored thiophene dendrimers for photovoltaic applications. *J. Am. Chem. Soc.* 129, 14257–14270. doi: 10.1021/ja073455y
- Li, C., Duan, C., Han, C., and Xu, H. (2018a). Secondary acceptor optimization for full-exciton radiation: toward sky-blue thermally activated delayed fluorescence diodes with external quantum efficiency of $\approx 30\%$. *Adv. Mater.* 30:1804228. doi: 10.1002/adma.201804228
- Li, C., Wang, Y., Sun, D., Li, H., Sun, X., Ma, D., et al. (2018b). Thermally activated delayed fluorescence pendant copolymers with electron- and hole-transporting spacers. *ACS Appl. Mater. Interfaces* 10, 5731–5739. doi: 10.1021/acsami.8b00136
- Li, J., Nakagawa, T., MacDonald, J., Zhang, Q., Nomura, H., Miyazaki, H., et al. (2013). Highly efficient organic light-emitting diode based on a hidden thermally activated delayed fluorescence channel in a heptazine derivative. *Adv. Mater.* 25, 3319–3323. doi: 10.1002/adma.201300575
- Li, Y., Xie, G., Gong, S., Wu, K., and Yang, C. (2016). Dendronized delayed fluorescence emitters for non-doped, solution-processed organic light-emitting diodes with high efficiency and low efficiency roll-off simultaneously: two parallel emissive channels. *Chem. Sci.* 7, 5441–5447. doi: 10.1039/C6SC00943C
- Liang, X., Yan, Z. P., Han, H. B., Wu, Z. G., Zheng, Y. X., Meng, H., et al. (2018). Peripheral amplification of multi-resonance induced thermally activated delayed fluorescence for highly efficient OLEDs. *Angew. Chem. Int. Ed.* 57, 11316–11320. doi: 10.1002/anie.201806323
- Lin, B. C., Cheng, C. P., You, Z. Q., and Hsu, C. P. (2005). Charge transport properties of tris(8-hydroxyquinolino)aluminum(III): why it is an electron transporter. *J. Am. Chem. Soc.* 127, 66–67. doi: 10.1021/ja045087t
- Liu, B., Dang, F., Feng, Z., Tian, Z., Zhao, J., Wu, Y., et al. (2017a). Novel Iridium(III) complexes bearing dimesitylboron groups with nearly 100% phosphorescent quantum yields for highly efficient organic light-emitting diodes. *J. Mater. Chem. C* 5, 7871–7883. doi: 10.1039/C7TC02369C
- Liu, B., Dang, F., Tian, Z., Feng, Z., Jin, D., Dang, W., et al. (2017b). High triplet energy level achieved by tuning the arrangement of building blocks in phosphorescent polymer backbones for furnishing high electroluminescent performances in both blue and white organic light-emitting devices. *ACS Appl. Mater. Interfaces* 9, 16360–16374. doi: 10.1021/acsami.7b04509
- Liu, Y., Li, C., Ren, Z., Yan, S., and Bryce, M. R. (2018). All-organic thermally activated delayed fluorescence materials for organic light-emitting diodes. *Nat. Rev. Mater.* 3:18020. doi: 10.1038/natrevmats.2018.20
- Lu, J., Zheng, Y., and Zhang, J. (2015a). Rational design of phenoxazine-based donor-acceptor-donor thermally activated delayed fluorescent molecules with high performance. *Phys. Chem. Chem. Phys.* 17, 20014–20020. doi: 10.1039/c5cp02810h
- Lu, J., Zheng, Y., and Zhang, J. (2015b). Tuning the color of thermally activated delayed fluorescent properties for spiro-acridine derivatives by structural modification of the acceptor fragment: a DFT study. *RSC Adv.* 5, 18588–18592. doi: 10.1039/c4ra15155k
- Marcus, R. A. (1964). Chemical and electrochemical electron-transfer theory. *Annu. Rev. Phys. Chem.* 15, 155–196.
- Marcus, R. A. (1993). Electron transfer reactions in chemistry: theory and experiment. *Rev. Mod. Phys.* 65, 599–610.
- Meng, G., Chen, X., Wang, X., Wang, N., Peng, T., and Wang, S. (2019). Isomeric bright sky-blue TADF emitters based on bisacridine decorated DBNA: impact of donor locations on luminescent and electroluminescent properties. *Adv. Optical. Mater.* 7:1900130. doi: 10.1002/adom.201900130
- Nobuyasu, R. S., Ren, Z., Griffiths, G. C., Batsanov, A. S., Data, P., Yan, S., et al. (2016). Rational design of TADF polymers using a donor-acceptor monomer with enhanced TADF efficiency induced by the energy alignment of charge transfer and local triplet excited states. *Adv. Opt. Mater.* 4, 597–607. doi: 10.1002/adom.201500689
- Pal, A. K., Krotkus, S., Fontani, M., Mackenzie, C. F. R., Cordes, D. B., Slawin, A. M. Z., et al. (2018). High-efficiency deep-blue-emitting organic light-emitting diodes based on Iridium(III) carbene complexes. *Adv. Mater.* 30:1804231. doi: 10.1002/adma.201804231
- Sancho-García, J. C. (2007). Assessment of density-functional models for organic molecular semiconductors: the role of hartree-fock exchange in charge-transfer processes. *Chem. Phys.* 331, 321–331. doi: 10.1016/j.chemphys.2006.11.002

- Santos, P. L., Ward, J. S., Data, P., Batsanov, A. S., Bryce, M. R., Dias, F. B., and Monkman, A. P. (2016). Engineering the singlet-triplet energy splitting in a TADF molecule. *J. Mater. Chem. C* 4, 3815–3824. doi: 10.1039/c5tc03849a
- Sharma, N., Spuling, E., Mattern, C. M., Li, W., and Fuhr, O., Tsuchiya, Y., et al. (2019). Turn on of sky-blue thermally activated delayed fluorescence and circularly polarized luminescence (CPL) via increased torsion by a bulky carbazophane donor. *Chem. Sci.* 10, 6689–6696. doi: 10.1039/c9sc01821b
- Sommer, G. A., Mataranga-Popa, L. N., Czerwieniec, R., Hofbeck, T., Homeier, H. H., Müller, T. J. J., et al. (2018). Design of conformationally distorted donor-acceptor dyads showing efficient thermally activated delayed fluorescence. *J. Phys. Chem. Lett.* 9, 3692–3697. doi: 10.1021/acs.jpclett.8b01511
- Tang, C. W., and Vanslyke, S. A. (1987). Organic electroluminescent diodes. *Appl. Phys. Lett.* 51, 913–915. doi: 10.1063/1.98799
- Tsujimoto, H., Ha, D. G., Markopoulos, G., Chae, H. S., Baldo, M. A., and Swager, T. M. (2017). Thermally activated delayed fluorescence and aggregation induced emission with through-space charge transfer. *J. Am. Chem. Soc.* 139, 4894–4900. doi: 10.1021/jacs.7b00873
- Uoyama, H., Goushi, K., Shizu, K., Nomura, H., and Adachi, C. (2012). Highly efficient organic light-emitting diodes from delayed fluorescence. *Nature* 492:234. doi: 10.1038/nature11687
- Wang, J., Lu, J., and Zhang, J. (2017). Tuning the electronic and optical properties of diphenylsulphone based thermally activated delayed fluorescent materials via structural modification: a theoretical study. *Dyes. Pigments* 143, 42–47. doi: 10.1016/j.dyepig.2017.03.064
- Wang, Q., Zhang, Y. X., Yuan, Y., Hu, Y., Tian, Q. S., Jiang, Z. Q., and Liao, L. S. (2019). Alleviating efficiency roll-off of hybrid single-emitting layer WOLED utilizing bipolar TADF material as host and emitter. *ACS Appl. Mater. Interfaces* 11, 2197–2204. doi: 10.1021/acsami.9b18665
- Wang, S., Zhao, L., Zhang, B., Ding, J., Xie, Z., Wang, L., and Wong, W. Y. (2018). High-energy-level blue phosphor for solution-processed white organic light-emitting diodes with efficiency comparable to fluorescent tubes. *Science* 6, 128–137. doi: 10.1016/j.isci.2018.07.016
- Wu, K., Wang, Z., Zhan, L., Zhong, C., Gong, S., Xie, G., et al. (2018). Realizing highly efficient solution-processed homojunction-like sky-blue OLEDs by using thermally activated delayed fluorescent emitters featuring an aggregation-induced emission property. *J. Phys. Chem. Lett.* 9, 1547–1553. doi: 10.1021/acs.jpclett.8b00344
- Wu, S. F., Li, S. H., Wang, Y. K., Huang, C. C., Sun, Q., Liang, J. J., et al. (2017). White organic LED with a luminous efficacy exceeding 100 lm w⁻¹ without light out-coupling enhancement techniques. *Adv. Funct. Mater.* 27:1701314. doi: 10.1002/adfm.201701314
- Xia, D., Wang, B., Chen, B., Wang, S., Zhang, B., Ding, J., et al. (2014). Self-host blue-emitting iridium dendrimer with carbazodendrons: nondoped phosphorescent organic light-emitting diodes. *Angew. Chem. Int. Ed.* 53, 1048–1052. doi: 10.1002/ange.201307311
- Yanai, T., Tew, D. P., and Handy, N. C. (2004). A new hybrid exchange–correlation functional using the coulomb-attenuating method (CAM-B3LYP). *Chem. Phys. Lett.* 393, 51–57. doi: 10.1016/j.cplett.2004.06.011
- Yang, Z., Mao, Z., Xie, Z., Zhang, Y., Liu, S., Zhao, J., et al. (2017). Recent advances in organic thermally activated delayed fluorescence materials. *Chem. Soc. Rev.* 46, 915–1016. doi: 10.1039/c6cs00368k
- Yu, L., Wu, Z., Xie, G., Zeng, W., Ma, D., and Yang, C. (2018). Molecular design to regulate the photophysical properties of multifunctional TADF emitters towards high-performance TADF-based OLEDs with EQEs up to 22.4% and small efficiency roll-offs. *Chem. Sci.* 9, 1385–1391. doi: 10.1039/C7SC04669C
- Zhang, H., Li, R., Deng, Z., Cui, S., Wang, Y., Zheng, M., et al. (2020). π -Conjugated oligomers based on aminobenzodifuranone and diketopyrrolopyrrole. *Dyes. Pigments* 181:108552. doi: 10.1016/j.dyepig.2020.108552
- Zhang, S., Yao, L., Peng, Q., Li, W., Pan, Y., Xiao, R., et al. (2015). Achieving a significantly increased efficiency in nondoped pure blue fluorescent OLED: a quasi-equivalent hybridized excited state. *Adv. Funct. Mater.* 25, 1755–1762. doi: 10.1002/adfm.201404260
- Zhao, Y., and Truhlar, D. G. (2008). The M06 suite of density functionals for main group thermochemistry, thermochemical kinetics, noncovalent interactions, excited states, and transition elements: two new functionals and systematic testing of four M06-class functionals and 12 other functionals. *Theor. Chem. Acc.* 120, 215–241. doi: 10.1007/s00214-007-0401-8
- Zhong, D., Yu, Y., Song, D., Yang, X., Zhang, Y., Chen, X. et al. (2019). Organic emitters with a rigid 9-phenyl-9-phosphafluorene oxide moiety as the acceptor and their thermally activated delayed fluorescence behavior. *ACS Appl. Mater. Interfaces* 11, 27112–27124. doi: 10.1021/acsami.9b05950
- Zhu, X. D., Tian, Q. S., Zheng, Q., Tao, X. C., Yuan, Y., Yu, Y. J., et al. (2019). A sky-blue thermally activated delayed fluorescence emitter based on multimodified carbazole donor for efficient organic light-emitting diodes. *Org. Electron.* 68, 113–120. doi: 10.1016/j.orgel.2019.02.001
- Zhu, Z. L., Ni, S. F., Chen, W. C., Chen, M., Zhu, J. J., Yuan, Y., et al. (2018). Tuning electrical properties of phenanthroimidazole derivatives to construct multifunctional deep-blue electroluminescent materials. *J. Mater. Chem. C* 6, 3584–3592. doi: 10.1039/C7TC04972B

Conflict of Interest: The authors declare that the research was conducted in the absence of any commercial or financial relationships that could be construed as a potential conflict of interest.

Copyright © 2020 Jin and Xin. This is an open-access article distributed under the terms of the Creative Commons Attribution License (CC BY). The use, distribution or reproduction in other forums is permitted, provided the original author(s) and the copyright owner(s) are credited and that the original publication in this journal is cited, in accordance with accepted academic practice. No use, distribution or reproduction is permitted which does not comply with these terms.



Metal-Ligand Coordination Induced Ionochromism for π -Conjugated Materials

Jinhui Liu, Long Han, Jieting Geng, Jing Hua* and Zhaobo Wang*

Key Laboratory of Rubber-Plastics Ministry of Education/Shandong Provincial Key Laboratory of Rubber-plastics, College of Polymer Science and Engineering, Qingdao University of Science and Technology, Qingdao, China

OPEN ACCESS

Edited by:

Qixin Zhou,
University of Akron, United States

Reviewed by:

Jun Ling,
Zhejiang University, China
Zhou Qiong,
China University of Petroleum, China
Kun Yang,
Southern University of Science and
Technology, China

*Correspondence:

Jing Hua
huajing72@qust.edu.cn
Zhaobo Wang
wangzhibo@qust.edu.cn

Specialty section:

This article was submitted to
Organic Chemistry,
a section of the journal
Frontiers in Chemistry

Received: 30 July 2020

Accepted: 01 September 2020

Published: 02 October 2020

Citation:

Liu J, Han L, Geng J, Hua J and
Wang Z (2020) Metal-Ligand
Coordination Induced Ionochromism
for π -Conjugated Materials.
Front. Chem. 8:589106.
doi: 10.3389/fchem.2020.589106

Keywords: sensors, metal ions, π -conjugated polymers, chemosensors, ionochromism

INTRODUCTION

π -Conjugated polymers refer to polymers in which double bonds (or triple bonds) and single bonds are alternately arranged, including π - π conjugated system, p- π conjugated system, and σ - π -conjugated system (Moon et al., 2007; Tan et al., 2009). It is a research hotspot in the multidisciplinary research field (Bhupathiraju et al., 2018; Biswas et al., 2020; Lee et al., 2020; Zhao et al., 2020) since Shirakawa and coworkers discovered that polyacetylene (PA) doped with I_2 or AsF_5 exhibited high conductivity more than 10^3 S/cm in 1997 (Chiang et al., 1977; Shirakawa et al., 1977). Some parent structures of π -conjugated polymers in the backbone are presented in **Figure 1A** (Hoebe et al., 2005). By far π -conjugated polymers are the most promising functional polymers in the field of cheap and portable electronic devices such as photovoltaic cells (Brabec et al., 2003; Chen et al., 2019), light-emitting diodes (Tang et al., 2013; Saito et al., 2018), prototype field-effect transistors (Dimitrakopoulos and Malenfant, 2002; Melkonyan et al., 2016; Zhang et al., 2017, 2018; Zhang H. et al., 2020) and coatings (Zeng et al., 2019; Zhang H. C. et al., 2020).

In recent years, researches on the π -conjugated system are booming in the fields of organic optoelectronics and sensors based on chromogenic effect. Chromogenic systems are required to be responsive to external inputs, such as metal ions (ionochromism), (Cheng and Tieke, 2014) electrons (electrochromism), (Thakur et al., 2012), or light (photochromism) (Bisoyi and Li, 2016) that could be used for image production. Among these chromogenic systems, ionochromism is realized through the coordination between metal and ligand, resulting in sensitivity to metal ions, which could be used as metal sensors. Trace metal detection plays a vital role in the environment, the human body, and equipment safety. According to the Environmental Protection Agency (EPA), thirteen heavy metal ions are listed as "priority pollutants" because the toxicity of heavy metal ions caused a series of environmental problems. It is of significance to detect the content of alkali metals ions for human condition monitoring.

This review aims to bring together the areas of metal-ligand coordination and π -conjugated systems. Materials based on metal-ligand coordination that show a polymerlike structure in solid-state refers to “metal-organic frameworks” (MOFs) (Kaneti et al., 2017; Ding et al., 2019), and in solution refers to “metallo-supramolecular polymers” (Winter and Schubert, 2016). MOFs and metallo-supramolecular polymers will not be considered in this review because they have been reviewed a lot in recent years. Therefore, this review focuses on the ionochromic properties of π -conjugated polymers with organic ligand as receptors for metal ions.

IONOCHROMISM

Ionochromic effect based on π -conjugated polymers generates from induced conductivity fluctuations either by destroying the conjugation of polymers (conformational effect) or by lowering charge carrier mobility (electrostatic effect). The conductivity of π -conjugated polymers is highly sensitive to the nature and regiospecificity of the side chains, resulting in sensory signal amplification through energy-transfer along polymer chains. **Figure 1B** illustrated the energy-transfer process, in which upon the excitations, the energy may migrate along the polymer backbone due to the conjugation. As a result, the π -conjugated polymers act as a molecular wire, and the conjugated system generates a response more significant than that afforded by a small interaction in an analogous small mono-receptor system (Zhou and Swager, 1995).

Organic ligand containing conjugated polymers are receptors for metal ions. The coordinating interaction between metal ions and ligand causes electrostatic or conformational changes, resulting in an ionochromic effect. Ionochromic performance in π -conjugated systems is expected to find use in portable optical devices for the detection of metal ions and some organic cations. The electron effect and steric hindrance effect of the ligand are selective for the type of metal. The ionochromic phenomenon in the π -conjugated polymer will be introduced according to the type of ligands.

Crown Ether

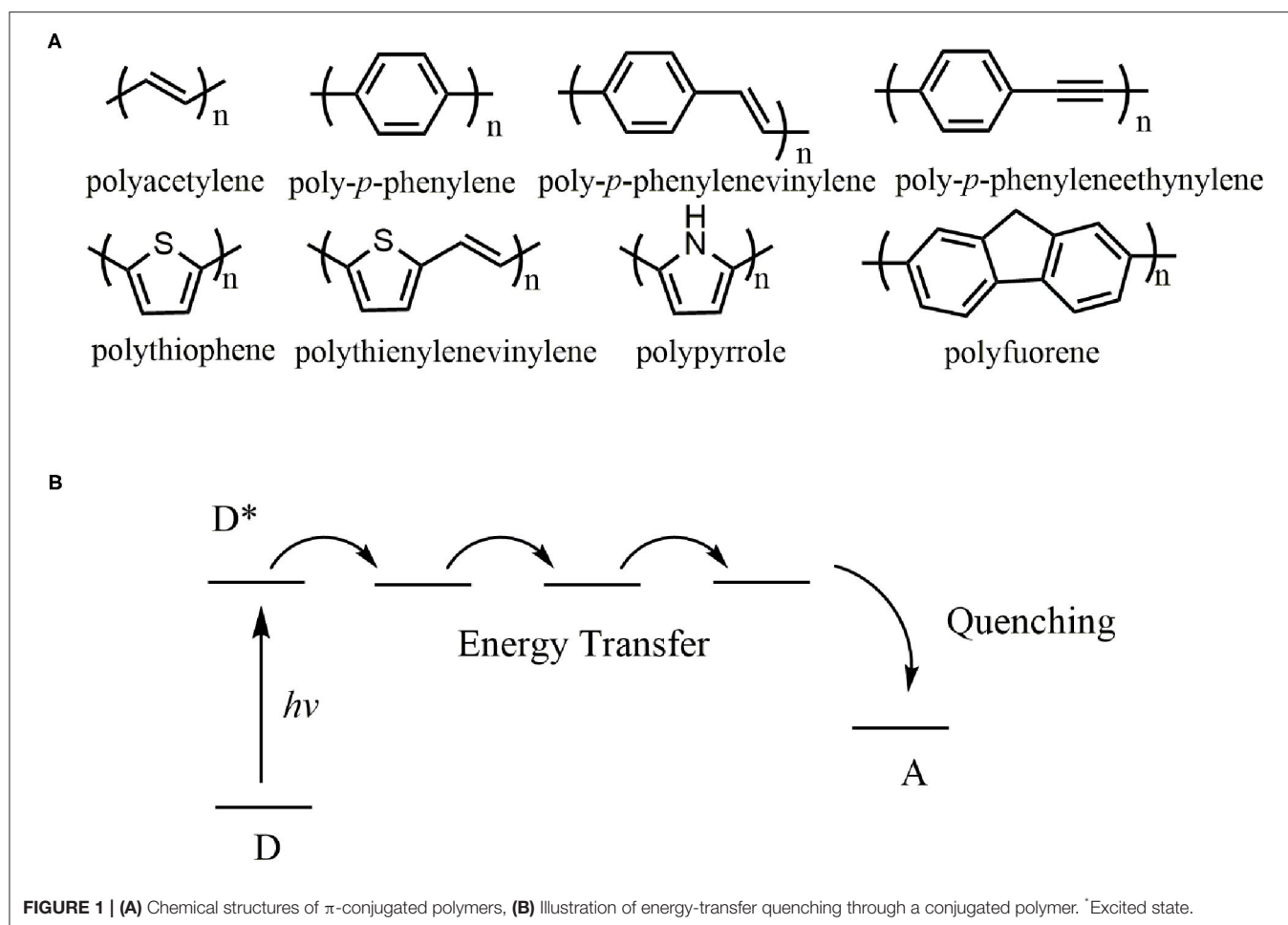
Crown ethers were discovered by the Nobel Prize winner Charles Pedersen (Pedersen, 1967) more than 50 years ago. Recent progress in the design and applications of chemosensors based on crown ethers for small molecules has been reviewed (Li et al., 2017). In contrast to small molecules, π -conjugated polymers have enormous advantages for sensing applications in terms of energy migration and facile exciton transport, which improve the electronic communication between receptors. Additionally, polymers could be processed into films exhibiting semi-permeability to ions. Herein, we focus attention on the design of crown ethers containing π -conjugated polymers and their applications in chemosensors.

Ionochromism was initially reported in the 1990s. Upon coordination with alkali-metal ions (K^+ , Na^+ , and Li^+), polythiophenes with crown ether side chains (**1**, **Figure 2**) (Bäuerle and Scheib, 1993; Marsella and

Swager, 1993) underwent interesting sensory effect because of dramatic conformational changes of polymer chains. Casanovas et al. (Casanovas et al., 2009) studied the affinity of crown ether functionalized polythiophenes for Na^+ , K^+ , and Li^+ by quantum mechanical calculations. The results showed that although the association of Li^+ to the polythiophenes derivatives is entropically unfavored, the binding energies increased in the order of $K^+ < Na^+ < Li^+$. The authors explain that the alkali ions with small dimensions underwent large fluctuations when the dimensions of the cavities changed, leading to an increase in thermal energy.

In addition to polythiophene, chemosensors based on other conjugated systems containing benzocrown or azacrown ethers were also developed. A multiple signal responsive chemosensor was realized by a poly(phenylene-ethynylene) polymer with pendent dibenzocrown groups (**2**), which was responsive to multi-excitation (K^+ , Cl^- , pH, or temperature change) (Ji et al., 2013). Additionally, exposure of a **2**-based film to ammonia increased fluorescence, making it a good candidate for gas sensing. Morgado et al. studied the ionochromic properties of poly(*p*-phenylenevinylene) (PPV) with benzocrown ether (Morgado et al., 2000). Single-layer devices with Al cathodes showed higher electroluminescence efficiencies than those with Ca cathodes due to the existence of aggregates, induced by the crown ether side groups.

Due to the easy chemical access to modification, the functionalization of polypyrrole is widely studied by incorporating various active groups on the nitrogen atom. However, the modification of polypyrrole generated a loss of conjugation, resulting in extremely low conductivity for poly(*N*-substituted pyrroles), of the order of 10^{-4} S/cm or less (Eaves et al., 1985; Bettelheim et al., 1987). Youssoufi et al. found that the equivalent 3-substituted pyrroles (**3**) gave rise to highly conducting polymer films, and they developed azacrown ether substituted polypyrroles with selective cation binding on voltammetric cycling in organic media (Youssoufi et al., 1993). In contrast to benzocrown ethers, a drawback of the azacrown ethers is that it exhibits low thermodynamic stability upon alkali and alkaline-earth metal ions (Ushakov et al., 2008). The main reason is that the planar structure of the junction section of the azacrown ether and benzene moieties. The increasing electron-withdrawing ability of the moiety conjugated to the crown ether is helpful for improving the thermodynamic stability. However, this method does not always lead to the expected enhancement of optical signal induced by metal ions but may conversely attenuate the signal (Izatt et al., 1996; Ushakov et al., 1997). Gromov et al. (Gromov et al., 2013) synthesized 4-pyridine-, 2-benzothiazole-, and 2-, and 4-quinoline-based styryl dyes with an *n*-methylbenzoazacrown ether as a ligand. Electron spectroscopy studies showed that these compounds had a high sensibility for alkali metal and alkaline earth metal cations. In terms of electrochromism and cation binding capacity, they proved to be far superior to those based on phenylazacrown ether. After complexing with Ba^{2+} , the fluorescence enhancement



factor reached 61. The discovery of high levels of macrocyclic pre-organization is one of the factors that determine the high cation binding capacity of sensor molecules based on N-methylbenzoaza-crown ether.

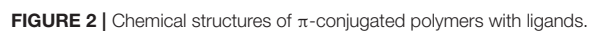
Alkali-metal ions, especially K^+ and Na^+ , are the messengers of living cells, controlling a series of physiological processes through the action of ion channels. Crown ether containing π -conjugated polymers are highly sensitive to alkali-metal ions and could be designed to medical detectors. Nevertheless, most researches focused on the ionochromism of sensors operating in organic solvents rather than in aqueous solutions (Xiang et al., 2014), which is impractical for applications. Additionally, most reported ion-selective films require long incubation times to generate a detectable response, precluding their practical use (Giovannitti et al., 2016). Single-component π -conjugated polymers (**4** and **5**) were synthesized that respond selectively and rapidly to varying concentrations of Na^+ and K^+ in aqueous media, respectively (Wustoni et al., 2019). Using a miniaturized organic electrochemical transistor chip, variations in the concentration of these two metal ions in a blood serum sample could be measured in real-time. The devices based on these crown ether containing polymers are valuable for analyzing cellular

machinery and detecting human body conditions that result in electrolyte imbalance.

Pyridine

The studies on crown ether substituted π -conjugated polymers have clearly demonstrated the ionochromism in alkali chemosensors. It is well-known that oligopyridine, such as bipyridine (bpy), terpyridine (tpy), and its derivatives exhibit super abilities to coordinate a large number of metal ions. If selecting oligopyridine as ligands for π -conjugated polymers, the range of metal ion sensors could be extended from alkali metal ion selective systems to transition metal ion selective systems. Additionally, pyridine and its derivatives not only have the electron-accepting ability to coordinate with metal ions, but also are reactive for metal complex-forming reactions, such as N-oxidation, N-protonation, and quaternization with RX, which can adjust their optical and electrical properties (Yamamoto et al., 1994).

In 1997, Wang et al. reported a transition metal-induced ionochromic polymer with bpy in the backbone (**6**) (Wang and Wasielewski, 1997). According to theoretical calculations, there is a 20° dihedral angle between two adjacent pyridyl rings in bpy when it is in its transoid-like conformation (Cumper et al.,



1962). As a result, bpy-based polymers are pseudoconjugated. With the addition of metal ions, the chelating effect of bpy ligand with the metal ions forces the pseudoconjugated conformation into a planar one, and thus makes the polymers fully conjugated, leading to the redshift in absorption spectra. Besides, incorporating bpy as a ligand directly into the backbone results in a more sensitive response with the addition of metal ions. Different linkers between bipyridine and conjugated polymer in the backbones cause differences in flexibility and rigidity of the resulting polymers. Bin Liu et al. studied the effect of linkages, including C-C single, vinylene, and ethynylene bonds, on the electronic properties and response sensitivities to metal ions (Liu et al., 2001). During the chelation with metal ions, the C-C single bond linkage provided better flexibility to the coplanarity of the pyridine unit. Therefore, C-C single bond possessed the highest sensitivity, and it was followed by vinylene bond, while ethynylene bond exhibited the lowest sensitivity. A conjugated polymer containing 2,6-substituted pyridine derivative (**7**) was synthesized for Pb^{2+} sensing (Liu et al., 2011). With the addition of Pb^{2+} , the color changed from yellow-green to brown, and this can be easily observed by the naked eye. The detection limit of the polymer is less than 1 ppm, while the threshold of Pb^{2+} in drugs is 5–10 ppm. Therefore, **7** could be adopted to design an excellent sensor for Pb^{2+} detection.

Increasing the association constant of a molecular recognition event could improve the sensitivity of a sensor. Terpyridine (tpy) ligand possesses an excellent ability to coordinate various of metal ions with higher sensitivity than bipyridine. Zhang et al. prepared poly[p-(phenyleneethynylene)-alt-(thienyleneethynylene)] (PPETE) with bpy (**8**) and tpy (**9**) as receptors, respectively (Zhang et al., 2002). With the addition of Ni^{2+} , **9** was quenched to 10.9% of its original emission intensity, while **8** was only quenched to 38.2%, illustrating that tpy was more sensitive to Ni^{2+} ion. Rabindranath et al. reported tpy substituted polyiminofluorenes (**10**) (Rabindranath et al., 2009). Fe^{2+} , Co^{2+} , Ni^{2+} , Cu^{2+} , Pd^{2+} , Fe^{3+} , Gd^{3+} , and Zr^{4+} led to complete quenching of the green emission for **10**, while Zn^{2+} , Cd^{2+} , and Eu^{3+} caused a weak red emission, which was redshifted by 10–30 nm compared with pure **10**. Additionally, a biscomplex formed upon the addition of Zn^{2+} , leading to red luminescent precipitation. This effect can be used for the detection of Zn^{2+} .

Although tpy exhibits high coordinating ability with a large number of metal ions, the preparation of tpy ligands is expensive and very time-consuming. In contrast to bpy, 2,6-bis(10-methylbenzimidazolyl)pyridine (bip) ligands can be more easily synthesized on a large scale (Beck et al., 2005). Kalie Cheng et al. reported a polyimide fluorene (**11**) with bip ligand (Cheng and Tieke, 2014) and studied the optical properties with Zn^{2+} and Cu^{2+} . Due to charge transfer from ion-specific metal to ligand, the **11**/ Zn^{2+} film is orange, while the **11**/ Cu^{2+} film is purple. Due to the oxidation of the polymer backbone, the **11**/ Zn^{2+} and **11**/ Cu^{2+} films will turn blue if anodically oxidized to 750 mV vs. FOC., and the color change is reversible. The conjugated polymer with bip ligand exhibited high contrast and short switching times in color change upon 12 dipping cycles.

However, the long-term stability of bip with metal ions is lower than that of tpy based systems.

Some biomacromolecules such as DNA, RNA, and proteins are easy to be inhibited by Pd^{2+} *in vivo* and *in vitro* (Kielhorn et al., 2002). Additionally, Pd^{2+} is able to elicit a series of cytotoxic effects, resulting in severe primary skin and eye irritations. It is essential to investigate a sensor for highly selective and sensitive detection of Pd^{2+} . Xiang et al. reported three conjugated polymers (**12–14**) via Sonogashira reaction (Xiang et al., 2014). The conjugated backbones of **13** and **14** are twisted, which were proved to be selective for Ni^{+} . In contrast to **13** and **14**, **12** exhibited high selectivity for Ag^{+} because of its linear conjugated backbone. Theoretically, the same functional group should have the same metal ion recognition capability. According to the ionochromic effect of **12–14**, changes of linkage site for recognition groups resulted in different metal ion selectivity. Cyclic voltammetry measurement for **12–14** was carried out to analyze the cation selectivity by LUMO and HOMO energy levels. The LUMO levels of **12** are slightly lower than that of **13** and **14**, indicating that their electron affinity is in the order of $\text{12} > \text{14} \approx \text{13}$. Additionally, the HOMO levels of **13** and **14** are slightly raised relative to **12**, illustrating that the energy barrier of hole injection from the anode is in the order of $\text{13} = \text{14} < \text{12}$. As a result, both electron and hole affinities of **12** are improved, resulting in enhanced carrier injection and transport. Moreover, smaller coordination cavity in **13** and **14** fits well with the size of Ni^{+} because of their twisted conjugated backbones and smaller radius of Ni^{+} . This work provided guidelines to tune the structure of conjugated polymers for the design and preparation of the selective metal ion sensors.

Despite the successful development of chemosensors in conjugated polymers, most of the examples are in the solution state, and seldom chemosensors in neat π -conjugated polymer films have been reported. This is because of strong interpolymer π - π interactions resulting in the self-quenching of luminescence in such a condensed solid-state phase (Sahoo et al., 2014). It is a non-negligible challenge to control such random and strong interactions in the solid-state. Hosomi et al. reported π -conjugated polymer with bipyridine moieties as ligand and permethylated α -cyclodextrin (PM α -CD) as the main chain (**15**). The PM α -CD suppresses the interactions between π -conjugated and enabled the polymers to show efficient emission even in the solid-state (Hosomi et al., 2016). Additionally, the metal-ion recognition ability of **15** is maintained in the solid-state, leading to reversible changes in the luminescent color in response to cations. The prepared π -polymer is expected to be applicable for recyclable luminescent sensors to detect different metal ions.

1,10-Phenanthroline

1,10-Phenanthroline (phen) is an electron-poor, rigid planar, hydrophobic, and heteroaromatic ligand that has played an important role in the development of coordination chemistry (Cockrell et al., 2008; Bencini and Lippolis, 2010; Iqbal et al., 2016). Phen is a bidentate ligand for transition metal ions whose nitrogen atoms are beautifully placed to act cooperatively in cation binding. In contrast to the parent bpy and tpy systems, phen is characterized by two inwardly pointing nitrogen donor

atoms, which is held juxtaposed. As a result, phen is pre-organized for strong and entropically favored metal binding. A luminescent phen-containing π -conjugated copolymer (**16**) responsive with Zn^{2+} , Ir^{3+} , and Eu^{3+} was reported (Yasuda et al., 2003). The λ_{max} of **16** is shifted from 385 to 404 nm on the addition of NiCl_2 . Photoluminescence intensity of **1** steeply decreases in the presence of Ni^{2+} because of the chelating effect of the phen unit to Ni^{2+} . Other metal ions also caused similar shifts of λ_{max} . Mainly, Li^+ , Mg^{2+} , Al^{3+} , Zn^{2+} , Ag^+ , and La^{3+} caused a redshift of λ_{max} to a smaller degree of about 10 ± 35 nm; Fe^{3+} , Co^{2+} , Ni^{2+} , Cu^{2+} , and Pd^{2+} gave rise to a larger redshift by about 20 ± 50 nm and complete quenching of photoluminescence. This quenching phenomenon is related to an energy transfer from the π -conjugated polymer to the metal complexes. Yasuda group further synthesized a copolymer composed of alternating phen/9,9-dioctylfluorene (**17**) (Yasuda and Yamamoto, 2003). The color of emitted light from the polymer complex could be tuned from blue to red by transition metal ions (Co^{2+} , Ni^{2+} , Cu^{2+} , and Pd^{2+}) upon absorption spectra. Additionally, Satapathy et al. reported conjugated polymers containing phenanthroline that show remarkable sensing capabilities toward Fe^{2+} (Satapathy et al., 2012).

Calixarene

Calixarenes have unique hole structures, which can be functionalized to recognize metal ions. Moreover, the hydrophobic cavity of the calixarene scaffold can accommodate various gases and organic molecules (Rudkevich, 2007). With the addition of metal ions or small molecules, calixarenes undergo dramatic geometric changes, including phenol ring flips between cone, partial cone, and 1,3-alternate conformational isomers (Gutsche, 1998). The small molecular of calixarene-based sensors for recognition of transition metal cations have been recently reviewed (Kumar et al., 2019), and here only list some calixarene-based conjugated polymer sensors. Calixarene-functionalized polymers (**18** and **19**) were first reported in the 1990s (Marsella et al., 1995). Binding constant measurements of the calixarene-bithiophene generated a K_a (7.6×10^7) for Na^+ which is approximately 100 times stronger than K^+ and 40 times stronger than Li^+ . A stronger binding constant means higher sensitivity. Ion recognition behavior of **18** and **19** toward Li^+ , Na^+ , and K^+ was analyzed by UV-vis absorption and fluorescence emission spectroscopy. The resulting polymers exhibit good selectivity toward Na^+ , with a 24 nm blue shift for **66** and 32 nm red shift for **67**.

Other calixarene-based receptors in π -conjugated polymers were reported (Wosnick and Swager, 2004; Costa et al., 2008), in which the calixarene groups were mainly as pendant groups. The direct attachment of the calixarene unit (at the upper rim) to a conjugated polymer (**20**) has also been reported (Yu et al., 2003). The conical configuration of calixarene makes the polymer chain segment a zigzag orientation. The segmental structure in **20** imposes great localization of the carriers, and the rapid self-exchange between discrete units causes the conductivity of such a segmented system. Protonation promoted the electron exchange resulted in high conductivity for **20**. Hence, electroactive calixarene polymer that requires protonation to

be highly conductive was prepared, which is useful for the design of actuating materials. A fluorescent polymer (**21**) in which calixarene scaffolds are the part of uninterrupted linear polymeric backbone was first reported (Molad et al., 2012). Short conjugated fragments combined with the nonlinear geometry gave rise to rather moderate sensitivity with selected stimuli. The coordination of the calixarenes in the π -conjugated polymers allows for the recognition of small molecules, such as NO.

Imidazole

Imidazole-based ligands are widely used due to their reversible fluorescence. This reversibility is realized by protonation/deprotonation upon an acid/base or metallation/demetallation with metal ions/suitable counter ligands (Jiang et al., 2010). As an important functional conjugated polymer material, polydiacetylene (PDA) has received more and more attention since the first report in 1969 (Wegner, 1969). PDA has significant color conversion and fluorescence enhancement under various environmental stimuli, including heat (Takeuchi et al., 2017), organic solvent (Yoon et al., 2007), bioanalyte (Zhou et al., 2013), ion (Wang et al., 2016), and so on. In response to different stimuli, PDA can be changed to different colors, such as purple, yellow, orange, or red, of which the transition from blue to red is the most common type. Due to their spontaneous color change and fluorescence emission development under stimulation, many PDA liposomes with specific receptor groups have been designed and widely used to detect metal ions such as Hg^{2+} and Cu^{2+} (Lee et al., 2009; Xu et al., 2011).

An imidazole-functionalized disubstituted polyacetylene (**22**) was prepared (Zeng et al., 2008). **22** was not sensitive to alkali and alkaline earth metal ions, and transition metals Cd^{2+} , Mn^{2+} , Ag^+ , and Zn^{2+} , because of the poor coordination ability of the imidazole receptor with these ions. Nevertheless, Pb^{2+} , Al^{3+} , and Cr^{3+} could quench the fluorescence of **22** not completely, while Cu^{2+} , Co^{2+} , Fe^{2+} , Fe^{3+} , and Ni^{2+} could quench its fluorescence more efficiently. Particularly, Cu^{2+} quenched the fluorescence entirely at a very low concentration (1.48 ppm). Satapathy et al. reported imidazole-based polymers (**23–25**) that present significant ion recognition ability toward Fe^{2+} in semi-aqueous solutions (Satapathy et al., 2012). The fluorescence lifetime of polymer **25** (11.4-fold) decreased larger than that of **23** (4.6-fold) and **24** (6.2-fold) further, illustrating that **25** showed superior sensing capability by virtue of its stronger molecular wire effect. The fluorescence of these three polymers recovered by adding phenanthroline or $\text{Na}_2\text{-EDTA}$. Additionally, the selectivity of **23–25** for Fe^{2+} interaction was not interfered by other competing metal ions.

CONCLUSIONS AND OUTLOOK

π -Conjugated polymers represent useful chemical platforms for the design of chemosensors for metal ions. In this review, we have summarized the types and characteristics of functional groups that chelating with different metal ions as well as the ionochromic effect of the π -conjugated polymers based on these functional groups. In the past few decades, significant progress has been made in the development of novel chemosensors in

environmental protection, food and drug testing, and human health monitoring. Although there has been a lot of research on these materials, preparing chemical sensors with high sensitivity, long-term stability, and selectivity is still a critical challenge. The chemical and physical relationship between ligand and metal coordination also needs to be further studied to improve the theoretical guidance for the preparation of metal sensors.

REFERENCES

- Bäuerle, P., and Scheib, S. (1993). Molecular recognition of alkali-ions by crown-ether-functionalized poly(alkylthiophenes). *Adv. Mater.* 5, 848–853. doi: 10.1002/adma.19930051113
- Beck, J. B., Ineman, J. M., and Rowan, S. J. (2005). Metal/ligand-induced formation of metallo-supramolecular polymers. *Macromolecules* 38, 5060–5068. doi: 10.1021/ma050369e
- Bencini, A., and Lippolis, V. (2010). 1,10-phenanthroline: a versatile building block for the construction of ligands for various purposes. *Coord. Chem. Rev.* 254, 2096–2180. doi: 10.1016/j.ccr.2010.04.008
- Bettelheim, A., White, B. A., Raybuck, S. A., and Murray, R. W. (1987). Cheminform abstract: electrochemical polymerization of amino-, pyrrole-, and hydroxy-substituted tetraphenylporphyrins. *ChemInform* 18:18. doi: 10.1002/chin.198733064
- Bhupathiraju, N., Sayeedi, M., Rizvi, W., Singh, S., Batteas, J. D., and Drain, C. M. (2018). Practical, high-yield synthesis of thiol-terminated diacetylenes for formation of conductive monolayers. *Tetrahedron Lett.* 59, 3629–3631. doi: 10.1016/j.tetlet.2018.08.057
- Bisoyi, H. K., and Li, Q. (2016). Light -driven liquid crystalline materials: from photo -induced phase transitions and property modulations to applications. *Chem. Rev.* 116, 15089–15166. doi: 10.1021/acs.chemrev.6b00415
- Biswas, S., Kim, K., Nam, I. W., Choi, M., Bae, J. H., and Kim, H. (2020). Highly conductive and thermally stable nanoparticle-conjugated polymer compounds through environmentally friendly in situ synthesis. *Prog. Org. Coat.* 142:105606. doi: 10.1016/j.porgcoat.2020.105606
- Brabec, C. J., Dyakonov, V., Parisi, J., and Sariciftci, N. S. (2003). *Organic Photovoltaics: Concepts and Realization*. London: Springer Series in Materials Science. doi: 10.1007/978-3-662-05187-0
- Casanovas, J., Preat, J., Zanuy, D., and Aleman, C. (2009). Sensing abilities of crown ether functionalized polythiophenes. *Chemistry* 15, 4676–4684. doi: 10.1002/chem.200802006
- Chen, H. J., Lyu, G. Y., Yue, Y. F., Wang, T. W., Li, D. P., Shi, H., et al. (2019). Improving the photovoltaic performance by employing alkyl chains perpendicular to the π -conjugated plane of an organic dye in dye-sensitized solar cells. *J. Mater. Chem. C* 7, 7249–7258. doi: 10.1039/c9tc01520e
- Cheng, K. L., and Tieke, B. (2014). Polyiminofluorene with conjugated benzimidazolylpyridine substituent groups: Optical properties, ionochromism and coordinative self-assembly into electrochromic films. *RSC Adv.* 4, 25079–25088. doi: 10.1039/c4ra03969f
- Chiang, C. K., Ficher, C. R., Park, Y. W., Heeger, A. J., Shirakawa, H., Louis, E. J., et al. (1977). Electrical conductivity in doped polyacetylene. *Phys. Rev. Lett.* 39:1098. doi: 10.1103/PhysRevLett.40.1472
- Cockrell, G. M., Zhang, G., VanDerveer, D. G., Thummel, R. P., and Hancock, R. D. (2008). Enhanced metal ion selectivity of 2,9-di-(pyrid-2-yl)-1,10-phenanthroline and its use as a fluorescent sensor for cadmium(II). *J. Am. Chem. Soc.* 130, 1420–1430. doi: 10.1021/ja077141m
- Costa, A. I., Ferreira, L. F., and Prata, J. V. (2008). Novel fluorescent (p-phenylene ethynylene)-calix [4] arene-based polymer: design, synthesis, and properties. *J. Polym. Sci. Part A Polym. Chem.* 46, 6477–6488. doi: 10.1002/pola.22957
- Cumpher, C. W. N., Ginman, R. F. A., and Vogel, A. I. (1962). 226. Physical properties and chemical constitution. Part xxxv. The electric dipole moments of some phenanthrolines and bipyridyls. *J. Chem. Soc.* 4:1188–1192. doi: 10.1039/jr9620001188
- Dimitrakopoulos, C. D., and Malenfant, P. R. L. (2002). Organic thin film transistors for large area electronics. *Adv. Mater.* 14:99–117. doi: 10.1002/1521-4095(20020116)14:2<99::AID-ADMA99>3.0.CO;2-9
- Ding, M. L., Flaig, R. W., Jiang, H. L., and Yaghi, O. M. (2019). Carbon capture and conversion using metal-organic frameworks and mof-based materials. *Chem. Soc. Rev.* 48, 2783–2828. doi: 10.1039/c8cs00829a
- Eaves, J. G., Munro, H. S., and Parker, D. (1985). Electroactive thin films from the anodic electropolymerisation of iron(ii) and ruthenium(ii) tris(n-bipyridylpyrrole) complexes. *J. Chem. Soc. Chem. Commun.* 11, 684–685. doi: 10.1039/C39850000684
- Giovannitti, A., Nielsen, C. B., Rivnay, J., Kirkus, M., Harkin, D. J., White, A. J. P., et al. (2016). Sodium and potassium ion selective conjugated polymers for optical ion detection in solution and solid state. *Adv. Funct. Mater.* 26, 514–523. doi: 10.1002/adfm.201503791
- Gromov, S. P., Dmitrieva, S. N., Vedernikov, A. I., Kurchavov, N. A., Kuz'mina, L. G., Sazonov, S. K., et al. (2013). Synthesis, structure, and characterization of chromo(fluoro)ionophores with cation-triggered emission based on n-methylaza-crown-ether styryl dyes. *J. Org. Chem.* 78, 9834–9847. doi: 10.1021/jo401555a
- Gutsche, C. D. (1998). *Calixarenes Revisited*. London: RSC Publishing.
- Hoeben, F. J., Jonkheijm, P., Meijer, E. W., and Schenning, A. P. (2005). About supramolecular assemblies of π -conjugated systems. *Chem. Rev.* 105, 1491–1546. doi: 10.1021/cr030070z
- Hosomi, T., Masai, H., Fujihara, T., Tsuji, Y., and Terao, J. (2016). A typical metal-ion-responsive color-tunable emitting insulated π -conjugated polymer film. *Angew. Chem. Int. Ed.* 55, 13427–13431. doi: 10.1002/anie.2016.03160
- Iqbal, A., Tian, Y. J., Wang, X. D., Gong, D. Y., Guo, Y. L., Iqbal, K., et al. (2016). Carbon dots prepared by solid state method via citric acid and 1,10-phenanthroline for selective and sensing detection of Fe^{2+} and Fe^{3+} . *Sensor. Actuat. B Chem.* 237, 408–415. doi: 10.1016/j.snb.2016.06.126
- Izatt, R. M., Pawlak, K., and Bradshaw, J. S. (1996). Thermodynamic and kinetic data for macrocycle interaction with cations, anions, and neutral molecules. *Cheminform* 27:322. doi: 10.1002/chin.199611336
- Ji, X. F., Yao, Y., Li, J. Y., Yan, X. Z., and Huang, F. H. (2013). A supramolecular cross-linked conjugated polymer network for multiple fluorescent sensing. *J. Am. Chem. Soc.* 135, 74–77. doi: 10.1021/ja3108559
- Jiang, J., Xiao, X., Ping, Z., and He, T. (2010). Colorimetric naked-eye recognizable anion sensors synthesized via raft polymerization. *J. Polym. Sci. A Polym. Chem.* 48, 1551–1556. doi: 10.1002/pola.23922
- Kaneti, Y. V., Tang, J., Salunkhe, R. R., Jiang, X. C., Yu, A. B., Wu, K. C. W., et al. (2017). Nanoarchitected design of porous materials and nanocomposites from metal-organic frameworks. *Adv. Mater.* 29:1604898. doi: 10.1002/adma.201604898
- Kielhorn, J., Melber, C., Keller, D., and Mangelsdorf, I. (2002). Palladium – a review of exposure and effects to human health. *Int. J. Hyg. Environ. Health* 205, 417–432. doi: 10.1078/1438-4639-00180
- Kumar, R., Sharma, A., Singh, H., Suating, P., Kim, H. S., Sunwoo, K., et al. (2019). Revisiting fluorescent calixarenes: from molecular sensors to smart materials. *Chem. Rev.* 119, 9657–9721. doi: 10.1021/acs.chemrev.8b00605
- Lee, D. C., Sellers, D. L., Liu, F., Boydston, A. J., and Pun, S. H. (2020). Synthesis and characterization of anionic poly(cyclopentadienylene vinylene) and its use in conductive hydrogels. *Angew. Chem. Int. Ed. Engl.* 132, 13532–13538. doi: 10.1002/anie.202004098
- Lee, J., Jun, H., and Kim, J. (2009). Polydiacetylene-liposome microarrays for selective and sensitive mercury(II) detection. *Adv. Mater.* 21:3674–3677. doi: 10.1002/adma.200900639
- Li, J., Yim, D., Jang, W. D., and Yoon, J. (2017). Recent progress in the design and applications of fluorescence probes containing crown ethers. *Chem. Soc. Rev.* 46, 2437–2458. doi: 10.1039/c6cs00619a

AUTHOR CONTRIBUTIONS

JL and JH: conceptualization and design. LH and ZW: acquisition of data. JG: software. JL and LH: analysis of data. JL: drafting of article. JL, LH, JG, JH, and ZW: final approval of manuscript. All authors: contributed to the article and approved the submitted version.

- Liu, B., Dai, H. G., Bao, Y. Y., Du, F. F., Tian, J., and Bai, R. K. (2011). 2,6-substituted pyridine derivative-containing conjugated polymers: synthesis, photoluminescence and ion-sensing properties. *Polym. Chem.* 2, 1699–1705. doi: 10.1039/c1py00149c
- Liu, B., Yu, W.-L., Pei, J., Liu, S.-Y., Lai, Y.-H., and Huang, W. (2001). Design and synthesis of bipyridyl-containing conjugated polymers: effects of polymer rigidity on metal ion sensing. *Macromolecules* 34, 7932–7940. doi: 10.1021/ma0106651
- Marsella, M. J., Newland, R. J., Carroll, P. J., and Swager, T. M. (1995). Ionoresistivity as a highly sensitive sensory probe: investigations of polythiophenes functionalized with calix[4]arene-based ion receptors. *J. Am. Chem. Soc.* 117, 9842–9848. doi: 10.1021/ja00144a009
- Marsella, M. J., and Swager, T. M. (1993). Designing conducting polymer-based sensors - selective ionochromic response in crown-ether containing polythiophenes. *J. Am. Chem. Soc.* 115, 12214–12215. doi: 10.1021/ja00078a090
- Melkonyan, F. S., Zhao, W., Drees, M., Eastham, N. D., Leonardi, M. J., Butler, M. R., et al. (2016). Bithiophenesulfonamide building block for π -conjugated donor-acceptor semiconductors. *J. Am. Chem. Soc.* 138, 6944–6947. doi: 10.1021/jacs.6b03498
- Molad, A., Goldberg, I., and Vigalok, A. (2012). Tubular conjugated polymer for chemosensory applications. *J. Am. Chem. Soc.* 134, 7290–7292. doi: 10.1021/ja301918f
- Moon, J. H., McDaniel, W., MacLean, P., and Hancock, L. E. (2007). Live-cell-permeable poly (p-phenylene ethynylene). *Angew. Chem. Int. Ed.* 46, 8223–8225. doi: 10.1002/anie.200701991
- Morgado, J., Cacialli, F., Friend, R. H., Chuah, B. S., Moratti, S. C., and Holmes, A. B. (2000). Luminescence properties of ppv-based copolymers with crown ether substituents. *Synth. Met.* 111–112, 449–452. doi: 10.1016/S0379-6779(99)00397-5
- Pedersen, C. J. (1967). Cyclic polyethers and their complexes with metal salts. *J. Am. Chem. Soc.* 89, 7017–7036. doi: 10.1021/ja00986a052
- Rabindranath, A. R., Maier, A., Schafer, M., and Tiekke, B. (2009). Luminescent and ionochromic polyiminofluorene with conjugated terpyridine substituent groups. *Macromol. Chem. Phys.* 210, 659–668. doi: 10.1002/macp.200800542
- Rudkevich, D. M. (2007). Progress in supramolecular chemistry of gases. *Eur. J. Org. Chem.* 2007, 3255–3270. doi: 10.1002/ejoc.200700165
- Sahoo, D., Sugiyasu, K., Tian, Y., Takeuchi, M., and Scheblykin, I. G. (2014). Effect of conjugated backbone protection on intrinsic and light-induced fluorescence quenching in polythiophenes. *Chem. Mater.* 26, 4867–4875. doi: 10.1021/cm5021959
- Saito, H., Kuwabara, J., Yasuda, T., and Kanbara, T. (2018). Synthesis of polyfluoro arylene-based poly(arylenevinylene)s via pd-catalyzed dehydrogenative direct alkenylation. *Macromol. Rapid Commun.* 39:1800414. doi: 10.1002/marc.201800414
- Satapathy, R., Padhy, H., Wu, Y. H., and Lin, H. C. (2012). Synthesis and characterization of reversible chemosensory polymers: modulation of sensitivity through the attachment of novel imidazole pendants. *Chem. Eur. J.* 18, 16061–16072. doi: 10.1002/chem.201201437
- Shirakawa, H., Louis, E. J., MacDiarmid, A. G., Chiang, C. K., and Heeger, A. H. (1977). Synthesis of electrically conducting organic polymers: halogen derivatives of polyacetylene, (ch)x. *J. Chem. Soc. Chem. Commun.* 1, 578–580. doi: 10.1039/C39770000578
- Takeuchi, M., Imai, H., and Oaki, Y. (2017). Effects of the intercalation rate on the layered crystal structures and stimuli-responsive color-change properties of polydiacetylene. *J. Mater. Chem. C* 5, 8250–8255. doi: 10.1039/c7tc02218b
- Tan, H., Liu, N. S., He, B. P., Wong, S. Y., Chen, Z. K., Li, X., et al. (2009). Facile synthesis of hybrid silica nanocapsules by interfacial templating condensation and their application in fluorescence imaging. *Chem. Commun.* 41, 6240–6242. doi: 10.1039/b914366a
- Tang, C., Liu, X. D., Liu, F., Wang, X. L., Xu, H., and Huang, W. (2013). Recent progress in polymer white light-emitting materials and devices. *Macromol. Chem. Phys.* 214, 314–342. doi: 10.1002/macp.201200305
- Thakur, V. K., Ding, G. Q., Ma, J., Lee, P. S., and Lu, X. H. (2012). Hybrid materials and polymer electrolytes for electrochromic device applications. *Adv. Mater.* 24, 4071–4096. doi: 10.1002/adma.201200213
- Ushakov, E. N., Alifimov, M. V., and Gromov, S. P. (2008). Design principles for optical molecular sensors and photocontrolled receptors based on crown ethers. *Russ. Chem. Rev.* 77, 39–58. doi: 10.1070/RC2008v077n01ABEH003757
- Ushakov, E. N., Gromov, S. P., Fedorova, O. A., and Alifimov, M. V. (1997). Crown-containing styryl dyes. 19. complexation and cation-induced aggregation of chromogenic aza-15-crown-5-ethers. *Russ. Chem. Bull.* 46, 463–471. doi: 10.1007/BF02495396
- Wang, B., and Wasielewski, M. R. (1997). Design and synthesis of metal ion-recognition-induced conjugated polymers: an approach to metal ion sensory materials. *J. Am. Chem. Soc.* 119, 12–21. doi: 10.1021/ja962229d
- Wang, D. E., Zhao, L., Yuan, M. S., Chen, S. W., Li, T. B., and Wang, J. Y. (2016). Fabrication of polydiacetylene liposome chemosensor with enhanced fluorescent self-amplification and its application for selective detection of cationic surfactants. *ACS Appl. Mater. Interfaces* 8, 28231–28240. doi: 10.1021/acsami.6b10794
- Wegner, G. (1969). Topochemische reaktionen von monomeren mit konjugierten dreifachbindungen / topochemical reactions of monomers with conjugated triple bonds. *Z. Naturforsch. B* 24, 824–832. doi: 10.1515/znbb-1969-0708
- Winter, A., and Schubert, U. S. (2016). Synthesis and characterization of metallo-supramolecular polymers. *Chem. Soc. Rev.* 45, 5311–5357. doi: 10.1039/c6cs00182c
- Wosnick, J. H., and Swager, T. M. (2004). Enhanced fluorescence quenching in receptor-containing conjugated polymers: a calix[4]arene-containing poly(phenylene ethynylene). *Chem Commun.* 23, 2744–2745. doi: 10.1039/b411489b
- Wustoni, S., Combe, C., Ohayon, D., Akhtar, M. H., McCulloch, I., and Inal, S. (2019). Membrane-free detection of metal cations with an organic electrochemical transistor. *Adv. Funct. Mater.* 29:1904403. doi: 10.1002/adfm.201904403
- Xiang, G., Wang, L. Y., Cui, W., An, X. N., Zhou, L. X., Li, L., et al. (2014). 2-pyridine-1h-benzo d imidazole based conjugated polymers: a selective fluorescent chemosensor for Ni^{2+} or Ag^{+} depending on the molecular linkage sites. *Sensor. Actuat. B Chem.* 196, 495–503. doi: 10.1016/j.snb.2014.02.047
- Xu, Q. L., Lee, K. M., Wang, F., and Yoon, J. (2011). Visual detection of copper ions based on azide- and alkyne-functionalized polydiacetylene vesicles. *J. Mater. Chem.* 21, 15214–15217. doi: 10.1039/c1jm11660f
- Yamamoto, T., Maruyama, T., Zhou, Z.-H., Ito, T., Fukuda, T., Yoneda, Y., et al. (1994). Π -conjugated poly(pyridine-2,5-diyl), poly(2,2'-bipyridine-5,5'-diyl), and their alkyl derivatives. Preparation, linear structure, function as a ligand to form their transition metal complexes, catalytic reactions, n-type electrically conducting properties, optical properties, and alignment on substrates. *J. Am. Chem. Soc.* 116, 4832–4845. doi: 10.1021/ja00090a031
- Yasuda, T., Yamaguchi, I., and Yamamoto, T. (2003). A new soluble 1,10-phenanthroline-containing π -conjugated polymer: synthesis and effect of metal complexation on optical properties. *Adv. Mater.* 15, 293–296. doi: 10.1002/adma.200390070
- Yasuda, T., and Yamamoto, T. (2003). Synthesis and characterization of new luminescent 1,10-phenanthroline- and pyridine-containing π -conjugated polymers. their optical response to protic acid, Mn^{2+} , and solvents. *Macromolecules* 36, 7513–7519. doi: 10.1021/ma030280d
- Yoon, J., Chae, S. K., and Kim, J. M. (2007). Colorimetric sensors for volatile organic compounds (vocs) based on conjugated polymer-embedded electropun fibers. *J. Am. Chem. Soc.* 129, 3038–3039. doi: 10.1021/ja067856+
- Yousoufi, H. K., Hmyene, M., Garnier, F., and Delabouglise, D. (1993). Cation recognition properties of polypyrrole 3-substituted by azacrown ethers. *J. Chem. Soc. Chem. Commun.* 20, 1550–1552. doi: 10.1002/chin.199410200
- Yu, H. H., Xu, B., and Swager, T. M. (2003). A proton-doped calix 4 arene-based conducting polymer. *J. Am. Chem. Soc.* 125, 1142–1143. doi: 10.1021/ja028545b
- Zeng, Q., Cai, P., Li, Z., Qin, J. G., and Tang, B. Z. (2008). An imidazole-functionalized polyacetylene: convenient synthesis and selective chemosensor for metal ions and cyanide. *Chem. Commun.* 9, 1094–1096. doi: 10.1039/b717764j
- Zeng, W. X., Deng, Z. F., Wang, H. R., Zhang, H. C., and Zhou, Q. X. (2019). Benzodifuranone based color-changing epoxy-polyamine coating. *Dyes Pigm.* 164, 198–205. doi: 10.1016/j.dyepig.2019.01.016
- Zhang, H., Deng, R., Wang, J., Li, X., Chen, Y. M., Liu, K., et al. (2017). Crystalline organic pigment-based field-effect transistors. *ACS Appl. Mater. Interfaces* 9, 21891–21899. doi: 10.1021/acsami.7b03170

- Zhang, H., Li, R., Deng, Z., Cui, S., Wang, Y., Zheng, M., et al. (2020). Π -conjugated oligomers based on aminobenzodifuranone and diketopyrrolopyrrole. *Dyes Pigm.* 181:108552. doi: 10.1016/j.dyepig.2020.108552
- Zhang, H. C., Yang, K., Zhang, K., Zhang, Z. Z., Sun, Q. K., and Yang, W. J. (2018). Thionating iso-diketopyrrolopyrrole-based polymers: from p-type to ambipolar field effect transistors with enhanced charge mobility. *Polym. Chem.* 9, 1807–1814. doi: 10.1039/c8py00292d
- Zhang, H. C., Zeng, W. X., Du, H. L., Ma, Y. T., Ji, Z. T., Deng, Z. F., et al. (2020). Comparison for color change between benzodifuranone and benzodipyrrolidone based epoxy coating. *Dyes Pigm.* 175:108171. doi: 10.1016/j.dyepig.2019.108171
- Zhang, Y., Murphy, C. B., and Wayne E Jones, J. (2002). Poly[p-(phenyleneethynylene)-alt-(thienyleneethynylene)] polymers with oligopyridine pendant groups: highly sensitive chemosensors for transition metal ions. *Macromolecules* 35, 630–636. doi: 10.1021/ma011479y
- Zhao, X. H., Liang, X. G., and Sun, Q. J. (2020). Spray printed conjugated polymer on tissue paper for highly sensitive pressure sensors. *Polym. Int.* doi: 10.1002/pi.6022
- Zhou, G. D., Wang, F., Wang, H. L., Kambam, S., Chen, X. Q., and Yoon, J. (2013). Colorimetric and fluorometric assays based on conjugated polydiacetylene supramolecules for screening acetylcholinesterase and its inhibitors. *ACS Appl. Mater. Interfaces* 5, 3275–3280. doi: 10.1021/am400260y
- Zhou, Q., and Swager, T. M. (1995). Fluorescent chemosensors based on energy migration in conjugated polymers: the molecular wire approach to increased sensitivity. *J. Am. Chem. Soc.* 117, 12593–12602. doi: 10.1021/ja00155a023

Conflict of Interest: The authors declare that the research was conducted in the absence of any commercial or financial relationships that could be construed as a potential conflict of interest.

Copyright © 2020 Liu, Han, Geng, Hua and Wang. This is an open-access article distributed under the terms of the Creative Commons Attribution License (CC BY). The use, distribution or reproduction in other forums is permitted, provided the original author(s) and the copyright owner(s) are credited and that the original publication in this journal is cited, in accordance with accepted academic practice. No use, distribution or reproduction is permitted which does not comply with these terms.



Terpyridine-Containing π -Conjugated Polymers for Light-Emitting and Photovoltaic Materials

Pan Liu, Ganhui Shi and Xuegang Chen*

Key Laboratory of Rubber-Plastic of Ministry of Education (QUST), School of Polymer Science and Engineering, Qingdao University of Science and Technology, Qingdao, China

2,2':6',2''-Terpyridine (tpy) is a versatile moiety used in the construction of small novel molecules or polymers. Extending or coupling tpy with π -conjugation structures can result in interesting optoelectronic properties. This mini-review summarizes the significant progress made over the past decades in the study of tpy-containing π -conjugated polymers and their application in light-emitting and photovoltaic materials. When coordinated with metal ions, tpy exhibits immense potential for the synthesis of metallo-supramolecular or metallo-polymer materials. Therefore, tpy-based metallo-polymers are the primary focus of this study. Selected examples will be reviewed with a special emphasis on the properties of these functional systems, which can consequently help further their application in light-to-electricity or electricity-to-light conversion fields.

Keywords: terpyridine, light-emitting materials, photovoltaic, metallo-polymers, energy conversion

OPEN ACCESS

Edited by:

Qixin Zhou,
University of Akron, United States

Reviewed by:

Xiangyu Zou,
Shaanxi University of
Technology, China
Shengwei Shi,
Wuhan Institute of Technology, China

*Correspondence:

Xuegang Chen
xgchen@qust.edu.cn

Specialty section:

This article was submitted to
Organic Chemistry,
a section of the journal
Frontiers in Chemistry

Received: 06 August 2020

Accepted: 07 September 2020

Published: 14 October 2020

Citation:

Liu P, Shi G and Chen X (2020)
Terpyridine-Containing π -Conjugated
Polymers for Light-Emitting and
Photovoltaic Materials.
Front. Chem. 8:592055.
doi: 10.3389/fchem.2020.592055

INTRODUCTION

2,2':6',2''-Terpyridine (tpy) ligands are effective coordinating agents and key building blocks in supramolecular chemistry and materials because the 4'-position of the central pyridine ring can be easily substituted. Since tpy can yield stable complexes with d-block metal ions, it is widely used in linear polynuclear metal complexes, grids, and metallomacrocycles, as well as metal coordination polymers (Hofmeier and Schubert, 2004; Puntoriero et al., 2008; Wild et al., 2011; Schultz et al., 2012; Chakraborty and Newkome, 2018; Schmolke et al., 2019; Qian et al., 2020). Nowadays, energy conversion materials play a vital role in modern life and industry. Among these, photoelectric materials, which include both electricity-to-light and light-to-electricity conversion materials, are especially important (Deng et al., 2018, 2019; Zhang et al., 2019, 2020). The advantages of tpy-based metallo-polymers, increased coordination with transition metal ions, easily modifiable molecular structure, performance, excellent electrochemical properties, and good thermal stability, render them appropriate candidates for application in photoelectric materials and devices. Here, we review the most important results that deal with the synthesis of π -conjugated polymers containing tpy moieties, with an emphasis on metallo-polymers, and their application in light-emitting and photovoltaic materials and devices.

LIGHT-EMITTING MATERIALS

Terpyridine in the Side Chain

As a tridentate ligand, tpy can form stable complexes with many metal ions, including transition metal ions and rare earth ions, and is therefore used in light-emitting materials. Several organic

light-emitting diodes (OLEDs) based on tpy complexes were fabricated and evaluated, and the tpy units introduced into the side chain of the functional polymers were usually coordinated with metals. In 2011, Dumur et al. (2011) published a study about the synthesis of two random copolymers bearing pendant mixed-ligand orthometallated tpy-based cationic Ir(III) complexes and their application emitters in light-emitting electrochemical cells (LECs) or as dopants in OLEDs. The polymers were obtained from the copolymerization of tpy-containing monomers and styrene through nitroxide-mediated polymerization. The resulting polymers possessed good film-forming properties, which were attributed to the polystyrene structures in the main chain. However, the absence of charge carriers and phase segregation made it difficult to inject holes, leading to the development of poor emission properties, such as brightness ($70 \text{ cd}\cdot\text{m}^{-2}$) and efficiency ($5 \text{ cd}\cdot\text{m}^{-2}$). Furthermore, the results showed that in cationic metallo-polymers, a minimum iridium concentration of 5% is necessary for light emission.

Lanthanides, or rare earths, compose the 5d block of the periodic table. Most Ln(III) ions are luminescent and play a vital role in lighting and light conversion (Ozawa and Itoh, 2003; Kotova et al., 2018), and tpy and tpy-like ligands showed several interesting luminescent properties when combined with lanthanide ions (Beck and Rowan, 2003). Ghosh et al. (2015) reported the multicolor luminescent properties of elastin-like polymers (ELPs) with tpy derivatives incorporated into their side chains. The tpy ligand was conjugated with an ELP through the amidation reaction between 4-amino-functionalized-tpy and a carboxyl group in the ELP. The tpy moieties acted not only as ligands for complexation with lanthanide ions [including Eu(III), Tb(III), Dy(III), Er(III), and Nd(III)] but also as an antenna. Consequently, they showed strong light absorption and then transferred the energy to the emitting metal ions, which resulted in high emission efficiency and sharp emission peaks. The photoluminescence (PL) spectra ranged from the visible to the near-infrared (NIR) regions (1,450–1,600 nm), and the direct excitation wavelength (λ_{exc}) of the ligands was 395 nm. Since the lanthanide ions have no absorption at 395 nm, the NIR luminescence was associated with the intramolecular energy transfer from the photosensitizing organic ligands. Ru et al. (2014) also reported a similar energy transfer from polymer ligands to the emitting level of the rare earth ions in luminescent materials of Eu(III) coordinated by a tpy-functionalized poly(ionic liquid). The emission spectrum excited at 340 nm showed the characteristics of Eu^{3+} emissions in the 570–725-nm range without any broad emission band from the polymers. Yang et al. (2013) reported three nearly monochromatic red electroluminescent (EL) chelating polymers containing carbazole segments and tpy moieties, which serve as neutral ligands to coordinate with the $\text{Eu}(\text{2-thenoyltrifluoroacetate})^3$ complex. Electroluminescence studies demonstrated that the EL devices of Eu-polymers based on tpy as a neutral ligand exhibited red bright emissions. Moreover, a maximum luminance of $68.2 \text{ cd}\cdot\text{m}^{-2}$ was recorded for the double-layer devices.

In addition to their advantageous coordination with metal ions, π -conjugated tpy units in the side chains can also bring

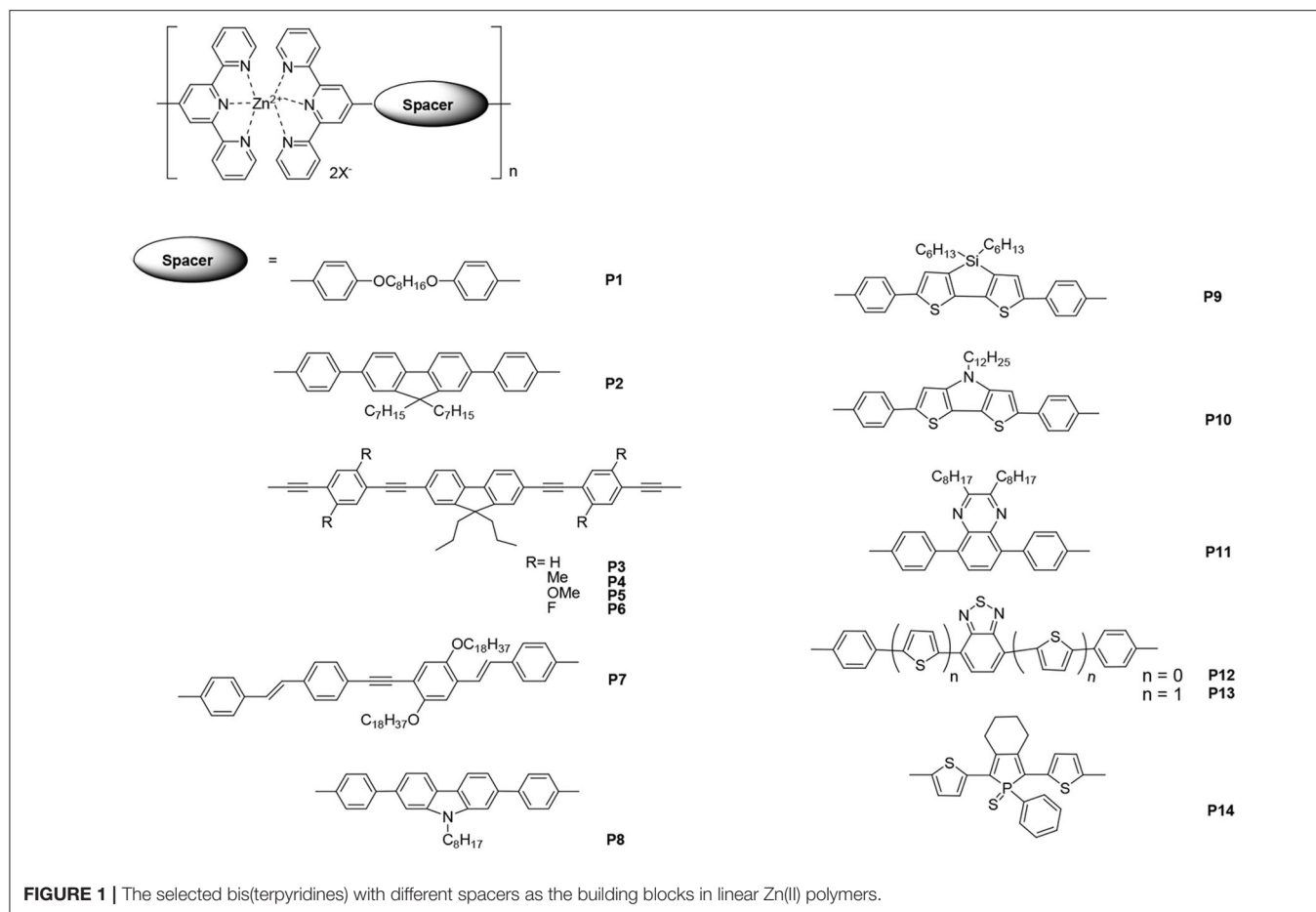
about various interesting structures and their corresponding properties. In 2017, Wang et al. (2017) reported about the preparation of a novel white-light-emitting fluorescent polymeric material via aggregation of a single fluorescent chromophore through intermolecular quadruple hydrogen bonding. The material was later used as a gel to fabricate a protected quick response code. Interestingly, the pyridinium salt monomer, which was a donor-acceptor structure and attached to the tpy unit, emitted blue light, whereas the supramolecular polymer gel created by radical polymerization showed strong white fluorescence under UV light. Two fluorescence emission peaks were observed at ~ 474 and 571 nm, which was the result of the aggregation of the chromophore and the formation of a charge transfer complex based on the tpy moieties in the polymers' side chain.

Terpyridine as Part of the Main Chain

The linear polymers containing tpy units are discussed in this section. The metallo-polymers produced by the introduction of metal ions into the π -conjugated main chains could possess interesting optical properties. Zinc ions are the most common metal ions used for light-emitting materials because complexation with zinc ions will not cause fluorescence quenching and may even enhance fluorescence. **Figure 1** lists the selected zinc-tpy-based polymers that are employed in light-emitting materials.

Emission properties such as wavelength and/or efficiency can be regulated by modifying the conjugated spaces connected with bis(tpys). In 2003, Yu et al. (2003) reported the synthesis of a family of self-assembled zinc-tpy-based polymers, which emit violet to yellow light, via self-assembly reactions. The spaces between the bispyridines were involved in flexible and rigid structures. Most of the resulting metallo-polymers exhibited higher PL quantum yields compared with that of monomers, and the emission was attributed to intra-ligand $^1(\pi-\pi)$ fluorescence. Among these polymers, polymers **P1** and **P2** were fabricated into an EL device with a single layer configuration. Blue (CIE: $x = 0.15$, $y = 0.21$) and yellow (CIE: $x = 0.46$, $y = 0.50$) emissions with a maximum luminance of 1,700 and 2,380 $\text{cd}\cdot\text{m}^{-2}$ were obtained, respectively. The results indicated that these Zn(II)-containing metallo-polymers are promising light-emitting materials for polymer light-emitting devices (PLEDs). Chen and Lin (2007) reported similar metallo-polymers **P3–P6**, in which central π -aromatic 9,9-dipropylfluorenes were linked to tpy units through phenylene/ethynylene fragments. Overall, the different substituents on the metallo-polymers caused adjustable photophysical and thermal properties. The decomposition temperatures (T_d) of the monomers under a nitrogen atmosphere ranged from 297 to 351°C, while those of the corresponding polymers ranged from 325 to 410°C. The EL emission colors of polymers **P4**, **P5**, and **P6** were yellow to orange (at a bias voltage of ~ 10 V), and the turn-on voltages of all devices were 6 V. The polymer **P5** showed the best power efficiency, external quantum yield, and brightness, which were 0.33 $\text{cd}\cdot\text{A}^{-1}$ (at 14 V), 1.02%, and 931 $\text{cd}\cdot\text{m}^{-2}$

¹Singlet excited state.



(at 14 V), respectively. In another study, a series of main-chain metallo-polymers, e.g., **P7**, was prepared through the self-assembly of rigid-linear π -conjugated bis(tpy) monomers with Zn(II) ions (Winter et al., 2009). Solution-processing methods such as spin coating and inkjet printing were applied to prepare thin homogeneous films for photophysical studies; the metallo-polymer **P7** exhibited intense yellow PL emission [PL quantum yield of 0.82 in $\text{CHCl}_3/(\text{CH}_3)_2\text{NC}(\text{O})\text{H}$]. Compared with the corresponding PL spectra of **P7** in the solid state, a red shift was observed at the emission maximum (~ 30 nm). Furthermore, the EL performances displayed the potential of these polymers as light-emitting materials for PLEDs.

Li et al. (2016) synthesized three new building blocks containing the tpy electron-acceptor motif and the electron-donor fused-ring carbazole, dithienosilole, and dithienopyrrole motifs. The introduction of Zn(II) initiated the self-assembly polymerization that led to the formation of their corresponding metallo-polymers. The PL maxima of polymers **P8**, **P9**, and **P10** in the film were 443, 553, and 586 nm, respectively. Compared with the monomeric building blocks, the sharp red shifts in the polymers' PL arose from the incorporation of the transition metal ion into the backbones of the polymers, which also enhances the electron-deficient ability of the tpy moieties. Consistent with their photophysical properties, the modification by spacers with

strong electron-donating ability increased the highest occupied molecular orbital (HOMO) level, whereas coordination with Zn(II) led to lower unoccupied molecular orbital (LUMO), which resulted in light-emitting materials with narrow band gaps (i.e., 2.07, 1.97, and 1.56 eV for **P8**, **P9**, and **P10**, respectively).

There have also been studies about introducing certain dye segments into the main chains of tpy-based metallo-polymers. Wild et al. (2013) described a variety of Zn(II) bis(tpy) metallo-polymers with a spacer dye moiety surrounded by thiophene donors. The tuning of the photophysical properties of these polymers can be obtained by systematically modifying the dye and the conjugation length. Owing to the dynamic nature of the Zn(II) complex, a great number of emission colors can be obtained depending on the energy transfer processes used and by carefully regulating the mixing ratio of blue **P11** ($\lambda_{\text{PL}} = 443$ nm), green **P12** ($\lambda_{\text{PL}} = 503$ nm), and red **P13** ($\lambda_{\text{PL}} = 606$ nm) light-emitting metallo-homopolymers. Moreover, in order to screen the thin-film photophysical properties in a reproducible and material-saving manner, the inkjet printing technique was employed to separately print every single color and subsequently print one solvent layer to assemble statistical copolymers.

Contrarily, Vitvarová et al. (2017) synthesized a novel building block that comprised a substituted phosphole ring

surrounded by two thiophene rings with tpy fragments as end-groups. It was then coordinated with metal ions such as Co^{2+} , Cu^{2+} , Fe^{2+} , Ni^{2+} , and Zn^{2+} to produce metallo-supramolecular polymers (MSPs). The MSP with Fe^{2+} ion couplers showed very slow constitutional dynamics and a strong band of metal-to-ligand charge transfer (MLCT) transitions, whereas the MSPs with Co^{2+} , Cu^{2+} , and Ni^{2+} ion couplers exhibited variable dynamics and no MLCT bands. All of these MSPs showed luminescence quenching. However, the zinc-containing polymer **P14**, which exhibited very fast constitutional dynamics, showed the highest luminescence intensity at ~ 641 nm of PL maximum (luminescence quantum efficiency $\Phi = 0.5$) without any MLCT transitions. Evidently, luminescence or quench is not related to MLCT transitions.

Other metals such as cadmium (Chen et al., 2007) and rare earth metals (Sato and Higuchi, 2012) can also be employed in the construction of tpy-based luminescent MSPs. Furthermore, several novel structures such as copolymers containing electron-withdrawing and electron-donating building blocks (Schlütter et al., 2010) and 2D (Fermi et al., 2014; Yin et al., 2018) polymers have been reported in the past decade.

PHOTOVOLTAIC MATERIALS

Owing to their flexibility, low cost, and ease of fabrication and manipulation, organic photovoltaic cells (OPVs) have garnered much attention in recent years (Hains et al., 2010). Studies on OPVs aim to improve the range of absorption, efficiency, charge transport, and stability of organic materials and cell devices. One of the key ways to achieve this is by improving the spectral match between solar light and organic sensitizing materials. Since ruthenium complexes exhibit reversible Ru(II)/Ru(III) redox processes and MLCT transitions in the range 500–600 nm, organic materials based on ruthenium polypyridine complexes are widely used in OPVs (Zakeeruddin et al., 2002; Numata et al., 2013). Cheng et al. (2008) firstly reported synthesis and photovoltaic performances of the metallo-polymers based on tpy units. Here, selected polymers containing Ru(II) -tpy chromophores, which are well-known photoactive moieties, will be discussed. In these metallo-polymers, the occurrence of ttps in side chains is rare, so most of them have Ru(II) -tpy as a part of their main chains (Figure 2).

Vellis et al. (2008) reported a new series of conjugated building blocks that bear terminal tpy moieties, which were connected to the central cores that were substituted with fluorine or phenylene segments through a vinylene bond. Coordinated with Ru(II) , the metallo-polymers **P15**, **P16**, and **P17** can be obtained without any catalyst. In addition, a star-shaped metallo-polymer based on triphenylamine was also synthesized. The absorption range of the Ru(II) -tpy-based metallo-polymers was 300–550 nm, which was a result of the ligand-centered (LC) transitions at shorter wavelengths and MLCT transitions at longer wavelengths. In

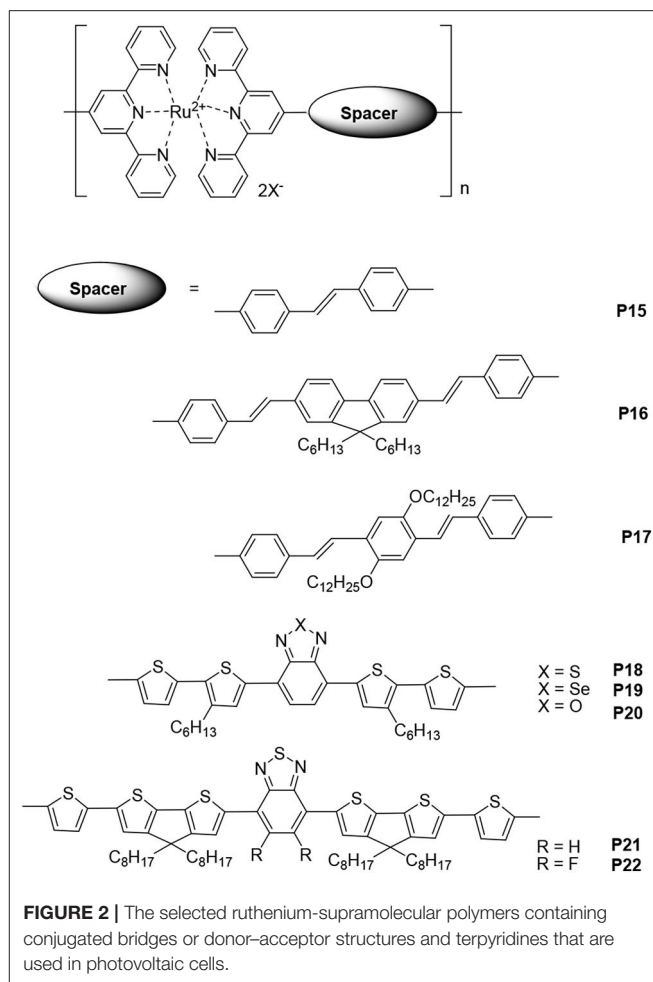


FIGURE 2 | The selected ruthenium-supramolecular polymers containing conjugated bridges or donor-acceptor structures and terpyridines that are used in photovoltaic cells.

order to evaluate the photovoltaic properties of these metallo-polymers, bulk heterojunction devices with the structure ITO/PEDOT/ Ru(II) -polymers/P3HT:PCBM (1:1 w/w)/Ca/Al were also fabricated. Among these polymers, polymer **P15** exhibited the highest power conversion efficiency (PCE) value (0.71%). The short-circuit current (J_{sc}), open-circuit voltage (V_{oc}), and fill factor (FF) values were $4.2 \text{ mA}\cdot\text{cm}^{-2}$, 0.48 V, and 35%, respectively. It needs to be noted that the preliminary results were obtained without optimization of device fabrication conditions.

Introducing electron-donor and electron-acceptor structures can decrease the HOMO level and increase the absorption range and thereby increase the photovoltaic cell performance. Padhy et al. (2011) reported about Ru(II) -supramolecular polymers **P18**, **P19**, and **P20**. The ideal HOMO/LUMO levels, reduced energy gaps, and broad absorption range (300–750 nm) were obtained by introducing donor-acceptor structures, such as electron-acceptor benzothiadiazole, benzoselenodiazole, and benzoxadiazole units and electron-donor thiophene units, into the main chains of the metallo-polymers. The optimal photovoltaic cell device, based on the blended polymer **P18**:PCBM = 1:1 (w/w), had PCE = 0.45%, $V_{oc} = 0.61$ V, $J_{sc} =$

2.18 mA·cm⁻², and FF = 34.1%. Feng et al. (2013) synthesized bis(tpy) ligands with cyclopentadithiophene-benzothiazole conjugated bridges, and supramolecular polymers (**P21** and **P22**) containing Ru(II) were obtained via a supramolecular self-assembly process. In the main chains of these polymers, the cyclopentadithiophene and thiophene units were used as electron donors (D), and benzothiazole and fluorinated benzodiazole units were used as electron acceptors (A). The low-lying HOMO levels for **P21** and **P22** were -5.22 and -5.27 eV, respectively, and their electrochemical band gaps were 1.60 and 1.58 eV, respectively. Owing to the stronger π - π stacking, a result of the F-H, F-S, and/or F-F interactions, polymer **P22** exhibited a mobility one order of magnitude higher than that of polymer **P21**. The hole mobilities of **P21** and **P22** were 7.5×10^{-6} cm²·V⁻¹s⁻¹ and 2.8×10^{-5} cm²·V⁻¹s⁻¹, respectively. The photovoltaic device fabricated with polymer **P22** and with ITO/PEDOT:PSS/polymer:PC₇₁BM/Ca/Al structure exhibited the highest PCE (2.66%) with a V_{oc} = 0.73 V, J_{sc} = 7.12 mA·cm⁻², and FF = 0.51. The improved performance was a result of the introduction of the fluorine atom that then caused the low-lying HOMO level, narrow band gap, high hole mobility, and fine phase separation. Thus, the results of photovoltaic devices based on metallo-polymers are definitely inspiring.

Furthermore, a number of metallo-copolymers, block copolymers, and random copolymers have been reported in a few studies (Duprez et al., 2005; Padhy et al., 2012). Although their photovoltaic performances are not excellent, the incorporated π -conjugated units have several interesting properties. In fact, metal ions were not necessary to construct novel conjugated main chains. A recent study described the synthesis of various conjugated polymers containing only tpy segments, in which tpy-substituted carbazole (TPCz) was used as the electron donor, followed by the fabrication and evaluation of photovoltaic cells (Wang et al., 2020).

REFERENCES

- Beck, J. B., and Rowan, S. J. (2003). Multistimuli, multiresponsive metallo-supramolecular polymers. *J. Am. Chem. Soc.* 125, 13922–13923. doi: 10.1021/ja038521k
- Chakraborty, S., and Newkome, G. R. (2018). Terpyridine-based metallosupramolecular constructs: tailored monomers to precise 2D-motifs and 3D-metallocages. *Chem. Soc. Rev.* 47, 3991–4016. doi: 10.1039/C8CS00030A
- Chen, X., Ma, L., Cheng, Y., Xie, Z., and Wang, L. (2007). Luminescent supramolecular polymers: Cd²⁺-directed polymerization and properties. *Polym. Int.* 56, 648–654. doi: 10.1002/pi.2183
- Chen, Y. Y., and Lin, H. C. (2007). Synthesis and characterization of light-emitting main-chain metallo-polymers containing bis-terpyridyl ligands with various lateral substituents. *J. Polym. Sci. A Polym. Chem.* 45, 3243–3255. doi: 10.1002/pola.22073
- Cheng, K. W., Mak, C. S. C., Chan, W. K., Ng, A. M. C., and Djuricic, A. B. (2008). Synthesis of conjugated polymers with pendant ruthenium terpyridine trithiocyanato complexes and their applications in heterojunction photovoltaic cells. *J. Polym. Sci. A Polym. Chem.* 46, 1305–1317. doi: 10.1002/pola.22471

PERSPECTIVE

The introduction of metal ions to the main chains or side chains of polymers imparts them with a variety of properties. In light-emitting devices, different combinations of metals and ligands emit different colors, and they have high EL efficiency and brightness. Conversely, compared with the traditional polymers, in which the structures are connected by covalent bonds, the preparation of metallo-polymers has mild reaction conditions and does not require any catalyst, and the polymer structures are definite and easy to modify. Consequently, the HOMO/LUMO levels, energy gaps, spectral match with solar light, morphologies of polymer films, and photovoltaic device performances can be improved by carefully designing bridges connected to bis(tpy). Therefore, it is possible to predict that an increasing number of tpy-containing complexes or polymers can be synthesized in the future, that the unknown and puzzling problems involved in supramolecular chemistry of tpy and metal ions can be elucidated, and that better performances for light-to-electricity or electricity-to-light conversion materials and devices can be achieved.

AUTHOR CONTRIBUTIONS

PL and GS collected, arranged documents, and wrote some paragraphs for draft. XC prepared full text and revised. All authors contributed to the article and approved the submitted version.

FUNDING

This contribution was financially supported by the National Natural Science Foundation of China (NSFC) (No. 20804022) and the Natural Science Foundation of Shandong Province (No. ZR2011BM001).

- Deng, Z., Ai, T., Li, R., Yuan, W., Zhang, K., Du, H., et al. (2019). Conjugated polymers containing building blocks 1,3,4,6-tetraarylpyrrolo[3,2-b]pyrrole-2,5-dione (isoDPP), benzodipyrrolidone (BDP) or naphthodipyrrolidone (NDP): a review. *Polymers* 11:1683. doi: 10.3390/polym11101683
- Deng, Z., Li, L., Ai, T., Hao, X., and Bao, W. (2018). Centrosymmetric thiophenemethylenoxindole-based donor-acceptor copolymers for organic field-effect transistors. *Macromol. Rapid Commun.* 2018:1800073. doi: 10.1002/marc.201800073
- Dumur, F., Guillauneuf, Y., Guerlin, A., Wantz, G., Bertin, D., Miomandre, F. et al. (2011). Random copolymers with pendant cationic mixed-ligand terpyridine-based iridium(III) complexes: synthesis and application in light emitting devices. *Macromol. Chem. Phys.* 212, 1616–1628. doi: 10.1002/macp.201100167
- Duprez, V., Biancardo, M., Spanggaard, H., and Krebs, F. C. (2005). Synthesis of conjugated polymers containing terpyridine-ruthenium complexes: photovoltaic applications. *Macromolecules* 38, 10436–10448. doi: 10.1021/ma051274f
- Feng, K., Shen, X., Li, Y., He, Y., Huang, D., and Peng, Q. (2013). Ruthenium(II) containing supramolecular polymers with cyclopentadithiophene-benzothiazole conjugated bridges for photovoltaic applications. *Polym. Chem.* 4, 5701–5710. doi: 10.1039/c3py00628j

- Fermi, A., Bergamini, G., Roy, M., Gingras, M., and Ceroni, P. (2014). Turn-on phosphorescence by metal coordination to a multivalent terpyridine ligand: a new paradigm for luminescent sensors. *J. Am. Chem. Soc.* 136, 6395–6400. doi: 10.1021/ja501458s
- Ghosh, K., Balog, E. R. M., Kahn, J. L., Shepherd, D. P., Martinez, J. S., and Rocha, R. C. (2015). Multicolor luminescence from conjugates of genetically encoded elastin-like polymers and terpyridine-lanthanides, *macromol. Chem. Phys.* 216, 1856–1861. doi: 10.1002/macp.201500103
- Hains, A. W., Liang, Z., Woodhouse, M. A., and Gregg, B. A. (2010). Molecular semiconductors in organic photovoltaic cells. *Chem. Rev.* 110, 6689–6735. doi: 10.1021/cr9002984
- Hofmeier, H., and Schubert, U. S. (2004). Recent developments in the supramolecular chemistry of terpyridine-metal complexes. *Chem. Soc. Rev.* 33, 373–399. doi: 10.1039/B400653B
- Kotova, O., Bradberry, S. J., Savvasachi, A. J., and Gunnlaugsson, T. (2018). Recent advances in the development of luminescent lanthanide-based supramolecular polymers and soft materials. *Dalton Trans.* 47, 16377–16387. doi: 10.1039/C8DT03768J
- Li, F., Hu, Z., Qiao, H., Liu, L., Hu, J., Chen, X., et al. (2016). Terpyridine-based donor-acceptor metallo-supramolecular polymers with tunable band gaps: synthesis and characterization. *Dyes Pigm.* 132, 142–150. doi: 10.1016/j.dyepig.2016.04.031
- Numata, Y., Zhang, S., Ynag, X., and Han, L. (2013). Cosensitization of ruthenium-polypyridyl dyes with organic dyes in dye-sensitized solar cells. *Chem. Lett.* 42, 1328–1335. doi: 10.1246/cl.130701
- Ozawa, L., and Itoh, M. (2003). Cathode ray tube phosphors. *Chem. Rev.* 103, 3835–3856. doi: 10.1021/cr0203490
- Padhy, H., Ramesh, M., Patra, D., Satapathy, R., Pola, M. K., Chu, H.-C., et al. (2012). Synthesis of main-chain metallo-copolymers containing donor and acceptor bis-terpyridyl ligands for photovoltaic applications. *Macromol. Rapid Commun.* 33, 528–533. doi: 10.1002/marc.201100752
- Padhy, H., Sahu, D., Chiang, I.-H., Patra, D., Kekuda, D., Chu, C.-W., et al. (2011). Synthesis and applications of main-chain Ru(II) metallo-polymers containing bis-terpyridyl ligands with various benzodiazole cores for solar cells. *J. Mater. Chem.* 21, 1196–1205. doi: 10.1039/C0JM02532A
- Puntoriero, F., Campagna, S., Stadler, A. M., and Lehn, J.-M. (2008). Luminescence properties and redox behavior of Ru(II) molecular racks. *Coord. Chem. Rev.* 252, 2480–2492. doi: 10.1016/j.ccr.2007.12.009
- Qian, Y., Yang, H., and Wang, Y. (2020). A novel bis(terpyridine) with π conjugated phenyl viologen and its metallo- supramolecular polymers: synthesis and electrochromism. *Dyes Pigm.* 176:108251. doi: 10.1016/j.dyepig.2020.108251
- Ru, Q., Xue, Z., Wang, Y., Liu, Y., and Li, H. (2014). Luminescent materials of europium(III) coordinated by a terpyridine-functionalized poly(ionic liquid). *Eur. J. Inorg. Chem.* 2014, 469–474. doi: 10.1002/ejic.201301168
- Sato, T., and Higuchi, M. (2012). A vapoluminescent Eu-based metallo-supramolecular polymer. *Chem. Commun.* 48, 4947–4949. doi: 10.1039/c2cc30972f
- Schlütter, F., Wild, A., Winter, A., Hager, M. D., Baumgaertel, A., Friebe, C., et al. (2010). Synthesis and characterization of new self-assembled metallo-polymers containing electron-withdrawing and electron-donating bis(terpyridine) Zinc(II) moieties. *Macromolecules* 43, 2759–2771. doi: 10.1021/ma902110v
- Schmolke, W., Ahmadi, M., and Seiffert, S. (2019). Enhancement of metallo-supramolecular dissociation kinetics in telechelic terpyridine-capped poly(ethylene glycol) assemblies in the semi-dilute regime. *Phys. Chem. Chem. Phys.* 21, 19623–19638. doi: 10.1039/C9CP03911B
- Schultz, A., Li, X., Barkakaty, B., Moorfield, C. N., Wesdemiotis, C., and Newkome, G. R. (2012). Stoichiometric self-assembly of isomeric, shape-persistent, supramacromolecular bowtie and butterfly structures. *J. Am. Chem. Soc.* 134, 7672–7675. doi: 10.1021/ja303177v
- Vellis, P. D., Mikroyannidis, J. A., Lo, C.-N., and Hsu, C.-S. (2008). Synthesis of terpyridine ligands and their complexation with Zn^{2+} and Ru^{2+} for optoelectronic applications. *J. Polym. Sci. A Polym. Chem.* 46, 7702–7712. doi: 10.1002/pola.23073
- Vitvarová, T., Svoboda, J., Hissler, M., and Vohlídal, J. (2017). Conjugated metallo-supramolecular polymers containing a phosphole unit. *Organometallics* 36, 777–786. doi: 10.1021/acs.organomet.6b00822
- Wang, H., Ji, X., Li, Z., Zhu, C. N., Yang, X., Li, T., et al. (2017). Preparation of a white-light-emitting fluorescent supramolecular polymer gel with a single chromophore and use of the gel to fabricate a protected quick response code. *Mater. Chem. Front.* 1, 167–171. doi: 10.1039/C6QM00164E
- Wang, S.-H., Wang, T.-W., Tsai, H.-C., Yang, P.-C., Huang, C.-F., and Lee, R.-H. (2020). Synthesis of the diketopyrrolopyrrole/terpyridine substituted carbazole derivative based polythiophenes for photovoltaic cells. *RSC Adv.* 10, 9525–9535. doi: 10.1039/C9RA09649C
- Wild, A., Teichler, A., Ho, C.-L., Wang, X.-Z., Zhan, H., Schlütter, F., et al. (2013). Formation of dynamic metallo-copolymers by inkjet printing: towards white-emitting materials. *J. Mater. Chem. C* 1, 1812–1822. doi: 10.1039/c2tc00552b
- Wild, A., Winter, A., Schlütter, F., and Schubert, U. S. (2011). Advances in the field of π -conjugated 2,2':6',2''-terpyridines. *Chem. Soc. Rev.* 40, 1459–1511. doi: 10.1039/C0CS00074D
- Winter, A., Friebe, C., Chipper, M., Hager, M. D., and Schubert, U. S. (2009). Self-assembly of π -conjugated bis(terpyridine) ligands with zinc(II) ions: new metallosupramolecular materials for optoelectronic applications. *J. Polym. Sci. A Polym. Chem.* 47, 4083–4098. doi: 10.1002/pola.23469
- Yang, C., Xu, J., Zhang, Y., Li, Y., Zheng, J., Liang, L., et al. (2013). Efficient monochromatic red-light-emitting PLEDs based on a series of nonconjugated Eu-polymers containing a neutral terpyridyl ligand. *J. Mater. Chem. C* 1, 4885–4901. doi: 10.1039/c3tc30681j
- Yin, G.-Q., Wang, H., Wang, X.-Q., Song, B., Chen, L.-J., Wang, L., et al. (2018). Self-assembly of emissive supramolecular rosettes with increasing complexity using multitopic terpyridine ligands. *Nat. Commun.* 9, 567–577. doi: 10.1038/s41467-018-02959-w
- Yu, S. C., Kwok, C. C., Chan, W. K., and Che, C. M. (2003). Self-assembled electroluminescent polymers derived from terpyridine-based moieties. *Adv. Mater.* 15, 1643–1647. doi: 10.1002/adma.200305002
- Zakeeruddin, S. M., Nazeeruddin, M. K., Humphry-Baker, R., Péchy, P., Quagliotto, P., Barolo, C., et al. (2002). Synthesis, and application of amphiphilic ruthenium polypyridyl photosensitizers in solar cells based on nanocrystalline TiO_2 films. *Langmuir* 18, 952–954. doi: 10.1021/la0110848
- Zhang, H., Li, R., Deng, Z., Cui, S., Wang, Y., Zheng, M., et al. (2020). π -Conjugated oligomers based on aminobenzodifuranone and diketopyrrolopyrrole. *Dyes Pigm.* 181:108552. doi: 10.1016/j.dyepig.2020.108552
- Zhang, H., Liu, M., Yang, W., Judin, L., Hukka, T. I., Priimagi, A., et al. (2019). Thionation enhances the performance of polymeric dopant-free hole-transporting materials for perovskite solar cells. *Adv. Mater. Interfaces* 2019:1901036. doi: 10.1002/admi.201901036

Conflict of Interest: The authors declare that the research was conducted in the absence of any commercial or financial relationships that could be construed as a potential conflict of interest.

Copyright © 2020 Liu, Shi and Chen. This is an open-access article distributed under the terms of the Creative Commons Attribution License (CC BY). The use, distribution or reproduction in other forums is permitted, provided the original author(s) and the copyright owner(s) are credited and that the original publication in this journal is cited, in accordance with accepted academic practice. No use, distribution or reproduction is permitted which does not comply with these terms.



The Application of Organic Semiconductor Materials in Spintronics

Yixiao Zhang^{1,2}, Lidan Guo^{1,2*}, Xiangwei Zhu^{1,2} and Xiangnan Sun^{1,2,3*}

¹ Key Laboratory of Nanosystem and Hierarchical Fabrication, Chinese Academy of Sciences (CAS) Center for Excellence in Nanoscience, National Center for Nanoscience and Technology, Beijing, China, ² Center of Materials Science and Optoelectronics Engineering, University of Chinese Academy of Sciences, Beijing, China, ³ School of Materials Science and Engineering, Zhengzhou University, Zhengzhou, China

OPEN ACCESS

Edited by:

Haichang Zhang,
Qingdao University of Science and
Technology, China

Reviewed by:

Maning Liu,
Tampere University, Finland
Shian Ying,
Shandong University of Science and
Technology, China

*Correspondence:

Lidan Guo
guold@nanoctr.cn
Xiangnan Sun
sunxn@nanoctr.cn

Specialty section:

This article was submitted to
Organic Chemistry,
a section of the journal
Frontiers in Chemistry

Received: 30 July 2020

Accepted: 16 September 2020

Published: 22 October 2020

Citation:

Zhang Y, Guo L, Zhu X and Sun X
(2020) The Application of Organic
Semiconductor Materials in
Spintronics. *Front. Chem.* 8:589207.
doi: 10.3389/fchem.2020.589207

π -Conjugated semiconductors, primarily composed of elements with low atomic number, are regarded as promising spin-transport materials due to the weak spin-orbit coupling interaction and hence long spin relaxation time. Moreover, a large number of additional functions of organic semiconductors (OSCs), such as the abundant photo-electric properties, flexibility, and tailorability, endow the organic spintronic devices more unique properties and functionalities. Particularly, the integration of the photo-electric functionality and excellent spin transport property of OSCs in a single spintronic device has even shown great potential for the realization of spin manipulation in OSCs. In this review, the application of OSCs in spintronic study will be succinctly discussed. As the most important and extensive application, the long-distance spin transport property of OSCs will be discussed first. Subsequently, several multifunctional spintronic devices based on OSCs will be summarized. After that, the organic-based magnets used for the electrodes of spintronic devices will be introduced. Finally, according to the latest progress, spin manipulation in OSCs via novel spintronic devices together with other prospects and challenges will be outlined.

Keywords: organic spintronics, π -conjugated semiconductor, spin transport, multifunctional spintronic device, spin manipulation, spin valve

INTRODUCTION

A huge revolution has been made in the field of information storage since the discovery of the giant magnetoresistance effect and the development of spintronics in the past of 30 years (Baibich et al., 1988; Wolf et al., 2001). Organic semiconductors (OSCs) composed of light elements have weak spin-orbit coupling (SOC) interaction and thus long spin relaxation time with second level (Boehme and Lupton, 2013). According to the present researches, it has been shown that there is a great potential of excellent spin transport characteristic of OSCs at room temperature (Sun et al., 2013; Zhang et al., 2013; Guo et al., 2019b). In addition, the abundant functionalities of OSCs and interfacial properties between ferromagnetic electrodes and OSCs have further increased the application modes of OSCs in spintronics, which have attracted wide attention in the areas of chemistry, materials, and physics (Guo et al., 2019a).

In this review, the application strategies of OSCs in spintronic study will be summarized succinctly. First, spin transport as the most important application of OSCs in spintronics will be introduced. Second, combined with the unique properties of OSCs, several functional spintronic

devices will be introduced, including spin memory devices, spin photoresponse devices, spin photovoltaic devices, spin organic light-emitting diodes (spin-OLED), and flexible spin devices. Third, organic-based magnets which can be used as magnetic electrodes will be introduced. Finally, the prospects and challenges for realizing spin manipulation in OSCs will be discussed.

APPLICATION OF OSCS IN SPIN TRANSPORT

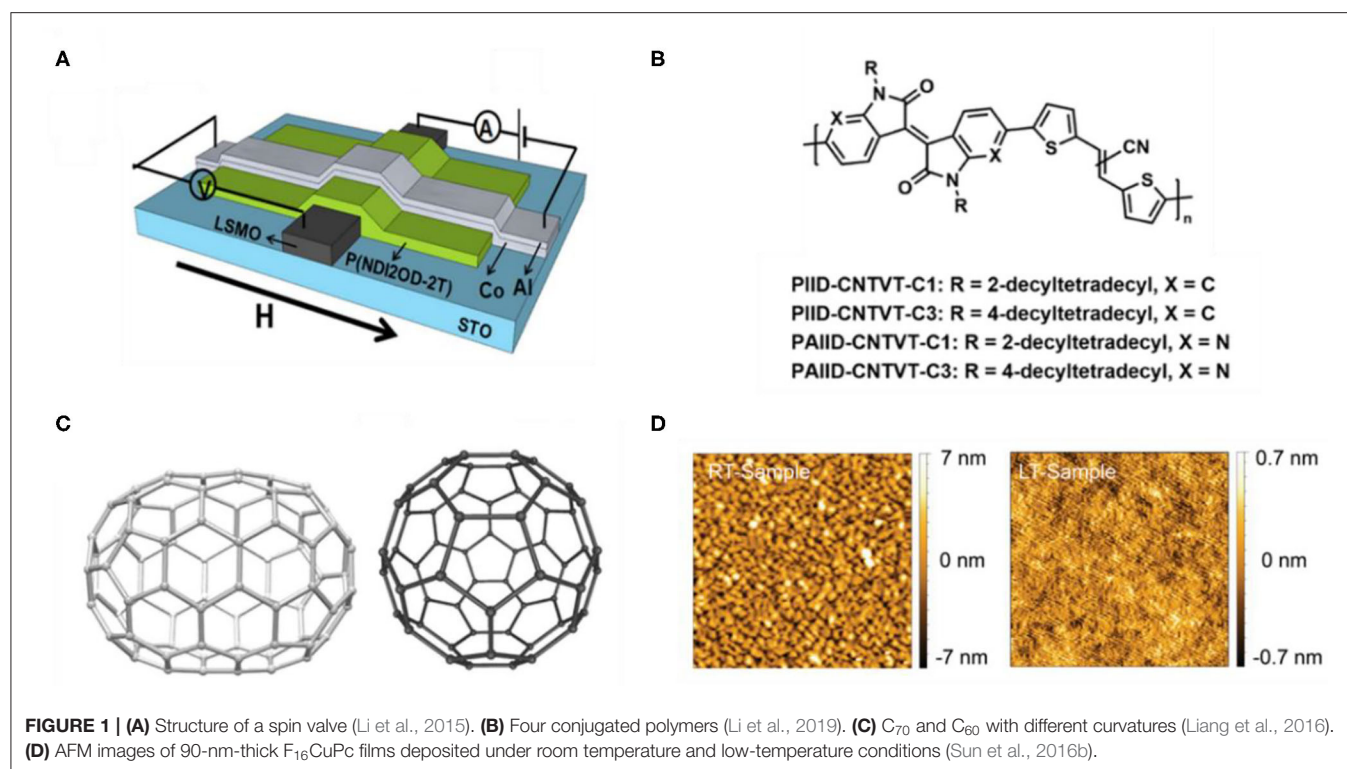
The long spin relaxation time of OSCs gives a great advantage in spin transport, and such advantage also constitutes the basis of functional spintronic devices. Spin valve is one of the most typical devices for spin transport study, which is composed of a spin-transport layer sandwiched between two ferromagnetic electrodes (**Figure 1A**) (Dediu et al., 2009; Sun et al., 2014a). The spin-polarized electrons are injected from one of the electrodes and transport in OSC thin film; finally, they are detected from another electrode (Jang and Richter, 2017). With sweeping the external magnetic field to configure the magnetization direction of the two electrodes as parallel (P) or antiparallel (AP), the device resistance can be tuned as low- (R_P) or high-resistance states (R_{AP}), respectively, which is the so-called spin valve effect and expressed by magnetoresistance [$MR = (R_{AP} - R_P)/R_{AP}$]. Such spin valve effect is the important evidence for demonstrating that the spin-polarized electrons have been successfully transported in OSC thin film, and the thickness of OSC can be considered as the spin transport length of OSCs (Sun et al., 2013; Zhang et al., 2013). It is worth noting that the aforementioned conclusion must be based on reliable spin valve preparation, that is, the soft OSC thin films should be ensured without the penetration resulting from the metal atoms during the device fabrication.

Based on the reliable spin valves, a series of studies on the molecular structure, composition, and aggregation structure of OSCs can be carried out, which have critical influence on the spin-transport performance. For instance, Li et al. have designed four conjugated polymers with analogous structures based on isoindigo (IID) units and researched the relation between molecular structure and spin transport property by measuring the spin valve effect (**Figure 1B**). They found that the introduction of pyridinic nitrogen can improve the MR value; however, the extent of alkyl chain branching points gets the opposite result (Li et al., 2019). Moreover, the effect of molecular curvature degree on spin relaxation time and spin transport length has been discussed. Liang et al. have observed that the spin transport length in the C_{70} thin film is apparently longer than that in C_{60} thin film at all temperatures through fabricating reliable carbon-based organic spin valves (**Figure 1C**) (Liang et al., 2016). The aforementioned researches provide guidance for how to avoid the negative effects on spin transport originated from molecular structure. As for element composition, Nguyen et al. have studied and compared the spin responses in different devices based on π -conjugated polymers made of protonated, H-, and deuterated, D-hydrogen. Because of D-hydrogen having a weaker hyperfine interaction, the results show that the device

based on D-hydrogen obtained a longer spin diffusion length and a larger MR (Nguyen et al., 2010). Furthermore, the effect of the aggregation structures of OSCs on spin transport property has been researched. By controlling the substrate temperature when thermally evaporating the molecular layer, Sun et al. have fabricated two types of spin valves based on polycrystalline and amorphous fluorinated copper phthalocyanine ($F_{16}CuPc$) thin film, respectively (**Figure 1D**) (Sun et al., 2016b). By comparing the magnetoresistance results of the two types of devices, distinctly, the spin valve with amorphous thin film of $F_{16}CuPc$ possesses larger MR and longer spin transport length due to the lower spin scattering from the grain boundary and greater resistance to the top electrode penetration.

In addition to spin valve, pure spin current device is another type of device to study spin transport, which has the trilayer structure of ferromagnet/OSC/nonmagnetic (Ando et al., 2013; Jiang et al., 2015; Sun et al., 2016a). A pure spin current is a flow of electron spin angular momentum carried by electrons; however, there is no net charge current that can be detected in the external circuit because the flow direction of electrons with opposite spin orientation are opposite according to spin pumping principle. The pure spin current is injected by spin pumping through a ferromagnetic resonance in the magnetic insulator (Ando et al., 2013; Watanabe et al., 2014). Different from the hopping spin transport mechanism in spin valves, the spin transport in the pure spin current device is due to an exchange interaction between polarons at the interface, which is much faster than the carrier mobility (Jiang et al., 2015). Based on pure spin current device, Watanabe et al. have demonstrated the ability of polarons to carry pure spin currents over hundreds of nanometers with millisecond spin relaxation time (Watanabe et al., 2014). Thus, keeping the study of pure spin current is meaningful, which plays a crucial role in transmitting, processing, and storing information (Watanabe et al., 2014).

In fact, although the application of OSCs in spin transport study has been developed for more than 10 years, there are still some challenges that need to be conquered. First, the effective and universal preparation method of reliable spin valve is still lacking, which has seriously limited the progress of room-temperature operable spin valve, functional spintronic devices, and the repeatability of devices. So far, several methods directed at top electrode preparation with low damage on organic materials have been proposed, such as depositing top electrodes at cryogenic temperature (Sun et al., 2016b) and top electrode transfer method (Ding et al., 2018). Second, systematical studies on the relationship between the spin transport characteristic and material composition and structure are still few. Thus, more researches are required for enriching the theoretical and experimental foundation of organic spintronics. Third, a mass of novel materials with high mobility or unique properties, such as soluble semiconductors, organic single crystal, and co-crystal materials, are urgently needed to be applied in spin transport study (Wang et al., 2016; Tsurumi et al., 2017). However, relative technical matters should be solved before this, such as the problem of spin-scattering increasement caused by solvent residue, the vacancy formed by solvent evaporation, and the demand for novel preparation method of spintronic device



based on crystal materials. Therefore, novel device fabrication techniques are urgently explored in the following research, especially the construction of reliable lateral spintronic devices; however, the progress is still slow.

APPLICATION OF OSCS IN FUNCTIONAL SPIN DEVICES

Aside from the excellent spin transport property, some of the OSCs also possess distinct electro-optical characteristics or flexibility, which make the OSCs applicable to the construction of multifunctional spin devices.

Spin Memory Devices

Because of the non-linear electrical property of OSC-based spin valve, the electrical memory effect can be combined with the spin-valve effect and even for achieving the electrically controllable MR. The mechanism of the electrical memory in spin valves is the formation and break of conductive filaments, which is controlled by the external voltage and the design of interface (Wang et al., 2015). The interface is required to be a critical state, so that the filaments can easily form and break by changing the external voltage. Therefore, it is easy to realize different non-volatile resistive states, which is the typical performance of spin memory devices.

Based on the commonly used π -conjugated OSC of tris(8-hydroxyquinolino)aluminum (Alq_3) and the wide voltage irreversible area of device, Hueso et al. have reported the first hybrid spin valve with electrically non-volatile memory

functionalities simultaneously (Hueso et al., 2007). Inspired by this work, a full electrical controllable magnetoresistance with multiple tunable non-volatile states (Prezioso et al., 2011) and its capability of information processing (Prezioso et al., 2013) have been further investigated in a similar spin valve based on the same OSC. The excellent memory ability of 32 states or 5-bit storage in this Alq_3 -based spin valve lays the foundation of multi-state storage devices.

In fact, although the existing researches amply indicate the feasibility of spin-valve effect plus electrical memory, how to accurately control the critical interface for realizing both the spin injection or detection and electrical memory is still a tough work in this direction. Several factors have influence on such critical interfacial state of the filament formation and break, such as the device preparation method, the surface roughness, and morphology of the OSC. The mixture of multiple factors makes it difficult to summarize a universal rule for reaching this critical state; therefore, a large number of experiments and more efforts are needed. In addition, only a few OSCs have been applied in spin memory devices; other diverse OSCs are eagerly expected to be used to broaden and deepen the research of this device (Yuan et al., 2019; Liu et al., 2020). Furthermore, such type of spin memory device still has a big gap for future practical application; the working stability even at room temperature will be a long-term objective.

Spin Photoresponse Devices

In addition to the semiconductor characteristic, most of the OSCs also have abundant optical properties and thus can be used for sensors. Photoresponse effect is one of the common optical

properties where the photogenerated carriers will influence the device resistance during the external light irradiation. On the basis of this point, $F_{16}CuPc$, possessing photoresponse and air stability, served as the spacer of spin valve, and four resistance states can be output in a spin photoresponse device as shown in **Figure 2A** (Sun et al., 2016b). In this device, the photogenerated carriers are non-spin-polarized, so that the photogenerated carriers can only influence the output current but for the absolute spin-polarized current. To release the photoresponse characteristic of OSCs, several important techniques play a key role, including the application of liquid nitrogen during the fabrication of organic layer and top electrode, and the interface layer of leaky- AlO_x , which facilitates the real spin transport occurring in $F_{16}CuPc$ and thus the photoresponse effect. Meanwhile, a large MR of about 4% and a long spin transport distance of 180 nm at room temperature have been detected, which prove the excellent properties of this device again. For the future development, more π -conjugated materials with excellent spin transport and photosensitive abilities are required to be applied in spin photoresponse devices, and novel functions may be explored concomitantly.

Spin Photovoltaic Devices

Recently, the photovoltaic character of OSCs has also been successfully used in spintronic study. By combining the spin valve effect and photovoltaic effect together, spin photovoltaic device, one of the important multifunctional spintronic devices, has been realized. On the basis of the reliable fabrication of spintronic device and high-efficiency spin injection, the spin transport through the OSC layer should be ensured, otherwise, the spin photovoltaic effect should not be implemented.

Based on C_{60} , which possesses both high electron mobility and photovoltaic property, Sun et al. have fabricated the first organic spin photovoltaic device (Sun et al., 2017). As an independent spin valve, a large MR of 6.5% has been measured at room temperature, which shows the excellent spin transport property of C_{60} and the great quality of device. In such device, the photogenerated current originated from the photovoltaic effect of C_{60} plays an important role as a modulator of output current, where the non-spin-polarized part of injected spin-polarized electrons by bias can be controllably recombined with the photogenerated holes, thus the amplitude of final output current and the MR value can be modulated (**Figure 2B**). The variation of the range of output current can even reach from positive to negative, and undoubtedly, the photovoltaic character of OSCs implies significant function in this device. In view of the great potential of photovoltaic property for developing spin photovoltaic device, H_2Pc , hole-transport small molecular semiconductor, has been used as the spacer for further investigating the spin photovoltaic property (Bairagi et al., 2020). Benefiting from the stability in ambient conditions of H_2Pc , a large MR of 7% and prominent spin photovoltaic characteristic at room temperature have been measured.

Although an increasing number of works have been reported toward spin photovoltaic device, the current situation still remains at the proof of principle and the photovoltaic effect of the used materials is too weak. At present, a number of

excellent photovoltaic materials have been synthesized in the organic photovoltaic field (Yuan et al., 2019; Liu et al., 2020). However, many challenges remain in the application of these materials in spin photovoltaic device; for instance, most of these materials can only be formed as membrane via solution processing, which may easily lead to residual solvent and thus the spin scattering. Therefore, novel techniques and OSCs are still needed for improving both the photovoltaic effect and the spin transport ability in spin photovoltaic devices.

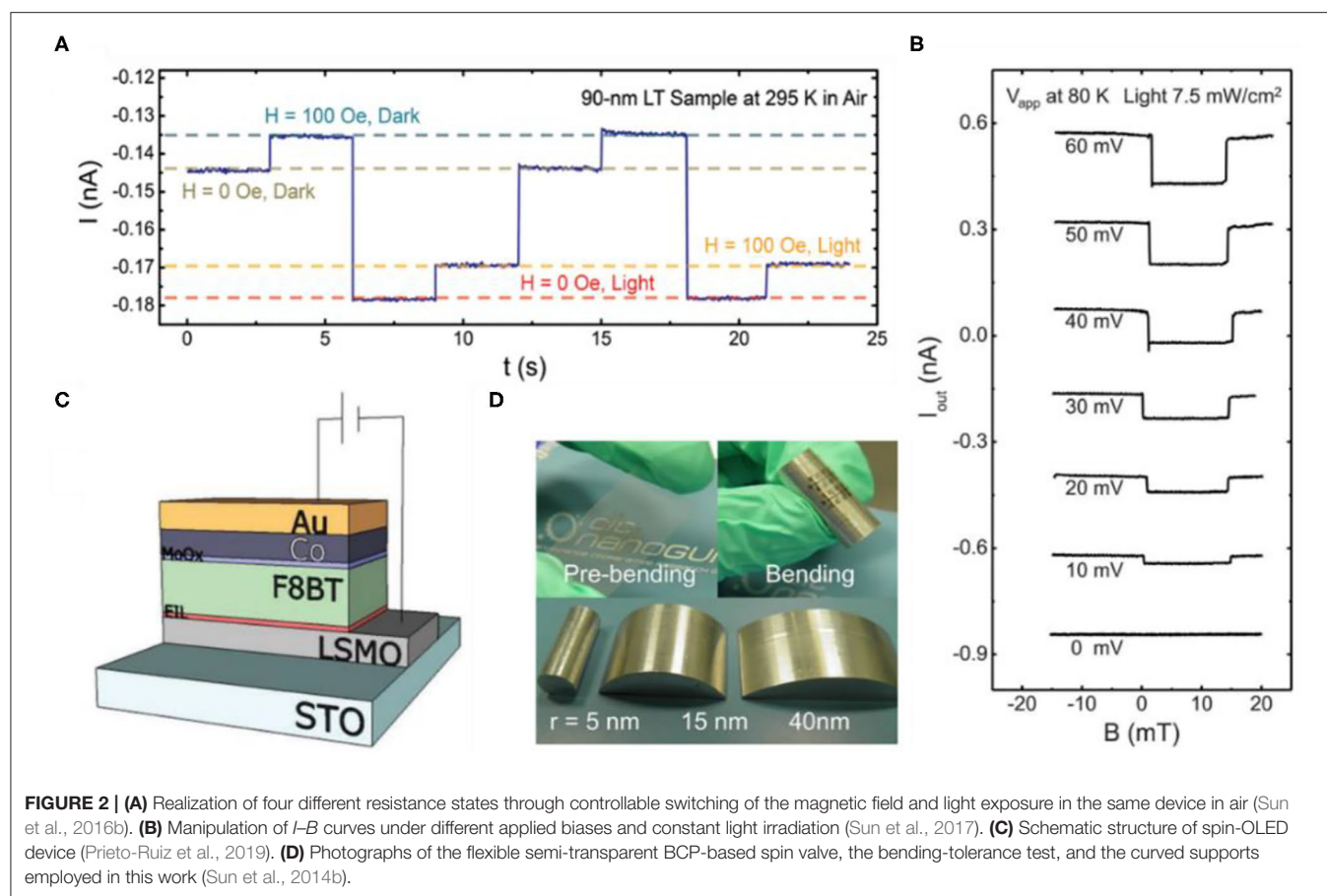
Spin-OLED

The electroluminescent (EL) property of OSCs, which has already been applied in organic light-emitting diodes (OLED), can also be used for building multifunctional spintronic devices. With the bipolar spin injection, the electroluminescence efficiency can be modulated by the relative direction of the two ferromagnetic electrodes according to the quantum efficiency mechanism. Based on Alq_3 , a frequently used OSC with light emitting property, Nguyen et al. have proposed and investigated the first spin-OLED (Nguyen et al., 2012). According to the quantum mechanism, the singlet probability can reach 1/2 modulated by external magnetic field, which is larger than the normal OLED with non-magnetic electrodes (Bergenti et al., 2004), so that the luminous efficiency can be enhanced by spin injection. The device shows the magneto-electroluminescence (MEL) of 1% at bias voltage of 3.5 V and 10 K, with the coercive fields of electrodes adjusted by the emission intensity. The key of the achievement is that they choose a deuterated organic polymer interlayer of poly(phenylene-vinylene) (H-DOO-PPV), which has a weak hyperfine interaction and hence excellent spin transport property (Nguyen et al., 2010). The spin diffusion length of deuterated poly(dioctyloxy)phenyl vinylene (D-DOO-PPV) is about 45 nm, which is about three times more than that of H-DOO-PPV polymer (Nguyen et al., 2012). Also, they inserted a thin buffer layer of LiF to improve the efficiency of injection (Schulz et al., 2011). Afterwards, for enhancing the MEL, Prieto-Ruiz et al. selected the light-emitting conjugated polymer poly(9,9-dioctylfluorene-co-benzothiadiazole) (F8BT) as the spacer because of its high green EL intensity and bipolar character (**Figure 2C**) (Prieto-Ruiz et al., 2019). The device realizes spin valve effect in spin-OLED at high bias voltage of 14 V through a careful engineering of the organic/inorganic interfaces, so that the MEL is enhanced on the order of 2.4% at 9 V and 20 K, based on the antiparallel configuration of the ferromagnetic electrodes.

These works offer more possibilities of multifunctional spintronic devices. However, as a spin-OLED, higher MEL are required to break through by optimizing the interface and enhancing the efficiency of spin injection. Moreover, operation at room temperature is still a goal in this area.

Flexible Spin Devices

OSCs with mechanical flexibility are widely used in preparing flexible organic electronic devices. However, there are a few studies on flexible spintronic devices. The first flexible spin valve was fabricated based on bathocuproine (BCP), and a large MR of 3.5% is observed at room temperature (Sun et al., 2014b). More



importantly, the spin valve has shown excellent stability after the endurance measurements of the bending radius and the bending time (**Figure 2D**). Both the I - V and the MR characteristics are almost unchanged, even up to a bending radius of 5 mm or after bending for 50 times.

The aforementioned work has shown a beginning toward application; however, the thermal-evaporated OSCs apparently limit the actual use, while solution-processed OSCs are the mainstream in the flexible application. Moreover, the requirement of room-temperature stable operation has also posed a challenge in this type of spintronic device.

ORGANIC-BASED MAGNETS AS THE MAGNETIC ELECTRODES

The conductivity mismatch between ferromagnetic electrodes and OSC thin films is a main factor for limiting the spin injection efficiency (Schmidt et al., 2000). Utilizing organic-based magnets to replace ferromagnetic electrode, which has lower energy level, is an efficient method to avoid this problem (Yoo et al., 2010).

$V[TCNE]_x$ ($x \approx 2$, TCNE: tetracyanoethylene), which possesses the merits of high magnetic ordering temperature, fully spin-polarized semiconducting electronic structure, chemical

tunability, and low-temperature processing, was first applied as one of the electrodes to fabricate spin valves (Manriquez et al., 1991; Yoo et al., 2010). Based on the MR measurements of temperature dependence and bias dependence, the results suggest that the organic-based magnets can be used as a spin injector or detector. After this, an all-organic-based spin valve has been fabricated based on the same organic magnet. The device structure is shown in **Figure 3A**, with two $V[TCNE]_x$ layers as the injector and detector, respectively (Li et al., 2011). A new model of spin-dependent tunneling between highly spin-polarized band can successfully demonstrate the process of spin injection and detection in the all-organic spin valves. Recently, an all-organic dual spin valve with three organic spin-selective layers has been reported, which introduced single molecular magnets of manganese and cobalt phthalocyanines (MnPc and CoPc) as the injector and detector (Banerjee and Pal, 2018). There are four configurations with two spin-flip interfaces at most. When the injector and detector have asymmetric thickness and different single molecular magnets, it can achieve four separate resistive states as 2-bit logic.

Although the previously mentioned applied organic-based magnets have shown promising application in spintronic study, more novel organic-based magnets are still needed to be developed and used in this direction. Moreover, organic-based

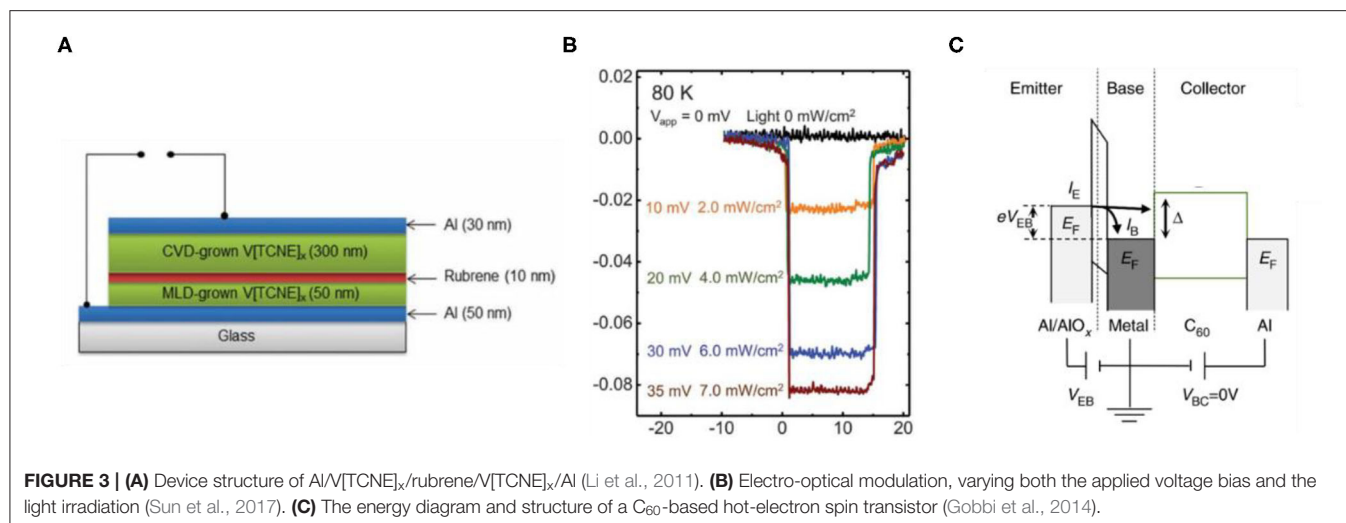


TABLE 1 | A summarized table of organic semiconductor applications in spintronics with the corresponding references.

Application	Device structure (bottom to top)	Temperature (K)	References
Spin valve	LSMO/ PIID-CNTVT-C1 /Ni ₈₀ Fe ₂₀ /Au	50–200	Li et al., 2019
	LSMO/ PIID-CNTVT-C3 /Ni ₈₀ Fe ₂₀ /Au		
	LSMO/ PAIID-CNTVT-C1 /Ni ₈₀ Fe ₂₀ /Au		
	LSMO/ PAIID-CNTVT-C3 /Ni ₈₀ Fe ₂₀ /Au	20–300	Liang et al., 2016
	LSMO/ C₆₀ /Co/Au		
Pure spin current devices	LSMO/ C₇₀ /Co/Au	10–300	Nguyen et al., 2010
	LSMO/ DOO-PPV /Co		
	Co/AIO _x / F₁₆CuPc /Ni ₈₀ Fe ₂₀	7–295	Sun et al., 2016b
	Ni ₈₀ Fe ₂₀ / PBTTT /Pt	200–300	Watanabe et al., 2014
	LSMO/ Alq₃ /AIO _x /Co	100–300	Prezioso et al., 2011
Spin photoresponse	Co/AIO _x / F₁₆CuPc /Ni ₈₀ Fe ₂₀	7–295	Sun et al., 2016b
Spin photovoltaic	Co/AIO _x / C₆₀ /Ni ₈₀ Fe ₂₀	80–295	Sun et al., 2017
	Co/AIO _x / H₂Pc /Ni ₈₀ Fe ₂₀	300	Bairagi et al., 2020
Spin-OLED	LSMO/ DOO-PPV /LiF/Co/Au	10–300	Nguyen et al., 2012
	LSMO/ PEIE/F8BT /MoO _x /Co/Au	20–200	Prieto-Ruiz et al., 2019
Flexible spin devices	Co/AIO _x / BCP /Ni ₈₀ Fe ₂₀	300	Sun et al., 2014b
All-organic spin devices	Al/ V[TCNE]_x/rubrene/V[TCNE]_x/Al	120–200	Li et al., 2011
Spin manipulation	Co/AIO _x / C₆₀ /Ni ₈₀ Fe ₂₀	80–295	Sun et al., 2017

Organic semiconductors are in bold type.

magnets also have a potential in the application of flexible devices, and the endurance measurement and bending strength measurement are required to be filled up in the future study.

SPIN MANIPULATION IN OSCS

It is of great significance to achieve spin manipulation in OSCs, and strong SOC and Hanle effect are the basis of spin manipulation in a traditional way. The weak SOC interaction of OSCs, on the one hand, contributes to the long-distance spin transport, but on the other hand, it makes spin manipulation particularly difficult. So far, the output spin signal can be preliminarily controlled based on spin photovoltaic device reported by Sun et al. (2017) (Figure 3B), which indicates

that the multifunctional spintronic device depending on the photoelectric properties of OSCs has presented a possibility of spin manipulation. However, it is just a simple and primary idea, which still needs further detailed research.

In addition, starting from the device structure design, the hot-electron spin transistor with three-terminal structure has also shown a promising application in spin manipulation (Figure 3C) (Appelbaum et al., 2007; Huang et al., 2007; Appelbaum, 2011; Gobbi et al., 2014). Through two spin injection ways with opposite direction, hot-electron spin injection and electric spin injection, a controllable spin-polarized current may be finally output. However, for ensuring both efficient spin injection in two ways, the preparation level of such device needs to be improved greatly.

CONCLUSION

In conclusion, the application of OSCs in the aspects of spin transport, spin functional devices, all-organic spin devices, and spin manipulation has been introduced in this review (Table 1). Also, the advanced achievements and obstacles for further development are discussed. For the future, according to the other achievements in organic electronic fields and spintronics, more types of OSCs are required to be applied, such as the interfacial materials, high-mobility materials, organic single crystals, supramolecules, and thermoelectric materials. Furthermore, taking advantage of the OSCs, novel multifunctional spintronic devices need to be urgently explored, for instance, the combination of organic spin valve and field effect transistor, which are always pursued in organic spintronics. With the development of organic spintronics, more strategies of OSC application will be explored to overcome the present challenges and keep this field attractive and active.

REFERENCES

- Ando, K., Watanabe, S., Mooser, S., Saitoh, E., and Siringhaus, H. (2013). Solution-processed organic spin-charge converter. *Nat. Mater.* 12, 622–627. doi: 10.1038/nmat3634
- Appelbaum, I. (2011). Introduction to spin-polarized ballistic hot electron injection and detection in silicon. *Philos. Trans. R. Soc. A* 369, 3554–3574. doi: 10.1098/rsta.2011.0137
- Appelbaum, I., Huang, B., and Monsma, D. J. (2007). Electronic measurement and control of spin transport in silicon. *Nature* 447, 295–298. doi: 10.1038/nature05803
- Baibich, M. N., Broto, J. M., Fert, A., Nguyen Van Dau, F., Petroff, F., Etienne, P., et al. (1988). Giant magnetoresistance of (001)Fe/(001)Cr magnetic superlattices. *Phys. Rev. Lett.* 61, 2472–2475. doi: 10.1103/PhysRevLett.61.2472
- Bairagi, K., Romero, D. G., Calavalle, F., Catalano, S., Zuccatti, E., Llopis, R., et al. (2020). Room-temperature operation of a p-type molecular spin photovoltaic device on a transparent substrate. *Adv. Mater.* 32:e1906908. doi: 10.1002/adma.201906908
- Banerjee, A., and Pal, A. J. (2018). All-organic dual spin valves with well-resolved four resistive-states. *Small* 14:e1801510. doi: 10.1002/smll.201801510
- Bergenti, I., Dediu, V., Arisi, E., Mertelj, T., Murgia, M., Riminucci, A., et al. (2004). Spin polarised electrodes for organic light emitting diodes. *Org. Electron.* 5, 309–314. doi: 10.1016/j.orgel.2004.10.004
- Boehme, C., and Lupton, J. M. (2013). Challenges for organic spintronics. *Nat. Nanotechnol.* 8, 612–615. doi: 10.1038/nnano.2013.177
- Dediu, V. A., Hueso, L. E., Bergenti, I., and Taliani, C. (2009). Spin routes in organic semiconductors. *Nat. Mater.* 8, 707–716. doi: 10.1038/nmat2510
- Ding, S., Tian, Y., Wang, H., Zhou, Z., Mi, W., Ni, Z., et al. (2018). Reliable spin valves of conjugated polymer based on mechanically transferrable top electrodes. *ACS Nano* 12, 12657–12664. doi: 10.1021/acsnano.8b07468
- Gobbi, M., Pietrobon, L., Atxabal, A., Bedoya-Pinto, A., Sun, X., Golmar, F., et al. (2014). Determination of energy level alignment at metal/molecule interfaces by in-device electrical spectroscopy. *Nat. Commun.* 5:4161. doi: 10.1038/ncomms5161
- Guo, L., Gu, X., Zhu, X., and Sun, X. (2019a). Recent advances in molecular spintronics: multifunctional spintronic devices. *Adv. Mater.* 31:e1805355. doi: 10.1002/adma.201805355
- Guo, L., Qin, Y., Gu, X., Zhu, X., Zhou, Q., and Sun, X. (2019b). Spin transport in organic molecules. *Front. Chem.* 7:428. doi: 10.3389/fchem.2019.00428
- Huang, B., Monsma, D. J., and Appelbaum, I. (2007). Coherent spin transport through a 350 micron thick silicon wafer. *Phys. Rev. Lett.* 99:177209. doi: 10.1103/PhysRevLett.99.177209
- Hueso, L. E., Bergenti, I., Riminucci, A., Zhan, Y. Q., and Dediu, V. (2007). Multipurpose magnetic organic hybrid devices. *Adv. Mater.* 19, 2639–2642. doi: 10.1002/adma.200602748
- Jang, H. J., and Richter, C. A. (2017). Organic spin-valves and beyond: spin injection and transport in organic semiconductors and the effect of interfacial engineering. *Adv. Mater.* 29, 1602739. doi: 10.1002/adma.201602739
- Jiang, S. W., Liu, S., Wang, P., Luan, Z. Z., Tao, X. D., Ding, H. F., et al. (2015). Exchange-dominated pure spin current transport in Alq3Molecules. *Phys. Rev. Lett.* 115:086601. doi: 10.1103/PhysRevLett.115.086601
- Li, B., Kao, C. Y., Yoo, J. W., Prigodin, V. N., and Epstein, A. J. (2011). Magnetoresistance in an all-organic-based spin valve. *Adv. Mater.* 23, 3382–3386. doi: 10.1002/adma.201100903
- Li, D., Wang, X., Lin, Z., Zheng, Y., Jiang, Q., Zheng, N., et al. (2019). Tuning charge carrier and spin transport properties via structural modification of polymer semiconductors. *ACS Appl. Mater. Inter.* 11, 30089–30097. doi: 10.1021/acsami.9b07863
- Li, F., Li, T., Chen, F., and Zhang, F. (2015). Excellent spin transport in spin valves based on the conjugated polymer with high carrier mobility. *Sci. Rep.* 5:9355. doi: 10.1038/srep09355
- Liang, S., Geng, R., Yang, B., Zhao, W., Chandra Subedi, R., Li, X., et al. (2016). Curvature-enhanced spin-orbit coupling and spinterface effect in fullerene-based spin valves. *Sci. Rep.* 6:19461. doi: 10.1038/srep19461
- Liu, Q., Jiang, Y., Jin, K., Qin, J., Xu, J., Li, W., et al. (2020). 18% Efficiency organic solar cells. *Sci. Bull.* 65, 272–275. doi: 10.1016/j.scib.2020.01.001
- Manriquez, J. M., Yee, G. T., McLean, R. S., Epstein, A. J., and Miller, J. S. (1991). A room-temperature molecular/organic-based magnet. *Science* 252, 1415–1417. doi: 10.1126/science.252.5011.1415
- Nguyen, T. D., Ehrenfreund, E., and Vardeny, Z. V. (2012). Spin-polarized light-emitting diode based on an organic bipolar spin valve. *Science* 337, 204–209. doi: 10.1126/science.1223444
- Nguyen, T. D., Hukic-Markosian, G., Wang, F., Wojcik, L., Li, X. G., Ehrenfreund, E., et al. (2010). Isotope effect in spin response of pi-conjugated polymer films and devices. *Nat. Mater.* 9, 345–352. doi: 10.1038/nmat2633
- Prezioso, M., Riminucci, A., Bergenti, I., Graziosi, P., Brunel, D., and Dediu, V. A. (2011). Electrically programmable magnetoresistance in multifunctional organic-based spin valve devices. *Adv. Mater.* 23, 1371–1375. doi: 10.1002/adma.201003974
- Prezioso, M., Riminucci, A., Graziosi, P., Bergenti, I., Rakshit, R., Cecchini, R., et al. (2013). A single-device universal logic gate based on a magnetically enhanced memristor. *Adv. Mater.* 25, 534–538. doi: 10.1002/adma.201202031
- Prieto-Ruiz, J. P., Miralles, S. G., Prima-García, H., López-Muñoz, A., Riminucci, A., Graziosi, P., et al. (2019). Enhancing light emission in interface engineered

AUTHOR CONTRIBUTIONS

YZ wrote the paper. LG and XZ completed the spelling and grammar check and copyright section. LG and XS supervised this review and completed all the submissions. All authors joined the discussion and revision of this paper.

FUNDING

This work was supported financially by the Ministry of Science and Technology of the People's Republic of China (Grant Nos. 2016YFA0200700, 2017YFA0206600), the National Natural Science Foundation of China (Grant Nos. 51803040, 51822301, 21673059, and 91963126), the CAS Instrument Development Project (Grant No. YJKYYQ20170037), the Strategic Priority Research Program of the Chinese Academy of Sciences (Grant No. XDB36020000), Beijing National Laboratory for Molecular Sciences (Grant No. BNLMS201907), and the CAS Pioneer Hundred Talents Program.

- spin-OLEDs through spin-polarized injection at high voltages. *Adv. Mater.* 31:1806817. doi: 10.1002/adma.201806817
- Schmidt, G., Ferrand, D., and Molenkamp, L. W. (2000). Fundamental obstacle for electrical spin injection from a ferromagnetic metal into a diffusive semiconductor. *Phys. Rev. B* 62, 4790–4793. doi: 10.1103/PhysRevB.62.R4790
- Schulz, L., Nuccio, L., Willis, M., Desai, P., Shakya, P., Kreouzis, T., et al. (2011). Engineering spin propagation across a hybrid organic/inorganic interface using a polar layer. *Nat. Mater.* 10, 39–44. doi: 10.1038/nmat2912
- Sun, D., Ehrenfreund, E., and Vardeny, Z. V. (2014a). The first decade of organic spintronics research. *Chem. Commun.* 50, 1781–1793. doi: 10.1039/C3CC47126H
- Sun, D., van Schooten, K. J., Kavand, M., Malissa, H., Zhang, C., Groesbeck, M., et al. (2016a). Inverse spin hall effect from pulsed spin current in organic semiconductors with tunable spin-orbit coupling. *Nat. Mater.* 15, 863–869. doi: 10.1038/nmat4618
- Sun, X., Bedoya-Pinto, A., Llopis, R., Casanova, F., and Hueso, L. E. (2014b). Flexible semi-transparent organic spin valve based on bathocuproine. *Appl. Phys. Lett.* 105:083302. doi: 10.1063/1.4894114
- Sun, X., Bedoya-Pinto, A., Mao, Z., Gobbi, M., Yan, W., Guo, Y., et al. (2016b). Active morphology control for concomitant long distance spin transport and photoresponse in a single organic device. *Adv. Mater.* 28, 2609–2615. doi: 10.1002/adma.201503831
- Sun, X., Gobbi, M., Bedoya-Pinto, A., Txoperena, O., Golmar, F., Llopis, R., et al. (2013). Room-temperature air-stable spin transport in bathocuproine-based spin valves. *Nat. Commun.* 4:2794. doi: 10.1038/ncomms3794
- Sun, X., Velez, S., Atxabal, A., Bedoya-Pinto, A., Parui, S., Zhu, X., et al. (2017). A molecular spin-photovoltaic device. *Science* 357, 677–680. doi: 10.1126/science.aan5348
- Tsurumi, J., Matsui, H., Kubo, T., Häusermann, R., Mitsui, C., Okamoto, T., et al. (2017). Coexistence of ultra-long spin relaxation time and coherent charge transport in organic single-crystal semiconductors. *Nat. Phys.* 13, 994–998. doi: 10.1038/nphys4217
- Wang, L., Yang, C., Wen, J., Gai, S., and Peng, Y. (2015). Overview of emerging memristor families from resistive memristor to spintronic memristor. *J. Mater. Sci. Mater. Electron.* 26, 4618–4628. doi: 10.1007/s10854-015-2848-z
- Wang, Y., Zhu, W., Dong, H., Zhang, X., Li, R., and Hu, W. (2016). Organic cocrystals: new strategy for molecular collaborative innovation. *Top. Curr. Chem.* 374:83. doi: 10.1007/s41061-016-0081-8
- Watanabe, S., Ando, K., Kang, K., Mooser, S., Vaynzof, Y., Kurebayashi, H., et al. (2014). Polaron spin current transport in organic semiconductors. *Nat. Phys.* 10, 308–313. doi: 10.1038/nphys2901
- Wolf, S. A., Awschalom, D. D., Buhrman, R. A., Daughton, J. M., von Molnar, S., Roukes, M. L., et al. (2001). Spintronics: a spin-based electronics vision for the future. *Science* 294, 1488–1495. doi: 10.1126/science.1065389
- Yoo, J. W., Chen, C. Y., Jang, H. W., Bark, C. W., Prigodin, V. N., Eom, C. B., et al. (2010). Spin injection/detection using an organic-based magnetic semiconductor. *Nat. Mater.* 9, 638–642. doi: 10.1038/nmat2797
- Yuan, J., Zhang, Y., Zhou, L., Zhang, G., Yip, H.-L., Lau, T.-K., et al. (2019). Single-junction organic solar cell with over 15% efficiency using fused-ring acceptor with electron-deficient core. *Joule* 3, 1140–1151. doi: 10.1016/j.joule.2019.01.004
- Zhang, X., Mizukami, S., Kubota, T., Ma, Q., Oogane, M., Naganuma, H., et al. (2013). Observation of a large spin-dependent transport length in organic spin valves at room temperature. *Nat. Commun.* 4:1392. doi: 10.1038/ncomms2423

Conflict of Interest: The authors declare that the research was conducted in the absence of any commercial or financial relationships that could be construed as a potential conflict of interest.

Copyright © 2020 Zhang, Guo, Zhu and Sun. This is an open-access article distributed under the terms of the Creative Commons Attribution License (CC BY). The use, distribution or reproduction in other forums is permitted, provided the original author(s) and the copyright owner(s) are credited and that the original publication in this journal is cited, in accordance with accepted academic practice. No use, distribution or reproduction is permitted which does not comply with these terms.



IDTI Dyes for Fluoride Anion Chemosensors

Xinqiang Yuan^{1†}, Xin Shi^{1†}, Cheng Wang², Yuqian Du², Peng Jiang¹, Xizhou Jiang³, Yongqiang Sui³, Xiaoli Hao^{1*} and Lin Li^{2,3*}

¹ National and Local Joint Engineering Laboratory for Slag Comprehensive Utilization and Environmental Technology, School of Materials Science and Engineering, Shaanxi University of Technology, Hanzhong, China, ² Key Laboratory of Rubber-Plastics of Ministry of Education/Shandong Province, School of Polymer Science & Engineering, Qingdao University of Science & Technology, Qingdao, China, ³ Prinx Chengshan (Shan Dong) Tire Co., Ltd., Rongcheng, China

Fluoride anions play a key role in human health and chemical engineering, such as in organic synthesis and biological processes. The development of high-sensitivity naked-eye detection sensors for fluoride anions in organic solutions is crucial and challenging. In this study, (3Z,3'Z)-3,3'-[4,4,9,9-tetrakis(4-hexylphenyl)-4,9-dihydro-s-indaceno(1,2-b:5,6-b')dithiophene]-2,7-diylbis(methan-1-yl-1-ylidene) bis(6-bromo-indolin-2-one) (IDTI) was designed and used as a fluoride chemosensor for the first time. IDTI is a highly sensitive fluoride sensor with a detection limit of as low as 1×10^{-7} M. In addition, upon the reaction of IDTI with fluoride anions in a tetrahydrofuran (THF) solution, color changes from red to yellow under ambient light and from purple to green under UV light were detectable by the naked eye. These studies indicate that IDTI is a promising fluoride chemosensor.

Keywords: IDTI, chemosensors, fluoride anion, color changing, spectroscopy

INTRODUCTION

The development of high-efficiency and sensitive fluoride anion (F^-) sensors is crucial, since F^- plays a key role in chemical military fields, industry, organic synthesis, biological and medical processes, and even human health (Wade et al., 2011; Li et al., 2012; Yang et al., 2012, 2013; Sun et al., 2017). With the rapid development of the chemical industry, F^- exists not only in aqueous environments but also in organic media, such as waste organic liquor. As such, several different optical chemosensors for fluoride anions in organic solutions have been developed (Zhang et al., 2018). However, the most reported fluoride anion sensors can only detect F^- at concentrations in the 10^{-5} M level.

Fluoride anions, which are among the smallest anions, exhibit strong electronegative properties. Such properties enable F^- to form strong hydrogen bonds with $-NH$ groups or easily deprotonate the $-NH$ protons of the designed receptor, resulting in an evident optical spectrum change either in the absorption or emission spectrum (Kaur and Choi, 2015; Feng et al., 2018). Some sensors can even change their color under ambient light or UV light, with the change detectable by the naked eye (Wang et al., 2018; Antonio et al., 2020). Recently, Zhang et al. (2018) reported polymers containing 1,4-diketo-pyrrolo[3,4-c]pyrrole (DPP)-substituted *t*-butoxy carbonyl (*t*-Boc) units with good solubility. After thermal annealing processing, the *t*-Boc units could be removed, and lactam hydrogen appeared. They reported that the resulting polymer cannot only be used for the detection of F^- but also the extraction of F^- from the organic solution. Later, Wu et al. (2019) designed a dye containing hydroxyl to detect F^- in dimethyl sulfoxide (DMSO); this approach exhibited a detection limit of as low as $1.79 \mu M$. Deng et al. (2020) reported aminobenzodifuranone

OPEN ACCESS

Edited by:

Qixin Zhou,
University of Akron, United States

Reviewed by:

Jun-Jun Zhang,
Xi'an Technological University, China
Jinfang Zhang,
North University of China, China

*Correspondence:

Xiaoli Hao
haoxiaoli111@163.com
Lin Li
qustliin@hotmail.com

[†]These authors have contributed
equally to this work

Specialty section:

This article was submitted to
Organic Chemistry,
a section of the journal
Frontiers in Chemistry

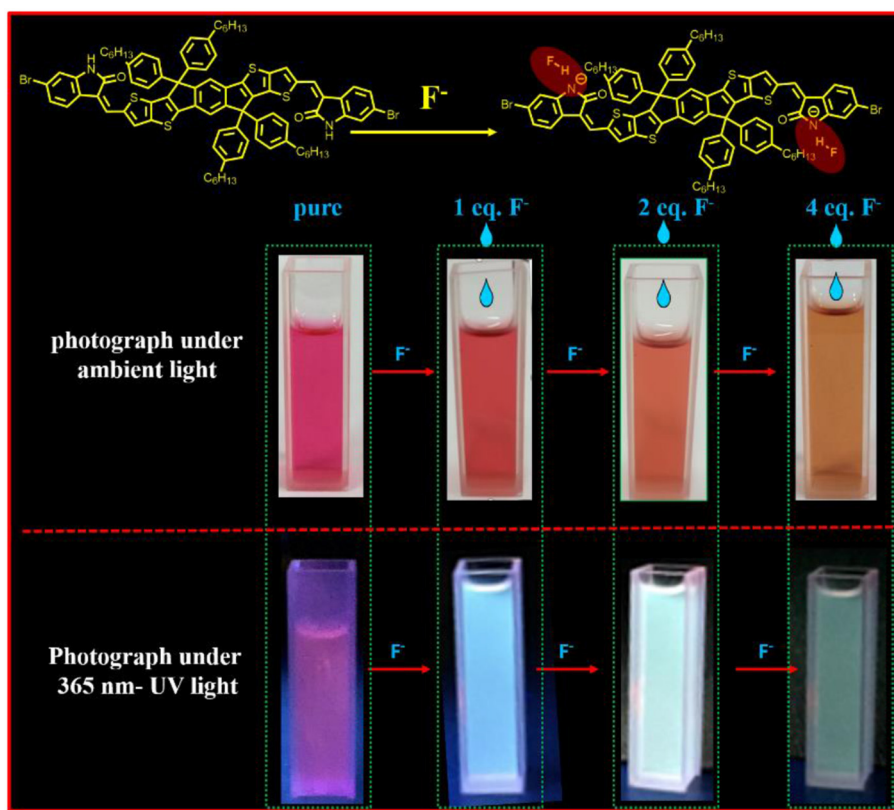
Received: 05 August 2020

Accepted: 18 September 2020

Published: 23 October 2020

Citation:

Yuan X, Shi X, Wang C, Du Y, Jiang P,
Jiang X, Sui Y, Hao X and Li L (2020)
IDTI Dyes for Fluoride Anion
Chemosensors.
Front. Chem. 8:591860.
doi: 10.3389/fchem.2020.591860



Graphical Abstract | The new dye, IDTI, firstly used as a fluoride anion chemosensor, has a high sensitivity with the fluoride anion detection limit of as low as 1×10^{-7} M. And the IDTI solutions have the interesting color changing properties, once meet the fluoride anion, from red to yellow under ambient light and from purple to green under UV light were detectable by the naked eye. The IDTI is a promising fluoride chemosensor.

dyes for F^- chemosensors, which could not only detect F^- but also distinguish solvents containing F^- . Hitherto, large optical spectrum shifts, obvious color changes that can be detected by the naked eye, and sensitive fluoride chemosensors are still rare and quite important. In this work, a new π -conjugated dye, (3Z,3'Z)-3,3'-[4,4,9,9-tetrakis(4-hexylphenyl)-4,9-dihydro-s-indaceno(1,2-b:5,6-b')dithiophene]-2,7-diylbis(methan-1-yl-1-ylidene)bis(6-bromo-indolin-2-one) (IDTI), was designed and used as a fluoride anion sensor for the first time. This dye exhibited promising sensitivity toward F^- in organic solvents.

MATERIALS AND METHODS

The procedure for the synthesis of IDTI is as follows. In a 50-ml round-bottomed flask, 6-bromooxindole (0.63 g, 3.0 mmol) and 2,7-dicarbaldehyde-4,4,9,9-tetrakis(4-hexylphenyl)-4,9-dihydro-s-indaceno(1,2-b:5,6-b')dithiophene **1** (1.074 g, 1.0 mmol) were suspended in absolute dry alcohol (15 ml). Subsequently, piperidine (0.25 ml) was added using a syringe needle. The reaction mixture was then stirred and refluxed for 18 h. After cooling to room temperature, the mixture was filtered, washed with ethanol, and dried under vacuum to yield a brown powder product (1.23 g, 84.2%). Microanalysis found

C, 70.47%; H, 5.68%; N, 1.96%; S, 8.80% (C, 70.57%; H, 5.65%; N, 1.91%; S, 8.76%).

RESULTS AND DISCUSSION

The produced IDTI exhibited low solubility in most common organic solvents; however, such solubility was sufficient for studying the behavior of the fluoride anion chemosensor. The interaction between the IDTI chromophore and F^- was first investigated through color changes that were detectable by the naked eye. Tetrabutylammonium fluoride (TBAF, 5.0×10^{-4} M) was gradually added to a 1.0×10^{-5} M solution of IDTI in tetrahydrofuran (THF). As shown in **Figure 1A**, the pure IDTI in THF exhibited a rose color under ambient light and a purple color under UV light (365 nm). However, once F^- was added, color changes were observed under both light sources. With the addition of 1, 2, and 4 eq. of F^- , the color of the IDTI solution under irradiation of ambient light changed from rose to red, orange, and yellow, respectively. Likewise, the emission color gradually changed from purple to blue, cyan, and green with the corresponding amounts of F^- . This result indicates that IDTI could be used to detect F^- through color changes that can be observed with the naked eye. Such color changes could be due to the deprotonation of the lactam NH moiety of the IDTI core by

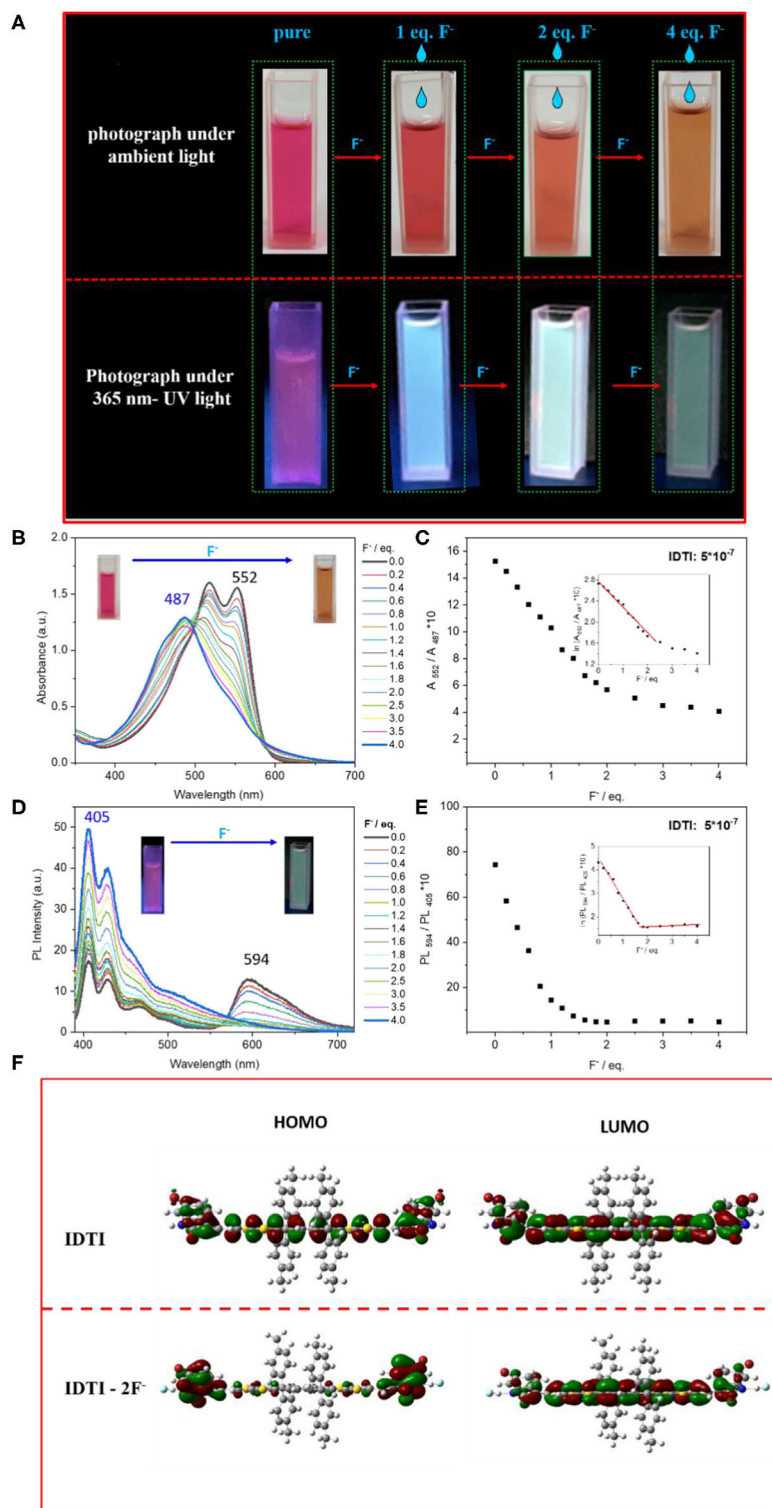
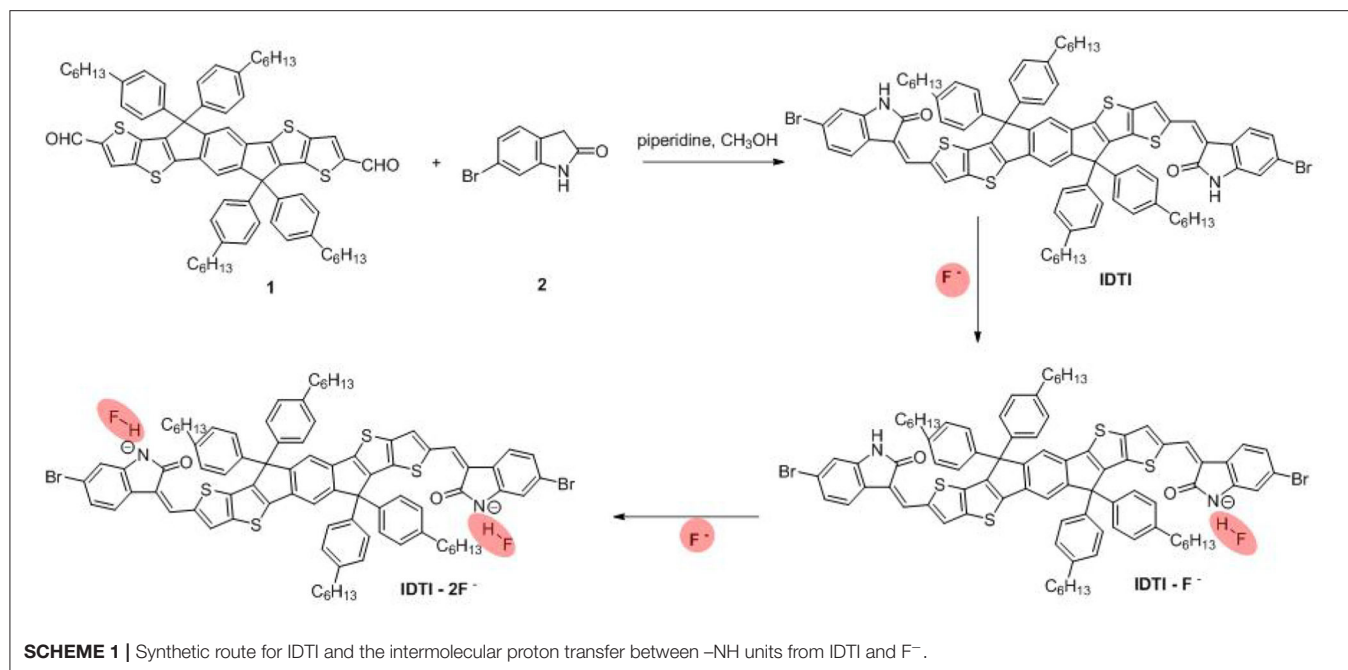


FIGURE 1 | (A) Photograph of the IDTI solution with or without additional different eq. fluoride anion under ambient light or 365 nm UV light. **(B,D)** UV/vis absorption **(B)** and PL fluorescence spectra **(D)** of IDTI (5.0×10^{-7} M) in the presence of F⁻ (0–4.0 eq.) in tetrahydrofuran (THF). **(C,E)** Ten times the absorption intensity ratio of IDTI (5×10^{-6} M) after mixing with F⁻ in THF between 552 and 487 nm (A_{552}/A_{487} nm) vs. fluoride anion concentration **(C)** and the PL fluorescence intensity ratio of IDTI (5×10^{-6} M) after mixing with F⁻ in THF between 594 and 405 nm (PL_{594}/PL_{405} nm) **(E)** vs. fluoride anion concentration. The inset is the natural logarithm of 10 times the absorption intensity ratio A_{552}/A_{487} nm and PL_{594}/PL_{405} nm vs. fluoride anion concentration, respectively. **(F)** Molecular orbital surfaces of the highest occupied molecular orbital (HOMO) and lowest unoccupied molecular orbital (LUMO) energy levels of IDTI and IDTI-2F⁻ obtained at the B3LYP/6-31G* level.



F^- [intermolecular proton transfer (IPT), **Scheme 1**] (Chen et al., 2012, 2017). IDTI exhibited electronically neutral properties in the absence of F^- . However, once F^- was added, F^- could react with the NH units of the IDTI core to form IDTI- F^- ; the IPT process resulted in a color change of the dye. Furthermore, with higher concentrations of F^- in the solvent, further IPT could proceed between F^- and NH to produce IDTI-2 F^- (Sun et al., 2017).

The above color changes were further characterized by spectroscopy. Instead of an IDTI concentration of 1.0×10^{-5} M, 5.0×10^{-7} M IDTI in THF was investigated. As shown in **Figure 1B**, the spectrum for pure IDTI in the THF solution exhibited a maximum absorption at 552 nm and a shoulder peak at 515 nm. With the gradual addition of F^- , the two peaks located at 552 and 515 nm successively decreased and became blue shifted, which finally disappeared. Moreover, a new peak at 487 appeared at 1.4 eq. of ammonium fluoride and became progressively higher with increasing F^- concentration. These absorption spectra showed a clear isosbestic point at 495 nm. To examine the sensitivity of IDTI toward F^- , we investigated the radiometric curves. **Figure 1C** shows the graph of 10 times the absorption intensity ratio of IDTI between 552 and 487 nm vs. the F^- concentration, which appears to be a quadratic function; the inset shows the graph of the natural logarithm of these data. The inset of **Figure 1C** shows one slope in the correlation, and the linear relationship between the absorption intensity and F^- concentration can be described by the equation: $\ln(A_{552}/A_{487} \text{ nm}) = -0.50 [F^-] + 2.76$ ($[F^-] < 1.0 \times 10^{-6}$ M). **Figure 1D** shows the fluorescence spectra of IDTI (5.0×10^{-7} M) in the presence of F^- (0–4.0 eq.) in THF. The fluorescence spectra exhibited the same trend as the absorption spectra for IDTI; in particular, a blue shift of the spectra was observed upon the addition of F^- to the THF solvent. Pure IDTI in the THF solution

exhibited maximum emission at 594 nm. With the addition of F^- , this peak successively decreased, while the peak at 405 nm progressively increased. **Figure 1E** shows the graph of 10 times the fluorescence intensity ratio of IDTI between 594 and 405 nm vs. the F^- concentration, while the inset shows the graph of the natural logarithm of these data. The inset of **Figure 1E** shows the presence of two slopes in the correlation, and the linear relationship between the absorption intensity and F^- concentration at low concentrations can be described by the following equation: $\ln(A_{594}/A_{405} \text{ nm}) = -0.71 [F^-] + 4.3$ ($[F^-] < 8 \times 10^{-7}$ M). As shown in **Figures 1C,E**, both the absorption spectra and PL fluorescence spectra showed a clear distinction between the solution with an F^- concentration of 1.0×10^{-7} M and the pure IDTI solution, which indicates that IDTI is a sensitive fluoride chemosensor. The linear relationship between the absorption/PL fluorescence intensity and F^- concentration indicates that IDTI could be used to quantitatively analyze the fluoride concentration.

To understand the electron distributions before and after F^- binding, the frontier molecular orbital (FMO) feature was calculated at the B3LYP/6-31 (d, p) level using simplified IDTI, in which the long hexyl chain was replaced with a methyl group. As shown in **Figure 1F**, the distributions of the HOMO and LUMO orbitals of IDTI were similar, as FMO were mainly localized around the IDTI back bone. After the binding of F^- , the HOMO and LUMO orbital distributions were quite different. Most of the electron wavefunctions became delocalized along the conjugation backbone for the LUMO, which is similar to electron distribution of IDTI. However, the electron distribution of the HOMO of IDTI-2 F^- was mainly located at both ends of IDTI, particularly the indole units. This result indicates that after the fluoride bonding, upon the excitation of IDTI-2 F^- , an electron transfer from the end indole groups to the conjugated

backbone proceeded. The fluoride-bonded indole units seem to exhibit stronger electron-withdrawing properties than indole, which results in a strong push–pull system (core of IDTI-fluoride-bonded indole). Normally, a strong push–pull system could result in a bathochromic shift; however, in this work, a blue shift occurred (Trilling et al., 2019; Zhang et al., 2020).

CONCLUSION

In this study, a new type of colorimetric chemosensor dye based on IDTI with high sensitivity toward fluoride anions was designed and investigated. IDTI can interact with fluoride anions to exhibit color changes that are visible to the naked eye; such color changes were from red to orange or yellow under ambient light and from purple to green or blue under 365-nm UV light. The color change could be ascribed to the intermolecular proton transfer between IDTI and F^- . The spectroscopy studies indicate that IDTI could be used to quantitatively analyze the fluoride concentration with a detection limit of as low as 1×10^{-7} M. This work has also demonstrated that IDTI is a promising dye for fluoride chemosensors with the advantages of high sensitivity and naked-eye detection.

REFERENCES

- Antonio, S. R., Sergio, G. A., Joaquín, C. G. M., and Julian, R. L. (2020). A study of silylated tris(styryl)benzenes as potential fluorescent sensors for aqueous fluoride. *Dyes Pigments* 182:108610. doi: 10.1016/j.dyepig.2020.108610
- Chen, X. X., Leng, T. H., Wang, C. Y., Shen, Y. J., and Zhu, W. H. (2017). A highly selective naked-eye and fluorescent probe for fluoride ion based on 1,8-naphthalimide and benzothiazole. *Dyes Pigments* 141, 299–305. doi: 10.1016/j.dyepig.2017.02.008
- Chen, Z. J., Wang, L. M., Zou, G., Zhang, L., Zhang, J. G., Cai, X. F., et al. (2012). Colorimetric and ratiometric fluorescent chemosensor for fluoride ion based on perylene diimide derivatives. *Dyes Pigments* 94, 410–415. doi: 10.1016/j.dyepig.2012.01.024
- Deng, Z. F., Li, R., Geng, J. T., Zheng, M., Li, L. Q., Shi, X., et al. (2020). Efficient colorimetric fluoride anion chemosensors with varied colors based on simple aminobenzodifuranone. *Front. Chem.* 8:231. doi: 10.3389/fchem.2020.00231
- Feng, Y. T., Li, X. L., Ma, H. W., Zhang, Z. X., Zhang, M., and Hao, S. Y. (2018). A simple fluorescent film probe for the detection of fluoride anion in organic solution. *Dyes Pigments* 153, 200–205. doi: 10.1016/j.dyepig.2018.02.004
- Kaur, M., and Choi, D. H. (2015). Diketopyrrolopyrrole: brilliant red pigment dye-based fluorescent probes and their applications. *Chem. Soc. Rev.* 44, 58–77. doi: 10.1039/C4CS00248B
- Li, Q., Yue, Y., Guo, Y., and Shao, S. (2012). Fluoride anions triggered “OFF–ON” fluorescent sensor for hydrogen sulfate anions based on a BODIPY scaffold that works as a molecular keypad lock. *Sens Actuators B Chem.* 173, 797–801. doi: 10.1016/j.snb.2012.07.105
- Sun, Q. K., Chen, M. S., Liu, Z. W., Zhang, H. C., and Yang, W. J. (2017). Efficient colorimetric fluoride anion chemosensors based on simple naphthodipyrrolidone dyes. *Tetrahedron Lett.* 58, 2711–2714. doi: 10.1016/j.tetlet.2017.05.079
- Trilling, F., Sachnik, O., and Scherf, U. (2019). π -Expanded diketopyrrolopyrroles as acceptor building blocks for the formation of novel donor-acceptor copolymers. *Polym. Chem.* 10, 627–632. doi: 10.1039/C8PY01435c
- Wade, C. R., Ke, I. S., and Gabbai, F. P. (2011). Sensing of aqueous fluoride anions by cationic stibine–palladium complexes. *Angew. Chem. Int. Ed.* 124, 493–496. doi: 10.1002/ange.201106242

DATA AVAILABILITY STATEMENT

All datasets presented in this study are included in the article/supplementary material.

AUTHOR CONTRIBUTIONS

XY wrote the manuscript. XS prepared the materials and carried out in experiments. CW revised the manuscript and reference. YD and PJ helped for the characterization. XJ and YS helped in testing and analysis. XH and LL gave the ideas and supervised the whole work. All authors contributed to the article and approved the submitted version.

FUNDING

This study was financially supported by the National Natural Science Foundation of China (21905164, 51703111), Project of Shaanxi Provincial Department of Education (17JK0140), and Scientific Research Fund Project of Shaanxi University of Technology (SLGPT2019KF01-02, SLGKYQD2-24).

- Wang, R., Li, J. F., Li, G., Hao, C., Zhang, Y. X., Wang, S. H., et al. (2018). Synthesis of 1-amino-12-hydroxyl-perylene tetra-(alkoxycarbonyl) for selective sensing of fluoride. *Dyes Pigments* 156, 225–232. doi: 10.1016/j.dyepig.2018.04.012
- Wu, Y. C., Shi, C. Q., Chen, Z. G., Zhou, Y. B., Liu, S. M., and Zhao, J. Q. (2019). A novel hydroxyl-containing polyimide as a colorimetric and ratiometric chemosensor for the reversible detection of fluoride ions. *Polym. Chem.* 10, 1399–1406. doi: 10.1039/C8PY01697F
- Yang, C. L., Xu, J., Ma, J. Y., Zhu, D. Y., Zhang, Y. F., Liang, L. Y., et al. (2012). An efficient long fluorescence lifetime polymer-based sensor based on europium complex as chromophore for the specific detection of F^- , CH_3COO^- , and $H_2PO_4^-$. *Polym. Chem.* 3, 2640–2648. doi: 10.1039/C2PY20408H
- Yang, H., Zheng, M., Li, Y. P., Zhang, B. L., Li, J. F., Bu, L. Y., Liu, W., et al. (2013). N-Monoalkylated 1,4-diketo-3,6-diphenylpyrrolo[3,4-c]-pyrroles as effective one- and two-photon fluorescence chemosensors for fluoride anions. *J. Mater. Chem. A* 1, 5172–5178. doi: 10.1039/C3TA00160A
- Zhang, H., Li, R., Deng, Z., Cui, S., Wang, Y., Zheng, M., et al. (2020). π -Conjugated oligomers based on aminobenzodifuranone and diketopyrrolopyrrole. *Dyes Pigments* 181:108552. doi: 10.1016/j.dyepig.2020.108552
- Zhang, H. C., Yang, K., Chen, C., Wang, Y. H., Zhang, Z. Z., Tang, L. L., et al. (2018). 1,4-Diketo-pyrrolo[3,4-c]pyrroles (DPPs) based insoluble polymer films with lactam hydrogens as renewable fluoride anion chemosensor. *Polymer* 149, 266–272. doi: 10.1016/j.polymer.2018.07.011

Conflict of Interest: The authors declare that the research was conducted in the absence of any commercial or financial relationships that could be construed as a potential conflict of interest.

Copyright © 2020 Yuan, Shi, Wang, Du, Jiang, Jiang, Sui, Hao and Li. This is an open-access article distributed under the terms of the Creative Commons Attribution License (CC BY). The use, distribution or reproduction in other forums is permitted, provided the original author(s) and the copyright owner(s) are credited and that the original publication in this journal is cited, in accordance with accepted academic practice. No use, distribution or reproduction is permitted which does not comply with these terms.



The Crystallinity Control of Polymer Donor Materials for High-Performance Organic Solar Cells

Dingding Qiu^{1,2}, Muhammad Abdullah Adil^{1,2}, Kun Lu^{1,2*} and Zhixiang Wei^{1,2*}

¹ Chinese Academy of Sciences Key Laboratory of Nanosystem and Hierarchical Fabrication, Chinese Academy of Sciences Center for Excellence in Nanoscience, National Center for Nanoscience and Technology, Beijing, China, ² University of Chinese Academy of Sciences, Chinese Academy of Sciences, Beijing, China

OPEN ACCESS

Edited by:

Haichang Zhang,
Qingdao University of Science and
Technology, China

Reviewed by:

Meng Zheng,
University of Padua, Italy
Zhifeng Deng,
Shaanxi University of
Technology, China

*Correspondence:

Kun Lu
lvk@nanoctr.cn
Zhixiang Wei
weizx@nanoctr.cn

Specialty section:

This article was submitted to
Organic Chemistry,
a section of the journal
Frontiers in Chemistry

Received: 05 September 2020

Accepted: 12 October 2020

Published: 24 November 2020

Citation:

Qiu D, Adil MA, Lu K and Wei Z (2020)
The Crystallinity Control of Polymer
Donor Materials for High-Performance
Organic Solar Cells.
Front. Chem. 8:603134.
doi: 10.3389/fchem.2020.603134

Bulk heterojunction (BHJ) organic solar cells (OSCs) can be regarded as one of the most promising energy generation technologies for large-scale applications. Despite their several well-known drawbacks, the devices where polymers are employed as the donor are still leading the OSC universe in terms of performance. Such performance generally depends upon various critical factors such as the crystallinity of the material, the crystallization process during the film formation, and also the final film morphology. Despite a few reviews on the structure of the polymer donor materials and device performance, not enough attention has been paid toward the crystallinity problem. Herein, the structure and crystallinity of the representative polymer donor materials and the corresponding device properties have been briefly reviewed. Furthermore, several typical methods for controlling the crystallinity of materials have been summarized and illustrated as well. Moreover, the obstacles lying in the way of successful commercialization of such polymer solar cells have been systematically discussed. The in-depth interpretation of the crystallinity of the polymer donors in this article may stimulate novel ideas in material design and device fabrication.

Keywords: polymer solar cell, crystallinity, donor, aggregation, bulk heterojunction

INTRODUCTION

Bulk heterojunction (BHJ) organic solar cells (OSCs) have recently achieved extremely high power conversion efficiencies (PCEs) exceeding 18% owing to their interesting trademark properties (Liu et al., 2020). Over the past several decades, the researchers have put in tremendous efforts in the development and improvement of the corresponding materials (Li et al., 2005; Liao et al., 2013; Zhang et al., 2015), exploring alternate and better preparation methodologies (Gurney et al., 2019; Hu et al., 2020; Wang et al., 2020), presenting elaborate and accurate mechanisms for proving their findings, and so on (Ji et al., 2020; Meng et al., 2020). Hence, the parameters defining the OSC performance; the open circuit voltage (V_{OC}), short circuit current (J_{SC}), and the fill factor (FF), have been on a continual rise, which is a welcoming characteristic to meet the requirements of industrial applications (Cui et al., 2019; Liu et al., 2020).

The widely accepted working mechanism of the BHJ OSCs is illustrated in **Figure 1**. First, the donor and acceptor materials absorb the incident photons to generate excitons, which are basically electron and hole pairs. Next, these excitons diffuse toward the donor-acceptor interface, where after overcoming the Coulomb interaction force between them, the exciton gets separated into independent electrons and hole moieties. Finally, these independent electrons and holes transport toward the cathode and anode, respectively, and are collected by the corresponding electrodes.

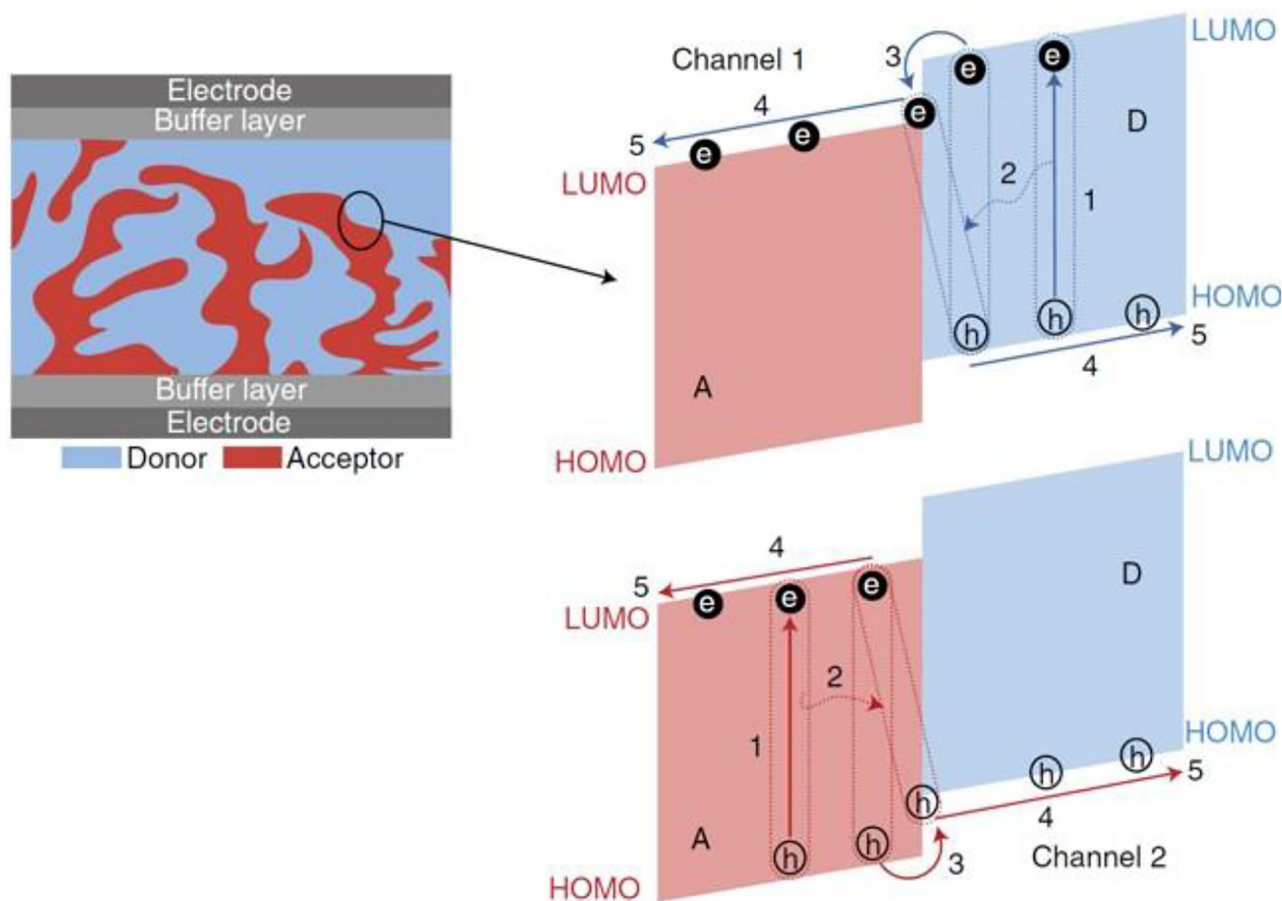


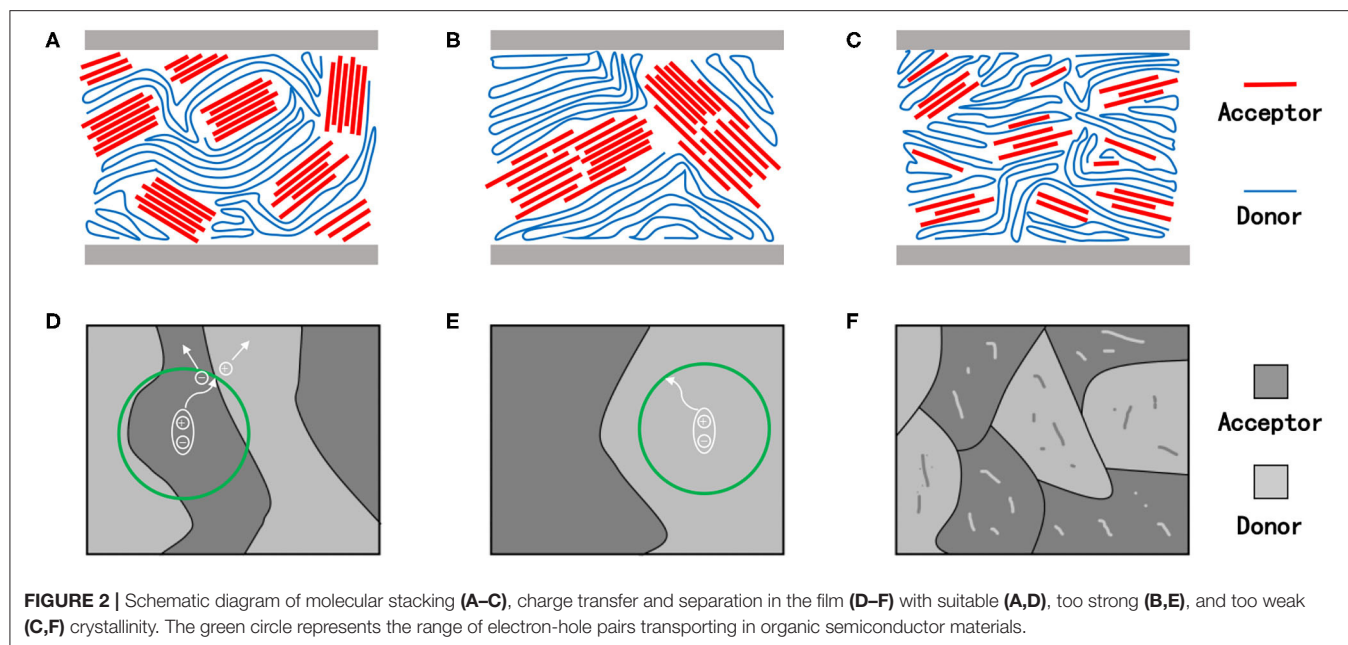
FIGURE 1 | The operating mechanism of OPVs: (1) absorption of photons and creation of excitons; (2) diffusion of excitons to D/A interfaces; (3) dissociation of excitons to free charge carriers (holes and electrons) at D/A interfaces; (4) transportation of the charge carriers to electrodes; (5) extraction of the charge carriers at the electrodes. Copyright 2018, Macmillan Publishers Limited, part of Springer Nature.

It is generally believed that the selection of the appropriate active layer materials is one of the most important factors that affect the device performance. During the past few decades, such materials can be said to have undergone three stages of evolution. The first-generation materials were basically a combination of the famous poly(3-hexylthiophene) (P3HT) donor with a fullerene acceptor, where the resulting devices were capable of achieving PCEs of about 5% (Li et al., 2005). Later on, after the development of D-A copolymer systems and forming corresponding blends with fullerene derivatives, a massive improvement in the performance was observed as PCEs of over 11% were obtained (Zhao J. et al., 2016). Finally, the emergence of non-fullerene acceptors (NFAs) enabled the researchers to effectively control the OSC parameters, and ultimately, blending them with the matched high-bandgap polymer donors pushed the PCE values beyond a remarkable 17% (Xue et al., 2017; Cui et al., 2019). It is quite an extraordinary observation that despite their numerous drawbacks, currently, almost all the BHJ OSCs devices that exhibit excellent performance include polymers as their donor component.

In preparation of the OSCs, the crystallinity-related aspects are of major concern. A better way of understanding this important issue is to divide it into two parts, i.e., the crystallinity of the involved conjugated molecules, and the relationship between the crystallinity and the film morphology on device performance.

The Crystallinity of Conjugated Molecules

Crystallinity, as the name suggests, describes the proportion of the ordered (crystalline) regions due to conjugation within a certain polymer and is a very important physical quantity in polymer science. Its value varies from polymer to polymer and hence there exists a wide range. Even for the same polymer, a slight variation in the processing conditions can lead to different crystallinity values. In BHJ OSCs, both polymer and small molecules possess large conjugated regions and therefore induce crystallinity in the system (Jiang et al., 2020). The source of crystallinity usually determines its influencing factors upon a certain system. Molecules with large conjugated regions demonstrate an extraordinary self-stability due to their large



π -electron delocalization. Hence, through the overlapping of intermolecular π -electron clouds, these molecules can further achieve lower energies and therefore improved overall stability. As a result, the molecules with large conjugated planes have a certain tendency to self-aggregate, which is the source of their crystallinity (Manzhos, 2020). Therefore, the larger the molecular conjugated plane, the stronger will be the flatness of the stable conformation, which will lead to a stronger aggregation effect, and ultimately, stronger crystallinity will be attained. Also, factors such as the aggregation of alkyl chains and the non-covalent interaction between molecules have a certain impact on the molecular crystallinity.

The Relationship Between Crystallinity and Film Morphology on Device Performance

The most widely utilized solution-based spin coating method to prepare thin OSCs active layers is essentially a crystallization process of multiple molecules. In this process, the phase separation occurs and largely determines whether or not the resulting film will form a nanoscale interpenetrating network structure, which in turn affects the performance of the final device (Bin et al., 2020). The crystallinity of the donor and acceptor molecules can be regarded as an important driving force for obtaining suitable phase separation for both polymers and small molecules and therefore determines the film's morphology and affects the final device performance (Heeger, 2014). Neither too strong nor too weak crystallinity is generally conducive to the formation of preferred morphology. Attaining the contrary to what has been said usually leads to poor device configurations.

The desired molecular crystallinity, as well as the crystallization process for an ideal OSC, has been demonstrated in **Figures 2A,D**. Under the circumstance, the domain size of the active layer film should be equivalent to the exciton diffusion length of the involved materials while maintaining

beneficial contact with the adjacent layers. Such a morphology, coupled with good phase purity, would enable the process of photoexcitation, exciton diffusion, charge separation, and charge transport in the device to be highly efficient, ultimately resulting in excellent device photoelectric performances (Bin et al., 2020). Therefore, attaining precise control of the crystallinity of materials and the crystallization process during device fabrication is important for obtaining high-performance devices.

Domains with excessive (too strong) crystallinity are illustrated in **Figures 2B,E**. As mentioned earlier, for a single molecule, the stronger its crystallinity, the greater will be its self-aggregation tendency, and the larger will be the domain size within the thin films, which will eventually lead to very high charge mobility (Guo et al., 2012). In blend films, however, the large domain size leads to modest phase separation and poor film morphology (Ge et al., 2020). Considering the short exciton lifetimes and about 10-nm diffusion length in organic semiconductor materials, the photogenerated excitons yielded in the active layer film with large domain size would not be able to reach the donor–acceptor interface to achieve proper charge separation, but will recombine and ultimately result in terrible devices performance (Heeger, 2014). In addition, the excessively large domain sizes are usually accompanied by relatively large film roughness and further lead to intimate contact with the hole and electron transport layers, resulting in heat generation and current loss from the corresponding cells (Williams et al., 2012).

Likewise, extremely poor molecular crystallinity is also undesirable in pursuit of fabricating high-performing devices (**Figures 2C,F**) as it usually leads to poor film formation, as well as weak aggregation in the system, and thus, obtaining films with good morphology and high phase purity becomes difficult. Hence, when materials with low crystallinity are employed, amorphous regions are often observed in the corresponding active layers thin films, which ultimately hinder the charge

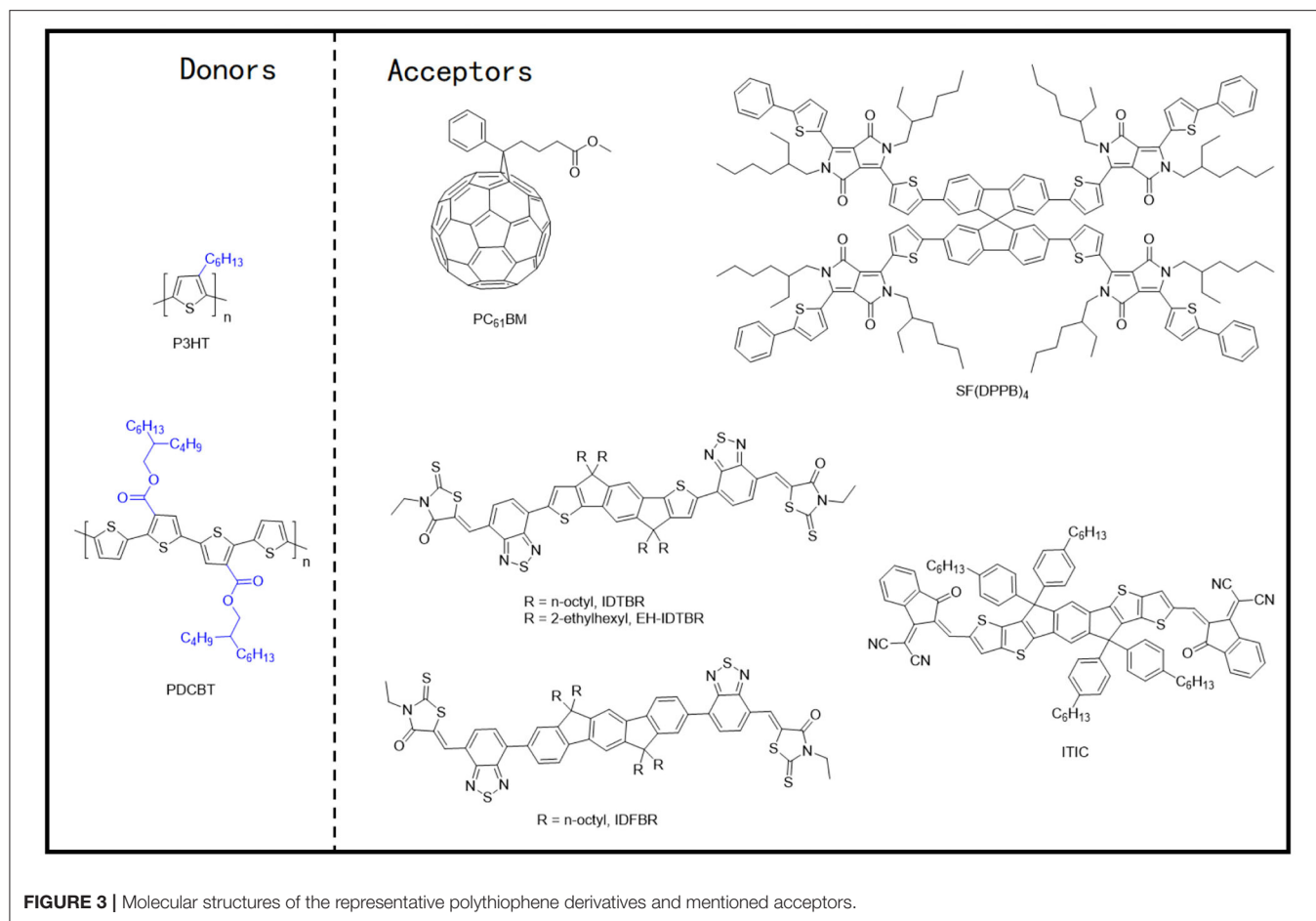


FIGURE 3 | Molecular structures of the representative polythiophene derivatives and mentioned acceptors.

transport and sacrifice the photovoltaic performances of the device (Li et al., 2016a).

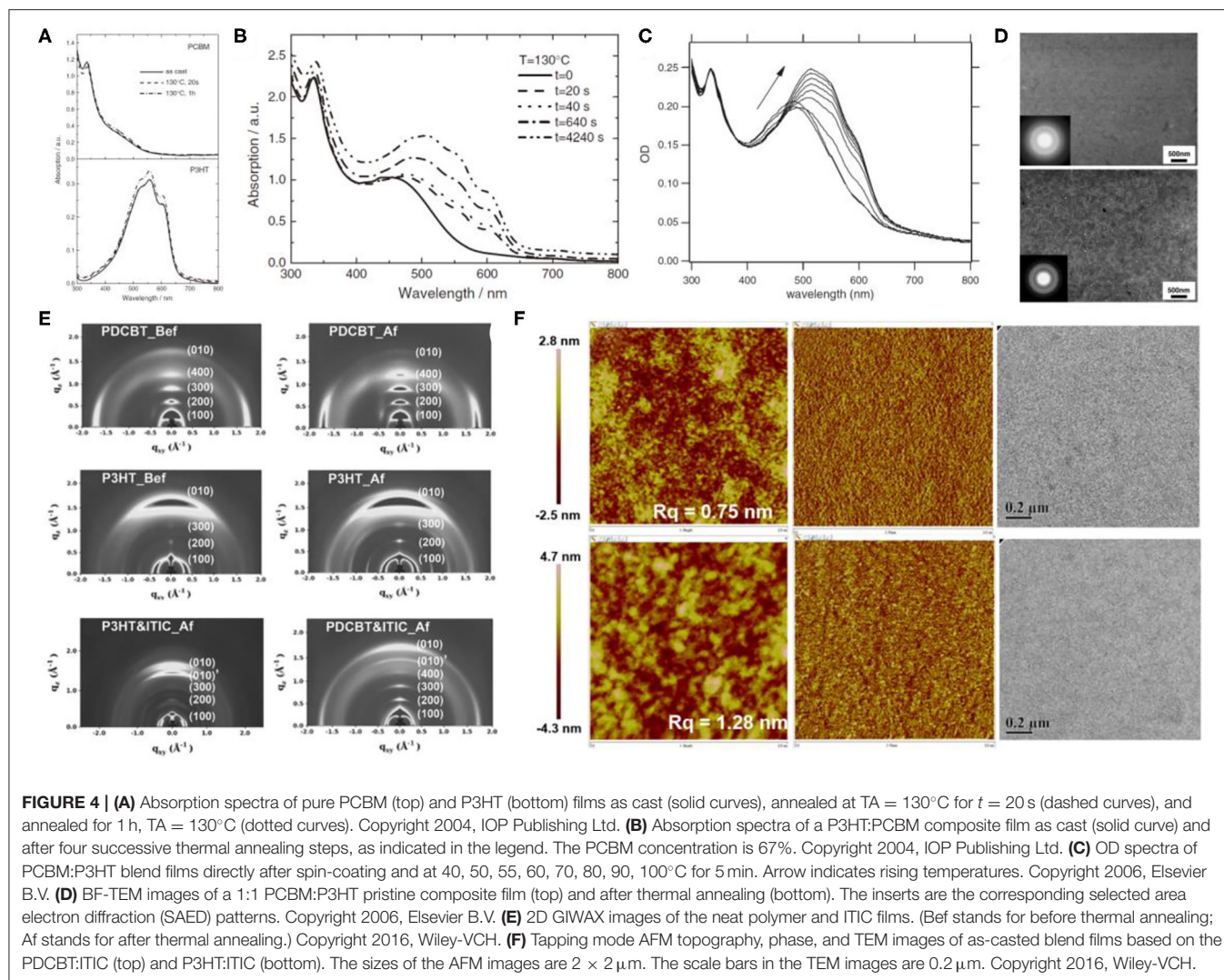
Herein, we review the molecular structure, crystallinity, and crystallization behavior of typical polymer donor materials in the blend films, along with the methods to control them. We will first classify the existing polymer donor materials into five categories according to their structure. Then, a variety of reported crystallinity modification methods would be analyzed, which are mainly divided into molecular structure and post-processing conditions. Finally, we will put forward a few key challenges and efforts to overcome those challenges for the polymer donor materials for OSCs. We hope and believe that this article's overall introduction to the crystallinity problem in polymer donor materials may provide some valuable inspiration for the further development of this field.

POLYMER DONORS FOR EFFICIENT OSCs

Polythiophene Derivatives

During the early progression stages of the BHJ OSCs, polythiophene derivatives (PTs) used to be the most widely studied polymer donor materials as they were initially found to possess good photovoltaic characteristics. With the long polythiophene skeleton and alkyl side chains for

solubilization, PTs hold both high crystallinity and good solution processability. P3HT (**Figure 3**) has been the most representative polythiophene-based polymer donor material in the field of OSCs. In one such example, Li et al. blended P3HT with [6,6]-phenyl-C₆₁-butyric acid methyl ester (PC₆₁BM) and achieved a PCE of 4.37% (Li et al., 2005). They suggested that the slower film formation rate brought higher molecular packing order in the blend, which can be indirectly proven by the increased film roughness, enhanced interband photon absorption, and improved mobility, and eventually led to an excellent photovoltaic performance. Later on, the crystallinity and morphology of the well-known P3HT:PCBM blends have been extensively studied. Comparing the absorption spectra of the pure P3HT and PCBM with their corresponding blend under various annealing times (**Figures 4A,B**) conclusively proves the crystallization of P3HT in the blend films (Chirvase et al., 2004). Similarly, the blend film exhibits a gradually increasing absorption peak at about 600 nm (**Figure 4C**) at increased annealing temperature, as well as a sharp signal peak (**Figure 4E**) in the GIWAXS spectrum, both of which reflect the strong crystallinity of the P3HT polymer (Savenije et al., 2006; Qin et al., 2016). The morphology of the PCBM:P3HT blend film has also been illustrated in **Figure 4D**, which exhibits a preferred nanoscale interpenetrating network structure.



However, relatively lower V_{OC} , J_{SC} , and FF values have been attained as a consequence of utilizing a fullerene acceptor and an unoptimized film morphology.

Recently, the application of the NFAs has significantly improved the performance of the P3HT-based devices. In one such example, the indacenodithiophene (IDT) core-based NFAs, IDTBR, and EH-IDTBR, demonstrating highly planar molecular configuration, not only showed very good crystallinity, but also led to a highly complementary absorption spectrum with P3HT and hence produced an elevated PCE of 6.3 and 6%, respectively (Holliday et al., 2016). Interestingly, these two NFAs lost their face-on orientation after forming blends with the P3HT polymer, which might have reduced the devices' performance to a certain extent. Similarly, the performance of the P3HT based device was further improved by inserting a second NFA (IDFBR) into the P3HT:IDTBR blend film, forming a ternary system, which led to the added component induced optimization of phase morphology (Baran et al., 2017). On the contrary, introducing a spirobifluorene (SF) core-based NFA, SF(DPPB)₄,

with a cross-shaped molecular geometry, into the active layer with P3HT led to the generation of a remarkable V_{OC} of 1.41 V due to the energy level alignment. The corresponding devices ultimately produced a PCE of 5.16% (Li S. et al., 2016). From the results, it is evident that the face-on molecular orientation in the blend films has been achieved as the molecular geometry of SF(DPPB)₄ prevented the strong aggregation of P3HT and strengthened the phase separation after thermal annealing.

It is widely accepted that the relatively large bandgap and high ionization potential of P3HT would cause weak light absorption and relatively low V_{OC} values that eventually undermine the device's performance. Therefore, great efforts have been induced to ameliorate P3HT and develop new polythiophene donor materials. PDCBT, one of such outstanding polymer molecules (Figure 3), thus obtaining PCEs of 7.0% and 10.16% with PC₇₁BM and ITIC as acceptors, respectively (Qin et al., 2016). The GIWAXS spectrum revealed that the alkoxycarbonyl-substituted PT showed enhanced crystallinity and preferred face-on molecular orientation (Figure 4E), which may be due to the

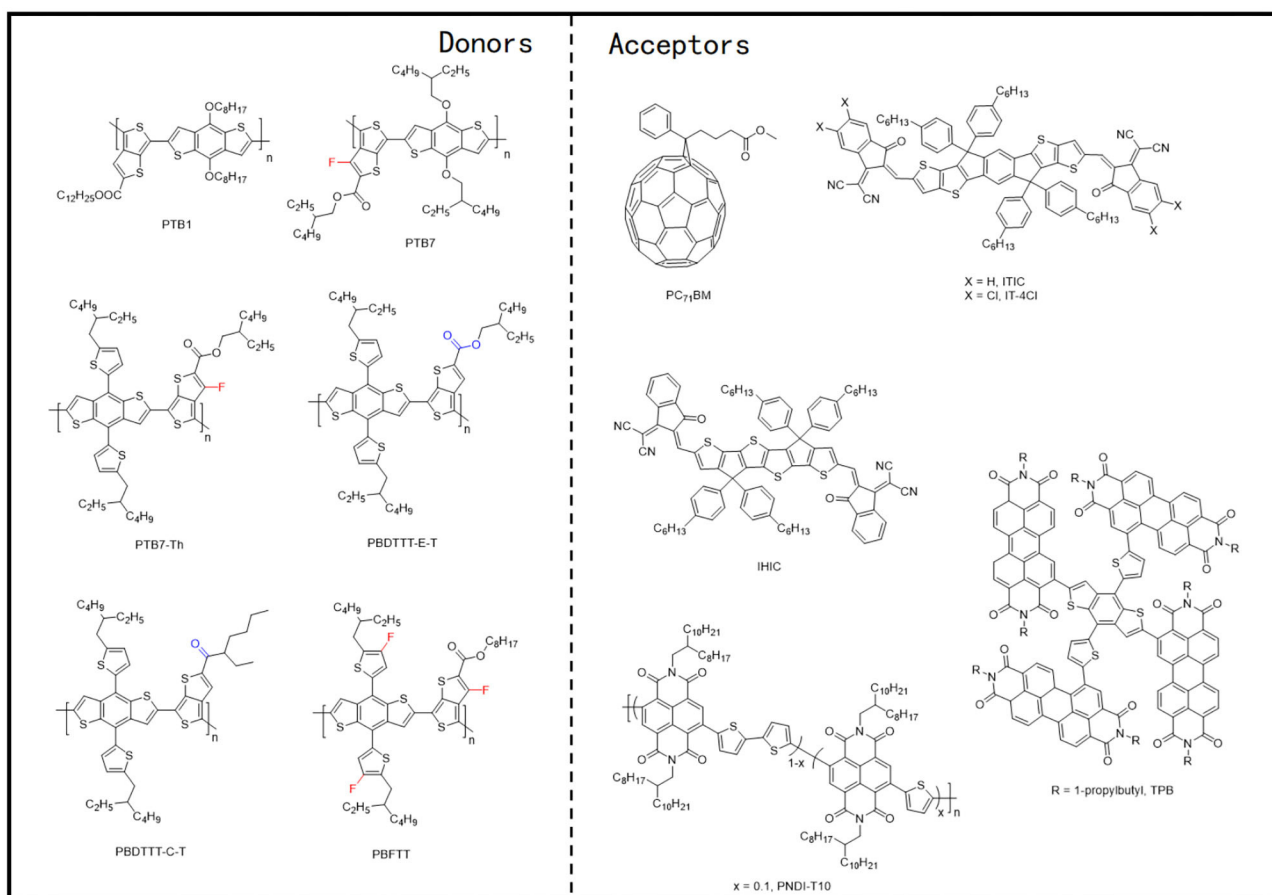


FIGURE 5 | Molecular structures of representative D-A copolymers and mentioned acceptors.

dipole–dipole interactions between C=O (carbonyl)...S(thienyl) groups in PDCBT, and polar alkoxy carbonyl substituents and dicyanomethyleneindanone moieties in ITIC. As a result, a preferred film morphology and appropriate phase separation (**Figure 4F**) have been obtained and therefore led to improved device performance.

Despite the relatively inferior photovoltaic performances of PT-based devices, the advantages of low consumption and easy synthesis still make them one of the most promising donor materials for industrial applications. However, to do so, it is an urgent requirement to adjust the energy levels and absorption spectra of PT materials through simple side-chain engineering, halogenation strategies, or other easy methods.

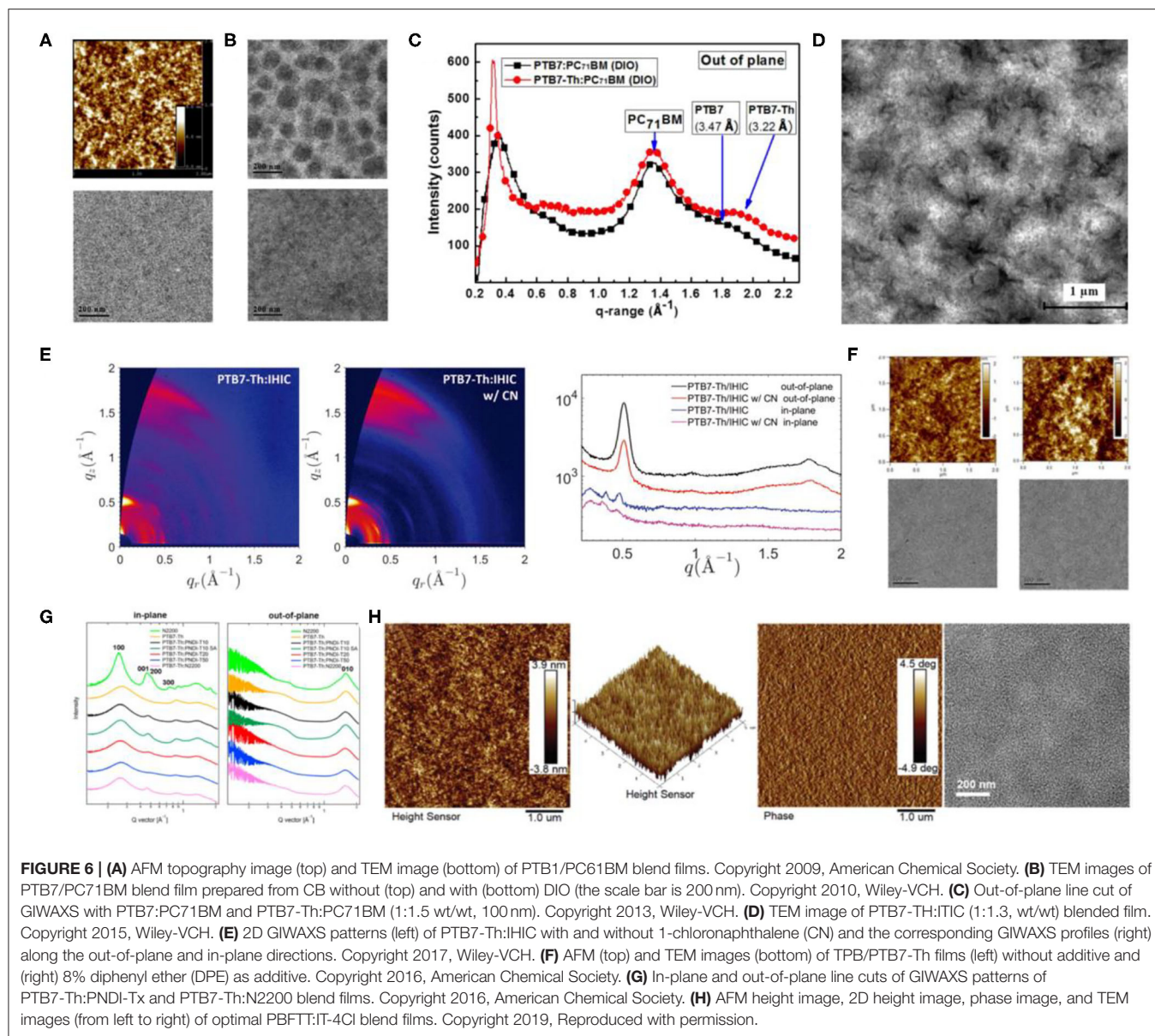
D-A Copolymer

With an alternating electron-rich unit (D) and an electron-deficient unit (A), the D-A copolymers are generally distinguished by their low bandgap, wide light absorption wavelength range, and adjustable characteristics of energy level and photon absorption. Because of the intramolecular push–pull electronic effects, simple side-chain engineering, fluorination strategies, etc., can affect the energy levels of the entire molecule

and therefore change the optimal molecular configuration to modify the molecular stacking performance and crystallinity. Generally, the electron-deficient unit of the D-A copolymers is an ester substituted thieno[3,4-b]thiophene (TT), whereas the substituted benzo[1,2-b:4,5-b']dithiophene (BDT) and 4,8-di(thiophen-2-yl)benzo[1,2-b:4,5-b']dithiophene (BDT-T) are utilized as the electron-rich units.

D-A Copolymer Based on BDT Units

In 2008, Liang et al. synthesized a polymer donor based on alternating TT and BDT units, called PTB1 (**Figure 5**), which achieved a PCE of 5.6% after being blended with PC₇₁BM. They later extended the PBT series to PBT7 through side-chain and halogenation modification (Liang et al., 2009). Compared with P3HT, PTB1 displayed better molecular planarity and improved crystallinity, which upon blending with PC₇₁BM brought a uniformly distributed nano-interpenetrating network structure [nanofibers structure of about ~5-nm width (**Figure 6A**)]. With attributes such as a narrow bandgap (1.6 eV) and high hole mobility ($4.5 \times 10^{-4} \text{ cm}^2/\text{V} \cdot \text{s}$), OSCs based on PTB1:PC₇₁BM resulted in better device performance than the P3HT:PCBM system. After replacing the alkyl chain with 2-ethylhexyl and



fluorinating the TT unit, PTB7 (**Figure 5**) was synthesized, and the PCE of the devices with the same acceptor material reached 7.4% (Liang et al., 2010). Elevated V_{OC} , derived from fluorination, and 1,8-diiodooctane (DIO) doping-induced uniform phase separation (**Figure 6B**) favoring charge separation and transfer can be credited as the main reasons for the excellent performance of the PTB series donor-based devices.

D-A Copolymer Based on BDT-T Units

Later on, one of the most investigated polymer molecules, PTB7-Th, rose to the scene (**Figure 5**), which was designed and proposed by Liao et al. through the incorporation of 2-ethylhexyl-thienyl group into the BDT unit (BDT-T) in PTB7 (Liao et al., 2013). This inclusion led to an improved co-planarity of the molecular backbone that not only resulted in a 25-nm

red shift in the absorption edge but also induced a better π - π stacking and preferred face-on molecular orientation (shorter π - π stacking distances of 3.22 Å; **Figure 6C**). As a result, the PTB7-Th: PC₇₁BM-based device gave a high PCE of 7.64%. Such excellent device performance gained researchers' attention and hence NFAs started to be employed with PTB7-Th. Lin et al. designed and synthesized one of the most representative NFA, ITIC and upon blending it with PTB7-Th, yielded a PCE of 6.80% due to the broad absorption, balanced charge transport, good donor/acceptor miscibility and proper phase-separation (**Figure 6D**) (Lin et al., 2015). The same group later synthesized an improved NFA, IHIC, which exhibited strong NIR absorption but weak visible absorption, and prepared an efficient semitransparent-ST-OSC with a PCE of 9.77% (Wang et al., 2017). The GIWAXS characterization (**Figure 6E**)

illustrates that the PTB7-Th:IHIC blend film demonstrated relatively stronger crystallinity and preferential face-on oriented domains, leading to high and balanced charge mobility and good donor–acceptor compatibility. Similarly, The α -substituted PDI derivatives, TPB with twisted 3D structure, has also been employed as acceptors with PTB7-Th and gave a high PCE of 8.47%, which was attributed to the extraordinarily high J_{SC} values ($>18 \text{ mA} \cdot \text{cm}^{-2}$). This high current value has been attained as a consequence of the increased contact area between the active layer and interfacial electrode, due to the smooth film morphology brought about by the DPE doping (Figure 6F) (Wu et al., 2016). Furthermore, PTB7-Th has also been blended with a naphthodithiophene (NDI)-based polymer NFA, PNDI-T10, which led to a PCE of 7.6% (Li et al., 2016b). A preferred domain size of 10–20 nm, as proved by the resonant soft X-ray scattering characterization, predominant face-on orientation (Figure 6G), and a balanced μ_h/μ_e ratio of 2, contributing to efficient charge separation and transfer, has been attributed to this performance. In general, PTB7-Th can be termed as one of the most promising polymer donor materials, because of its narrow bandgap, strong absorption, suitable crystallinity, and good compatibility with most acceptors.

Side-chain engineering and halogenation strategies have also been conducted for PTB7-Th and produced several excellent OSCs. Huo et al. replaced the alkyl side chain on the thiophene of the BDT-T unit with alkoxycarbonyl and alkylcarbonyl and synthesized PBDTTT-E-T and PBDTTT-C-T (Figure 5) (Huo et al., 2011). Comparing with the corresponding alkyl-substituted analogs, PBDTTT-E-T and PBDTTT-C-T exhibited better thermal stabilities, red-shifted absorption spectra, lower HOMO and LUMO energy levels, and significantly higher hole mobility and hence led to greatly improved photovoltaic properties. Moreover, Su et al. fluorinated both BDT-F and the TT units and synthesized PBFTT polymer (Figure 5), which after being blended with IT-4Cl obtained a PCE of 11.1% for ST-OSC (Su et al., 2019). The fluorination not only led to a higher extinction coefficient and stronger crystallinity in the system but also endowed the blend films with small RMS roughness, smooth surface morphology, and uniform bulk morphology (Figure 6H), which fit perfectly with the thin electrodes required for ST-OSCs.

D- π -A Copolymer With Thiophene π -Bridge

In recent years, the donor- π -acceptor (D- π -A) principle has widely been applied in the polymer donor material design, where an electron-rich unit (D), a π -bridge (π , usually thiophene), and an electron-deficient unit (A) alternately constitute the backbone structure of the polymer. Comparing with the earlier mentioned D-A copolymer donors, these possess larger conjugated planes, stronger absorption, and hence better device performance. Among the rich variety of D- π -A copolymers, the BDT-T is the most commonly used D unit, whereas benzo[1,2-c:4,5-c']dithiophene-4,8-dione (BDD) and 2H-benzo[d][1,2,3]triazole (BTz) are usually employed as the A units.

BDT-T and BDD Unit-Based D- π -A Copolymer With Thiophene as the π -Bridge

The PBDB-T polymer can be considered as the first widely studied polymer donor material based on the BDT-T and BDD units (Figure 7), which revealed a strong aggregation effect in the solution state (Figure 8A) and, when blended with the PC₆₁BM as acceptor, exhibited a PCE of 6.67% (Qian et al., 2012). Likewise, upon utilizing the representative NFA, ITIC, with PBDB-T, the corresponding J_{SC} almost doubled and reached $16.81 \text{ mA} \cdot \text{cm}^{-2}$, ultimately producing an excellent PCE of 11.21%. Such a high performance was attributed to preferred film morphology and phase separation by the authors (Figure 8B) (Zhao W. et al., 2016). Furthermore, a fused-ring acceptor with asymmetric side chains, IDT-OB, has also been combined with PBDB-T, where the resultant devices were able to produce a PCE of 10.12%, as a consequence of suitable nanoscale phase separation (Figure 8C) and dominant face-on stacking orientation in a wide range of thickness (Figure 8D) (Feng et al., 2017). Moreover, constituting an all-polymer system, PZ1, a polymer NFA led to a relatively high PCE of 9.19% when blended with the PBDB-T donor (Zhang Z. G. et al., 2017).

Zhang et al. later on designed and synthesized PM6 (showed in Figure 7), another well-known copolymer of BDT-T and BDD units (Zhang et al., 2015). The PM6:PC₇₁BM-based device showed a high PCE of 9.2% with a V_{OC} of 0.98 V, which is one of the highest fullerene acceptor-based device performances at that time. However, although the neat film of PM6 exhibited strong crystallinity and a dominant face-on packing with respect to the electrodes, the π - π stacking of the polymer in the blend films was completely disrupted after blending with PC₇₁BM (Figure 8E), which is obviously unfavorable for charge transfer. The introduction of the NFAs solved this problem and greatly improved the photovoltaic performance of PM6-based devices. Later, the same group synthesized an NFA based on selenopheno[3,2-b]thiophene fused electron-rich central building block and end-capped electron-withdrawing group, named SeTIC4Cl (Wang et al., 2018), and ultimately, the corresponding PM6:SeTIC4Cl devices demonstrated a very high PCE of 13.32%. The AFM, TEM, and GIWAXS characterization revealed that the PM6 and SeTIC4Cl in the blend films can be crystallized independently, and the best face-on crystalline orientation and molecular packing can be obtained after DIO treatment (Figures 8F,G). Likewise, one of the most outstanding NFAs, BTP-4F, or more commonly known as the Y6 molecule, and its chlorinated homolog, Y6-Cl (BTP-4Cl), have been employed to constitute OSCs with PM6 as the donor and achieved record PCEs of 15.6 and 16.5%, respectively (Cui et al., 2019). Considering its popularity, Karki et al. examined the PM6:Y6 blend films to investigate the source of its excellent performance (Karki et al., 2019). They stated that the PM6:Y6 blend system exhibited a low energetic offset, a low energetic disorder, and beneficial morphology, which aids in reducing the voltage losses and retaining high FF and J_{SC} values simultaneously.

Hence, owing to the excellent photovoltaic performance of polymers based on BDT-T and BDD units, a lot of research has been conducted for their modification. In one such example,

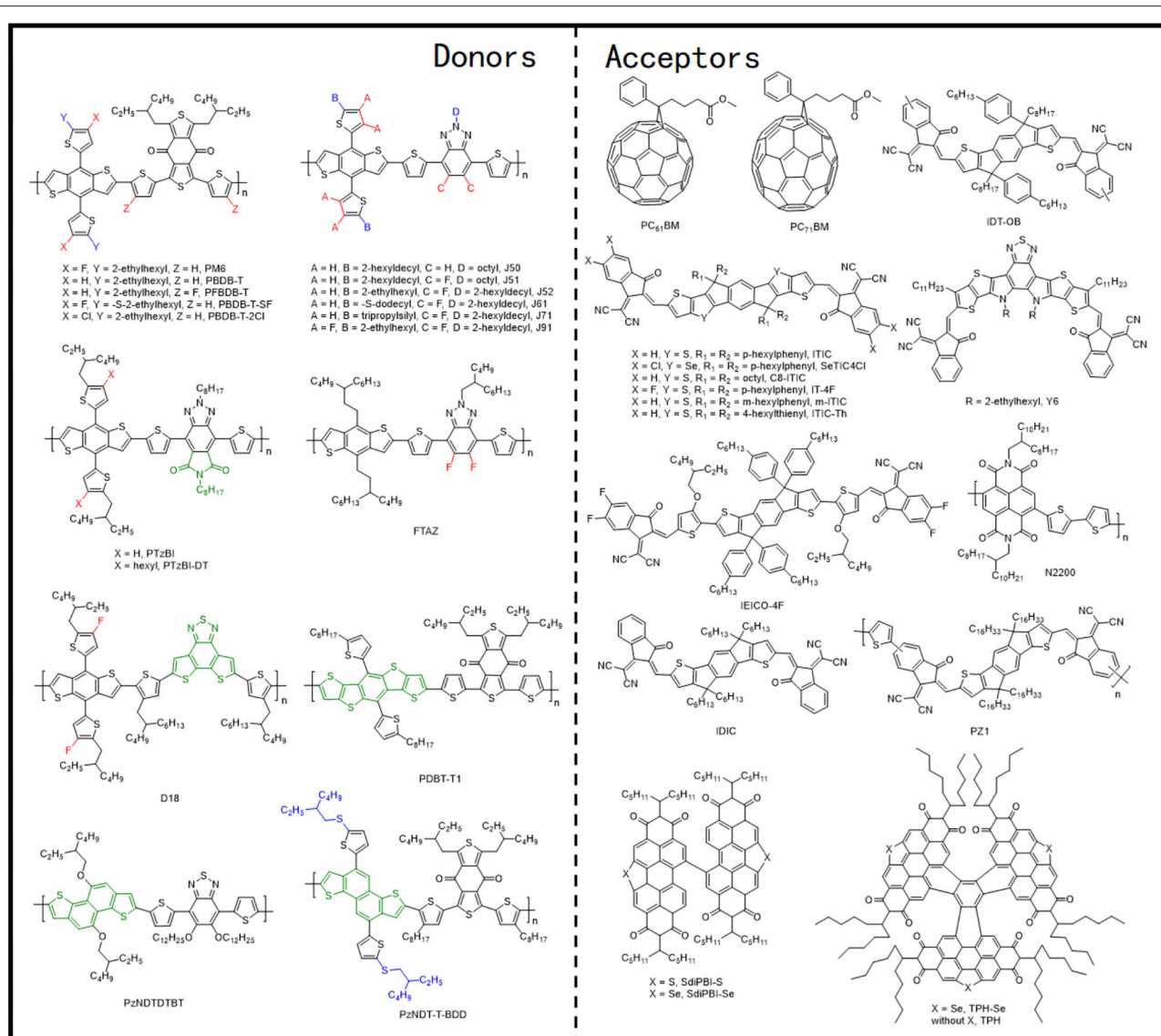


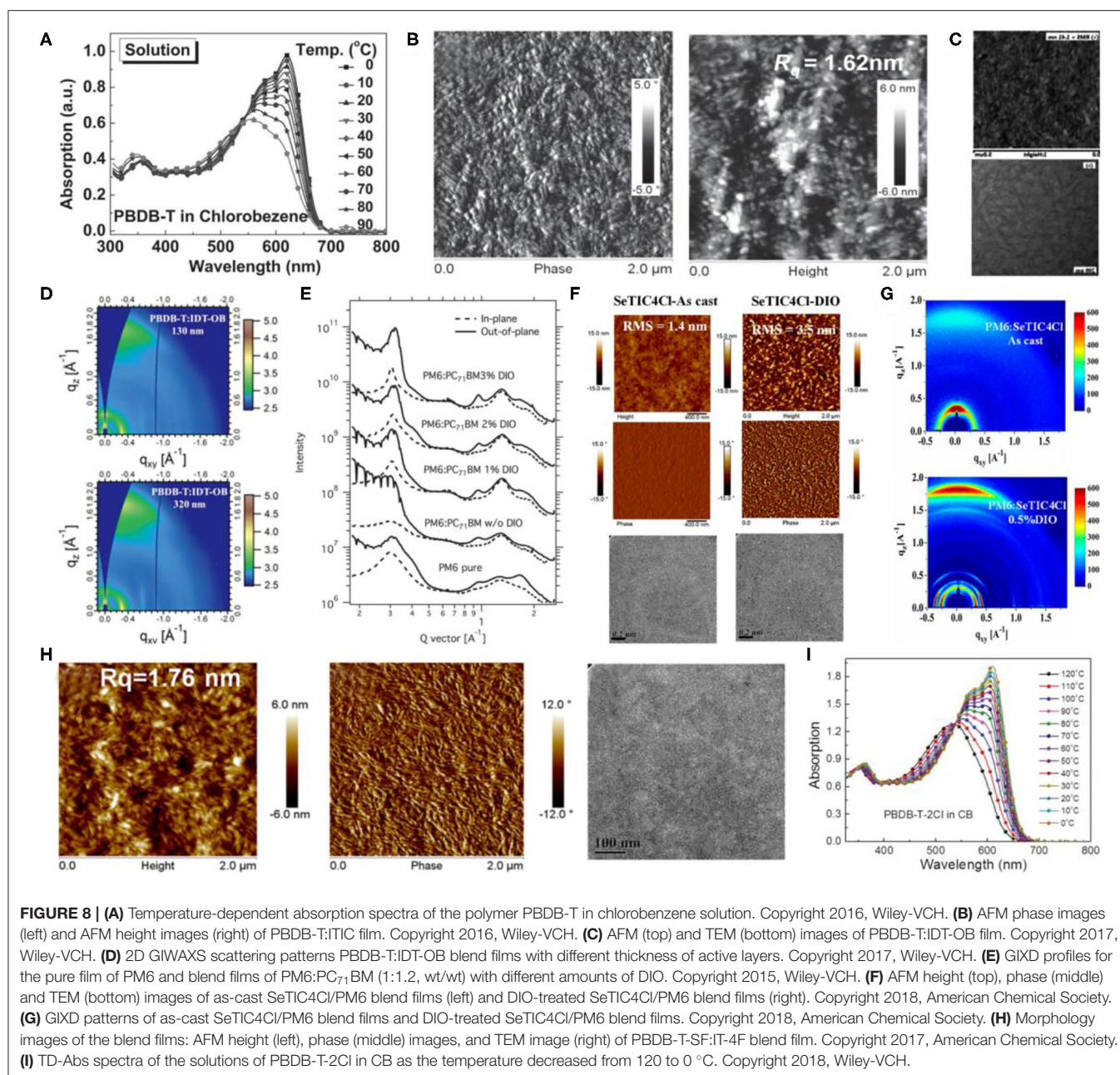
FIGURE 7 | Molecular structures of representative D- π -A copolymers with T π -bridge and mentioned acceptors.

PFBDB-T (**Figure 7**) has been synthesized after fluorination on the π -bridge of PBDB-T. The corresponding PFBDB-T:C8-ITIC devices thus led to a high PCE of 13.2%, as a consequence of fluorination-dependent reduced energy losses within the blend (Fei et al., 2018). Similarly, Zhao et al. replaced the 2-ethylhexyl on the BDT-T unit of PM6 with a thioether group and obtained PBDB-T-SF polymer as shown in **Figure 7**. After blending it with IT-4F, the devices yielded a remarkable PCE of 13% (Zhao et al., 2017). Moreover, the PBDB-T-SF:IT-4F blend morphological properties were observed to be very similar to that of PBDB-T:ITIC blend films in terms of nanoscale phase separation and appropriate domain sizes (**Figure 8H**). In another example, PBDB-T-2Cl (**Figure 7**) has been successfully synthesized by substituting the fluorine atom on the BDT-T unit of the PM6 polymer with a chlorine atom,

which displayed a temperature-dependent absorption spectrum in solution (**Figure 8I**). The PBDB-T-2Cl:IT-4F-based devices ultimately displayed a PCE of >14% with good stability (Zhang et al., 2018).

BDT-T and BTz Unit-Based D- π -A Copolymer With Thiophene π -Bridge

The BTz units generally have a hydrogen atom attached to the nitrogen atom in the system, which indicates the possibility of an additional alkyl chain attachment with the backbone that can enhance the solubilization. The J series polymer molecules have been the most reported polymers based on the BDT-T and BTz units. One of such polymers, J50 (**Figure 7**), has been synthesized via alternately connected alkyl-substituted BDT-T, thiophene π -bridge, and alkyl-substituted BTz units. Likewise, further



modification of the acceptor unit utilizing the bifluorination strategy led to the synthesis of another impressive polymer, J51 (Figure 7) (Gao et al., 2016a). All polymer solar cells (PSCs) based on J51:N2200 demonstrated a high PCE of 8.27%, as a consequence of predominant face-on orientation (Figure 9A) and semicrystalline structure. Similarly, blending the J51 polymer with the ITIC acceptor led to a better complementary absorption spectrum and therefore further improved the efficiency to 9.26% (Gao et al., 2016b). Likewise, the J52 polymer has been synthesized by replacing the substituents on the donor and acceptor units with the most commonly used 2-ethylhexyl alkyl chain (Figure 7), and blending it with an ultranarrow bandgap

NFA, IEICO-4F, led to a PCE of 9.3% with an excellent J_{SC} of $21.9 \text{ mA} \cdot \text{cm}^{-2}$ (Yao et al., 2017). The favorable nanoscale phase separation (Figure 9B), minor bimolecular recombination, and efficient overall charge collection processes have been attributed for such a performance from the corresponding combination. Later, further side-chain engineering, aimed at the BDT-T unit, has been carried out by substituting the alkyl chains by a thioether group, which resulted in the formation of J61 polymer. The corresponding device with *m*-ITIC acceptor resulted in a PCE of 11.77%, thanks to the better matched and fine-tuned donor-acceptor energy levels (Yang et al., 2016). Trialkylsilyl has also been employed as a substituent on the BDT-T unit to obtain a low

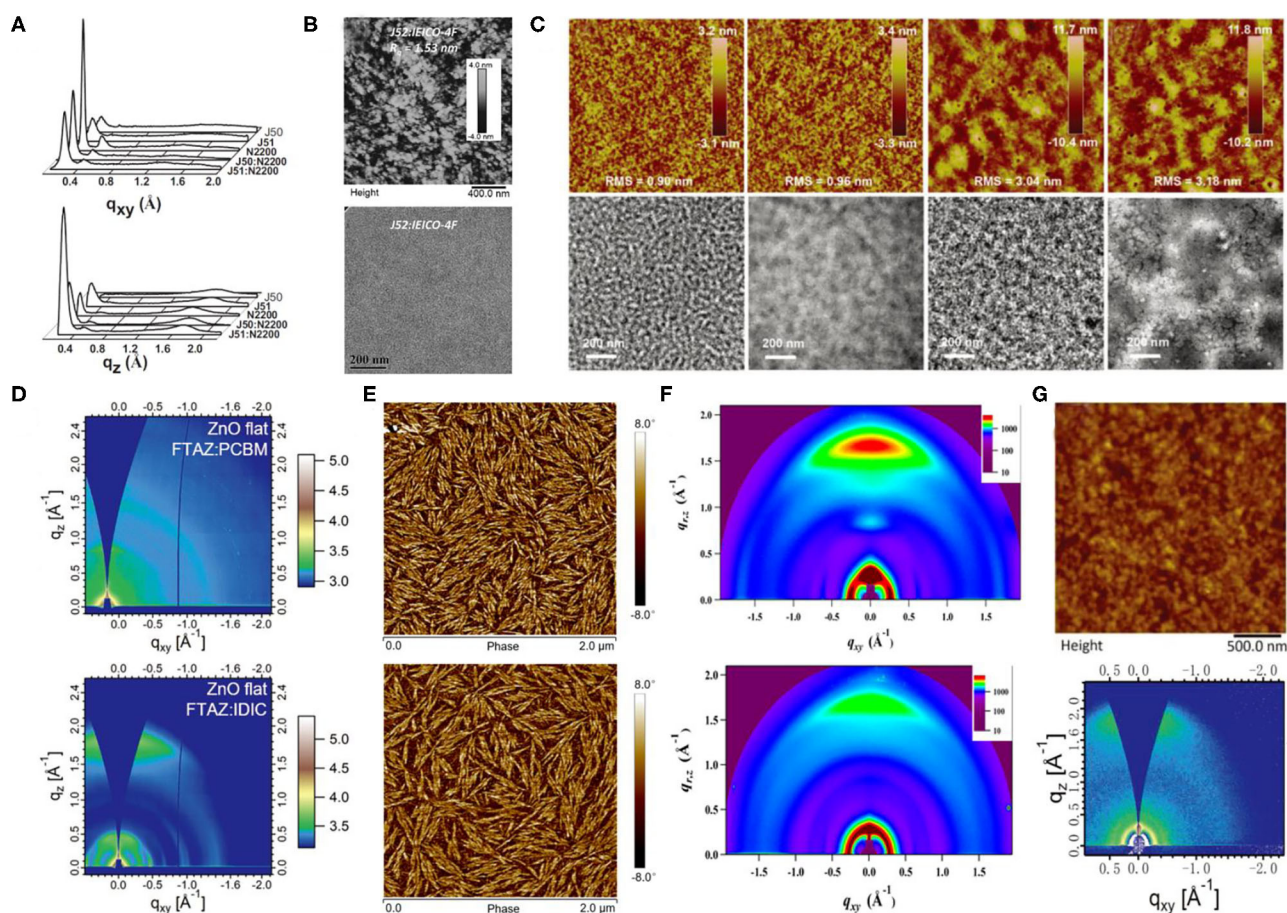


FIGURE 9 | (A) Line cuts of GIWAXS images in in-plane (top) and out-of-plane (bottom) direction for the polymers J50, J51, N2200, and the polymer blends of J51:N2200 (2:1, wt/wt) and J50:N2200 (2:1, wt/wt) films. Copyright 2015, Wiley-VCH. (B) AFM height image (top) and TEM pattern (bottom) of the binary films at a donor ratio of 0.3:0.7. Copyright 2017, Wiley-VCH. (C) AFM height images ($5 \times 5 \mu\text{m}$, top) and TEM images (bottom) for PTzBI:ITIC, PTzBI:ITIC processed with 0.5% dibenzyl ether (DBE), PTzBI-DT:ITIC and PTzBI-DT:ITIC processed with DBE/DIO (from left to right). Copyright 2017, Wiley-VCH. (D) The 2D GIWAXS patterns for FTAZ:IDIC and FTAZ:PCBM blended films with 0.25% DIO on flat ZnO substrates. Copyright 2018, Wiley-VCH. (E) AFM phase images for D18:Y6 blend films without (top) and with (bottom) SVA. Copyright 2020, Science China Press. (F) 2D GIWAXS patterns of (top) neat PDBT-T1 film and (bottom) optimal PDBT-T1:ScdPBI-Se blend film (0.25% DIO). Copyright 2015, American Chemical Society. (G) Tapping mode AFM topography (top) and 2D GIWAXS image (bottom) of PzNDT-T-BDD/IDIC blend film. The size of the AFM image is $2.5 \times 2.5 \mu\text{m}$. Copyright 2018, Wiley-VCH.

HOMO copolymer J71 (Figure 7), whereby blending it with ITIC acceptor displayed a PCE of 11.41% (Bin et al., 2016). To take advantage of the fluorination effect, the same group difluorinated the BDT-T unit of J51 and obtained the J91 polymer (Figure 7). An impressive PCE of 11.63% was achieved after blending it with *m*-ITIC as a consequence of more intense absorption, low-lying HOMO energy level, and higher charge carrier mobility (Xue et al., 2017).

In addition to side-chain engineering and halogenation strategies, the BTz unit has also been modified by diimide functionalization, leading to the formation of novel acceptor materials, PTzBI and PTzBI-2-decyltetradecyl (DT) (Figure 7), which possessed improved crystallinity and preferred molecular packing orientation (Figure 9C), which endowed the corresponding devices with ITIC as acceptor with PCEs of 10.24 and 9.43%, respectively (Fan et al., 2017b).

Other D- π -A Copolymer With Thiophene π -Bridge

Similar to previous examples, the BDT unit has also been utilized to polymerize with the thiophene and BTz units, which led to the formation of another group of FTAZ (Figure 7) type of polymers. However, forming FTAZ:PC₆₁BM blend films led to a system where both donor and acceptor exhibited weak scattering peaks, which indicated a weak molecular packing, and thus, the relevant OSCs showed a moderate PCE of 5.99% (Lin et al., 2018). Involving an NFA, IDIC, however, yielded an enhanced PCE of 12.14% as the corresponding devices benefited from improved crystallinity and dominant face-on orientation relative to the electrodes (Figure 9D). Another important D- π -A polymer that must be mentioned is D18 (Figure 7), which when blended with Y6 acceptor produced an outstanding efficiency of 18.22% (Liu et al., 2020). Such a remarkable performance has been attributed to the large molecular conjugate plane of BDT-T and DTBT

units that promoted the polymer stacking and enhanced the μ_h value, as well as the evenly distributed nanofiber structure about 20 nm (**Figure 9E**). Likewise, combining another two thiophene rings on the base of BDT-T to extend the conjugated area, the DTBDT-T unit has also been introduced to the D- π -A polymer system, which led to the successful synthesis of several donor materials such as PDBT-T1 (**Figure 7**). Several perylene bisimide (PBI)-based small molecule acceptors with a twisted conformation have been blended with PDBT-T1, and hence, the OSC devices based on PDBT-T1:SdiPBI-S, PDBT-T1:SdiPBI-Se, PDBT-T1:TPH, and PDBT-T1:TPH-Se delivered PCEs of 7.16, 8.4, 8.28, and 9.28%, respectively (Sun et al., 2015; Meng et al., 2016a,b). These kinds of acceptors with strong aggregation effect showed good compatibility and preferred face-on orientation with PDBT-T1 in the blend films (**Figure 9F**). Thienyl side-chains functionalized ITIC-Th has also been mixed with PDBT-T1, and the corresponding device showed a PCE of 9.6%, which has been attributed to balanced charge transport and predominant intermolecular π - π interactions vertical to the substrates in the blend films (Lin et al., 2016).

Replacing the benzene of the BDT unit with naphthalene is also a common strategy to extend the conjugated area, where the obtained NDI is employed as an electron-rich unit in the D- π -A polymers. It is practically evident that the “zigzag” NDT (zNDT)-based D-A polymers often possess unique and excellent optoelectronic properties when combined with a suitable acceptor. Shi et al. combined NDI, benzo[c][1,2,5]thiadiazole (BT) unit, and thiophene π -bridge alternately and synthesized a polymer donor, named PzNDTDTBT (**Figure 7**) (Shi et al., 2013). Forming the corresponding blends with PC₇₁BM showed a moderate PCE of 5.07% due to poor compatibility and large domain size. Later, copolymer PzNDT-T-BDD (**Figure 7**) consisting of zNDI and BDD units has been synthesized, and the resulting devices with IDIC as the acceptor showed an improved PCE of 9.72% (Jiang et al., 2018). Facile π - π stacking, appropriate absorption complementation, and active layer morphology have been credited for this performance enhancement (**Figure 9G**).

In general, the D- π -A copolymers are the most researched donor materials as they exhibit the best performances in the BHJ OSCs. Broad and strong absorption, strong crystallinity, good compatibility with NFAs, simple property controllability, and preferred face-on orientation in blend films grant them huge potentials for better device performance and even for commercial applications.

Copolymers of Electron-Deficient Units and Bithiophene

This system involves a relatively simple and operation-friendly methodology to take advantage of the modest synthesis techniques of the PTs, as well as the excellent performance of D-A copolymers simultaneously. The most common electron-deficient units used are BT and BTz. Besides, thieno[3,4-c]pyrrole-4,6-dione (TPD) and 2,2'-bithiophene-3,3'-dicarboximide (BTI) have also been reported. In this regard, the fBT-based donor polymer, PffBT4T-2DT (**Figure 10**), has been synthesized by combining the BT and

the tetrathiophene alternatively. Upon mixing it with an NFA with high-lying LUMO, SF-PDI₂ led to a PCE of 6.3%, largely due to appropriate energy level matching and favorable BHJ morphology (**Figure 11A**) (Zhao et al., 2015). An unbalanced hole and electron mobility, however, resulted in unsatisfactory performance. Later, another NFA, IDTBR, has been employed with the same donor, and the corresponding devices displayed an improved PCE of 10%. This enhancement has been attributed to the low voltage losses and good luminescence yields in the blend films (Baran et al., 2016). Similarly, utilizing the side-chain engineering to replace the DT on the thiophene unit of PffBT4T-2DT with a 2-octyldodecyl, PffBT4T-2OT (**Figure 10**) has been synthesized. Hence, the OSCs based on PffBT4T-2OT:PC₇₁BM achieved a PCE of 9.2%, thanks to an increase in both the domain size and exciton diffusion length during thermal annealing (Zhang et al., 2019). Furthermore, PFBT4T-C5Si-50% and PFBT4T-C5Si-25% have been synthesized by partly replacing the DT side chain using a siloxane-terminated side group (**Figure 10**), which demonstrated strong crystallinity and temperature-dependent solution absorption spectrum (**Figure 11B**) (Liu et al., 2017). Using PC₇₁BM as an acceptor, the corresponding blend films exhibited preferred morphology and face-on stacking orientation even at film thicknesses up to 600 nm (**Figure 11C**). Similarly, P3TEA (**Figure 10**), another well-researched polymer whose structure comprises alternately connected BT unit and ester-substituted trithiophene, when blended with SF-PDI₂, showed a PCE of 9.5% due to the efficient charge generation and separation, despite having a negligible driving force (Liu J. et al., 2016). Likewise, replacing the acceptor with a PDI-tetramer NFA, FTTB-PDI4, led to an improved PCE of 10.58% as a consequence of stronger π - π stacking and higher domain purity in the blend films (**Figure 11D**) (Zhang J. et al., 2017).

In another example, by inserting one BTz unit between every five thiophenes and performing ortho or para bifluorination on those thiophenes, Li et al. synthesized two polymer donors, PTFB-O and PTFB-P, as shown in **Figure 10** (Li et al., 2016a). The corresponding devices based on PTFB-O:ITIC, due to suitable crystallinity (**Figure 11E**) and good donor and acceptor compatibility, showed a modest PCE of 9.9%. Chen et al. similarly added a BDT unit into the copolymer of BTz unit and bithiophene, which led to the synthesis of PvBDTTAZ (**Figure 10**). Mixing it with NFA IDTBR thus led to an impressive PCE of 11.6%, which was attributed to high crystallinity and small domains for both donor and acceptor within the blend films (**Figure 11F**) (Chen et al., 2017). Interestingly, ester substitution and fluorination have been applied to form a unique polymer donor, PBTZ-C4T (**Figure 10**), maintaining an A₁- π -A₂ architecture. Blending it with ITIC-Th led to a PCE of 9.34%, owing to a better planar geometry, improved light absorption, and high crystallinity (**Figure 11G**) (Guo et al., 2019).

Apart from the molecules mentioned above, TBD and BTI units have also been often employed to construct copolymer donor materials with bithiophene. Through copolymerization of TPD and BTI as the electron acceptor unit and terthiophene (3T) as the electron donor unit, Guo et al. synthesized

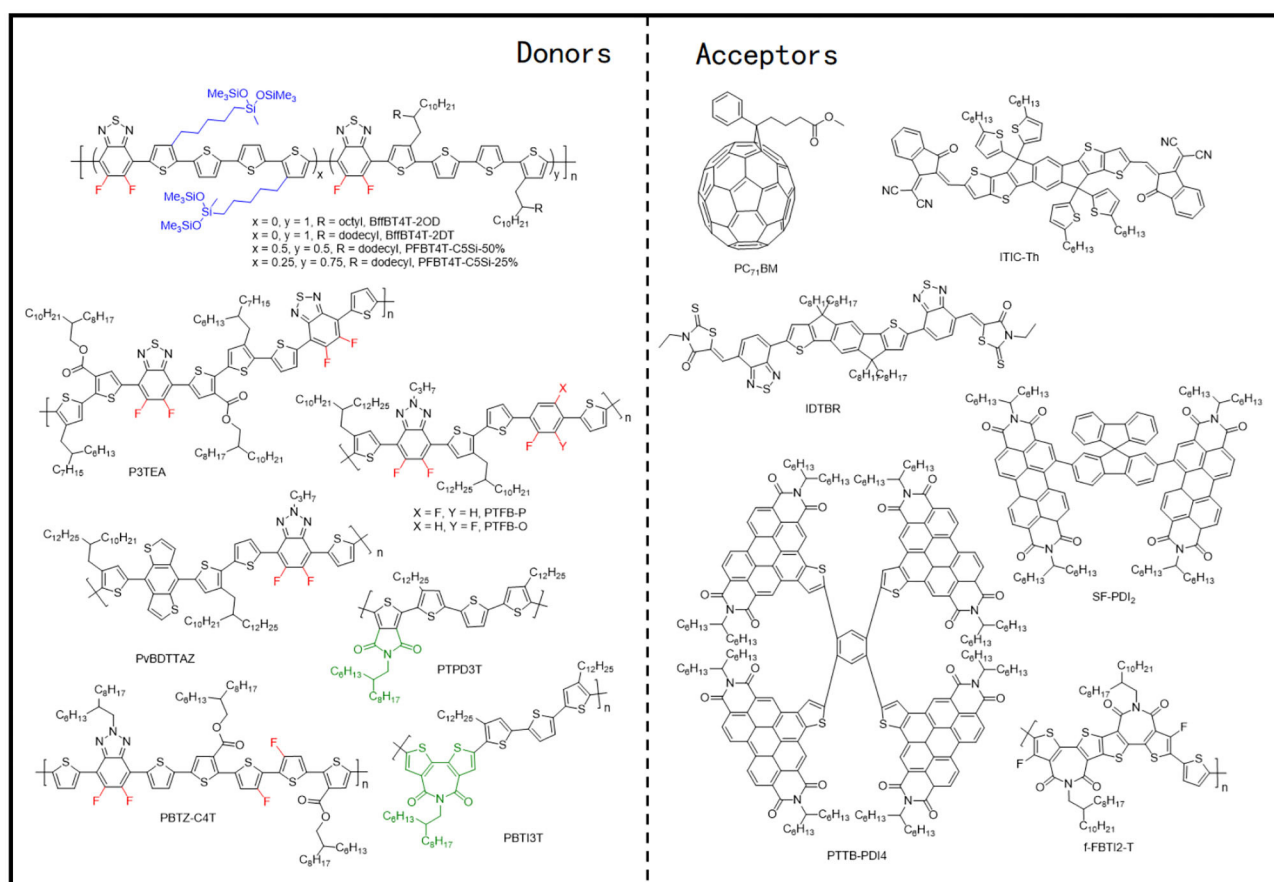


FIGURE 10 | Molecular structures of representative copolymers of the electron-deficient unit and bithiophene and mentioned acceptors.

PTPD3T and PBTI3T (**Figure 10**) and upon their incorporation with PC₇₁BM acceptor, extremely high FFs of 76% to 80% with PCEs of about 8.7% have been achieved (Guo et al., 2013). The distinguished FF values have been attributed to close π - π interplanar spacings, face-on molecular oriented microstructures, ordered BHJ bicontinuous networks, and vertical phase gradation. Later, Sun et al. fused two fluorinated BTI units and combined it with a simple thiophene, obtaining a novel BTI-based polymer, f-BBTI2-T (**Figure 10**) (Sun et al., 2019). Because of the extended π -conjugation, reduced bandgap, and lower-lying LUMO energy level, the all-PSCs based on PTB7-Th:f-BBTI2-T exhibited an extraordinary PCE of 8.1%.

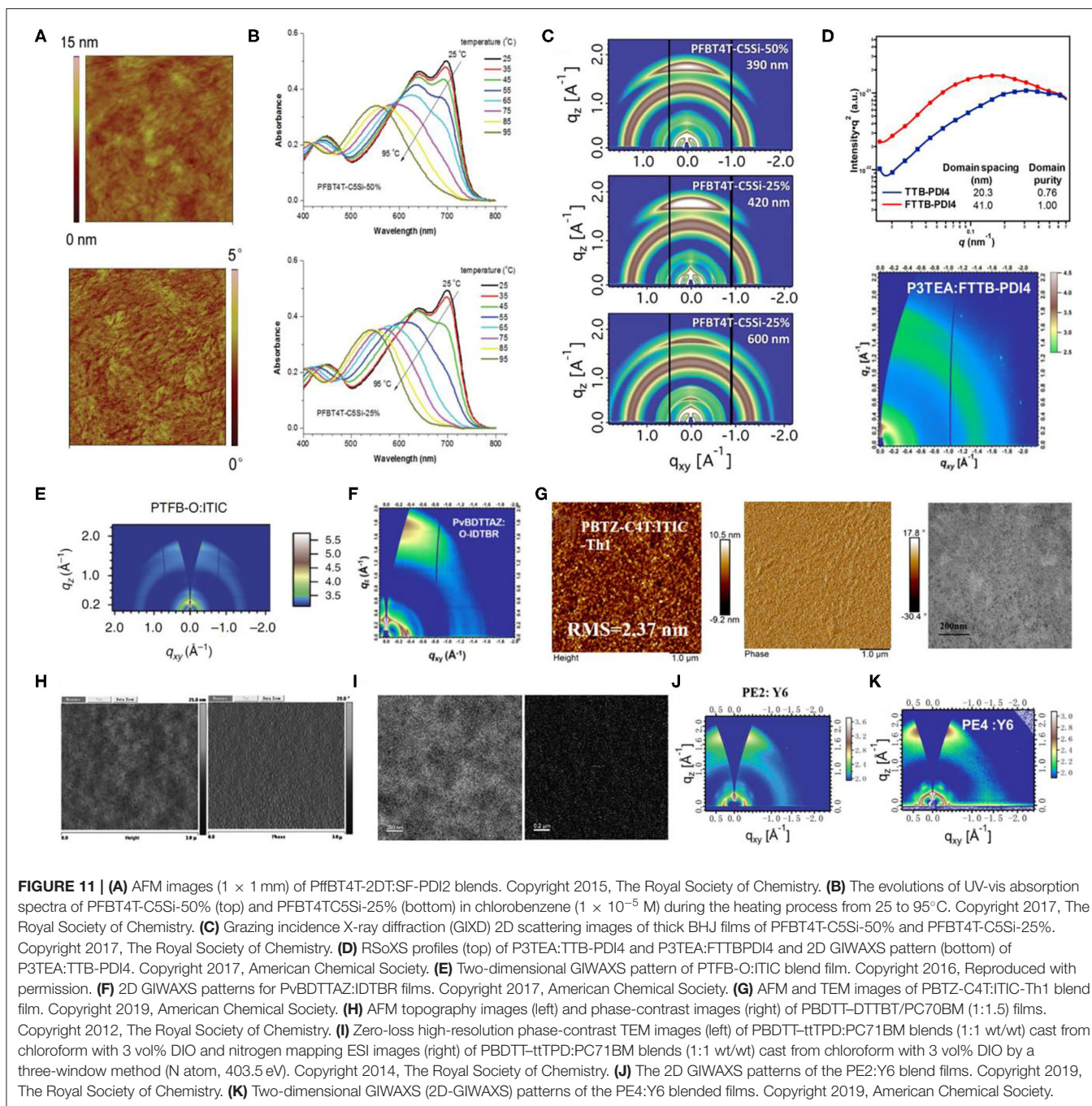
D- π -A Copolymer With TT π -Bridge

TT units possess a rigid and coplanar fused ring, which ensures a highly delocalized π -electron system and strong intermolecular π - π stacking, and thus has attracted much interest for the construction of high performance polymer materials for applications in optoelectronic devices. Utilizing the TT as the π -bridge in D- π -A copolymer is a commonly

used strategy to extend the conjugated plane and improve the crystallinity of materials.

By applying T and TT as the π -bridges, Guo et al. polymerized BDT-T and BT units and acquired two polymer donors, PBDTT-DTTBT and PBDTT-DTBT (**Figure 12**) (Guo et al., 2012). PCEs of 6.03 and 2.34%, respectively, have been attained for the corresponding blends with PC₇₁BM, as the PBDTT-DTTBT-based system has been able to produce two orders of magnitude higher hole mobility of $1.97 \times 10^{-3} \text{ cm}^2/\text{V} \cdot \text{s}$ (**Figure 11H**), as compared to PBDTT-DTBT ($1.58 \times 10^{-5} \text{ cm}^2/\text{V} \cdot \text{s}$), as a consequence of good crystallinity in the former. This huge difference in mobility and device performance has been attributed to the unequal conjugated areas of the TT and T π -bridges. Likewise, the polymer based on BDT and diketopyrrolopyrrole (DPP) units have also been modified by the application of TT π -bridge, whereby forming blends with PC₇₁BM as acceptor revealed a similar pattern as mentioned previously (Li et al., 2013). Moreover, an alkyl substituted TT π -bridge, 6-alkylthieno[3,2-b]thiophene has also been researched, where a PCE of 6.81% has been achieved for a PBDTT-tTPD:PC₇₁BM-based system (**Figure 11I**) (Kim et al., 2014).

NFAs have also been involved in the investigation of D- π -A copolymer with TT π -bridges. Chen et al. replaced the



T π -bridge of J52-SF with alkyl-substituted TT π -bridge and synthesized PE2 (Figure 12). This ultimately led to down-shifted HOMO energy levels, higher crystallinity, and stronger π - π stacking in the polymer (Figure 11J), and blending it with Y6 acceptor resulted in an impressive PCE of 13.50% (Chen et al., 2019). Later, a chlorinated homolog of PE2, PE4, has been reported by the same group (Figure 12), which displayed an excellent PCE of 14% when blended with a Y6 acceptor (Figure 11K) (Tang et al., 2019).

In fact, the latter three parts can be regarded as D- π -A copolymers containing thiophene, bithiophene, and thienothiophene units. In these materials, thiophene, bithiophene, and thienothiophene units can provide a larger range for π -electron delocalization and promote molecular packing. However, there are three main differences between them. First, from the perspective of synthesis, the synthesis steps and costs of thienothiophene units are higher than the thiophene and bithiophene units. Second, from the perspective of molecular

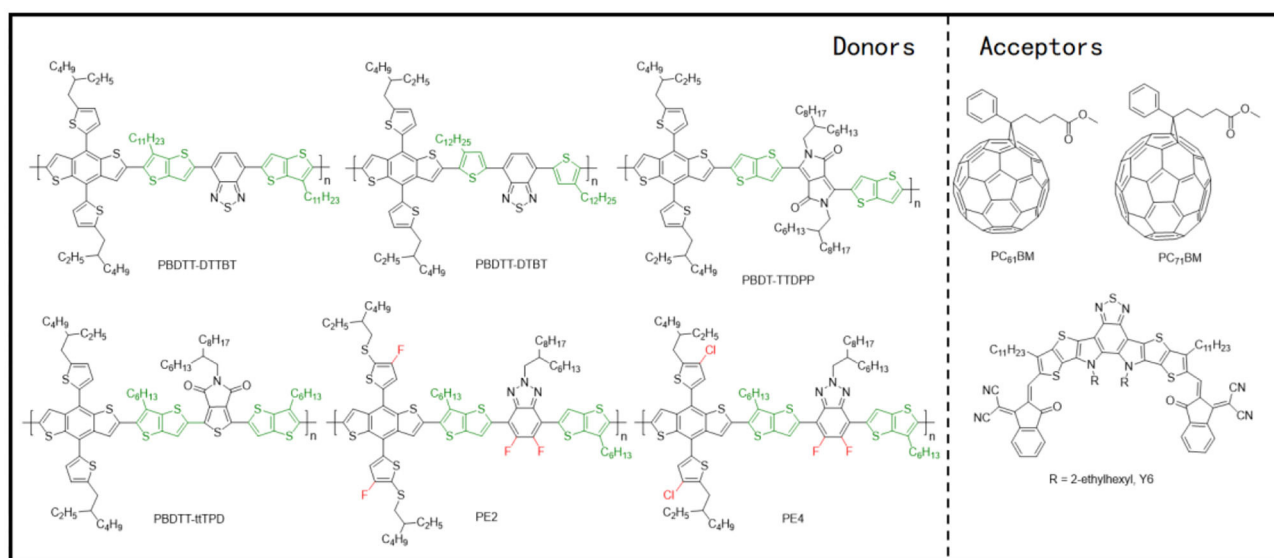


FIGURE 12 | Molecular structures of representative D- π -A copolymers with TT π -bridge and mentioned acceptors.

packing, the thienothiophene can provide a larger molecular conjugate plane as compared to the other two units and thereby promotes the molecular packing to the greatest extent. Finally, from the perspective of device performance, although the final film orientation and molecular packing get affected by all three units differently, and as an excellent device performance requires a proper rather than very strong crystallinity, there is no specific rule that can determine the impact of the three units on device performance, without further analyzing the specific donor and acceptor materials relationship.

The BHJ OSC devices' performance of the presented materials is summarized in **Table 1**.

METHODS OF CONTROLLING THE CRYSTALLINITY OF BLEND FILMS BASED ON POLYMER DONORS

Crystallization can be considered as a process of molecular aggregation changes under the influence of postprocessing conditions. Therefore, the nature of a certain molecule and postprocessing conditions have a decisive effect on the crystallization process and the final film morphology. The modification of the crystallinity and crystallization process has also been summarized according to this idea.

Polymer Molecular Structure

The driving force for the crystallization process is essentially the overlapping of π electron orbitals between the involved molecules and the increase of the delocalization range of π electrons. At the same time, the molecular structure determines the distribution of π electrons in the molecule. Therefore, controlling the molecular structure of the polymer can be regarded as the fundamental methodology to adjust the

crystallinity and the crystallization process in the blend film. Generally, an increase in the size of the conjugated plane, side-chain engineering, and halogenation (mainly fluorination and chlorination) are the most commonly used methods for adjusting the molecular structure of polymers.

Increasing the Conjugated Plane

Having an enlarged conjugated plane generally means more π electrons, as well as wider delocalized π orbitals in the system, which ultimately leads to enhanced interaction between the involved crystalline organic semiconductor molecules. Therefore, a larger conjugated plane with high flatness usually is an indicator of strong crystallinity. The most representative instances in this regard are the polymers with a TT π -bridge, as mentioned previously (Guo et al., 2012; Li et al., 2013; Kim et al., 2014; Chen et al., 2019; Tang et al., 2019). Similarly, polymers based on BDT-T or DTBDT units usually exhibit improved crystallinity than the BDT series. As illustrated in **Figure 6C**, the BDT-T-based D-A copolymer, PTB7-Th, showed an enhanced signal peak in the GIWAXS spectrogram as compared to its corresponding BDT-based homolog, PTB7, indicating that increased conjugation plane can indeed enhance the intermolecular aggregation effect.

Side-Chain Engineering

Side chains in organic semiconductor materials are generally introduced for solubilization, but they also affect the interaction between the molecules as well. Alkoxy, carbonyl, alkyl, alkoxy, thioether groups, and silyl groups have often been reported as the most used side chains (Fan et al., 2017a, 2018; Liu et al., 2018). The interaction between the side chains and the resulting changes in the molecular configuration generally affects the molecules' self-aggregation effect and thus affects the crystallinity. Unfortunately, there is no obvious rule to indicate which side chains can increase or decrease the molecular

TABLE 1 | The BHJ OSCs devices performance of the presented materials.

Active layer	J_{sc} (mA · cm ⁻²)	V_{oc} (V)	FF(%)	PCE (%)	References
P3HT:PC ₆₁ BM	10.6	0.61	67.4	4.37	Li et al., 2005
P3HT:IDTBR	13.9	0.72	60	6.30	Holliday et al., 2016
P3HT:EH-IDTBR	12.1	0.76	62	6.00	Holliday et al., 2016
P3HT:IDTBR:IDFBR	14.4	0.82	64	7.7	Baran et al., 2017
P3HT:SF(DPPB) ₄	8.29	1.14	55	5.16	Li S. et al., 2016
PDCBT:PC ₇₁ BM	11.0	0.91	72	7.2	Qin et al., 2016
PDCBT:ITIC	16.50	0.94	65.67	10.16	Qin et al., 2016
PTB1:PC ₇₁ BM	15.0	0.56	63.3	5.6	Liang et al., 2009
PTB7:PC ₇₁ BM	14.50	0.74	68.97	7.40	Liang et al., 2009
PTB7-Th:PC ₇₁ BM	14.02	0.79	69.1	7.64	Liao et al., 2013
PTB7-Th:ITIC	14.21	0.81	59.1	6.80	Lin et al., 2015
PTB7-Th:IHIC	19.01	0.754	68.1	9.77	Wang et al., 2017
PTB7-Th:TPB	17.9	0.79	58	8.47	Wu et al., 2016
PTB7-Th:PNDI-T10	12.9	0.83	71	7.6	Li et al., 2016b
PBDTTT-E-T:PC ₇₁ BM	14.59	0.58	62.6	6.21	Huo et al., 2011
PBDTTT-C-T:PC ₇₁ BM	17.48	0.74	58.7	7.59	Huo et al., 2011
PBFTT:IT-4Cl	19.7	0.76	73.9	11.1	Su et al., 2019
PBDB-T:PC ₆₁ BM	10.68	0.86	72.27	6.67	Qian et al., 2012
PBDB-T:ITIC	16.81	0.899	74.2	11.21	Zhao W. et al., 2016
PBDB-T:IDT-OB	16.18	0.88	71.1	10.12	Feng et al., 2017
PBDB-T:PZ1	16.05	0.830	68.99	9.19	Zhang J. et al., 2017
PM6:PC ₇₁ BM	12.7	0.98	74	9.2	Zhang et al., 2015
PM6:SeTIC4Cl	22.92	0.78	75	13.32	Wang et al., 2018
PM6:BTP-4F	24.9	0.834	75.3	15.6	Cui et al., 2019
PM6:BTP-4Cl	25.4	0.867	75.0	16.5	Cui et al., 2019
PFBDB-T:C8-ITIC	19.6	0.94	72	13.2	Fei et al., 2018
PBDB-T-SF:IT-4F	20.50	0.88	71.9	13.0	Zhao et al., 2017
PBDB-T-2Cl:IT-4F	21.8	0.86	77	14.4	Zhang et al., 2018
J51:N2200	14.18	0.83	70.24	8.27	Gao et al., 2016a
J51:ITIC	16.47	0.82	69	9.26	Gao et al., 2016b
J52:IEICO-4F	21.9	0.734	58.5	9.3	Yao et al., 2017
J61:m-ITIC	18.31	0.912	70.77	11.77	Yang et al., 2016
J71:ITIC	17.32	0.94	69.77	11.41	Bin et al., 2016
J91:m-ITIC	18.03	0.984	65.64	11.63	Xue et al., 2017
PTzBI:ITIC	18.29	0.87	64.34	10.24	Fan et al., 2017b
PTzBI-DT:ITIC	16.84	0.91	61.53	9.43	Fan et al., 2017b
FAZ:PC ₆₁ BM	9.90	0.814	74.3	5.99	Lin et al., 2018
FAZ:IDIC	21.4	0.840	67.5	12.14	Lin et al., 2018
D18:Y6	27.70	0.859	76.6	18.22	Liu et al., 2020
PDBT-T1:SdiPBI-S	11.65	0.90	65.5	7.16	Sun et al., 2015
PDBT-T1:SdiPBI-Se	12.48	0.947	69.7	8.4	Meng et al., 2016b
PDBT-T1:TPH	12.01	0.968	70.1	8.28	Meng et al., 2016a
PDBT-T1:TPH-Se	12.53	1.001	71.7	9.28	Meng et al., 2016a
PDBT-T1:ITIC-Th	16.24	0.88	67.1	9.6	Lin et al., 2016
PzNDTDTBT:PC ₇₁ BM	10.46	0.74	65.5	5.07	Shi et al., 2013
PzNDT-T-BDD:IDIC	15.65	0.875	71.05	9.72	Jiang et al., 2018
PfBT4T-2DT:SF-PDI ₂	11.1	0.99	58	6.3	Zhao et al., 2015
PfBT4T-2DT:IDTBR	15.2	1.08	62.2	10	Baran et al., 2016
PfBT4T-2OT:PC ₇₁ BM	17.5	0.75	72.4	9.2	Zhang et al., 2019
PFBT4T-C5Si-50%	16.98	0.75	70.98	9.26	Liu et al., 2017

(Continued)

TABLE 1 | Continued

Active layer	J_{sc} (mA · cm ⁻²)	V_{oc} (V)	FF(%)	PCE (%)	References
PFBT4T-C5Si-25%	18.93	0.76	74.4	10.95	Liu et al., 2017
P3TEA:SF-PDI ₂	13.27	1.11	64.3	9.5	Liu J. et al., 2016
P3TEA:FTTB-PDI4	14.05	1.14	66.4	10.58	Zhang Z. G. et al., 2017
PTFB-O:ITIC	15.5	0.92	70	9.9	Li et al., 2016a
PvBDTTAZ:IDTBR	16.44	1.084	64.4	11.6	Chen et al., 2017
PBTZ-C4T:ITIC-Th	16.59	0.84	66.65	9.34	Guo et al., 2019
PTPD3T:PC ₇₁ BM	12.3	0.786	78.7	7.72	Guo et al., 2013
PBTI3T:PC ₇₁ BM	12.8	0.850	76.3	8.42	Guo et al., 2013
PTB7-Th:f-FBTI2-T	13.60	1.05	56.5	8.1	Sun et al., 2019
PBDTT-DTTBT:PC ₇₁ BM	12.46	0.78	62.0	6.03	Guo et al., 2012
PBDTT-DTBT:PC ₇₁ BM	5.78	0.82	49.5	2.34	Guo et al., 2012
PBDT-TDPP:PC ₇₁ BM	14.58	0.73	50	5.34	Li et al., 2013
PBDTT-tTPD:PC ₇₁ BM	11.05	0.84	70	6.81	Kim et al., 2014
PE2:Y6	23.24	0.83	70	13.50	Chen et al., 2019
PE4:Y6	22.21	0.84	75.43	14.02	Tang et al., 2019

crystallinity. On the other hand, the structure of the side chains itself, as well as the connecting positions, also influences the crystallinity of molecules. Shi et al. synthesized a series of PffBZ copolymers with different side chains and revealed that the performance of the polymers with branching on the second position of the alkyl chain and the third position of the alkoxy chain delivered the best film morphology and molecular packing characteristics (Shi et al., 2020). Furthermore, adjusting the crystallinity through the molecular structure will also affect the energy levels, absorption, and other properties of the material. The systematic study of different side chains in different systems is an important research direction.

Halogenation Strategy

The halogenation strategy has been proven to be one of the simplest and most effective methods to improve the performance of both polymer donor- and NFA-based systems. Extensive research on fluorination methods has shown that the introduction of the fluorine atoms, having the largest electronegativity and small atomic radius, into organic semiconductor materials can significantly decrease the energy levels and improve molecular aggregation (Zhang et al., 2016; Xue et al., 2017). In this regard, by fluorinating the BT unit of PBnDT-DTBT, a D- π -A polymer, the researchers obtained PBnDT-DTffBT polymer that displayed increased aggregation as its thin films revealed an additional absorption shoulder peak in the spectra (Zhou et al., 2011). Similarly, a BDD-bithiophene-based polymer, PBDD4T-2F, with two fluorine atoms connected to two adjacent thiophenes showed stronger crystallinity than its non-fluorinated homologs, which led to relatively more complex absorption curves, as well as stronger peaks in the GIWAXS spectra (Zhang et al., 2016). Likewise, compared with the fluorine atoms, the chlorine atoms not only have a larger radius but are also capable to lower the corresponding energy levels even further, as their 3d orbitals can accept electrons from the conjugated skeleton. Furthermore, the chlorinated polymers

are relatively easier to synthesize than the fluorinated polymers. Mo et al., in this regard synthesized PBDTHD-ClBTDD, a D- π -A copolymer based on BDT-T and BT units with a chlorine atom attached to the BT unit, whose absorption spectra revealed a stronger vibronic shoulder, suggesting stronger π - π stacking in the system (Mo et al., 2017).

Post-processing Conditions

Solution processing is one of the major advantages that organic semiconductors have over their inorganic counterparts. During the spin coating process, the active layer solvent gradually volatilizes, and as a result, the solute molecules approach each other, and eventually, a film is formed. Because the fast cooling process is involved here, the post-film formation processes have a strong influence on the crystallization process and film morphology of the corresponding films. The utilization of solvent additives and thermal annealing can be regarded as two important external parameters that can significantly impact the final film characteristics.

Solvent Additives

Trichloromethane or chloroform (CF) is the most frequently used solvent for film preparation because of its excellent dissolution ability and low boiling point. However, the latter also results in the rapid drying of the films, leading to poor and unstable film morphologies (Li et al., 2013). To overcome this, a high boiling point additive has been introduced in the system that can lower the drying process and hence allow sufficient time to the corresponding active layer components for proper self-organization. As a result, an enhanced film morphology and ultimately device performance will be achieved. In this regard, DIO can be termed as the most commonly used additive to improve the performance of devices based on polymer materials such as PM6, PTB7-Th, PBDB-T, etc. (Zhang et al., 2015; Liu F. et al., 2016; Zhao W. et al., 2016).

Thermal Annealing

Thermal annealing can be regarded as a simple, widely used, and cost-efficient strategy that can effectively modify the crystallinity of the blend films in a controllable fashion. At high temperatures, the molecules in the films can self-assemble to repair the defects induced by the spin-coating crystallization process and ultimately improve the morphology of the films. Researches have shown that thermal annealing is effective for improving the exciton diffusion for some organic donor materials (Long et al., 2017). For PffBT4T-2OD polymer, composed of BTz and bithiophene units, Zhang et al. investigated the influence of thermal annealing on crystallite size, exciton diffusion, and charge harvesting in films and stated that thermal annealing increases domain size and exciton diffusion length simultaneously in the corresponding system (Zhang et al., 2019).

In contrast to the methods for regulating the molecular structure, the external parameters of film preparation enable better control of the molecular crystallization process and the film morphology with almost no other influence. Coupled with the simple operation, this methodology is more suitable for the improvement of film morphology and photovoltaic performance. Precise and utmost control, however, remains a complicated and difficult task.

Compatibility Between Donor and Acceptor

Even though there are at least two substances in the blend films forming the BHJ, the adjustment methods mentioned previously are largely aimed at a single substance, either donor or acceptor. Hence, things get quite complex when we talk about controlling the BHJ parameters. Compared with a neat film of a certain substance, compatibility between donor and acceptor can be regarded as the most essential concept in OSC active layer. Compatibility generally refers to the ability of two molecules to mix; however, the extent of it should neither be too excessive nor inadequate, just like crystallinity, as extensive compatibility will result in poor phase separation, small domain size, and low phase purity, whereas weak compatibility will result in excessively large grains. Furthermore, the compatibility between the two molecules is closely related to their respective structures and their interactions. It has been reported that many factors such as similar chemical structure, surface energy, molecular orientation, and crystallite and domain size will definitely affect the compatibility (Mai et al., 2016). For instance, Li et al. synthesized two difluorinated copolymers based on BTz and bithiophene units, PTFB-O and PTFB-P (Li et al., 2016a). The only difference between them is the position where the two fluorine atoms are substituted. Thus, this small detail led to different stable molecular configurations, different crystallinity, and different compatibility with the PC₇₁BM and ITIC acceptors. As a result, while the PTFB-O yielded >10% and 6.5% PCE for NFA and fullerene-based cells, respectively, the PTFB-P was found to be a much better match for the fullerene acceptor.

Compatibility is a relatively vague concept as it is almost impossible to predict whether the compatibility between two molecules is appropriate and can only be inferred from the results

of relevant film characterization. Hence, the adjustment of the compatibility between two molecules remains a research gap in the BHJ OSC field.

SUMMARY AND OUTLOOKS

In the past few decades, the performance of BHJ OSCs has experienced rapid progression, largely due to the continuous optimization and development of polymer donor and NFA materials. In this short review, structures, crystallization, and packing characteristics of representative polymer donors with various acceptors have been summarized, followed by methods for controlling the crystallinity and crystallization process of the relevant moieties. Thanks to the continuous efforts by outstanding scholars for the BHJ OSCs, this field is now seen as having great potential for industrial applications. However, numerous issues still need to be solved, which prevents further breakthroughs in the device performance, especially PCE.

In the past few years, most of the molecular design and development have been based on a trial model, without a great deal of theoretical guidance, as the theoretical research in the BHJ OSC field is not yet mature enough. For example, although it is a generally accepted consensus that uniform nanoscale interpenetrating network morphology and face-on-oriented molecular orientation are crucial to favorable FF, how to accurately control the material properties and device preparation conditions to obtain satisfactory FF remains an urgent problem. The development of theories that can directly correlate the concepts of polymer molecular structure, crystallinity, morphology of films, and FF of OSCs may provide new ideas for molecular design.

Second, compared with laboratory research, large-area devices are one of the most significant requirements for industrial applications. The preparation process of large-area OSCs often means a thicker and uneven active layer, which further poses more difficult challenges for the OSC materials. Compared with the small molecules, the highly crystalline polymer donors enable the corresponding films to show acceptable morphology, and thus, the resulting OSC devices can maintain a certain excellent performance, which still, however, is not up to the laboratory-scale standards. Hence, by taking advantage of the strong crystallinity of certain polymer donors, optimal self-assembly in the thick film preparation can be realized, and ultimately, thick film system OSCs with as little efficiency loss as possible can be obtained, thus solving the current issue in hand.

Finally, the environmental pollution during the preparation of OSCs, and the polymer donor structure-dependent instability of OSCs are also important problems that need to be resolved. The large conjugated planes of the polymer donor materials, even though enduing them with a strong self-aggregation effect and crystallinity, also make them less soluble. As a result, almost all OSCs based on polymer donor materials are processed using toxic CF or chlorobenzene solvents, and common environmentally friendly solvents such as water and alcohol are rendered completely unusable. Furthermore, the

polymer donors generally contain abundant π electrons and hence are prone to redox reactions when exposed to air and light, which brings severe device stability problems. How to increase the solubility and stability of the common polymer donor materials while maintaining strong crystallinity requires some more thinking to do.

In short, great progress has been made in the research of OSCs based on polymer donor materials, which makes the use of solar energy more convenient and a big step forward in bringing new vitality to the photovoltaic field. If the current progress can go further in terms of energy conversion efficiency and stability, this technology will be widely used in daily life,

with exceptional market prospects. We believe that having some outstanding scientific researchers in the field who are tirelessly working on material design and synthesis, theoretical research and development, and device preparation and optimization, the BHJ OSCs will gradually mature in the next few years and become an indispensable part of the entire social energy structure.

AUTHOR CONTRIBUTIONS

DQ and KL prepared the manuscript. MA and ZW helped to prepare and revise the manuscript. KL and ZW supervised the project. All authors discussed and commented on the paper.

REFERENCES

- Baran, D., Ashraf, R. S., Hanifi, D. A., Abdelsamie, M., Gasparini, N., Rohr, J. A., et al. (2017). Reducing the efficiency-stability-cost gap of organic photovoltaics with highly efficient and stable small molecule acceptor ternary solar cells. *Nat. Mater.* 16, 363–369. doi: 10.1038/nmat4797
- Baran, D., Kirchartz, T., Wheeler, S., Dimitrov, S., Abdelsamie, M., Gorman, J., et al. (2016). Reduced voltage losses yield 10% efficient fullerene free organic solar cells with >1 V open circuit voltages. *Energy Environ. Sci.* 9, 3783–3793. doi: 10.1039/C6EE02598F
- Bin, H., Angunawela, I., Qiu, B., Colberts, F. J. M., Li, M., Dyson, M. J., et al. (2020). Precise control of phase separation enables 12% efficiency in all small molecule solar cells. *Adv. Energy Mater.* 10, 1614–6832. doi: 10.1002/aenm.202001589
- Bin, H., Gao, L., Zhang, Z. G., Yang, Y., Zhang, Y., Zhang, C., et al. (2016). 11.4% Efficiency non-fullerene polymer solar cells with trialkylsilyl substituted 2D-conjugated polymer as donor. *Nat. Commun.* 7:13651. doi: 10.1038/ncomms13651
- Chen, S., Liu, Y., Zhang, L., Chow, P. C. Y., Wang, Z., Zhang, G., et al. (2017). A wide-bandgap donor polymer for highly efficient non-fullerene organic solar cells with a small voltage loss. *J. Am. Chem. Soc.* 139, 6298–6301. doi: 10.1021/jacs.7b01606
- Chen, Y., Geng, Y., Tang, A., Wang, X., Sun, Y., and Zhou, E. (2019). Changing the pi-bridge from thiophene to thieno[3,2-b]thiophene for the D-pi-A type polymer enables high performance fullerene-free organic solar cells. *Chem. Commun.* 55, 6708–6710. doi: 10.1039/C9CC02904D
- Chirvase, D., Parisi, J., Hummelen, J. C., and Dyakonov, V. (2004). Influence of nanomorphology on the photovoltaic action of polymer–fullerene composites. *Nanotechnology*. 15, 1317–1323. doi: 10.1088/0957-4484/15/9/035
- Cui, Y., Yao, H., Zhang, J., Zhang, T., Wang, Y., Hong, L., et al. (2019). Over 16% efficiency organic photovoltaic cells enabled by a chlorinated acceptor with increased open-circuit voltages. *Nat. Commun.* 10:2515. doi: 10.1038/s41467-019-10351-5
- Fan, B., Ying, L., Zhu, P., Pan, F., Liu, F., Chen, J., et al. (2017a). All-polymer solar cells based on a conjugated polymer containing siloxane-functionalized side chains with efficiency over 10%. *Adv. Mater.* 29:1703906. doi: 10.1002/adma.201703906
- Fan, B., Zhang, K., Jiang, X. F., Ying, L., Huang, F., and Cao, Y. (2017b). High-performance nonfullerene polymer solar cells based on imide-functionalized wide-bandgap polymers. *Adv. Mater.* 29:1606396. doi: 10.1002/adma.201606396
- Fan, B., Zhu, P., Xin, J., Li, N., Ying, L., Zhong, W., et al. (2018). High-performance thick-film all-polymer solar cells created via ternary blending of a novel wide-bandgap electron-donating copolymer. *Adv. Energy Mater.* 8:1703085. doi: 10.1002/aenm.201703085
- Fei, Z., Eisner, F. D., Jiao, X., Azzouzi, M., Rohr, J. A., Han, Y., et al. (2018). An alkylated indacenodithieno[3,2-b]thiophene-based nonfullerene acceptor with high crystallinity exhibiting single junction solar cell efficiencies greater than 13% with low voltage losses. *Adv. Mater.* 30:1705209. doi: 10.1002/adma.201705209
- Feng, S., Zhang, C., Liu, Y., Bi, Z., Zhang, Z., Xu, X., et al. (2017). Fused-ring acceptors with asymmetric side chains for high-performance thick-film organic solar cells. *Adv. Mater.* 29:1703527. doi: 10.1002/adma.201703527
- Gao, L., Zhang, Z. G., Bin, H., Xue, L., Yang, Y., Wang, C., et al. (2016a). High-efficiency nonfullerene polymer solar cells with medium bandgap polymer donor and narrow bandgap organic semiconductor acceptor. *Adv. Mater.* 28, 8288–8295. doi: 10.1002/adma.201601595
- Gao, L., Zhang, Z. G., Xue, L., Min, J., Zhang, J., Wei, Z., et al. (2016b). All-polymer solar cells based on absorption-complementary polymer donor and acceptor with high power conversion efficiency of 8.27%. *Adv. Mater.* 28, 1884–1890. doi: 10.1002/adma.201504629
- Ge, J., Xie, L., Peng, R., Fanady, B., Huang, J., Song, W., et al. (2020). 13.34 % Efficiency non-fullerene all-small-molecule organic solar cells enabled by modulating the crystallinity of donors via a fluorination strategy. *Angew. Chem. Int. Ed.* 59, 2808–2815. doi: 10.1002/anie.201910297
- Guo, H., Huang, B., Zhang, L., Chen, L., Xie, Q., Liao, Z., et al. (2019). Double acceptor block-containing copolymers with deep HOMO levels for organic solar cells: adjusting carboxylate substituent position for planarity. *ACS Appl. Mater. Interfaces*. 11, 15853–15860. doi: 10.1021/acsami.9b02212
- Guo, X., Zhang, M., Huo, L., Xu, F., Wu, Y., and Hou, J. (2012). Design, synthesis and photovoltaic properties of a new D- π -A polymer with extended π -bridge units. *J. Mater. Chem. A*. 22, 21024–21031. doi: 10.1039/c2jm32931j
- Guo, X., Zhou, N., Lou, S. J., Smith, J., Tice, D. B., Hennek, J. W., et al. (2013). Polymer solar cells with enhanced fill factors. *Nat. Photonics*. 7, 825–833. doi: 10.1038/nphoton.2013.207
- Gurney, R. S., Li, W., Yan, Y., Liu, D., Pearson, A. J., Wang, T., et al. (2019). Morphology and efficiency enhancements of PTB7-Th:ITIC nonfullerene organic solar cells processed via solvent vapor annealing. *J. Energy Chem.* 37, 148–156. doi: 10.1016/j.jechem.2018.12.015
- Heeger, A. J. (2014). 25th anniversary article: Bulk heterojunction solar cells: understanding the mechanism of operation. *Adv. Mater.* 26, 10–27. doi: 10.1002/adma.201304373
- Holliday, S., Ashraf, R. S., Wadsworth, A., Baran, D., Yousaf, S. A., Nielsen, C. B., et al. (2016). High-efficiency and air-stable P3HT-based polymer solar cells with a new non-fullerene acceptor. *Nat. Commun.* 7:11585. doi: 10.1038/ncomms11585
- Hu, D., Yang, Q., Chen, H., Wobben, F., Le Corre, V. M., Singh, R., et al. (2020). 15.34% efficiency all-small-molecule organic solar cells with an improved fill factor enabled by a fullerene additive. *Energy Environ. Sci.* 13, 2134–2141. doi: 10.1039/D0EE00714E
- Huo, L., Zhang, S., Guo, X., Xu, F., Li, Y., and Hou, J. (2011). Replacing alkoxy groups with alkylthienyl groups: a feasible approach to improve the properties of photovoltaic polymers. *Angew. Chem. Int. Ed.* 50, 9697–9702. doi: 10.1002/anie.201103313
- Ji, Y., Xu, L., Hao, X., and Gao, K. (2020). Energy loss in organic solar cells: mechanisms, strategies, and prospects. *Solar RRL*. 4:2000130. doi: 10.1002/solr.202000130
- Jiang, H., Li, X., Wang, H., Huang, G., Chen, W., Zhang, R., et al. (2020). Appropriate molecular interaction enabling perfect balance between induced

- crystallinity and phase separation for efficient photovoltaic blends. *ACS Appl. Mater. Interf.* 12, 26286–26292. doi: 10.1021/acsami.0c06326
- Jiang, Z., Li, H., Wang, Z., Zhang, J., Zhang, Y., Lu, K., et al. (2018). Naphtho[1,2-b:5,6-b']dithiophene-based conjugated polymers for fullerene-free inverted polymer solar cells. *Macromol. Rapid Commun.* 39:1700872. doi: 10.1002/marc.201700872
- Karki, A., Vollbrecht, J., Dixon, A. L., Schopp, N., Schrock, M., Reddy, G. N. M., et al. (2019). Understanding the high performance of over 15% efficiency in single-junction bulk heterojunction organic solar cells. *Adv. Mater.* 31:1903868. doi: 10.1002/adma.201903868
- Kim, J.-H., Park, J. B., Xu, F., Kim, D., Kwak, J., Grimsdale, A. C., et al. (2014). Effect of π -conjugated bridges of TPD-based medium bandgap conjugated copolymers for efficient tandem organic photovoltaic cells. *Energy Environ. Sci.* 7, 4118–4131. doi: 10.1039/C4EE02318H
- Li, G., Shrotriya, V., Huang, J., Yao, Y., Moriarty, T., Emery, K., et al. (2005). High-efficiency solution processable polymer photovoltaic cells by self-organization of polymer blends. *Nat. Mater.* 4, 864–868. doi: 10.1038/nmat1500
- Li, S., Liu, W., Shi, M., Mai, J., Lau, T.-K., Wan, J., et al. (2016). A spirobifluorene and diketopyrrolopyrrole moieties based non-fullerene acceptor for efficient and thermally stable polymer solar cells with high open-circuit voltage. *Energy Environ. Sci.* 9, 604–610. doi: 10.1039/C5EE03481G
- Li, Y., Chang, C.-Y., Chen, Y., Song, Y., Li, C.-Z., Yip, H.-L., et al. (2013). The effect of thieno[3,2-b]thiophene on the absorption, charge mobility and photovoltaic performance of diketopyrrolopyrrole-based low bandgap conjugated polymers. *J. Mater. Chem. C* 1, 7526–7533. doi: 10.1039/c3tc31600a
- Li, Z., Jiang, K., Yang, G., Lai, J. Y., Ma, T., Zhao, J., et al. (2016a). Donor polymer design enables efficient non-fullerene organic solar cells. *Nat. Commun.* 7:13094. doi: 10.1038/ncomms13094
- Li, Z., Xu, X., Zhang, W., Meng, X., Ma, W., Yartsev, A., et al. (2016b). High performance all-polymer solar cells by synergistic effects of fine-tuned crystallinity and solvent annealing. *J. Am. Chem. Soc.* 138, 10935–10944. doi: 10.1021/jacs.6b04822
- Liang, Y., Wu, Y., Feng, D., Tsai, S.-T., Son, H.-J., Li, G., et al. (2009). Development of new semiconducting polymers for high performance solar cells. *J. Am. Chem. Soc.* 131:56. doi: 10.1021/ja808373p
- Liang, Y., Xu, Z., Xia, J., Tsai, S. T., Wu, Y., Li, G., et al. (2010). For the bright future-bulk heterojunction polymer solar cells with power conversion efficiency of 7.4%. *Adv. Mater.* 22, E135–E138. doi: 10.1002/adma.200903528
- Liao, S. H., Jhuo, H. J., Cheng, Y. S., and Chen, S. A. (2013). Fullerene derivative-doped zinc oxide nanofilm as the cathode of inverted polymer solar cells with low-bandgap polymer (PTB7-Th) for high performance. *Adv. Mater.* 25, 4766–4771. doi: 10.1002/adma.201301476
- Lin, Y., Wang, J., Zhang, Z. G., Bai, H., Li, Y., Zhu, D., et al. (2015). An electron acceptor challenging fullerenes for efficient polymer solar cells. *Adv. Mater.* 27, 1170–1174. doi: 10.1002/adma.201404317
- Lin, Y., Zhao, F., He, Q., Huo, L., Wu, Y., Parker, T. C., et al. (2016). High-performance electron acceptor with thienyl side chains for organic photovoltaics. *J. Am. Chem. Soc.* 138, 4955–4961. doi: 10.1021/jacs.6b02004
- Lin, Y., Zhao, F., Prasad, S. K. K., Chen, J. D., Cai, W., Zhang, Q., et al. (2018). Balanced partnership between donor and acceptor components in nonfullerene organic solar cells with >12% efficiency. *Adv. Mater.* 30:1706363. doi: 10.1002/adma.201706363
- Liu, F., Zhou, Z., Zhang, C., Vergote, T., Fan, H., Liu, F., et al. (2016). A thieno[3,4-b]thiophene-based non-fullerene electron acceptor for high-performance bulk-heterojunction organic solar cells. *J. Am. Chem. Soc.* 138, 15523–15526. doi: 10.1021/jacs.6b08523
- Liu, J., Chen, S., Qian, D., Gautam, B., Yang, G., Zhao, J., et al. (2016). Fast charge separation in a non-fullerene organic solar cell with a small driving force. *Nat. Energy.* 1:16089. doi: 10.1038/nenergy.2016.89
- Liu, Q., Jiang, Y., Jin, K., Qin, J., Xu, J., Li, W., et al. (2020). 18% efficiency organic solar cells. *Sci. Bull.* 65, 272–275. doi: 10.1016/j.scib.2020.01.001
- Liu, T., Huo, L., Chandrasekhar, S., Chen, K., Han, G., Qi, F., et al. (2018). Optimized fibril network morphology by precise side-chain engineering to achieve high-performance bulk-heterojunction organic solar cells. *Adv. Mater.* 30:1707353. doi: 10.1002/adma.201707353
- Liu, X., Nian, L., Gao, K., Zhang, L., Qing, L., Wang, Z., et al. (2017). Low band gap conjugated polymers combining siloxane-terminated side chains and alkyl side chains: side-chain engineering achieving a large active layer processing window for PCE > 10% in polymer solar cells. *J. Mater. Chem. A* 5, 17619–17631. doi: 10.1039/C7TA05583H
- Long, Y., Hedley, G. J., Ruseckas, A., Chowdhury, M., Roland, T., Serrano, L. A., et al. (2017). Effect of annealing on exciton diffusion in a high performance small molecule organic photovoltaic material. *ACS Appl. Mater. Interf.* 9, 14945–14952. doi: 10.1021/acsami.6b16487
- Mai, J., Lau, T.-K., Li, J., Peng, S.-H., Hsu, C.-S., Jeng, U. S., et al. (2016). Understanding morphology compatibility for high-performance ternary organic solar cells. *Chem. Mater.* 28, 6186–6195. doi: 10.1021/acs.chemmater.6b02264
- Manzhos, S. (2020). Aggregate-state effects in the atomistic modeling of organic materials for electrochemical energy conversion and storage devices: a perspective. *Molecules* 25:2233. doi: 10.3390/molecules25092233
- Meng, D., Fu, H., Xiao, C., Meng, X., Winands, T., Ma, W., et al. (2016a). Three-bladed rylene propellers with three-dimensional network assembly for organic electronics. *J. Am. Chem. Soc.* 138, 10184–10190. doi: 10.1021/jacs.6b04368
- Meng, D., Sun, D., Zhong, C., Liu, T., Fan, B., Huo, L., et al. (2016b). High-performance solution-processed non-fullerene organic solar cells based on selenophene-containing perylene bisimide acceptor. *J. Am. Chem. Soc.* 138, 375–380. doi: 10.1021/jacs.5b11149
- Meng, H., Li, Y., Pang, B., Li, Y., Xiang, Y., Guo, L., et al. (2020). Effects of halogenation in b <- n embedded polymer acceptors on performance of all-polymer solar cells. *ACS. Appl. Mater. Interfaces.* 12, 2733–2742. doi: 10.1021/acsami.9b20214
- Mo, D., Wang, H., Chen, H., Qu, S., Chao, P., Yang, Z., et al. (2017). chlorination of low-band-gap polymers: toward high-performance polymer solar cells. *Chem. Mater.* 29, 2819–2830. doi: 10.1021/acs.chemmater.6b04828
- Qian, D., Ye, L., Zhang, M., Liang, Y., Li, L., and Huang, Y., et al. (2012). Design, application, and morphology study of a new photovoltaic polymer with strong aggregation in solution state. *Macromolecules* 45, 9611–9617. doi: 10.1021/ma301900h
- Qin, Y., Uddin, M. A., Chen, Y., Jang, B., Zhao, K., Zheng, Z., et al. (2016). Highly efficient fullerene-free polymer solar cells fabricated with polythiophene derivative. *Adv. Mater.* 28, 9416–9422. doi: 10.1002/adma.201601803
- Savenije, T. J., Kroeze, J. E., Yang, X., and Loos, J. (2006). The formation of crystalline P3HT fibrils upon annealing of a PCBM:P3HT bulk heterojunction. *Thin Solid Films* 511–512, 2–6. doi: 10.1016/j.tsf.2005.12.123
- Shi, S., Liao, Q., Wang, H., and Xiao, G. (2020). Narrow bandgap difluorobenzochalcogenadiazole-based polymers for high-performance organic thin-film transistors and polymer solar cells. *New J. Chem.* 44, 8032–8043. doi: 10.1039/D0NJ01006E
- Shi, S., Xie, X., Jiang, P., Chen, S., Wang, L., Wang, M., et al. (2013). Naphtho[1,2-b:5,6-b']dithiophene-based donor-acceptor copolymer semiconductors for high-mobility field-effect transistors and efficient polymer solar cells. *Macromolecules* 46, 3358–3366. doi: 10.1021/ma400177w
- Su, W., Fan, Q., Guo, X., Wu, J., Zhang, M., and Li, Y. (2019). Efficient as-cast semi-transparent organic solar cells with efficiency over 9% and a high average visible transmittance of 27.6. *Phys. Chem. Chem. Phys.* 21, 10660–10666. doi: 10.1039/C9CP01101C
- Sun, D., Meng, D., Cai, Y., Fan, B., Li, Y., Jiang, W., et al. (2015). Non-fullerene-acceptor-based bulk-heterojunction organic solar cells with efficiency over 7%. *J. Am. Chem. Soc.* 137, 11156–11162. doi: 10.1021/jacs.5b06414
- Sun, H., Tang, Y., Koh, C. W., Ling, S., Wang, R., and Yang, K. (2019). High-performance all-polymer solar cells enabled by an n-type polymer based on a fluorinated imide-functionalized arene. *Adv. Mater.* 31:1807220. doi: 10.1002/adma.201807220
- Tang, A., Zhang, Q., Du, M., Li, G., Geng, Y., Zhang, J., et al. (2019). Molecular engineering of D- π -A copolymers based on 4,8-Bis(4-chlorothiophen-2-yl)benzo[1,2-b:4,5-b']dithiophene (BDT-T-Cl) for high-performance fullerene-free organic solar cells. *Macromolecules* 52, 6227–6233. doi: 10.1021/acs.macromol.9b01233
- Wang, C., Moro, F., Ni, S., Zhang, Q., Pan, G., Yang, J., et al. (2020). Thermal-annealing effects on energy level alignment at organic heterojunctions and corresponding voltage losses in all-polymer solar cells. *Nano Energy* 72:104677. doi: 10.1016/j.nanoen.2020.104677
- Wang, J.-L., Liu, K.-K., Hong, L., Ge, G.-Y., Zhang, C., and Hou, J. (2018). Selenopheno[3,2-b]thiophene-based narrow-bandgap nonfullerene acceptor

- enabling 13.3% efficiency for organic solar cells with thickness-insensitive feature. *ACS Energy Lett.* 3, 2967–2976. doi: 10.1021/acsenerylett.8b01808
- Wang, W., Yan, C., Lau, T. K., Wang, J., Liu, K., Fan, Y., et al. (2017). Fused hexacyclic nonfullerene acceptor with strong near-infrared absorption for semitransparent organic solar cells with 9.77% efficiency. *Adv. Mater.* 29, 1701308. doi: 10.1002/adma.201701308
- Williams, E. L., Ooi, Z., Sonar, P., and Dodabalapur, A. (2012). Measurement of contact voltage drop and resistance in organic solar cells. *Appl. Phys. Lett.* 101:253902. doi: 10.1063/1.4772203
- Wu, Q., Zhao, D., Schneider, A. M., Chen, W., and Yu, L. (2016). Covalently bound clusters of alpha-substituted pdi-rival electron acceptors to fullerene for organic solar cells. *J. Am. Chem. Soc.* 138, 7248–7251. doi: 10.1021/jacs.6b03562
- Xue, L., Yang, Y., Xu, J., Zhang, C., Bin, H., Zhang, Z. G., et al. (2017). Side chain engineering on medium bandgap copolymers to suppress triplet formation for high-efficiency polymer solar cells. *Adv. Mater.* 29:1703344. doi: 10.1002/adma.201703344
- Yang, Y., Zhang, Z. G., Bin, H., Chen, S., Gao, L., Xue, L., et al. (2016). Side-chain isomerization on an n-type organic semiconductor ITIC acceptor makes 11.77% high efficiency polymer solar cells. *J. Am. Chem. Soc.* 138, 15011–15018. doi: 10.1021/jacs.6b09110
- Yao, H., Cui, Y., Yu, R., Gao, B., Zhang, H., and Hou, J. (2017). Design, synthesis, and photovoltaic characterization of a small molecular acceptor with an ultra-narrow band gap. *Angew. Chem. Int. Ed.* 56, 3045–3049. doi: 10.1002/anie.201610944
- Zhang, J., Li, Y., Huang, J., Hu, H., Zhang, G., Ma, T., et al. (2017). Ring-fusion of perylene diimide acceptor enabling efficient nonfullerene organic solar cells with a small voltage loss. *J. Am. Chem. Soc.* 139, 16092–16095. doi: 10.1021/jacs.7b09998
- Zhang, M., Guo, X., Ma, H., Ade, H., and Hou, J. (2015). A Large-bandgap conjugated polymer for versatile photovoltaic applications with high performance. *Adv. Mater.* 27, 4655–4660. doi: 10.1002/adma.201502110
- Zhang, S., Qin, Y., Uddin, M. A., Jang, B., Zhao, W., Liu, D., et al. (2016). A fluorinated polythiophene derivative with stabilized backbone conformation for highly efficient fullerene and non-fullerene polymer solar cells. *Macromolecules* 49, 2993–3000. doi: 10.1021/acs.macromol.6b00248
- Zhang, S., Qin, Y., Zhu, J., and Hou, J. (2018). Over 14% efficiency in polymer solar cells enabled by a chlorinated polymer donor. *Adv. Mater.* 30:1800868. doi: 10.1002/adma.201800868
- Zhang, Y., Sajjad, M. T., Blaszczyk, O., Parnell, A. J., Ruseckas, A., Serrano, L. A., et al. (2019). Large crystalline domains and an enhanced exciton diffusion length enable efficient organic solar cells. *Chem. Mater.* 31, 6548–6557. doi: 10.1021/acs.chemmater.8b05293
- Zhang, Z. G., Yang, Y., Yao, J., Xue, L., Chen, S., Li, X., et al. (2017). Constructing a strongly absorbing low-bandgap polymer acceptor for high-performance all-polymer solar cells. *Angew. Chem. Int. Ed.* 56, 13503–13507. doi: 10.1002/anie.201707678
- Zhao, J., Li, Y., Lin, H., Liu, Y., Jiang, K., Mu, C., et al. (2015). High-efficiency non-fullerene organic solar cells enabled by a difluorobenzothiadiazole-based donor polymer combined with a properly matched small molecule acceptor. *Energy Environ. Sci.* 8, 520–525. doi: 10.1039/C4EE02990A
- Zhao, J., Li, Y., Yang, G., Jiang, K., Lin, H., Ade, H., et al. (2016). Efficient organic solar cells processed from hydrocarbon solvents. *Nat. Energy* 1:15027. doi: 10.1038/nenergy.2015.27
- Zhao, W., Li, S., Yao, H., Zhang, S., Zhang, Y., Yang, B., et al. (2017). Molecular optimization enables over 13% efficiency in organic solar cells. *J. Am. Chem. Soc.* 139, 7148–7151. doi: 10.1021/jacs.7b02677
- Zhao, W., Qian, D., Zhang, S., Li, S., Inganas, O., Gao, F., et al. (2016). Fullerene-free polymer solar cells with over 11% efficiency and excellent thermal stability. *Adv. Mater.* 28, 4734–4739. doi: 10.1002/adma.201600281
- Zhou, H., Yang, L., Stuart, A. C., Price, S. C., Liu, S., and You, W. (2011). Development of fluorinated benzothiadiazole as a structural unit for a polymer solar cell of 7 % efficiency. *Angew. Chem. Int. Ed.* 50, 2995–2998. doi: 10.1002/anie.201005451

Conflict of Interest: The authors declare that the research was conducted in the absence of any commercial or financial relationships that could be construed as a potential conflict of interest.

Copyright © 2020 Qiu, Adil, Lu and Wei. This is an open-access article distributed under the terms of the Creative Commons Attribution License (CC BY). The use, distribution or reproduction in other forums is permitted, provided the original author(s) and the copyright owner(s) are credited and that the original publication in this journal is cited, in accordance with accepted academic practice. No use, distribution or reproduction is permitted which does not comply with these terms.



A Quantum-Mechanical Looking Behind the Scene of the Classic G·C Nucleobase Pairs Tautomerization

Ol'ha O. Brovarets^{1*}, Alona Muradova² and Dmytro M. Hovorun^{1,2}

¹ Department of Molecular and Quantum Biophysics, Institute of Molecular Biology and Genetics, National Academy of Sciences of Ukraine, Kyiv, Ukraine, ² Department of Molecular Biotechnology and Bioinformatics, Institute of High Technologies, Taras Shevchenko National University of Kyiv, Kyiv, Ukraine

OPEN ACCESS

Edited by:

Haichang Zhang,
Qingdao University of Science and
Technology, China

Reviewed by:

Hongdong Shi,
Shenzhen University, China
Qikun Sun,
Ulsan National Institute of Science and
Technology, South Korea
Xiaoli Hao,
Shaanxi University of
Technology, China

*Correspondence:

Ol'ha O. Brovarets'
o.o.brovarets@imbg.org.ua

Specialty section:

This article was submitted to
Organic Chemistry,
a section of the journal
Frontiers in Chemistry

Received: 16 June 2020

Accepted: 02 September 2020

Published: 26 November 2020

Citation:

Brovarets' OO, Muradova A and
Hovorun DM (2020) A
Quantum-Mechanical Looking Behind
the Scene of the Classic G·C
Nucleobase Pairs Tautomerization.
Front. Chem. 8:574454.
doi: 10.3389/fchem.2020.574454

For the first time, at the MP2/6-311++G(2df,pd)//B3LYP/6-311++G(d,p) level of theory, a comprehensive quantum-mechanical investigation of the physico-chemical mechanism of the tautomeric wobblization of the four biologically-important G·C nucleobase pairs by the participation of the monomers in rare, in particular mutagenic, tautomeric forms (marked with an asterisk) was provided. These novel tautomeric transformations (wobblization or shifting of the bases within the pair) are intrinsically inherent properties of the G·C nucleobase pairs. In this study, we have obtained intriguing results, lying far beyond the existing representations. Thus, it was shown that Löwdin's G^{*}·C^{*}(WC) base pair does not tautomerize according to the wobblization mechanism. Tautomeric wobblization of the G^{*}·C^{*}(rWC) (relative Gibbs free energy $\Delta G = 0.00$ /relative electronic energy $\Delta E = 0.00 \text{ kcal}\cdot\text{mol}^{-1}$) ("r"—means the configuration of the base pair in reverse position; "WC"—the classic Watson-Crick configuration) and G^{*}t·C^{*}(H) ($\Delta G = -0.19/\Delta E = 0.29 \text{ kcal}\cdot\text{mol}^{-1}$) ("H"—Hoogsteen configuration;"t" denotes the O6H hydroxyl group in the *trans* position) base pairs are preceded by the stages of the base pairs tautomerization by the single proton transfer (SPT). It was established that the G^{*}t·C^{*}(rH) ($\Delta G = 2.21/\Delta E = 2.81 \text{ kcal}\cdot\text{mol}^{-1}$) base pair can be wobbled through two different pathways *via* the traditional one-stage mechanism through the TSs, which are tight G⁺·C[−] ion pairs, stabilized by the participation of only two intermolecular H-bonds. It was found out that the G·C base pair is most likely incorporated into the DNA/RNA double helix with parallel strands in the G^{*}·C^{*}(rWC), G·C^{*}(rw_{WC}), and G^{*}·C(rw_{WC}) ("w"—wobble configuration of the pair) tautomeric forms, which are in rapid tautomeric equilibrium with each other. It was proven that the G^{*}·C^{*}(rWC) nucleobase pair is also in rapid tautomeric equilibrium with the eight tautomeric forms of the so-called Levitt base pair. It was revealed that a few cases of tautomerization *via* the DPT of the nucleobase pairs by the participation of the C8H group of the guanine had occurred. The biological role of the obtained results was also made apparent.

Keywords: DNA, RNA, G·C base pair, tautomerization mechanism, wobblization, wobble base pair, Levitt base pair, Löwdin's base pair

INTRODUCTION

Shortly after the establishment of the spatial organization of the DNA molecule by James Watson and Francis Crick (Watson and Crick, 1953a,b), the tautomeric hypothesis was formulated (Watson and Crick, 1953b; Crick and Watson, 1954), which considers the transformation or transition of the nucleotide bases from the main (canonical) into the rare (mutagenic) tautomeric form as the main source of the origin of spontaneous point mutations. Since that time, the topic of tautomerism has remained active over the decades to the present day (Löwdin, 1963, 1966; Topal and Fresco, 1976; Florian et al., 1994; Gorb et al., 2004; Brovarets' et al., 2014; Godbeer et al., 2015; Turaeva and Brown-Kennerly, 2015).

However, up until recently it was considered that only a few unusual tautomers existed for the G•C Watson-Crick nucleobase pair (Pous et al., 2008; Alvey et al., 2014; Brovarets' and Hovorun, 2014a; Nikolova et al., 2014; Poltev et al., 2016; Szabat and Kierzek, 2017; Brovarets' et al., 2019a,b; Srivastava, 2019). In particular, tautomerization *via* the double proton transfer (DPT) has been carefully investigated in the reverse Löwdin $G^* \cdot C^*(rWC)$, Hoogsteen (H) $G^* \cdot C^*(H)$, and reverse Hoogsteen $G^* \cdot C^*(rH)$ base pairs (Brovarets' et al., 2019b), leading to the novel structures: $G \cdot C_{O_2}^*(rWC)$, $G_{N_2}^* \cdot C(rWC)$, $G^*_{N_2} \cdot C(rWC)$, $G_{N_7}^* \cdot C(H)$, and $G^*_{N_7} \cdot C(rH)$.

Eventually a great contribution into the further development of the tautomeric hypothesis was made by Per-Orlov Löwdin (Löwdin, 1963, 1966) and Topal and Fresco (Topal and Fresco, 1976; Brovarets' et al., 2014). Thus, Per-Orlov Löwdin expressed the revolutionary, non-trivial opinion that the ability of the nucleotide bases to transform into the rare tautomeric form is provided by the electronic structure of the canonical DNA base pairs and qualitatively substantiated this assumption from the position of quantum mechanics. Subsequently, Topal and Fresco elaborated this approach in more detail, by using simple and visual models, and extended it for the explanation of the limited accuracy of codon-anticodon recognition (Topal and Fresco, 1976; Brovarets' et al., 2014).

In recent years, an alternative view in this area of the research was suggested, which could be characterized as the “Renaissance” of the tautomeric hypothesis [see Chapter Brovarets' and Hovorun (2018) and bibliography provided there]. According to this investigation the new, unusual pathways of the tautomeric interconversions between wobble (w) and Watson-Crick (WC) base pairs have been provided (Brovarets' and Hovorun, 2009, 2015a,b,c,d,e,f):

- for usual A•T and G•C DNA base pairs: $A \cdot T(WC) \leftrightarrow A^* \cdot T(w)/A \cdot T_{O_2}^*(w)/A \cdot T^*(w)$ and $G \cdot C(WC) \leftrightarrow G \cdot C_{\uparrow}^*(w)/G^* \cdot C_{\downarrow}(w)/G \cdot C_{\downarrow}^*(w)/G^* \cdot C_{\uparrow}(w)$ (Brovarets' and Hovorun, 2015a);
- for unusual purine-pyrimidine wobble A•C and G•T DNA base pairs: $A \cdot C(w) \leftrightarrow A \cdot C^*(WC)$ and $G \cdot T(w) \leftrightarrow G^* \cdot T(WC)$ (Brovarets' and Hovorun, 2009, 2015b,c);
- for incorrect purine-purine A•A, G•G, and A•G DNA base pairs: $A \cdot A(w) \leftrightarrow A^* \cdot A(WC)$, $G \cdot G(w) \leftrightarrow G^* \cdot G(WC)$,

$A \cdot G(WC) \leftrightarrow A \cdot G_{\downarrow}^*(w)$, $A \cdot G(WC) \leftrightarrow A^* \cdot G_{\uparrow}(w)$ (Brovarets' and Hovorun, 2015d,e);

- for pyrimidine-pyrimidine base pairs: $C \cdot T(WC) \leftrightarrow C^* \cdot T_{\uparrow}(w)$, $C \cdot T(WC) \leftrightarrow C \cdot T_{\downarrow}^*(w)$, $T \cdot T(w) \leftrightarrow T \cdot T^*(WC)$, $C \cdot C(w) \leftrightarrow C \cdot C^*(WC)$ (Brovarets' and Hovorun, 2015f).

Thus, by utilizing modern quantum-mechanical (QM) methods, the mechanisms of the mutagenic tautomerization of the pairs of nucleotide bases were investigated in detail, which were revealed to be active players in the field of spontaneous point mutagenesis (Brovarets' and Hovorun, 2018). It was established, in which cases Löwdin's approach was adequate and in which cases another approach should be reconsidered and supplemented.

Thus, it was suggested that the mechanism of the mutagenic tautomerization of the DNA base pairs, in particular classic Watson-Crick pairs, are accompanied by the mutual shifting (wobblization) of the bases one relative to the other into the minor or major DNA grooves at the intrapair sequential proton transfer (Brovarets' and Hovorun, 2015a; Brovarets' et al., 2019a). This valuable finding enables researchers to figure out, how the incorrect DNA base pairs, which architecture is different from the Watson-Crick configuration, can acquire the enzymatically-competent conformation, that guarantees their successful chemical incorporation into the composition of the main carrier of the genetic information—DNA—by the high-fidelity DNA-polymerase. Notably, even though these theoretical approaches have been realized in quite basic model objects, they correctly reflect the real state-of-affairs at the macromolecular level, since they have been experimentally confirmed for macromolecular objects.

In this research, the objects of the investigation have been extended—except the Watson-Crick (WC) nucleobase pair, to the other biologically-important G•C nucleobase pairs—reverse Watson-Crick G•C(rWC), Hoogsteen G•C(H), and reverse Hoogsteen G•C(rH). Also, it was exactly established why the classic A•T(WC) DNA base pair was selected for the construction of the genetic material (Brovarets' and Hovorun, 2009, 2015a,b,c,d,e,f; Brovarets' et al., 2018a). The novel mechanism of the mutagenic tautomerization of the biologically-important A•T DNA base pairs through the quasi-orthogonal transition state and also through the protonated amino-group (Brovarets' et al., 2018b,c,d,e,f) was revealed for the first time. Based on these data an assumption was expressed about their possible biological role.

At the same time, investigations into the mechanisms of the mutagenic tautomerization of the pairs of nucleotide bases seemed to be quite a complicated issue, which may not be evident at a first glance. Thus, recent investigations into the tautomerization mechanisms of the biologically-important G•C nucleobase pairs, in which monomers are in the rare, in particular mutagenic, tautomeric form, continue to challenge researchers by its mystery (Brovarets' et al., 2019a,b).

It is still not possible to formulate simple physico-chemical rules, that would predict the course of these biologically important processes. Obviously, this is due to the fact that despite the enormous theoretical and experimental efforts of

researchers, the present material remains insufficient for its final generalization.

This work aims to deepen the existing ideas about the microstructural mechanisms of the tautomerization of the biologically important pairs of nucleobases using the example of the G•C base pair (Brovarets' and Hovorun, 2014a), for which both monomers are in the rare tautomeric form.

Such a task is completely substantiated—we have investigated a few surprising tautomerizations, which significantly expand the existing ideas on tautomerization mechanisms and their biological applications. They will be outlined and discussed in more detail below.

COMPUTATIONAL METHODS

Density Functional Theory Calculations of the Geometry and Vibrational Frequencies

Equilibrium geometries of the investigated nucleobase pairs and the transition states (TSs) of their mutual tautomeric transformations, as well as their harmonic vibrational frequencies have been calculated at the B3LYP/6-311++G(d,p) level of QM theory (Hariharan and Pople, 1973; Krishnan et al., 1980; Lee et al., 1988; Parr and Yang, 1989; Tirado-Rives and Jorgensen, 2008), using the Gaussian'09 program package (Frisch et al., 2010). An applied level of theory has proved itself to be successful for the calculations of similar systems (Brovarets' and Hovorun, 2010a,b, 2015g; Matta, 2010; Brovarets' et al., 2015). A scaling factor that is equal to 0.9668 has been applied in the present work for the correction of the harmonic frequencies of all complexes and TSs of their tautomeric transitions (Palafox, 2014; Brovarets' and Hovorun, 2015g; Brovarets' et al., 2015; El-Sayed et al., 2015). We have confirmed the local minima and TSs, localized by a synchronous transit-guided quasi-Newton method (Peng et al., 1996), on the potential energy landscape by the absence or presence, respectively, of the imaginary frequency in the vibrational spectra of the complexes. We applied standard TS theory for the estimation of the activation barriers of the tautomerization reaction (Atkins, 1998).

All calculations have been carried in the continuum with $\epsilon = 1$, that adequately reflects the processes occurring in real biological systems without deprivation of the structurally functional properties of the bases in the composition of DNA/RNA and satisfactorily models the substantially hydrophobic recognition pocket of the DNA-polymerase machinery as a part of the replisome (Bayley, 1951; Dewar and Storch, 1985; Petrushka et al., 1986; García-Moreno et al., 1997; Mertz and Krishtalik, 2000; Brovarets' and Hovorun, 2014a,b).

Single Point Energy Calculations

We continued geometry optimizations with electronic energy calculations as single point calculations at the MP2/6-311++G(2df,pd) level of theory (Frisch et al., 1990; Kendall et al., 1992).

The Gibbs free energy G for all structures was obtained in the following way:

$$G = E_{\text{el}} + E_{\text{corr}}, \quad (1)$$

where E_{el} —electronic energy, while E_{corr} —thermal correction.

Evaluation of the Interaction Energies

Electronic interaction energies ΔE_{int} have been calculated at the MP2/6-311++G(2df,pd) level of theory as the difference between the total energy of the base pair and energies of the monomers, which have been corrected for the basis set superposition error (BSSE) (Boys and Bernardi, 1970; Gutowski et al., 1986) through the counterpoise procedure (Sordo et al., 1988; Sordo, 2001).

QTAIM Analysis

Bader's quantum theory of atoms in molecules (QTAIM) (Bader, 1990; Matta and Hernández-Trujillo, 2003; Matta et al., 2006; Cukrowski and Matta, 2010; Keith, 2010; Matta, 2014; Lecomte et al., 2015), using the program package AIMAll (Keith, 2010), was applied to analyze the electron density distribution. The presence of the bond critical point (BCP), namely the so-called (3,-1) BCP, and a bond path between the hydrogen donor and acceptor, as well as the positive value of the Laplacian at this BCP ($\Delta\rho > 0$), were considered as criteria for the H-bond formation (Bader, 1990; Matta and Hernández-Trujillo, 2003; Matta et al., 2006; Cukrowski and Matta, 2010; Matta, 2014; Lecomte et al., 2015). Wave functions were obtained at the level of QM theory used for geometry optimization.

The atomic numbering scheme used for the nucleobases is conventional (Saenger, 1984). In this study mutagenic or rare tautomeric forms of the bases (Brovarets' and Hovorun, 2009, 2014a, 2015a,b,c,d,e,f; Brovarets' and Hovorun, 2018; Brovarets' et al., 2018a,b,c,d,e,f; Brovarets' et al., 2019a,b) are denoted by the asterisk.

OBTAINED RESULTS AND THEIR DISCUSSION

So, based on the obtained data, let us firstly formulate the basic results, which have been obtained for the first time and which have the closest connection to the structural biology and molecular biophysics (Figures 1, 2, Table 1).

Before providing the discussion of the investigated material, let us firstly give attention to the novel mechanisms of the $G^* \cdot C^*(\text{rWC})$ tautomerization, which complement the results of the previous work (Brovarets' et al., 2019a).

1. So, in the $G^* \cdot C^*(\text{rWC})$ base pair, the non-usual DPT-tautomerization was fixed by the participation of the protons at the N3(C) and N2(G) atoms (Figure 1, part I): $G^* \cdot C^*(\text{rWC}) \leftrightarrow G_{\text{N2}}^* \cdot C(\text{rWC})$. This process is unusual, since the transfer of the proton from the C^* to the G^* base along the intermolecular (C)N3H...N1(G) H-bond provokes the rotation of the amino group of the G base into the *trans*-position relative to the C2=N3 double bond. As a result, a significantly non-planar $\text{TS}_{G^* \cdot C^*(\text{rWC}) \leftrightarrow G_{\text{N2}}^* \cdot C(\text{rWC})}$ of the tautomerization reaction is formed, which proceeds through the asynchronous mechanism and the significantly non-planar product of the tautomerization—the $G_{\text{N2}}^* \cdot C(\text{rWC})$ base pair, which is stabilized by the three intermolecular H-bonds (G)O6H...O2(C), (G)N1H...N3(C), and (C)N4H...N2(G).

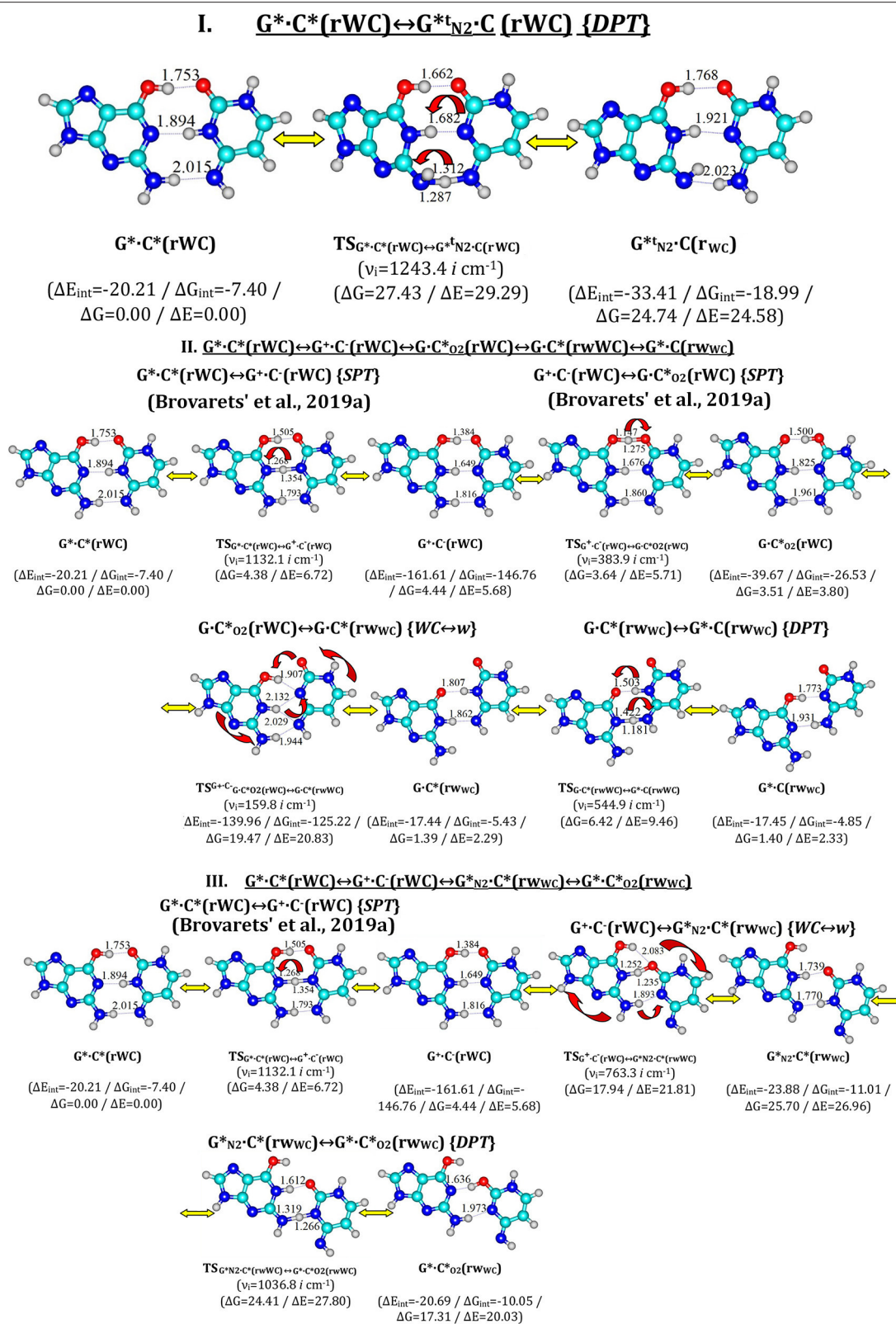


FIGURE 1 | Continued

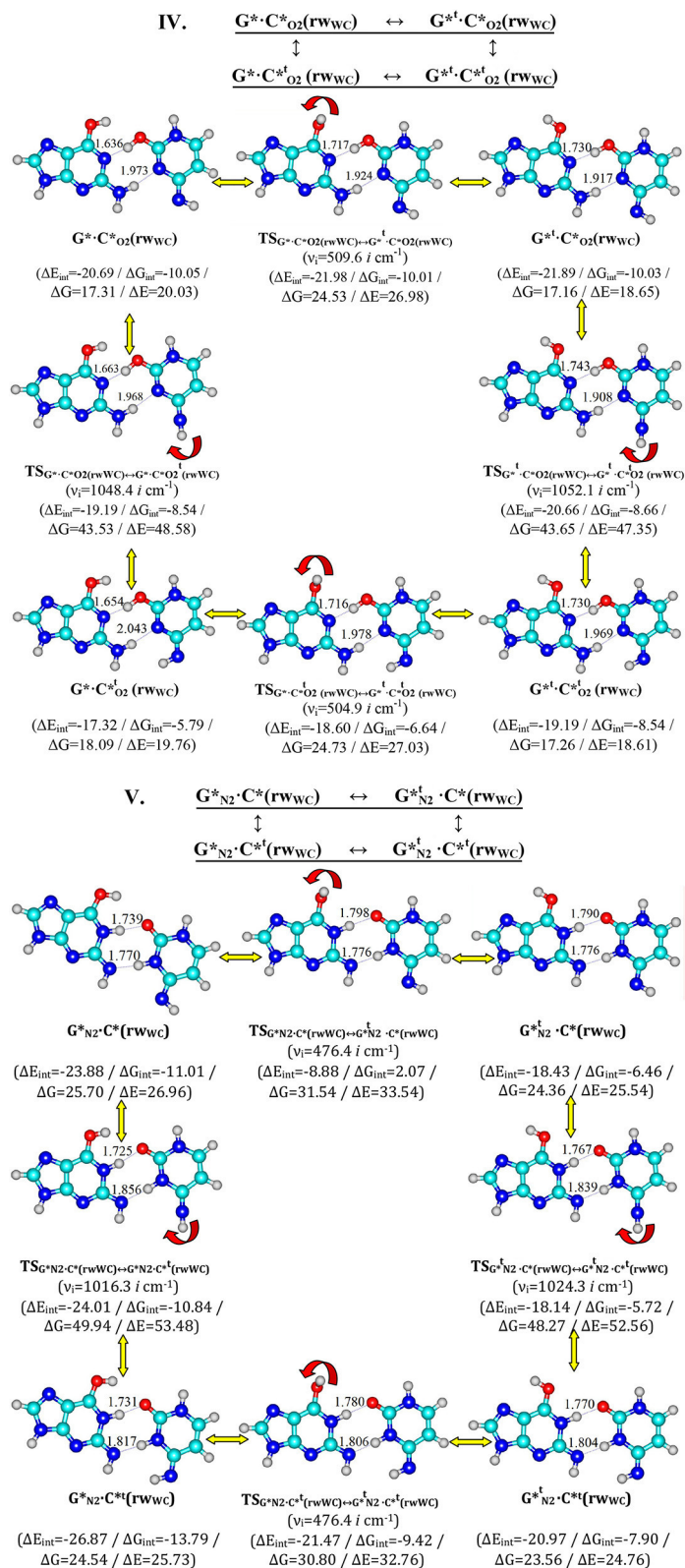


FIGURE 1 | Continued

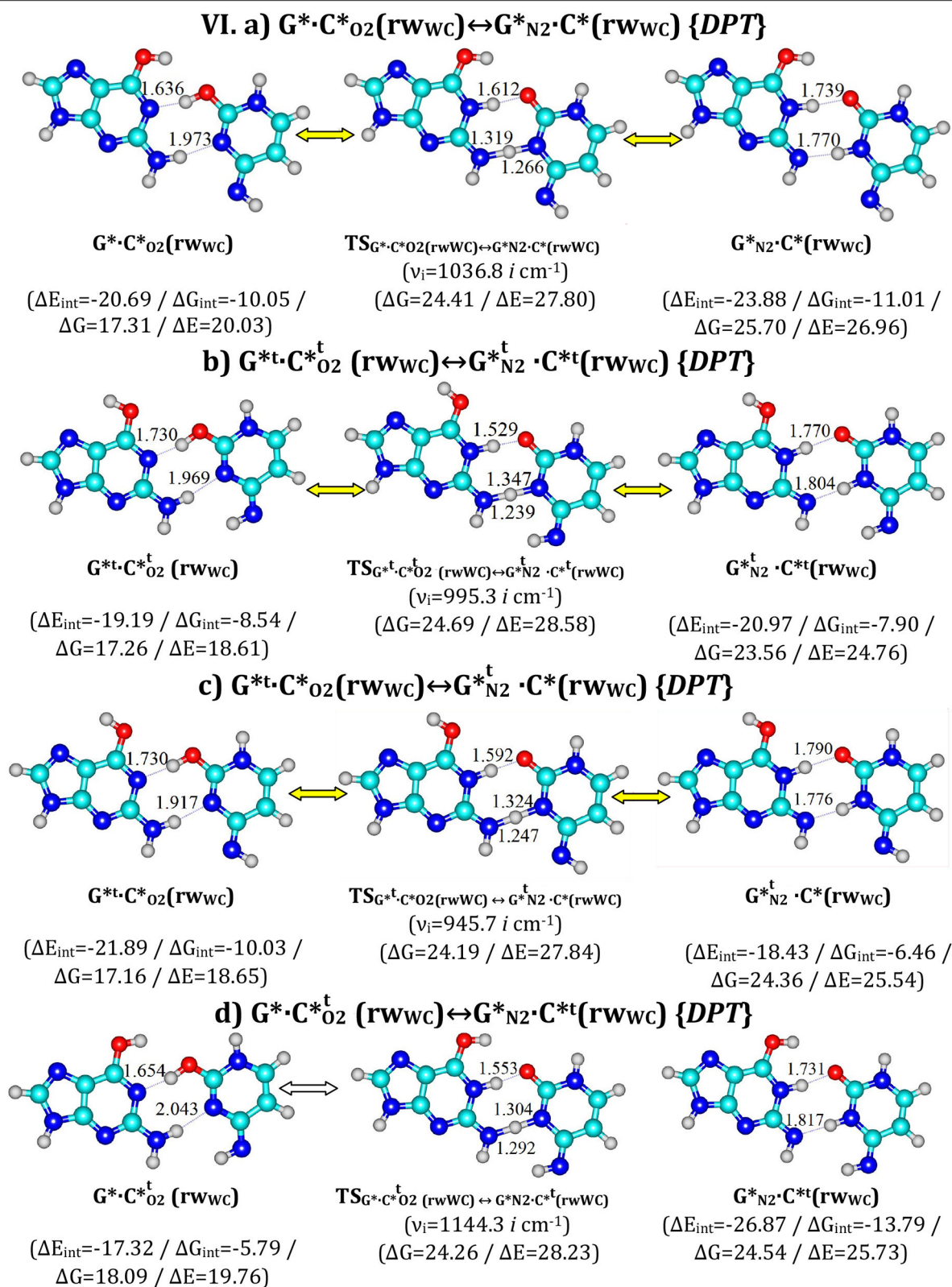


FIGURE 1 | Continued

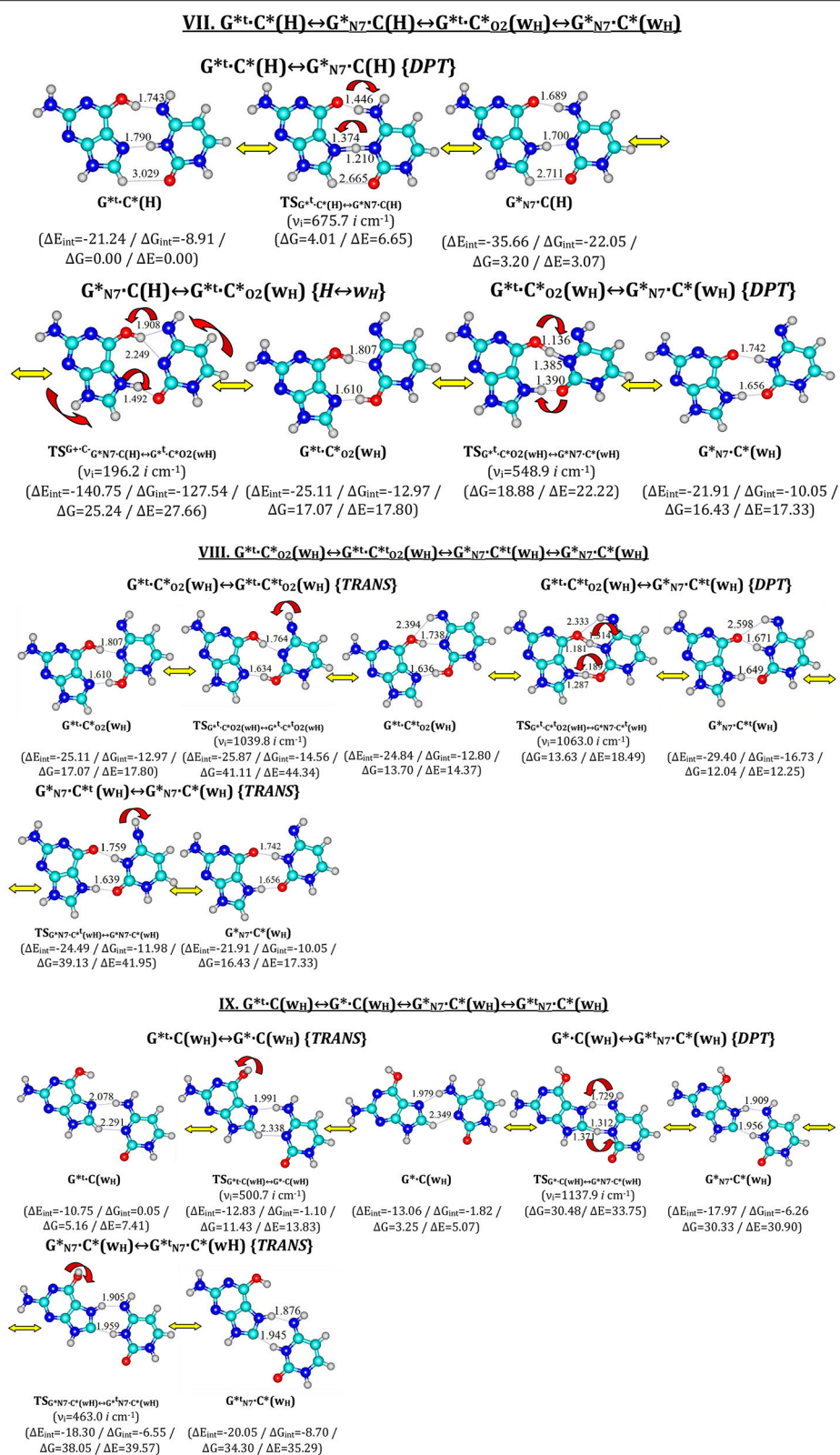


FIGURE 1 | Continued

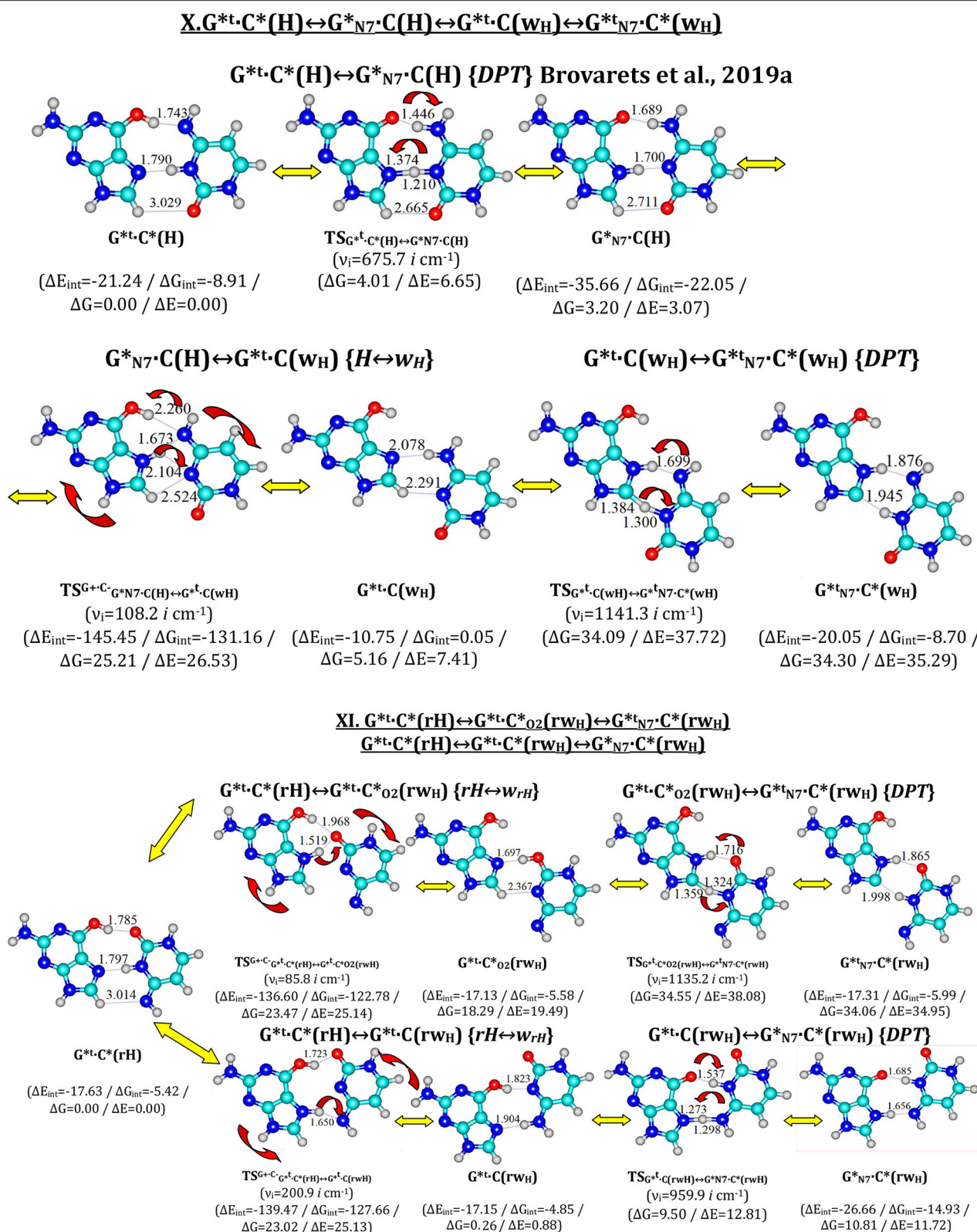


FIGURE 1 | Investigated pathways of the tautomeric wobblization of the biologically-important G•C nucleobase pairs – $G^* \cdot C^*(r_{wH})$, $G^* \cdot C^*(H)$ and $G^* \cdot C^*(rH)$ pairs obtained at the MP2/6-311++G(2df,pd)//B3LYP/6-311++G(d,p) level of QM theory. ΔG -relative Gibbs free energy and ΔE -electronic energy (in kcal·mol⁻¹; MP2/6-311++G(2df,pd)//B3LYP/6-311++G(d,p) level of QM theory); ΔE_{int} -electronic and ΔG_{int} -Gibbs free energies of the interaction (MP2/6-311++G(2df,pd)//B3LYP/6-311++G(d,p) level of QM theory, in kcal·mol⁻¹). ν_i -imaginary frequency. Intermolecular AH...B H-bonds are designated by dotted lines, their lengths H...B are presented in angstroms.

rWwc			
G••C•(rWC) $\Delta G=0.00$ / $\Delta E=0.00$	G•tN2•C(rWC) $\Delta G=24.74$ / $\Delta E=24.58$	G••C•(rWC) $\Delta G=4.44$ / $\Delta E=5.68$	G•C•o2(rWC) $\Delta G=3.51$ / $\Delta E=3.80$
G•C•(rWwc) $\Delta G=1.39$ / $\Delta E=2.29$	G••C•(rWwc) $\Delta G=1.40$ / $\Delta E=2.33$	G•tN2•C•(rWwc) $\Delta G=25.70$ / $\Delta E=26.96$	G••C•o2(rWwc) $\Delta G=17.31$ / $\Delta E=20.03$
G•t•C•o2(rWwc) $\Delta G=17.16$ / $\Delta E=18.65$	G••C•t•o2(rWwc) $\Delta G=18.09$ / $\Delta E=19.76$	G•t•C•t•o2(rWwc) $\Delta G=17.26$ / $\Delta E=18.61$	
G•tN2•C•(rWwc) $\Delta G=24.36$ / $\Delta E=25.54$	G••N2•C•t(rWwc) $\Delta G=24.54$ / $\Delta E=25.73$	G•tN2•C•t(rWwc) $\Delta G=23.56$ / $\Delta E=24.76$	
wH			
G•t•C•(H) $\Delta G=0.00$ / $\Delta E=0.00$	G••N7•C(H) $\Delta G=3.20$ / $\Delta E=3.07$	G•t•C•o2(wH) $\Delta G=17.07$ / $\Delta E=17.80$	G••N7•C•(wH) $\Delta G=16.43$ / $\Delta E=17.33$
G•t•C•t•o2(wH) $\Delta G=13.70$ / $\Delta E=14.37$	G••N7•C•t(wH) $\Delta G=12.04$ / $\Delta E=12.25$	G•t•C•(wH) $\Delta G=5.16$ / $\Delta E=7.41$	G••C•(wH) $\Delta G=3.25$ / $\Delta E=5.07$
G••N7•C•(wH) $\Delta G=30.33$ / $\Delta E=30.90$	G•t•N7•C•(wH) $\Delta G=34.30$ / $\Delta E=35.29$		
rWH			
G•t•C•(rH) $\Delta G=0.00$ / $\Delta E=0.00$	G•t•C•o2(rWH) $\Delta G=18.29$ / $\Delta E=19.49$	G•t•N7•C•(rWH) $\Delta G=34.06$ / $\Delta E=34.95$	G•t•C•(rWH) $\Delta G=0.26$ / $\Delta E=0.88$
G••N7•C•(rWH) $\Delta G=10.81$ / $\Delta E=11.72$			

FIGURE 2 | Total geometries of the investigated G•C nucleobase pairs, corresponding to the local minima, presented altogether with their relative Gibbs free energies ΔG and electronic energies (ΔE in kcal•mol⁻¹ under normal conditions) obtained at the MP2/6-311++G(2df,pd)//B3LYP/6-311++G(d,p) level of QM theory.

TABLE 1 | Energetic characteristics of the tautomers of the G•C nucleobase pairs obtained at the MP2/6-311++G(2df,pd)/B3LYP/6-311++G(d,p) level of QM theory in vacuum ($\epsilon = 1$) (see **Figure 2**).

N	G•C complex	ΔG^a	ΔE^b
rWC/rw_{WC}			
1	G ⁺ •C ⁺ (rWC)	0.00	0.00
2	G•C ⁺ (rw _{WC})	1.39	2.29
3	G ⁺ •C(rw _{WC})	1.40	2.33
4	G•C ⁺ O ₂ (rWC)	3.51	3.80
5	G ⁺ •C [−] (rWC)	4.44	5.68
6	G ⁺ •C ⁺ O ₂ (rw _{WC})	17.16	18.65
7	G ⁺ •C ⁺ O ₂ ⁺ (rw _{WC})	17.26	18.61
8	G ⁺ •C ⁺ O ₂ (rw _{WC})	17.31	20.03
9	G ⁺ •C ⁺ O ₂ ⁺ (rw _{WC})	18.09	19.76
10	G ⁺ •C ⁺ N ₂ ⁺ (rw _{WC})	24.36	25.54
11	G ⁺ •C ⁺ N ₂ ⁺ (rw _{WC})	24.54	25.73
12	G ⁺ •C ⁺ N ₂ ⁺ (rw _{WC})	23.56	24.76
13	G ⁺ •C ⁺ N ₂ ⁺ (rWC)	24.74	24.58
14	G ⁺ •C ⁺ N ₂ ⁺ (rw _{WC})	25.70	26.96
H/w_H			
15	G ⁺ •C ⁺ (H)	0.00	0.00
16	G ⁺ •N ₇ •C(H)	3.20	3.07
17	G ⁺ •C(w _H)	3.25	5.07
18	G ⁺ •C(w _H)	5.16	7.41
19	G ⁺ •N ₇ •C ⁺ (w _H)	12.04	12.25
20	G ⁺ •C ⁺ O ₂ ⁺ (w _H)	13.70	14.37
21	G ⁺ •N ₇ •C ⁺ (w _H)	16.43	17.33
22	G ⁺ •C ⁺ O ₂ ⁺ (w _H)	17.07	17.80
23	G ⁺ •N ₇ •C ⁺ (w _H)	30.33	30.90
24	G ⁺ •N ₇ •C ⁺ (w _H)	34.30	35.29
rHrw_H			
25	G ⁺ •C ⁺ (rH)	0.00	0.00
26	G ⁺ •C(rw _H)	0.26	0.88
27	G ⁺ •N ₇ •C ⁺ (rw _H)	10.81	11.72
28	G ⁺ •C ⁺ O ₂ ⁺ (rw _H)	18.29	19.49
29	G ⁺ •N ₇ •C ⁺ (rw _H)	34.06	34.95

^aRelative Gibbs free energy ($T=298.15\text{ K}$), $\text{kcal}\cdot\text{mol}^{-1}$.

^bRelative electronic energy, $\text{kcal}\cdot\text{mol}^{-1}$.

Its characteristic structural specificity has significant non-planarity and out-of-plane deformation of the purine ring of the O6H, N1H, and N2H atomic groups with *trans*-orientation relatively to the neighboring C2N3 bond.

- Further, it was found out that Löwdin's G⁺•C⁺(WC) DNA base pair, which is formed from the classic G•C(WC) DNA base pair through the DPT and is stabilized by the participation of the three intermolecular (G)O6H...N4(C), (C)N3H...N1(G), and (G)N2H...O2(C) H-bonds (Brovarets' and Hovorun, 2014a), does not tautomerize in the wobble manner.

In this case all localized transition states of tautomerization in this manner and its pathways are the same as in the case of the wobble mutagenic tautomerization of the G•C(WC) DNA base pair, which has been investigated and described earlier (Brovarets'

and Hovorun, 2015a). In other words, in order to tautomerize in the wobble-manner, the Löwdin's G⁺•C⁺(WC) DNA base pair should revert back to the classic G•C(WC) configuration (form) (Brovarets' and Hovorun, 2015a, 2018).

This bright fact allows us to claim that the functional role of the tautomeric G•C(WC)→G⁺•C⁺(WC) transition consists in the removal of the steric obstacles for the conformational G•C(WC)→G⁺•C⁺(rWC) transition (Brovarets' et al., 2019a) and is not directly related to the origin of the spontaneous point mutations—transitions and transversions, as it was suggested earlier (please, refer to work (Brovarets' and Hovorun, 2014a) and references provided therein for more details).

This aforementioned conformational transition, in its turn, guarantees the integration of the G•C(WC) nucleobase pair into the DNA/RNA with parallel strands.

- Opposite to the previously considered methods both the so-called correct and incorrect DNA base pairs (Brovarets' and Hovorun, 2009, 2015a,b,c,d,e,f; Brovarets' and Hovorun, 2018), the process of the tautomeric wobblization in the investigated G⁺•C⁺(rWC) (**Figure 1**, parts II and III), and G⁺•C⁺(H) (**Figure 1**, part X) base pairs is preceded by the process of the tautomerization *via* the single proton transfer (SPT). At this point, both processes of the wobblization of the G⁺•C⁺(rWC) base pair occur through the joint intermediate—tight G⁺•C[−] ion pair, which is stabilized by the participation of the three (G)O6⁺H...O2[−](C), (G)N1⁺H...N3[−](C), and (G)N2⁺H...N4[−]H(C) H-bonds (Brovarets' and Hovorun, 2014a). This dynamically non-stable intermediate is associated with the local minimum on potential (electronic) energy surface (PES). This situation is observed for the first time. Up until now the commonly accepted idea, that mutagenic tautomerization of the classic DNA base pairs is assisted by the intermediate corresponding to the local minimum on the PES, has not been confirmed.

The first process of the tautomeric wobblization of the G⁺•C⁺(rWC) base pair (**Figure 1**, part II)—G⁺•C⁺(rWC)↔G•C⁺O₂⁺(rWC)↔G•C⁺(rw_{WC})↔G⁺•C(rw_{WC})—is most likely tightly connected with the incorporation of the G•C(WC) base pair into the DNA/RNA with parallel strands (Watson and Crick, 1953b).

Another tautomerization process (**Figure 1**, part III)—G⁺•C⁺(rWC)↔G⁺•N₂•C⁺(rw_{WC})↔G⁺•C⁺O₂⁺(rw_{WC}), which proceeds through the unique TS_{G⁺•C⁺−(rWC)↔G⁺•C⁺O₂⁺(rw_{WC})} path with the (G)N1-H-O2(C) covalent bridge, is most probably concerned with the mechanisms of maintaining the RNA spatial architecture due to the incorporation of the non-stable (in the main tautomeric state) Levitt base pair (Crick and Watson, 1954; Levitt, 1969). This suggestion is based on the established structural mechanism of the tautomeric interconversion of the G⁺•C⁺(rWC) pair into the eight *stable planar tautomeric forms of the Levitt base pair* (Watson and Crick, 1953a) (**Figure 1**, parts IV–VI)—G⁺•C⁺O₂⁺(rw_{WC}), G⁺•C⁺O₂⁺(rw_{WC}), G⁺•C⁺O₂⁺(rw_{WC}), G⁺•C⁺O₂⁺(rw_{WC}), G⁺•C⁺O₂⁺(rw_{WC}), G⁺•C⁺O₂⁺(rw_{WC}), G⁺•C⁺O₂⁺(rw_{WC}), and G⁺•C⁺O₂⁺(rw_{WC}) (**Figure 2**,

Table 1)—and in principle, allows us to understand the dynamic of the formation of the Levitt base pair, which has not been considered before in the literature. It would be interesting to investigate how the tautomers of the Levitt base pair is stabilized in RNA by the H-bonds and surrounding environment further in the future (Oliva et al., 2007).

4. A quite interesting situation is observed for the tautomeric wobblization of the $G^{*t}.C^*(H)$ base pair (**Figure 1**, part VII): $G^{*t}.C^*(H) \leftrightarrow G_{N7}^{*t}.C(C) \leftrightarrow G^{*t}.C^*_{O2}(w_H) \leftrightarrow G_{N7}^{*t}.C^*(w_H)$.

The transition of the C^*_{O2} tautomer of the cytosine (C) within the $G^{*t}.C^*_{O2}(w_H)$ base pairs with *cis*-orientation of the N4H C-imino group into the *trans*-orientation through its inversion leads to the decreasing of the energy in the tautomerization (**Figure 1**, part VIII): $G^{*t}.C^*_{O2}(w_H) \leftrightarrow G^{*t}.C^*_{O2}(w_H) \leftrightarrow G_{N7}^{*t}.C^*(w_H) \leftrightarrow G_{N7}^{*t}.C^*(w_H)$. This decreasing of energy occurs when the affinity of the C^*_{O2} tautomer according to the “complementary” G^{*t} tautomer is higher than the C^*_{O2} tautomer. This decreasing of the energy with excess overrides the increasing of the internal energy of the C^*_{O2} tautomer at its tautomerization $C^*_{O2} \rightarrow C^*_{O2}$.

In the another pathway of the tautomeric wobblization of the $G^{*t}.C^*(H)$ base pair (**Figure 1**, part VII, VIII) the decreasing of energy in the course of the process is achieved by the conformational transition of the G^{*t} tautomer within the $G^{*t}.C(w_H)$ complex into the low-energy mutagenic tautomeric form G_{N7}^{*t} , which is zwitterion.

5. At this, the $G^{*t}.C(w_H) \leftrightarrow G_{N7}^{*t}.C^*(w_H)$ DPT tautomerization process does not really occur, since its barrier is negative under normal conditions (**Figure 1**, part IX): $G^{*t}.C(w_H) \leftrightarrow G^{*t}.C(w_H) \leftrightarrow G_{N7}^{*t}.C^*(w_H) \leftrightarrow G_{N7}^{*t}.C^*(w_H)$. The same situation is also observed for the $G^{*t}.C^*(H) \leftrightarrow G_{N7}^{*t}.C(H) \leftrightarrow G^{*t}.C(w_H) \leftrightarrow G_{N7}^{*t}.C^*(w_H)$ DPT tautomerization (**Figure 1**, part X).
6. Tautomeric wobblization of the $G^{*t}.C^*(rH)$ base pair (**Figure 1**, part XI) occurs through the two traditional pathways without any preparatory SPT stages through the TSs, which represent themselves as the covalently bonded tight $G^+.C^-$ ion pairs in reverse Hoogsteen conformation, which are only supported by two H-bonds: $G^{*t}.C^*(rH) \leftrightarrow G^{*t}.C^*_{O2}(rw_H) \leftrightarrow G_{N7}^{*t}.C^*(rw_H)$ and $G^{*t}.C^*(rH) \leftrightarrow G^{*t}.C^*(rw_H) \leftrightarrow G_{N7}^{*t}.C^*(rw_H)$. The transition of the G^{*t} tautomer within the $G^{*t}.C^*_{O2}(rw_H)$ complex into the G^* mutagenic tautomer through the orthogonal TS decreases the energy of the further process of tautomerization.
7. Also, in addition to the previously revealed processes, DPT tautomerization was also fixed by the participation of the proton at the C8 carbon atom of G, which lead to the dynamically-stable, but short-lived, complexes by the participation of the yilidic forms of the G base (**Figure 1**, parts IX–XI).
8. Finally, there are three more fixed mysteries, which deserve more attention. Several G•C base pairs, in which both bases were in the rare tautomeric form and their energy of stabilization significantly exceeded the analogical values for the classic G•C(WC) DNA base pair were fixed.

Despite the structural softness of the heterocycles of the G and C bases for the out-of-plane deformational bending (Hovorun et al., 1999), it was not revealed that there was any deviation from the plane in the investigated processes of the tautomerization of the base pairs.

Obtained data convincingly show that among all possible tautomeric wobblizations of the $G^*.C^*(rWC)$, $G^{*t}.C^*(H)$, and $G^{*t}.C^*(rH)$ DNA base pairs, which possess Watson-Crick, Hoogsteen, and reverse Hoogsteen configurations and both monomers of which are in the rare tautomeric form, at least one non-dissociative transition was absent, which would recover the tautomeric status of both the G^*/G^{*t} and C^* bases to the canonical G and C bases, correspondingly. This fact altogether with the results, obtained in our previous work (Brovarets' et al., 2019a), soundly exhibits why the Watson-Crick DNA base pairs were chosen for the building of genetic material (Brovarets' et al., 2018a).

CONCLUSION

Concluding the obtained results, we arrived to a summation after providing an investigation of the tautomeric wobblization of the biologically-important G•C(WC), $G^*.C^*(WC)$, $G^*.C^*(rWC)$, $G^{*t}.C^*(H)$, and $G^{*t}.C^*(rH)$ nucleobase pairs and extended the existing thoughts about the microstructural mechanisms of these processes, as well as about their functional roles. Thus, it was established that the G•C base pair is the most likely to be incorporated into the DNA/RNA double helix with parallel strands in the form of the $G^*.C^*_{O2}(rWC)$, $G^*.C^*(rw_{WC})$, and $G^*.C(rw_{WC})$ tautomers, which are in rapid tautomeric equilibrium with each other.

For the first time we have formulated rules, defining these biologically-important processes.

DATA AVAILABILITY STATEMENT

All datasets generated for this study are included in the article/supplementary material.

AUTHOR CONTRIBUTIONS

OB: idea formulation, setting of the task, calculation of the data, building of the graphs, data extrapolation, preparing, and proofreading of the draft of the manuscript. AM: idea formulation, calculation of the data, building of the graphs, preparing, and proofreading of the draft of the manuscript. DH: idea formulation, preparing, and proofreading of the draft of the manuscript. All authors contributed to the article and approved the submitted version.

ACKNOWLEDGMENTS

Authors sincerely grateful for computational facilities of joint computer cluster of SSI Institute for Single Crystals of the National Academy of Sciences of Ukraine (NASU) and Institute for Scintillation Materials of the NASU incorporated into Ukrainian National Grid.

REFERENCES

- Alvey, H. S., Gottardo, F. L., Nikolova, E. N., and Al-Hashimi, H. M. (2014). Widespread transient Hoogsteen base-pairs in canonical duplex DNA with variable energetics. *Nat. Comm.* 5, 4786–4794. doi: 10.1038/ncomms5786
- Atkins, P. W. (1998). *Physical Chemistry*. Oxford: Oxford University Press.
- Bader, R. F. W. (1990). *Atoms in Molecules: A Quantum Theory*. Oxford: Oxford University Press.
- Bayley, S. T. (1951). The dielectric properties of various solid crystalline proteins, amino acids and peptides. *Trans. Faraday Soc.* 47, 509–517. doi: 10.1039/tf9514700509
- Boys, S. F., and Bernardi, F. (1970). The calculation of small molecular interactions by the differences of separate total energies. Some procedures with reduced errors. *Mol. Phys.* 19, 553–566. doi: 10.1080/00268977000101561
- Brovarets', O. O., and Hovorun, D. M. (2009). Physicochemical mechanism of the wobble DNA base pairs Gua•Thy and Ade•Cyt transition into the mismatched base pairs Gua*•Thy and Ade•Cyt* formed by the mutagenic tautomers. *Ukr. Bioorg. Acta* 8, 12–18.
- Brovarets', O. O., and Hovorun, D. M. (2010a). Quantum-chemical investigation of tautomerization ways of Watson-Crick DNA base pair guanine-cytosine. *Ukr. Biochem. J.* 82, 55–60.
- Brovarets', O. O., and Hovorun, D. M. (2010b). Quantum-chemical investigation of the elementary molecular mechanisms of pyrimidine-purine transversions. *Ukr. Biochem. J.* 82, 57–67.
- Brovarets', O. O., and Hovorun, D. M. (2014a). Why the tautomerization of the G-C Watson-Crick base pair via the DPT does not cause point mutations during DNA replication? QM and QTAIM comprehensive analysis. *J. Biomol. Struct. Dynam.* 32, 1474–1499. doi: 10.1080/07391102.2013.822829
- Brovarets', O. O., and Hovorun, D. M. (2014b). Can tautomerisation of the A-T Watson-Crick base pair via double proton transfer provoke point mutations during DNA replication? A comprehensive QM and QTAIM analysis. *J. Biomol. Struct. Dynam.* 32, 127–154. doi: 10.1080/07391102.2012.755795
- Brovarets', O. O., and Hovorun, D. M. (2015a). New structural hypostases of the A-T and G-C Watson-Crick DNA base pairs caused by their mutagenic tautomerisation in a wobble manner: a QM/QTAIM prediction. *RSC Adv.* 5, 99594–99605. doi: 10.1039/C5RA19971A
- Brovarets', O. O., and Hovorun, D. M. (2015b). Tautomeric transition between wobble A-C DNA base mispair and Watson-Crick-like A-C* mismatch: microstructural mechanism and biological significance. *Phys. Chem. Chem. Phys.* 17, 15103–15110. doi: 10.1039/C5CP01568E
- Brovarets', O. O., and Hovorun, D. M. (2015c). How many tautomerisation pathways connect Watson-Crick-like G*•T DNA base mispair and wobble mismatches? *J. Biomol. Struct. Dynam.* 33, 2297–2315. doi: 10.1080/07391102.2015.1046936
- Brovarets', O. O., and Hovorun, D. M. (2015d). Wobble↔Watson-Crick tautomeric transitions in the homo-purine DNA mismatches: a key to the intimate mechanisms of the spontaneous transversions. *J. Biomol. Struct. Dynam.* 33, 2710–2715. doi: 10.1080/07391102.2015.1077737
- Brovarets', O. O., and Hovorun, D. M. (2015e). Novel physico-chemical mechanism of the mutagenic tautomerisation of the Watson-Crick-like A-G and C-T DNA base mispairs: a quantum-chemical picture. *RSC Adv.* 5, 66318–66333. doi: 10.1039/C5RA11773A
- Brovarets', O. O., and Hovorun, D. M. (2015f). A novel conception for spontaneous transversions caused by homo-pyrimidine DNA mismatches: a QM/QTAIM highlight. *Phys. Chem. Chem. Phys.* 17, 21381–21388. doi: 10.1039/C5CP03211C
- Brovarets', O. O., and Hovorun, D. M. (2015g). The nature of the transition mismatches with Watson-Crick architecture: the G*•T or G-T* DNA base mispair or both? A QM/QTAIM perspective for the biological problem. *J. Biomol. Struct. Dynam.* 33, 925–945. doi: 10.1080/07391102.2014.924879
- Brovarets', O. O., and Hovorun, D. M. (2018). "Renaissance of the tautomeric hypothesis of the spontaneous point mutations in DNA: new ideas and computational approaches," in *Mitochondrial DNA—New Insights*, ed Herve Seligmann (London: IntechOpen), 31–55. doi: 10.5772/intechopen.77366
- Brovarets', O. O., Oliynyk, T. A., and Hovorun, D. M. (2019a). Novel tautomerisation mechanisms of the biologically important conformers of the reverse Löwdin, Hoogsteen, and reverse Hoogsteen G*•C DNA base pairs via proton transfer: a quantum-mechanical survey. *Front. Chem.* 7:597. doi: 10.3389/fchem.2019.00597
- Brovarets', O. O., Oliynyk, T. A., and Hovorun, D. M. (2019b). "Novel conformers of the G-C DNA base pair and their mutual interconversions via the proton transfer: a quantum-mechanical study" in *Joint 12th EBSC Congress and 10th ICBP-IUPAP Congress*, Vol. 48 (Madrid), S90. doi: 10.1007/s00249-019-01373-4
- Brovarets', O. O., Tsiupa, K. S., Dinets, A., and Hovorun, D. M. (2018c). Unexpected routes of the mutagenic tautomerization of the T nucleobase in the classical A-T DNA base pairs: A QM/QTAIM comprehensive view. *Front. Chem.* 6:532. doi: 10.3389/fchem.2018.00532
- Brovarets', O. O., Tsiupa, K. S., and Hovorun, D. M. (2018a). The A-T(rWC)/A-T(H)/A-T(rH) ↔ A-T*(r_{WC})/A-T*(w_H)/A-T*(r_H) mutagenic tautomerization via sequential proton transfer: a QM/QTAIM study. *RSC Adv.* 8, 13433–13445. doi: 10.1039/C8RA01446A
- Brovarets', O. O., Tsiupa, K. S., and Hovorun, D. M. (2018b). Unexpected A-T(WC)↔A-T(rWC)/A-T(rH) and A-T(H)↔A-T(rH)/A-T(rWC) conformational transitions between the classical A-T DNA base pairs: A QM/QTAIM comprehensive study. *Int. J. Quantum. Chem.* 118:e25674. doi: 10.1002/qua.25692
- Brovarets', O. O., Tsiupa, K. S., and Hovorun, D. M. (2018d). Non-dissociative structural transitions of the Watson-Crick and reverse Watson-Crick A-T DNA base pairs into the Hoogsteen and reverse Hoogsteen forms. *Sci. Repts.* 8:10371. doi: 10.1038/s41598-018-28636-y
- Brovarets', O. O., Tsiupa, K. S., and Hovorun, D. M. (2018e). Novel pathway for mutagenic tautomerization of classical A-T DNA base pairs via sequential proton transfer through quasi-orthogonal transition states: a QM/QTAIM investigation. *PLoS ONE* 13:e0199044. doi: 10.1371/journal.pone.0199044
- Brovarets', O. O., Tsiupa, K. S., and Hovorun, D. M. (2018f). Surprising conformers of the biologically important A-T DNA base pairs: QM/QTAIM proofs. *Front. Chem.* 6:8. doi: 10.3389/fchem.2018.00008
- Brovarets', O. O., Zhuravivsky, R. O., and Hovorun, D. M. (2014). Does the tautomeric status of the adenine bases change upon the dissociation of the A*•A_{syn} Topal-Fresco DNA mismatch? A combined QM and QTAIM atomistic insight. *Phys. Chem. Chem. Phys.* 16, 3715–3725. doi: 10.1039/c3cp54708f
- Brovarets', O. O., Zhuravivsky, R. O., and Hovorun, D. M. (2015). DPT tautomerisation of the wobble guanine-thymine DNA base mispair is not mutagenic: QM and QTAIM arguments. *J. Biomol. Struct. Dynam.* 33, 674–689. doi: 10.1080/07391102.2014.897259
- Crick, F. H. C., and Watson, J. D. (1954). The complementary structure of deoxyribonucleic acid. *Proc. Roy. Soc. A* 223, 80–96. doi: 10.1098/rspa.1954.0101
- Cukrowski, I., and Matta, C. F. (2010). Hydrogen-hydrogen bonding: a stabilizing interaction in strained chelating rings of metal complexes in aqueous phase. *Chem. Phys. Lett.* 499, 66–69. doi: 10.1016/j.cplett.2010.09.013
- Dewar, M. J. S., and Storch, D. M. (1985). Alternative view of enzyme reactions. *Proc. Natl. Acad. Sci. U. S. A.* 82, 2225–2229. doi: 10.1073/pnas.82.8.2225
- El-Sayed, A. A., Tamara Molina, A., Alvarez-Ros, M. C., and Alcolea Palafox, M. (2015). Conformational analysis of the anti-HIV Nikavir prodrug: comparisons with AZT and thymidine, and establishment of structure-activity relationships/tendencies in other 6'-derivatives. *J. Biomol. Struct. Dynam.* 33, 723–748. doi: 10.1080/07391102.2014.909743
- Florian, J., Hroudá, V., and Hobza, P. (1994). Proton transfer in the adenine-thymine base pair. *J. Am. Chem. Soc.* 116, 1457–1460. doi: 10.1021/ja00083a034
- Frisch, M. J., Head-Gordon, M., and Pople, J. A. (1990). Semi-direct algorithms for the MP2 energy and gradient. *Chem. Phys. Lett.* 166, 281–289. doi: 10.1016/0009-2614(90)80030-H
- Frisch, M. J., Trucks, G. W., Schlegel, H. B., Scuseria, G. E., Robb, M. A., Cheeseman, J. R., et al. (2010). *GAUSSIAN 09 (Revision B.01)*. Wallingford CT: Gaussian Inc.
- García-Moreno, B. E., Dwyer, J. J., Gittis, A. G., Lattman, E. E., Spencer, D. S., and Stites, W. E. (1997). Experimental measurement of the effective dielectric in the hydrophobic core of a protein. *Biophys. Chem.* 64, 211–224. doi: 10.1016/S0301-4622(96)02238-7
- Godbeer, A. D., Al-Khalili, J. S., and Stevenson, P. D. (2015). Modelling proton tunnelling in the adenine-thymine base pair. *Phys. Chem. Chem. Phys.* 17, 13034–13044. doi: 10.1039/C5CP00472A

- Gorb, L., Podolyan, Y., Dziekonski, P., Sokalski, W. A., and Leszczynski, J. (2004). Double-proton transfer in adenine–thymine and guanine–cytosine base pairs. A post Hartree–Fock *ab initio* study. *J. Am. Chem. Soc.* 126, 10119–10129. doi: 10.1021/ja049155n
- Gutowski, M., Van Lenthe, J. H., Verbeek, J., Van Duijneveldt, F. B., and Chalasinski, G. (1986). The basis set superposition error in correlated electronic structure calculations. *Chem. Phys. Lett.* 124, 370–375. doi: 10.1016/0009-2614(86)85036-9
- Hariharan, P. C., and Pople, J. A. (1973). The influence of polarization functions on molecular orbital hydrogenation energies. *Theor. Chim. Acta* 28, 213–222. doi: 10.1007/BF00533485
- Hovorun, D. M., Gorb, L., and Leszczynski, J. (1999). From the nonplanarity of the amino group to the structural nonrigidity of the molecule: a post-Hartree–Fock *ab initio* study of 2-aminoimidazole. *Int. J. Quantum. Chem.* 75, 245–253. doi: 10.1002/(SICI)1097-461X(1999)75:3<245::AID-QUA14>3.0.CO;2-0
- Keith, T. A. (2010). *AIMall (Version 10.07.01)*. Available online at: aim.tkgristmill.com (accessed October 23, 2020).
- Kendall, R. A., Dunning, J. R., T. H., and Harrison, R. J. (1992). Electron affinities of the first-row atoms revisited. Systematic basis sets and wave functions. *J. Chem. Phys.* 96, 6796–6806. doi: 10.1063/1.462569
- Krishnan, R., Binkley, J. S., Seeger, R., and Pople, J. A. (1980). Self-consistent molecular orbital methods. XX. A basis set for correlated wave functions. *J. Chem. Phys.* 72, 650–654. doi: 10.1063/1.438955
- Lecomte, C., Espinosa, E., and Matta, C. F. (2015). On atom–atom “short contact” bonding interactions in crystals. *IUCr* 2, 161–163. doi: 10.1107/S2052252515002067
- Lee, C., Yang, W., and Parr, R. G. (1988). Development of the Colle–Salvetti correlation-energy formula into a functional of the electron density. *Phys. Rev. B* 37, 785–789. doi: 10.1103/PhysRevB.37.785
- Levitt, M. (1969). Detailed molecular model for transfer ribonucleic acid. *Nature* 224, 759–763. doi: 10.1038/224759a0
- Löwdin, P.-O. (1963). Proton tunneling in DNA and its biological implications. *Rev. Mod. Phys.* 35, 724–732. doi: 10.1103/RevModPhys.35.724
- Löwdin, P.-O. (1966). “Quantum genetics and the aperiodic solid: some aspects on the biological problems of heredity, mutations, aging, and tumors in view of the quantum theory of the DNA molecule,” in *Advances in Quantum Chemistry*, ed P.-O. Löwdin (New York, NY; London: Academic Press), 213–360. doi: 10.1016/S0065-3276(08)60076-3
- Matta, C. F. (2010). How dependent are molecular and atomic properties on the electronic structure method? Comparison of Hartree–Fock, DFT, and MP2 on a biologically relevant set of molecules. *J. Comput. Chem.* 31, 1297–1311. doi: 10.1002/jcc.21417
- Matta, C. F. (2014). Modeling biophysical and biological properties from the characteristics of the molecular electron density, electron localization and delocalization matrices, and the electrostatic potential. *J. Comput. Chem.* 35, 1165–1198. doi: 10.1002/jcc.23608
- Matta, C. F., Castillo, N., and Boyd, R. J. (2006). Atomic contributions to bond dissociation energies in aliphatic hydrocarbons. *J. Chem. Phys.* 125:204103. doi: 10.1063/1.2378720
- Matta, C. F., and Hernández-Trujillo, J. (2003). Bonding in polycyclic aromatic hydrocarbons in terms of the electron density and of electron delocalization. *J. Phys. Chem. A* 107, 7496–7504. doi: 10.1021/jp034952d
- Mertz, E. L., and Krishtalik, L. I. (2000). Low dielectric response in enzyme active site. *Proc. Natl. Acad. Sci. U. S. A.* 97, 2081–2086. doi: 10.1073/pnas.050316997
- Nikolova, E. N., Zhou, H., Gottardo, F. L., Alvey, H. S., Kimsey, I. J., and Al-Hashimi, H. M. (2014). A historical account of Hoogsteen base pairs in duplex DNA. *Biopolymers* 99, 955–968. doi: 10.1002/bip.22334
- Oliva, R., Tramontano, A., and Cavallo, L. (2007). Mg²⁺ binding and archaeosine modification stabilize the G15–C48 Levitt base pair in tRNAs. *RNA* 13, 1427–1436. doi: 10.1261/rna.574407
- Palafox, M. A. (2014). Molecular structure differences between the antiviral nucleoside analogue 5-iodo-2'-deoxyuridine and the natural nucleoside 2'-deoxythymidine using MP2 and DFT methods: conformational analysis, crystal simulations, DNA pairs and possible behavior. *J. Biomol. Struct. Dynam.* 32, 831–851. doi: 10.1080/07391102.2013.789402
- Parr, R. G., and Yang, W. (1989). *Density-Functional Theory of Atoms and Molecules*. Oxford: Oxford University Press.
- Peng, C., Ayala, P. Y., Schlegel, H. B., and Frisch, M. J. (1996). Using redundant internal coordinates to optimize equilibrium geometries and transition states. *J. Comput. Chem.* 17, 49–56. doi: 10.1002/(SICI)1096-987X(19960115)17:1<49::AID-JCC5>3.0.CO;2-0
- Petrushka, J., Sowers, L. C., and Goodman, M. (1986). Comparison of nucleotide interactions in water, proteins, and vacuum: model for DNA polymerase fidelity. *Proc. Natl. Acad. Sci. U. S. A.* 83, 1559–1562. doi: 10.1073/pnas.83.6.1559
- Poltev, V. I., Anisimov, V. M., Sanchez, C., Deriabina, A., Gonzalez, E., Garcia, D., et al. (2016). Analysis of the conformational features of Watson–Crick duplex fragments by molecular mechanics and quantum mechanics methods. *Biophysics* 61, 217–226. doi: 10.1134/S0006350916020160
- Pous, J., Urpi, L., Subirana, J. A., Gouyette, C., Navaza, J., and Campos, J. L. (2008). Stabilization by extra-helical thymine of a DNA duplex with Hoogsteen base pairs. *J. Am. Chem. Soc.* 130, 6755–6760. doi: 10.1021/ja078022+
- Saenger, W. (1984). *Principles of Nucleic Acid Structure*. New York, NY: Springer. doi: 10.1007/978-1-4612-5190-3
- Sordo, J. A. (2001). On the use of the Boys–Bernardi function counterpoise procedure to correct barrier heights for basis set superposition error. *J. Mol. Struct.* 537, 245–251. doi: 10.1016/S0166-1280(00)00681-3
- Sordo, J. A., Chin, S., and Sordo, T. L. (1988). On the counterpoise correction for the basis set superposition error in large systems. *Theor. Chim. Acta* 74, 101–110. doi: 10.1007/BF00528320
- Srivastava, R. (2019). The role of proton transfer on mutations. *Front. Chem.* 7:536. doi: 10.3389/fchem.2019.00536
- Szabat, M., and Kierzek, R. (2017). Parallel-stranded DNA and RNA duplexes: structural features and potential applications. *FEBS J.* 284, 3986–3998. doi: 10.1111/febs.14187
- Tirado-Rives, J., and Jorgensen, W. L. (2008). Performance of B3LYP density functional methods for a large set of organic molecules. *J. Chem. Theory Comput.* 4, 297–306. doi: 10.1021/ct700248k
- Total, M. D., and Fresco, J. R. (1976). Complementary base pairing and the origin of substitution mutations. *Nature* 263, 285–289. doi: 10.1038/263285a0
- Turaeva, N., and Brown-Kennerly, V. (2015). Marcus model of spontaneous point mutation in DNA. *Chem. Phys.* 461, 106–110. doi: 10.1016/j.chemphys.2015.09.005
- Watson, J. D., and Crick, F. H. C. (1953a). Molecular structure of nucleic acids: a structure for deoxyribose nucleic acid. *Nature* 171, 737–738. doi: 10.1038/171737a0
- Watson, J. D., and Crick, F. H. C. (1953b). The structure of DNA. *Cold. Spring Harb. Symp. Quant. Biol.* 18, 123–131. doi: 10.1101/SQB.1953.018.01.020

Conflict of Interest: The authors declare that the research was conducted in the absence of any commercial or financial relationships that could be construed as a potential conflict of interest.

Copyright © 2020 Brovarets', Muradova and Hovorun. This is an open-access article distributed under the terms of the Creative Commons Attribution License (CC BY). The use, distribution or reproduction in other forums is permitted, provided the original author(s) and the copyright owner(s) are credited and that the original publication in this journal is cited, in accordance with accepted academic practice. No use, distribution or reproduction is permitted which does not comply with these terms.

Advantages of publishing in Frontiers



OPEN ACCESS

Articles are free to read
for greatest visibility
and readership



FAST PUBLICATION

Around 90 days
from submission
to decision



HIGH QUALITY PEER-REVIEW

Rigorous, collaborative,
and constructive
peer-review



TRANSPARENT PEER-REVIEW

Editors and reviewers
acknowledged by name
on published articles

Frontiers

Avenue du Tribunal-Fédéral 34
1005 Lausanne | Switzerland

Visit us: www.frontiersin.org

Contact us: frontiersin.org/about/contact



REPRODUCIBILITY OF RESEARCH

Support open data
and methods to enhance
research reproducibility



DIGITAL PUBLISHING

Articles designed
for optimal readership
across devices



FOLLOW US

@frontiersin



IMPACT METRICS

Advanced article metrics
track visibility across
digital media



EXTENSIVE PROMOTION

Marketing
and promotion
of impactful research



LOOP RESEARCH NETWORK

Our network
increases your
article's readership